

Jet Physics
with
A Large Ion Collider Experiment
at the
Large Hadron Collider

Jochen Klein

Dissertation
submitted to the
Combined Faculties for the Natural Sciences and for Mathematics
of the Ruperto-Carola University of Heidelberg, Germany,
for the degree of
Doctor of Natural Sciences

put forward by

Dipl.–Phys. Jochen Klein

born in Mainz, Germany

Oral Examination: November 12th, 2014

Jet Physics
with
A Large Ion Collider Experiment
at the
Large Hadron Collider

Referees: Prof. Dr. Johanna Stachel
Prof. Dr. Ulrich Uwer

Abstract

In the presence of the strongly-interacting medium created in relativistic heavy-ion collisions, highly energetic partons from hard interactions lose energy through scattering and radiating. This effect, referred to as jet quenching, is observed as a suppression of particles with large momenta transverse to the beam axis (high- p_{\perp}). To study the impact of the medium evolution on the energy loss modelling in the Monte Carlo event generator JEWEL, we compare results obtained for different scenarios of Au–Au collisions at $\sqrt{s_{\text{NN}}} = 200$ GeV. For this purpose, JEWEL was extended to use the output of relativistic hydrodynamic calculations in the OSCAR2008H format. We find the modelling of common observables, e.g. the nuclear modification factor, to be rather insensitive to the details of the medium evolution, for which the analytically accessible Bjorken expansion can thus be considered adequate. The OSCAR interface now allows further studies also at LHC energies.

Jets of large transverse momentum are interesting yet rare probes. An online selection of relevant events is required to accumulate sufficient statistics in the experiments. Such a trigger was implemented into the Transition Radiation Detector (TRD) of ALICE. It requires the presence of several geometrically close high- p_{\perp} tracks. In the first LHC run, the operation of the TRD trigger comprised the preparation of the front-end electronics and the commissioning of the online tracking to ensure reliable data taking. From 2012 onwards, the TRD triggers were operated successfully in pp collisions at $\sqrt{s} = 8$ TeV and $\sqrt{s} = 2.76$ TeV as well as p–Pb collisions at $\sqrt{s_{\text{NN}}} = 5.02$ TeV. The recorded data show no bias in the measured spectra and fragmentation functions for charged jets with transverse momenta above ~ 100 GeV/ c .

The response of the medium to a traversing parton was studied by the measurement of correlations between a trigger jet and associated hadrons. Different proton abundances in jets and medium hadronization motivate the comparison of inclusive and proton associates, which is possible with the particle identification capabilities of ALICE. The measurements of jet-hadron and jet-proton azimuthal correlations in Pb–Pb collisions at $\sqrt{s_{\text{NN}}} = 2.76$ TeV show a reduced proton yield in the near-side ($\Delta\varphi \simeq 0$) peak. The away-side ($\Delta\varphi \simeq \pi$) peaks are consistent with each other even though a reduced proton yield seems to be favoured in the analyzed data set. A more conclusive statement on this result will require the analysis of further data with higher statistics.

Zusammenfassung

Hochenergetische Partonen aus harten Wechselwirkungen verlieren in Gegenwart eines stark-wechselwirkenden Mediums, wie es in relativistischen Schwerionenkollisionen erzeugt wird, Energie durch Streuung und Strahlung. Dieser Effekt wird als Unterdrückung von Teilchen mit hohem Impuls transversal zur Strahlachse (p_{\perp}) beobachtet und als „Jet Quenching“ bezeichnet. Um den Einfluss der Mediumentwicklung auf die Modellierung des Energieverlusts in dem Monte Carlo Generator JEWEL zu untersuchen, vergleichen wir Ergebnisse für verschiedene Mediumszenarien. Hierzu wurde JEWEL so erweitert, dass die Ergebnisse aus Berechnungen relativistischer Hydrodynamik im OSCAR2008H Format in JEWEL verwendet werden können. Wir finden keine große Abhängigkeit der Modellierung gängiger Jet Quenching Observablen von den Details der hydrodynamischen Entwicklung, für die damit die analytisch zugängliche Bjorken Expansion als adäquat angesehen werden kann.

Jets mit hohem Transversalimpuls sind interessante, aber seltene Sonden. Eine online Auswahl relevanter Ereignisse ist notwendig, um im Experiment Daten mit ausreichender Statistik aufzuzeichnen. Ein solcher Trigger wurde im Übergangsstrahlungsdetektor (TRD) von ALICE implementiert, indem eine Mindestzahl von eng benachbarten Teilchenspuren mit hohem p_{\perp} gefordert wird. Für den Betrieb im ersten LHC Run wurden die Front-End Elektronik und das online Tracking für eine stabile Datennahme vorbereitet. Von 2012 an wurden die TRD Trigger sowohl in pp Kollisionen bei $\sqrt{s} = 8$ TeV und $\sqrt{s} = 2.76$ TeV als auch in p-Pb Kollisionen bei $\sqrt{s_{NN}} = 5.02$ TeV erfolgreich betrieben. Die aufgezeichneten Daten zeigen keinen Bias in Spektren und Fragmentationsfunktionen für geladene Jets oberhalb von 100 GeV/c.

Die Reaktion des Mediums auf ein es durchquerendes Parton wurde mit der Messung von Korrelationen zwischen einem Triggerjet und assoziierten Hadronen untersucht. Der unterschiedliche Protonanteil in Jets und Mediumhadronisierung motiviert den Vergleich von assoziierten Hadronen und Protonen. Durch die Detektoren zur Teilchenidentifizierungen ist dies in ALICE möglich. Die Messungen azimuthaler Jet-Hadron und Jet-Proton Korrelationen in Pb-Pb Kollisionen bei $\sqrt{s_{NN}} = 2.76$ TeV zeigen eine reduzierte Anzahl von Protonen im Peak um das Triggerteilchen ($\Delta\varphi \simeq 0$). Auf der dem Trigger-Jet abgewandten Seite ($\Delta\varphi \simeq \pi$) sind die Korrelationsfunktionen miteinander konsistent, wobei in den analysierten Daten auch hier eine Protonreduktion favorisiert wird. Ein signifikantes Ergebnis erfordert die Analyse weiterer Daten mit höherer Statistik.

Contents

1	Introduction	1
1.1	Heavy-ion collisions	3
1.2	Relativistic hydrodynamics	6
1.3	Partonic energy loss	7
1.4	Experiments and measurements	8
1.5	Outline	10
2	Jet quenching in evolving media	13
2.1	Jet Evolution With Energy Loss (JEWEL)	14
2.2	Medium implementation	16
2.2.1	Bjorken medium	17
2.3	Interface to hydro-dynamical calculations	20
2.4	Impact on observables	22
2.4.1	Nuclear modification factor	26
2.4.2	Azimuthally sensitive R_{AA}	27
2.4.3	High- p_{\perp} v_2	29
2.5	Conclusions	30
3	Experimental access	33
3.1	Large Hadron Collider	33
3.1.1	Experiments at the LHC	35
3.2	ALICE at the LHC	36
3.2.1	Detector setup	37
3.2.2	Triggering and read-out	39
3.3	Transition Radiation Detector in ALICE	40
3.3.1	Front-end electronics	42
3.4	Reconstruction, simulation, and analysis	42
3.5	Jet finding in ALICE	44
4	Triggering with the TRD	47
4.1	Pretrigger system	49
4.2	On-line tracking	52
4.2.1	Local tracking	54
4.2.2	Local tracking simulation	60
4.2.3	Global tracking	61
4.2.4	Integration into the computing framework	62
4.2.5	Performance and quality assurance	63
4.3	Level-1 trigger	69

4.3.1	Commissioning	72
4.3.2	Trigger requests	75
4.3.3	Data taking	75
4.3.4	Performance of the jet trigger	77
4.4	Conclusions	82
5	Jet-hadron correlations	87
5.1	Analysis motivation from theory	88
5.2	Analysis outline	89
5.3	Correlation analysis	91
5.3.1	Event mixing	93
5.3.2	Experimental realization	94
5.4	Event selection and classification	95
5.4.1	Event selection	95
5.4.2	Centrality	96
5.4.3	Event plane	96
5.5	Track selection	98
5.6	Jet reconstruction	100
5.7	Proton identification	101
5.7.1	Specific energy loss	102
5.7.2	Time of flight	106
5.7.3	Efficiency and contamination	108
5.8	Correlation functions	113
5.9	Systematic effects	122
5.9.1	Jet selection	122
5.9.2	Flow-induced effects	122
5.9.3	Proton identification	124
5.9.4	Tracking efficiency	125
5.10	Interpretation	125
5.11	Conclusions	128
6	Summary	131
A	Medium implementation for JEWEL	135
A.1	Required interface	135
A.2	Medium configuration	137
A.3	JEWEL parameters	137
B	LHC operation	141
B.1	ALICE data taking periods	141
C	TRD operation and analysis	143
C.1	Overview	143
C.2	TRAP configurations	145
C.3	Data structures for online information	149
C.4	AliTRDTriggerAnalysis	149
C.5	Test runs for TRD triggers	151
C.5.1	pp at $\sqrt{s} = 7$ TeV	151
C.5.2	pp at $\sqrt{s} = 8$ TeV	151
C.6	Overview of TRD-triggered data	153

C.7	Run lists for analysis of TRD-triggered data	156
C.7.1	pp at $\sqrt{s} = 8$ TeV	156
C.7.2	p-Pb at $\sqrt{s_{\text{NN}}} = 5.02$ TeV	157
C.7.3	pp at $\sqrt{s} = 2.76$ TeV	157
D	Jet-hadron correlation analysis	159
D.1	Run lists	159
D.2	Track cuts	160
D.3	Proton identification	161
E	Acronyms	171

List of Figures

1.1	Overview of the Standard Model	2
1.2	QCD phase diagram	4
1.3	Geometry of a heavy-ion collision	6
1.4	Elliptic flow and charged hadron suppression	9
2.1	Fundamental parton splittings	13
2.2	Nuclear thickness functions and geometric cross sections	19
2.3	Hard interaction vertices and temperature profile	19
2.4	Effective density of media	22
2.5	Comparison of medium evolution	24
2.6	Transverse flow in hydrodynamical evolution	25
2.7	Pion p_{\perp} spectrum with vacuum shower	26
2.8	Nuclear modification factors of charged hadrons and jets	28
2.9	In- and out-of-plane geometry	29
2.10	Nuclear modification factor of jets in- and out-of-plane	30
2.11	High- p_{\perp} v_2 of jets	31
3.1	LHC injector chain and interaction points	34
3.2	LHC filling scheme	35
3.3	ALICE detector setup	38
3.4	Overview of the TRD installation and chamber cross section	41
3.5	Overview of TRD read-out	43
3.6	Simulation and reconstruction chain	43
3.7	Distribution of $\delta p_{\perp}^{\text{ch}}$ for random cones	46
4.1	Overview of TRD triggering	47
4.2	TRD trigger timing	48
4.3	Overview of TRD pretrigger system	49
4.4	Overview of CB-B	50
4.5	Pretrigger state machine	51
4.6	Pretrigger input alignment	52
4.7	Event display with online tracks	53
4.8	Data processing in one MCM	54
4.9	Digital filter chain	55
4.10	Local tracking in one MCM	56
4.11	Geometrical tracklet deflection	58
4.12	Tracklet reconstruction and correction	59
4.13	Comparison of raw and simulated tracklets	61

4.14	TRD online tracking class hierarchy	62
4.15	On-line tracking simulation	63
4.16	Tracklet efficiencies in Monte Carlo	64
4.17	Tracklet shifts in Monte Carlo	65
4.18	Tracklet shifts in Monte Carlo (chamber-wise)	66
4.19	Tracklet residuals	67
4.20	Tracklet multiplicities	68
4.21	η - φ coverage of TRD stacks and number of tracks per jet	69
4.22	Trigger efficiency from Monte Carlo simulations	70
4.23	Rejection factors of TRD jet trigger	71
4.24	Average pulse height distribution	72
4.25	Fraction of jet-triggered events	73
4.26	Statistics recorded with TRD jet trigger (2012)	77
4.27	Inspection rate and trigger rejection	78
4.28	Statistics recorded with TRD jet trigger (2013)	78
4.29	Consistency checks for TRD triggers	79
4.30	Raw jet p_{\perp} spectra	80
4.31	Raw jet p_{\perp} spectra (normalized per event)	81
4.32	Comparison of jet p_{\perp} spectra	82
4.33	η - φ distributions of jet axis	83
4.34	Jet fragmentation	84
4.35	Comparison of fragmentation functions	85
5.1	Higher harmonic anisotropic flow	88
5.2	Di-jet production at hadron colliders	89
5.3	Particle ratios in jets and bulk	89
5.4	Selection of collision geometries	90
5.5	Statistics in LHC10h and LHC11h (good)	96
5.6	Centrality estimates	97
5.7	Event plane angle and resolution	99
5.8	Jet-subtracted event plane	99
5.9	η - φ distributions for trigger and associated particles	100
5.10	Jet p_{\perp} spectra in central and semi-central events	101
5.11	TPC dE/dx and $N_{\sigma,p}$	102
5.12	TPC $N_{\sigma,p}$ templates	103
5.13	TPC $N_{\sigma,p}$ templates in momentum slice	104
5.14	Comparison of generated TPC templates to Monte Carlo truth	105
5.15	TOF time of flight and $N_{\sigma,p}$	106
5.16	TOF $N_{\sigma,p}$ templates	107
5.17	TOF mismatches	108
5.18	$N_{\sigma,p}$ fits for Monte Carlo	109
5.19	Global TPC and TOF fits	111
5.20	Raw hadron-hadron per-trigger yields	114
5.21	Raw hadron-proton per-trigger yields	115
5.22	Raw hadron-hadron per-trigger yields for mixed events	116
5.23	Hadron-hadron correlation functions ($\Delta\eta, \Delta\varphi$)	117
5.24	Hadron-hadron correlation functions ($\Delta\varphi$)	118
5.25	Jet-hadron correlation functions ($\Delta\eta, \Delta\varphi$)	119
5.26	Jet-hadron correlation functions ($\Delta\varphi$)	120

5.27	Ratio of correlation functions with associated hadrons and protons	121
5.28	Jet-hadron correlation for different jet p_{\perp} and radii	123
5.29	Comparison of measured correlation and flow only	124
5.30	$\Delta\eta$ - $\Delta\varphi$ correlations from toy Monte Carlo	126
5.31	Comparison of measurement and toy Monte Carlo	127
5.32	p -values for added signal	128
C.1	Top view of a TRD layer	144
D.1	Fits of TPC $N_{\sigma,p}$ (central events)	161
D.2	Fits of TPC $N_{\sigma,p}$ after TOF cut (central events)	162
D.3	Fits of TPC $N_{\sigma,p}$ (semi-central events)	163
D.4	Fits of TPC $N_{\sigma,p}$ after TOF cut (semi-central events)	164
D.5	Fits of TOF $N_{\sigma,p}$ (central events)	165
D.6	Fits of TOF $N_{\sigma,p}$ after TPC cut (central events)	166
D.7	Fits of TOF $N_{\sigma,p}$ (semi-central events)	167
D.8	Fits of TOF $N_{\sigma,p}$ after TPC cut (semi-central events)	168

List of Tables

1.1	Facilities with heavy-ion beams	4
2.1	Parameters for Bjorken medium	25
3.1	LHC design values	35
3.2	LHC running conditions	36
3.3	Overview of TRD parameters	41
4.1	Parameters for local online tracking	57
4.2	Available data from TRD triggers	66
4.3	Timeline of TRD trigger commissioning	73
4.4	TRD trigger contributions	74
4.5	Trigger flags for jet trigger analysis	80
5.1	ALICE Pb–Pb data samples	95
5.2	Event flags	95
A.1	Parameters for Bjorken medium	138
A.2	Parameters for OSCAR medium	138
A.3	Parameters for shower evolution	139
B.1	ALICE data taking periods	142
C.1	Mapping of read-out pads and channels	143
C.2	List of used TRAP configurations	146
C.3	Tracklet information in ESDs and AODs	149
C.4	Interface of AliVTrdTrack	150
C.5	Interface of AliESDTrdTrigger	150
C.6	Overview of TRD trigger tests in pp collisions 2011	152
C.7	Trigger classes with WU and HJT	153
C.8	Statistics recorded in pp collisions at $\sqrt{s} = 8$ TeV	154
C.9	Statistics recorded in p–Pb collisions at $\sqrt{s_{NN}} = 5.02$ TeV	155
C.10	Statistics recorded in pp collisions at $\sqrt{s} = 2.76$ TeV	155
D.1	Particle yields for central events	169
D.2	Particle yields for semi-central events	170

Chapter 1

Introduction

Nuclear matter has been the subject of research ever since Rutherford identified the nucleus as the dominant carrier of the atomic mass [1]. The interaction of the charged nucleus with the surrounding electrons was understood by electromagnetism [2, 3]. With the discovery of the proton and the neutron [4] as the constituents of the nucleus and the positron as anti-particle of the electron [5], the set of fundamental building blocks of matter appeared to be complete. However, electromagnetism could not account for the binding of neutral and positively charged particles in the nucleus. An additional interaction was required which had to be strong and of short range. Yukawa proposed a massive exchange particle to explain the properties of the so-called *strong interaction* [6].

Unexpectedly, many more strongly interacting particles, the *hadrons*, were discovered in short sequence – first in cosmic rays, later at accelerators [7, 8]. The proliferation of hadronic states suggested them to be non-elementary and called for new schemes to explain the observed spectrum. An early idea was to consider the hadrons as composed of lighter hadrons. This led to the bootstrap model [9], which predicted a hadron state density growing exponentially with mass.¹ Hagedorn realized that such a spectrum leads to a *limiting temperature* for the stable description of a hadron gas in terms of statistical mechanics [11]. The argument is based on the observation that an exponentially growing state density cannot be compensated by the thermal suppression of high-energy states and instead causes divergences, e.g. in the partition sum, if the temperature is sufficiently high.

Eventually, the eight-fold way [12] resulted in a good description of the known hadronic spectrum and correctly predicted the baryon Ω^- . It ordered the hadronic states as multiplets of an underlying $SU(3)_f$ (flavour) symmetry. While in the beginning the symmetry was considered an abstract concept, the observation of Bjorken scaling [13] in deeply inelastic scattering experiments [14] pointed to the existence of charged quasi-free spin- $\frac{1}{2}$ constituents within the nucleon. These *quarks* were assigned the quantum numbers emerging from group theory, such as isospin and strangeness. This resulted in a picture of hadrons as formed of quark anti-quark pairs or (anti-)quark triples [15], which are subject to the strong interaction.

In order to explain hadronic production cross sections and decay widths, another degree of freedom was needed at the quark level. It was realized by the introduction of the colour symmetry [16, 17]. Only colourless composites with integer multiples of the electron charge have been found to exist freely [18]. This empirical fact is called *confinement*.

By the time that the strong interaction was understood as a force between quarks, Quantum ElectroDynamics (QED) had been established as a quantum field theory for the description of

¹Today, this can easily be checked against the PDG hadron listings [10].

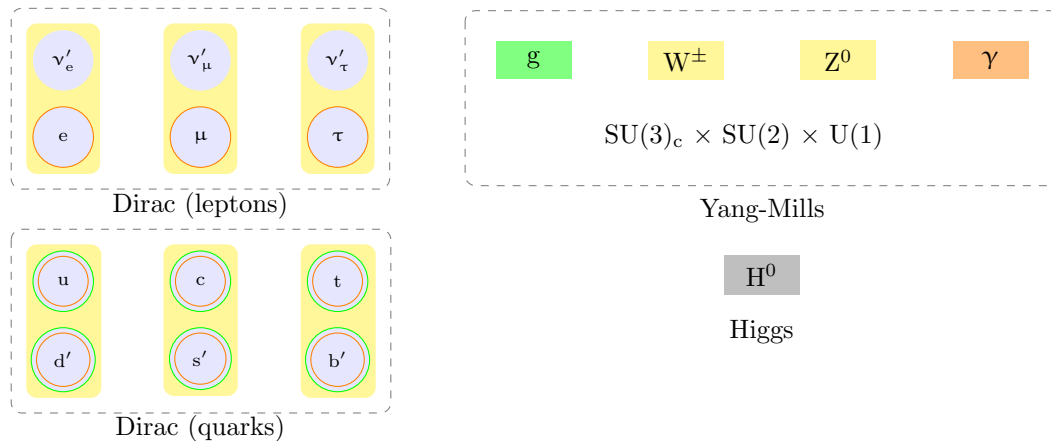


Figure 1.1: The Standard Model comprises three doublets of quarks and leptons each as fundamental spin- $\frac{1}{2}$ fermions. Interactions arise from the spin-1 gauge bosons of $SU(3) \times SU(2) \times U(1)$. The scalar Higgs field breaks the $SU(2) \times U(1)$ symmetry spontaneously and gives mass to the W^\pm and Z^0 bosons. The fermions acquire mass from Yukawa couplings to the Higgs fields; the mass eigenstates are linear combinations of the flavour eigenstates shown in the figure.

electromagnetic interactions. It was found to be renormalizable and to have a running coupling which increases with momentum transfer. Furthermore, it had been combined with the description of the weak interaction in the formulation of Quantum Flavour Dynamics (QFD). While QFD had proved very successful and was considered a template for other theories, the need for asymptotic freedom of the strong interaction (required to achieve Bjorken scaling in a quantum field theory) seemed incompatible with renormalizable quantum field theories. This disfavoured the formulation of a quantum field theory for the strong interaction at first. The breakthrough came with the notion that it was, in fact, possible to construct a well-behaved quantum field theory which was asymptotically free for a non-Abelian gauge group [19, 20]. From then on, *Quantum Chromodynamics (QCD)* [21] was seen as the theory describing the strong interaction. Experiments soon confirmed the non-Abelian SU(3)_c nature of the *gluons* as mediators of the strong interaction [22].

Together with the other elementary particles discovered later, these quantum field theories make up the Standard Model of particle physics as we know it today (see Figure 1.1). It comprises leptons and quarks as the fundamental fermions, both in three generations. The interactions are governed by an SU(3)_c × SU(2) × U(1) symmetry, resulting in eight gluons, W[±], Z⁰, and the photon. The Higgs boson was introduced as a consistent way to attribute mass to some of the gauge bosons. Recently, its discovery at the LHC was announced by the ATLAS and CMS collaborations [23, 24].

Today, the fundamental QCD Lagrangian²:

$$\mathcal{L} = -\frac{1}{4}F_{\alpha\beta}^A F_A^{\alpha\beta} + \bar{q}_a(i\mathcal{D} - m)q_b \quad (1.1)$$

with the quark fields q , the field strength tensor F and the covariant derivative \mathcal{D} is believed to contain all features of the strong interaction. Because of its asymptotic freedom, perturbation

²The gauge-fixing and ghost terms required for quantization are omitted here.

theory works very well for processes with high momentum transfers, i.e. at hard scales. Precision tests of QCD against experiments have been extremely successful in this regime, e.g. at LEP and recently at LHC. This is to the extent that current LHC experiments have not yet succeeded to find significant deviations from QCD or Standard Model predictions. It is one of the major goals of the LHC to search for physics beyond the Standard Model which also includes the electroweak sector.

On the other hand, there is also a low energy regime of QCD for which the couplings are large and perturbation theory breaks down. Here, non-trivial collective features must arise from the fundamental laws to explain the rich phenomenology, e.g. the formation of hadrons, nuclei, matter in neutron stars, and other processes with low momentum transfers. In this collective regime the fundamental partons are no longer the relevant degrees of freedom. Despite the belief that the QCD Lagrangian contains all the physics for such (bound) states, ab-initio calculations of QCD bound states or thermodynamics are prohibitively complicated.

However, a theoretical treatment of QCD in regimes where perturbation theories cannot be applied is very much needed to interpret the results from experiments. Different approaches have been invented. Effective theories have been developed to describe specific aspects of QCD. In many cases models are used that are motivated phenomenologically. With the advance of powerful computing resources, QCD has also been formulated on a discretized space-time lattice in a way that numerical algorithms can be applied [25].

Under conditions which allow for a thermodynamic description, the properties of QCD matter can be discussed in a phase diagram. Figure 1.2a shows the baryo-chemical potential μ_B on the horizontal and the temperature T on the vertical axis. At ultimately high temperatures and/or energy densities, the weakly coupled QCD predicts a state of matter in which quarks and gluons are the relevant degrees of freedom [26, 27]. Such a state is termed *Quark-Gluon Plasma* (QGP). From the limiting behaviour two phase transitions can be expected, namely a transition between a chirally symmetric phase and the nuclear phase in which chiral symmetry is broken (χ SB). The second one is between deconfined matter and ordinary nuclear matter. The quark anti-quark condensate $\langle q\bar{q} \rangle$ and the Polyakov loop can be used as order parameters for these phase transitions [28, 29, 30]. Lattice QCD calculations predict a critical temperature for the transition to deconfined matter around $T_c \approx 155$ MeV, and a critical energy density of ~ 1 GeV/fm³ [31, 32]. At high baryon densities and sufficiently low temperatures, as possible in the core of dense stars, a multitude of colour superconducting phases is predicted. Nuclear matter in a neutron star had already been considered by Itoh [33].

1.1 Heavy-ion collisions

Already at a workshop in 1974, it was discussed to use collisions of heavy nuclei to create strongly interacting matter of high energy density within a macroscopic volume [42]. This should allow to probe the QCD phase diagram by controlled laboratory experiments and study QCD thermodynamics by measuring properties of the Quark-Gluon Plasma. The ideas resulted in a series of experiments at various facilities, mostly by modifying existing accelerators for heavy-ions. Table 1.1 shows an overview of facilities where heavy-ion experiments have been conducted. For comparability the centre-of-mass energy is given per colliding nucleon pair.

Hard interactions in heavy-ion collisions are usually treated similarly to the case of nucleons, i.e. by separating the interaction of partons from nuclei and subsequent hadronization. Cross sections for hadron production are factorized into a Parton Density Function (PDF) $f_a(x, Q^2)$ evaluated at a scale Q^2 , a partonic cross section $\hat{\sigma}$ from a Matrix Element (ME), and a Fragmentation

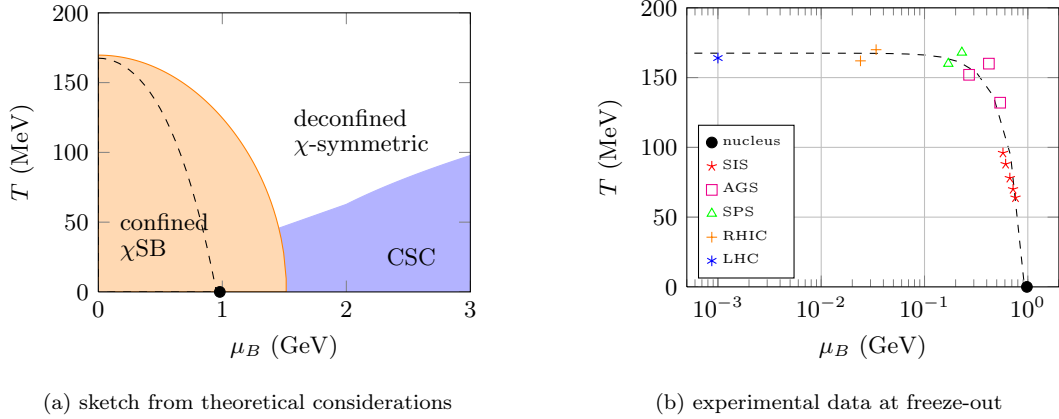


Figure 1.2: The QCD phase diagram, plotted here with temperature T against baryochemical potential μ_B , shows a hadronic state at low temperatures and densities, a partonic state at high temperatures, and colour super-conducting phases at low temperatures and high densities. At low densities and temperatures, chiral symmetry is broken (χ SB). Figure 1.2a sketches the phase transition as derived from a simple bag model [34, 35, 36]. Figure 1.2b shows the values at freeze-out obtained from experiments [37, 38, 39, 40, 41]. The dashed line in the left plot shows the experimentally observed freeze-out curve.

start	machine	facility	max $\sqrt{s_{NN}}$
1971	Bevalac	LBNL	~ 2 GeV
1975	UNILAC	GSI	~ 2 GeV
1990	SIS	GSI	~ 2 GeV
1986	AGS	BNL	~ 5 GeV
1986	SPS	CERN	~ 20 GeV
1994	SPS	CERN	~ 17 GeV
2000	RHIC	BNL	200 GeV
2010	LHC	CERN	2.76 TeV

Table 1.1: Heavy-ion collisions have been studied at a variety of accelerators [43, 44, 45, 46]. The energy, given as centre-of-mass energy per nucleon pair, covers several orders of magnitude by now.

tation Function (FF) $D_{c \rightarrow h}(z)$, with z being the momentum fraction of the emerging hadron:

$$d\sigma^{NN \rightarrow h+X} \propto \sum_{a,b,c} \int dx_a dx_b dz f_a(x_a, Q^2) f_b(x_b, Q^2) \cdot \hat{\sigma}^{(ab \rightarrow c \dots)} \cdot D_{c \rightarrow h}(z). \quad (1.2)$$

In fact, each of the final state partons from the ME produces a spray of hadrons, a so-called *jet*. The evolution can be formulated as a parton shower, i.e. a successive splitting of quarks and gluons until the initially virtual parton reaches a virtuality or p_{\perp} threshold. Below, the hadronization is based on phenomenological models. From the experimental side, the objective is to approach the partons from the hard scattering, for which a reconstruction of the jet is required. This procedure is not unique and different algorithms exist, which specify how the observed tracks must be recombined to form a jet. Only by specifying such an algorithm jets become well-defined objects. The first notion of such a prescription was based on events with all but a certain fraction of the energy in two cones [47]. Later, more involved algorithms were developed [48, 49, 50, 51]. With cone and sequential recombination algorithms there are now two classes of recent algorithms. The former group all particles within a cone to a jet. The latter build up jets by iteratively grouping particles together. Today, a commonly used set of algorithms is provided with the FastJet package [52].

But there are also crucial differences between nucleon-nucleon and heavy-ion collisions. As already known from deeply inelastic scattering experiments, the PDFs deviate for nucleons and nuclei. Thus, the initial state for the ME is changed. Furthermore, a geometric description of the collision in terms of an impact parameter is allowed because the de Broglie wave length is much shorter than the nuclear radius. The impact parameter determines the overlap of the colliding nuclei in the transverse plane and together with the beam direction fixes the reaction plane, see Figure 1.3. With a large number of nucleons in the overlap region soft processes translate kinetic energy into a *medium*. On the one hand, this results in a much more pronounced underlying event as compared to pp, on the other hand, the presence of a medium can also affect the jet evolution and change the FFs.

Figure 1.3 illustrates our picture of a heavy-ion collision at RHIC and LHC energies. It consists of different stages. Upon collision, the two nuclei traverse each other. Because of their Lorentz contraction this happens over a very short distance. Kinetic energy is translated by soft processes into energy density in the volume between the two nuclei. The system quickly (≤ 1 fm/c) thermalizes locally. The subsequent expansion is well-described by relativistic hydrodynamics. When temperature and density decrease a transition to the hadronic phase sets in. Without further interaction the particle composition is fixed up to decays. In the statistical model the hadron abundances are predicted to follow from temperature and baryo-chemical potential [53]. The yields of identified particles are used to extract these two parameters. Such results for different beam energies are shown in Figure 1.2b. The quality with which the statistical model with only two free parameters describes the data underlines the thermodynamic particle production. This is one example where a collective treatment is used. Another example is the classification of the events according to their impact parameter which is far too small to be measured in accelerator experiments. Instead, events are grouped in multiplicity percentiles of the total cross section, the so-called *centrality*. The mapping to an impact parameter can then be taken from Glauber Monte Carlo simulations [54].

Whereas high energy physics experiments mostly look at processes involving individual particles, heavy-ion physics often deals with collective descriptions. For example, initial energy densities are estimated from measurements of $\frac{dE_T}{d\eta}$ by arguments from Bjorken [55]. The energy density obtained from the measured $\frac{dE_{\perp}}{d\eta}$ is above the critical ε from lattice calculations already for top beam energies at the SPS. Further experimental results are discussed later.

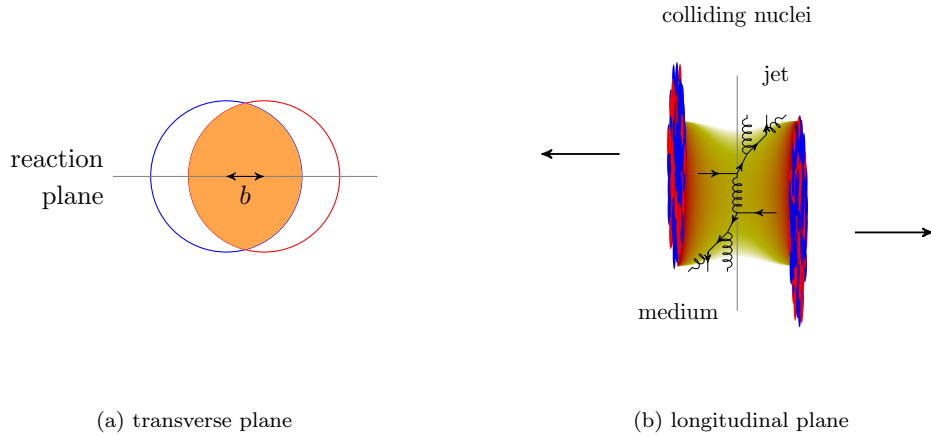


Figure 1.3: For heavy-ion collisions a geometrical picture of the collision geometry is justified. In the transverse plane (a), a collision is characterized by the impact parameter \vec{b} . In the longitudinal view (b), the created medium of nuclear matter is shown with a temperature profile as obtained from longitudinal (Bjorken) expansion.

1.2 Relativistic hydrodynamics

During a phase of local thermal equilibrium, the medium can be described by space-time dependent thermodynamical properties, e.g. T , μ , ε . Following a purely statistical model of a dense volume breaking up into hadrons proposed by Fermi [56], Landau suggested a hydrodynamical treatment [57]. Bjorken extended this model by further assumptions and arrived at a time evolution of such a system. Today, relativistic hydrodynamics can be solved numerically in 3+1 space-time dimensions.

Relativistic hydrodynamics is based on the conservation of energy and momentum, usually formulated as a continuity equation for the energy momentum tensor:

$$\partial_\mu T^{\mu\nu} = 0. \quad (1.3)$$

For ideal hydrodynamic without dissipative processes entropy must be conserved, i.e.:

$$\partial_\mu (su^\mu) = 0 \quad (1.4)$$

with the entropy density s and the normalized fluid four-velocity u^μ . Then, the energy momentum tensor can be expressed in terms of the pressure P and the energy density ε :

$$T^{\mu\nu} = (\varepsilon + P) u^\mu u^\nu - P g^{\mu\nu}. \quad (1.5)$$

To close this system of equations and make it solvable, an equation of state, i.e. the relation between energy, temperature, and pressure:

$$\varepsilon = \varepsilon(T, P) \quad (1.6)$$

is required in addition. The equation of state is a fundamental property of QCD, but difficult to obtain from ab-initio calculations.

These equations can be solved analytically for the simplifying assumptions used by Bjorken. He used the presence of a plateau in the rapidity distribution of particle production around the mid-rapidity region and neglected transverse expansion. This implies an inherent rapidity symmetry of the initial state which is also respected by the hydrodynamical equations. Then, all quantities depend only on the proper time and the time evolution of the energy density is determined by:

$$\frac{d\varepsilon}{d\tau} = -\frac{\varepsilon + P}{\tau}. \quad (1.7)$$

For an ideal relativistic gas with $\varepsilon = 3P \propto T^4$, we now obtain:

$$\varepsilon = \varepsilon_0 \cdot \left(\frac{\tau}{\tau_0}\right)^{-\frac{4}{3}}, \quad T = T_0 \cdot \left(\frac{\tau}{\tau_0}\right)^{-\frac{1}{3}}. \quad (1.8)$$

The result for the entropy density:

$$\frac{ds}{d\tau} = -\frac{s}{\tau} \quad (1.9)$$

implies the conservation of entropy per unit of rapidity. In these calculations no transverse expansion is taken into account.

If dissipative effects cannot be neglected bulk and shear viscosity can be added by modifying the energy momentum tensor. Then, only numerical solutions exist for non-trivial cases. A characteristic consequence of hydrodynamical expansion is that velocity instead of momentum is the common property, which shifts heavier particles to higher momenta, see Section 1.4.

1.3 Partonic energy loss

In a heavy-ion environment, jets are of particular interest as they evolve in the presence of the (expanding) medium and can be used as probes for the interaction with it. The hard interaction happens on a short time scale whereas the evolution of jet and medium takes longer. As already noted by Bjorken, a highly energetic parton travelling through a strongly interacting medium can scatter elastically and thereby lose energy [58]. In addition, gluon radiation is emitted in inelastic processes. In most models this process dominates the energy loss. Because of coherence effects the situation is more complicated as compared to elastic scatterings. The QED analogue of radiative energy loss was studied by Landau, Pomeranshuk, and Migdal (LPM) [59, 60, 61]. The QCD case is often referred to as non-Abelian LPM effect. Only for certain limiting cases analytic calculations of the QCD energy loss exist. A non-exhaustive set of commonly used calculations is described in the following. They are named by the initials of the respective authors and are also discussed in reviews [62, 63].

BDMPS-Z This model [64, 65, 66, 67] is based on a medium of static scattering centres [68].

Without recoil, no collisional energy loss can be included. The mean free path is assumed to be much longer than the Debye screening length of the medium such that only scatterings off one scattering centre have to be considered. The scatterings are assumed to be soft, i.e. the energy of the emitted gluon is much smaller than the parton energy. With these assumptions the resulting energy loss prediction features the characteristic quadratic dependence on the in-medium path length ($\propto \hat{q}L^2$), and the gluon spectrum $\omega dI/d\omega$ shows the $1/\sqrt{\omega}$ shape characteristic for LPM suppression.

ASW The model [69] uses a path integral formalism. It considers the incoming parton as a superposition of Fock states, which decohere by interacting with the medium and produce

real particles. In the respective limits, it reproduces the results of multiple soft scatterings and single hard scattering.

GLV The model [70, 71] builds on a reaction operator which generates a scattering off a scattering centre. The complete energy loss is then modelled in an opacity expansion, i.e. an expansion in the number of scatterings $\bar{n} = \frac{L}{\lambda}$ in the medium. For every n the contribution is induced from the $(n - 1)$ -term by means of the reaction operator. Using the same Gyulassy-Wang medium, also here the L^2 dependence is obtained.

AMY The Arnold-Moore-Yaffe approach describes the traversal of a parton through a thermal medium with a temperature far above the critical temperature. It is based on perturbative QCD using hard thermal loop improvements [72].

AdS/CFT In a very different approach, the conjectured duality of Conformal Field Theories (CFT) and super-gravities in Anti-de-Sitter (AdS) spaces [73] is exploited to map the strong coupling scenario of energy loss to its dual formulation [74].

In order to compare different calculations, certain models for the underlying medium are used, e.g. a static brick, Bjorken expansion, or results from hydro-dynamic calculations. Then, the transport coefficient \hat{q} , i.e. the squared transverse momentum kick per unit path length, is used to characterize the energy loss resulting from different models. The analytic calculations cover only part of the kinematic regime relevant for the evolution in a heavy-ion collision. Monte Carlo implementations are frequently used to generalize the results to all kinematics and to provide fully exclusive final states.

For the comparison with experimental data, the effect of partonic energy loss on hadronic spectra has to be calculated. In the simplest ansatz, the energy entering a fragmentation function is reduced by ΔE with a probability $P(\Delta E)$ according to the energy loss model. Due to different approximations the models need different energy densities to reproduce experimental data.

Often the energy loss is treated independently of the parton shower, whereas the more realistic scenario is to alter the parton shower such that medium interactions are correctly taken into account. While parton showers are well-suited for Monte Carlo implementations in event generators, the modelling of energy loss is complicated by coherence. While some implementations, e.g. HIJING [75], PYQUEN [76], or PQM [77] include energy loss on the single parton level, others modify the parton showers. Among the latter are YaJEM [78], QPYTHIA [79], and JEWEL [80, 81]. It has been shown that a probabilistic implementation of the LPM effect is possible [82], and it is implemented in JEWEL [83].

But not only the modification of the jet by the medium is interesting, also the reverse reaction carries information. The energy lost by the jet must be taken up by the medium. In a thermodynamic description of the medium, a velocity of sound can be calculated. Since the highly energetic particles travel much faster, a Mach cone has been predicted to emerge [84, 85, 86]. Such a medium response can be looked for in two- or three-particle correlations.

1.4 Experiments and measurements

All of the previously explained ideas and pictures evolved along with the interpretation of experimental data, with a close interplay of theory and experiment. In many respects, heavy-ion experiments are similar to those of particle physics but some requirements are substantially different. For heavy-ion collisions, it is crucial to reconstruct all events as complete as possible. This puts a challenge on the tracking detectors to cope with the highest multiplicities of the central collisions, e.g. $dN_{\text{ch}}/d\eta|_{y=0} = 1584 \pm 80$ for the 5 % most central collisions at LHC with

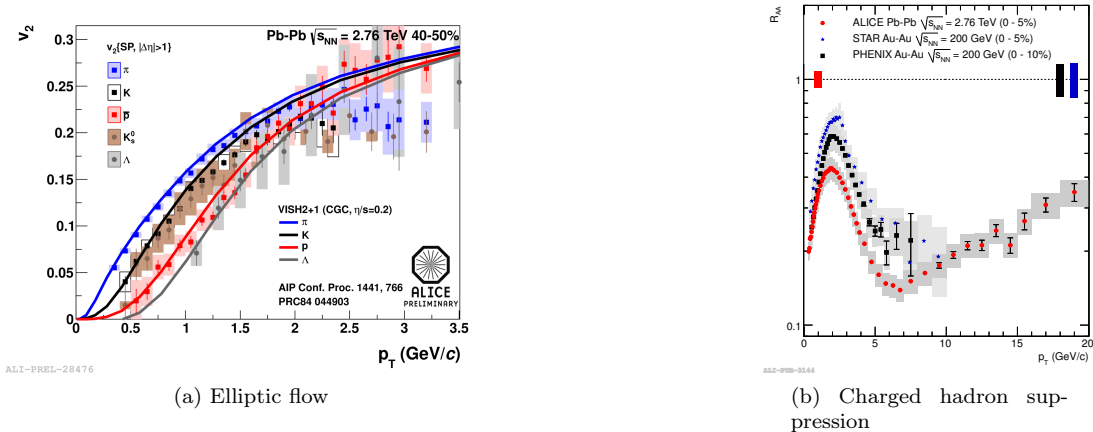


Figure 1.4: Left: The p_{\perp} dependence of elliptic flow (second azimuthal harmonic) for identified particles is well described by hydrodynamical calculations and, thus, supports the picture of a hydrodynamical evolution [96]. Right: The strong suppression of high- p_{\perp} charged particles supports the idea of partonic energy loss [97].

$\sqrt{s_{NN}} = 2.76$ TeV [87]. In addition, not only shall pseudo-rapidity and transverse momentum be measured but the particles should also be identified.

After many experiments had taken place at accelerators which were converted for heavy-ions (see Table 1.1), the Relativistic Heavy-Ion Collider (RHIC) was constructed as a dedicated heavy-ion machine and put into operation in the year 2000. The experiments (STAR, PHENIX, BRAHMS, PHOBOS) provided many interesting results [88, 89, 90, 91]. Also in the case of the Large Hadron Collider (LHC) heavy-ion operation was foreseen from the design phase on and integrated into the experimental programs of ALICE, ATLAS, and CMS. The higher energies at the LHC result in higher initial energy densities, larger system sizes, longer lifetimes, and higher reach in transverse mass. The latter is particularly relevant to separate jets from the underlying event of heavy-ion collisions. The initial energy densities at the LHC can be estimated to ~ 15 GeV/fm³, i.e. about a factor 3 higher than at RHIC [92]. Both values are well above the critical temperature for a phase transition.

The system size can be estimated by exploiting the Bosonic correlation of e.g. identical pions emitted from a collision. This technique, originally introduced in astronomy, is known as Hanbury Brown-Twiss interferometry [93, 94]. At LHC the HBT radius is found to be ~ 5 fm/c which corresponds to an increase of 10-35 % to RHIC results [95].

The azimuthal anisotropy of particle emission is quantified by decomposition into Fourier components [98]:

$$E \frac{d^3 N}{dp^3} = \frac{d^2 N}{2\pi p_{\perp} dp_{\perp} dy} \left(1 + \sum_{n=1}^{\infty} 2 v_n \cos(n(\varphi - \psi_n)) \right). \quad (1.10)$$

The coefficients v_n can be derived from the azimuthal correlation of two or more particles. The first and second component v_1 and v_2 are called *directed* and transverse *elliptic flow*. The latter arises dominantly from the initial spatial anisotropy which is translated into momentum anisotropy by the pressure gradient. Figure 1.4a shows the dependence on the transverse momentum as measured by ALICE. The size clearly indicates collective behaviour and the mass

ordering is consistent with a fluid velocity. The agreement with hydrodynamical calculations is good and also extends to measurements for identified particles. These comparisons indicate that the viscosity is small compared to the entropy density, usually quoted as η/s , and at least close to a lower boundary conjectured from AdS/CFT duality [99]. With a well-described hydrodynamical expansion, flow measurements allow us to constrain initial conditions and also the equilibration process.

The evolution of a parton shower is modified by the presence of a medium, resulting in energy loss. Thus, at a given transverse momentum the particle yield is suppressed as compared to the expectation in vacuum. A common way to quantify this effect is the *nuclear modification factor* R_{AA} which is the ratio of observed particles at a given transverse momentum and the number expected from scaling binary nucleon-nucleon collisions:

$$R_{AA} = \frac{d^2 N^{AA}/dp_{\perp} dy}{\langle N_{\text{coll}} \rangle d^2 N^{PP}/dp_{\perp} dy}. \quad (1.11)$$

The measurement of the nuclear modification factor for charged hadrons is shown in Figure 1.4b as a function of the transverse momentum. The data show a significant suppression with a non-trivial shape. The measurement allows us to constrain the energy loss mechanisms. The observation of high p_{\perp} suppression is referred to as *jet quenching*. The applicability of the binary collision scaling is confirmed by the measurement of a nuclear modification factor of unity for particles which do not interact strongly, e.g. photons. It should be noted that the bulk particle production from soft processes or the initial temperature instead scale with the number of participants.

Because of the complex final states and analyses, conclusions are often drawn from comparison of data with predictions from Monte Carlo event generators. For heavy-ion collisions, however, different models are used for the description of the hard interactions, the initial conditions of the medium, its hydrodynamical evolution, and the freeze-out to final state hadrons. There is a variety of Monte Carlo event generators with different focus, e.g. JEWEL and YaJEM for the modelling of jet quenching.

Some signals, e.g. jets of high transverse momentum, are so rare that they require an online selection of relevant events. Therefore, the experiments must have detectors suitable for this job. In ALICE, several detectors can contribute triggers for various event signatures. Among them is the Transition Radiation Detector which has provided triggers on cosmic rays, jets, and electrons.

1.5 Outline

The work done within this thesis comprises three topics. The first subject is the extension of the jet quenching Monte Carlo event generator JEWEL by an interface to relativistic hydrodynamic calculations. Chapter 2 begins with a description of the Monte Carlo modelling of jet quenching in the presence of a medium as implemented in JEWEL. To allow for the usage of arbitrary medium evolution, the medium implementation was split from the shower code. In addition, an interface for the OSCAR2008H format, a file format proposed by TECHQM for the exchange of the output of hydrodynamical calculations, was implemented. Here, we use data for Au–Au collisions at $\sqrt{s_{NN}} = 200$ GeV, which is available in the OSCAR2008H format. Comparisons of the quenching behaviour with the medium evolution from full hydrodynamics and a purely longitudinal Bjorken expansion are discussed.

The second topic was the preparation, commissioning, operation, and performance analysis of the Transition Radiation Detector level-1 trigger, focusing on a trigger on high- p_{\perp} charged jets.

Chapter 3 serves as a technical introduction and explains the experimental setup used for data taking with ALICE. Chapter 4 explains the triggering capabilities of the Transition Radiation Detector. The pretrigger system is required to provide a low-latency wake-up signal to the front-end electronics. The local online tracking, which builds the basis for the track-based TRD trigger, is discussed in detail. Technical implementations and the commissioning of the triggers during this thesis are discussed. This includes the path to production data taking. For the first time, the TRD was used to provide physics triggers. Finally, the performance analyses of the local online tracking and the jet trigger are described. Where appropriate, possible improvements for LHC Run 2 are pointed out.

The third part in Chapter 5 discusses the measurement of jet-hadron correlations with the goal to look for the medium response to a traversing parton, e.g. a Mach cone. An analysis is introduced which makes use of the particle identification capabilities of ALICE. The idea is to not only look for a structure in the inclusive correlation functions but to exploit the different proton abundances in jet fragmentation and bulk hadronization to separate the two components. The results for the data from the 2010 Pb–Pb run are discussed. In addition, a comparison to a simple toy Monte Carlo model is shown to judge the sensitivity of the analysis.

The last Chapter 6 summarizes the results and shows prospects for future developments. The results obtained within the ALICE Collaboration are also used in corresponding analysis notes (ALICE-internal so far).

Chapter 2

Jet quenching in evolving media

Partons used for the description of scattering processes at hard scales, e.g. at hadron colliders, cannot exist freely. Present in the initial state of a hard scattering, they must originate from hadrons. And partons produced in the final state must hadronize eventually. In a factorized approach, cf. Equation 1.2, one can use measured probabilities to find a certain parton in a given hadron (PDF) or to obtain a specific hadron from a given parton (FF). Often, this is not satisfactory for comparison to non-inclusive observables which are based on a fully determined final state in experiment. A more detailed description of the evolution from a parton to a hadron is desirable to arrive at an exclusive final state.

An incoming or outgoing parton involved in an interaction at a hard scale can undergo the fundamental branchings shown in Figure 2.1. These diagrams constitute the leading order contributions of a perturbative series and diverge for collinear and soft emissions. A description better than a fixed-order calculation can be achieved by re-summing the logarithmically enhanced parts to all orders in perturbation theory to leading logarithm accuracy. This results in a parton shower prescription for the fragmentation process [100].

In the parton shower language, a hard parton in the final state evolves from an initially large scale to a low one by sequential splittings. The large scale is fixed by the kinematics of the hard interaction. Starting from there, the scale of the next branching, if any, is calculated. The process continues for each of the daughters until a hadronization scale is reached below which perturbation theory is no longer applicable. Below that scale, usually on the order of ~ 1 GeV, one relies on phenomenological models. However, many characteristics of the fragmentation process are mostly determined by the parton shower, e.g. the intra-jet momentum distribution. A

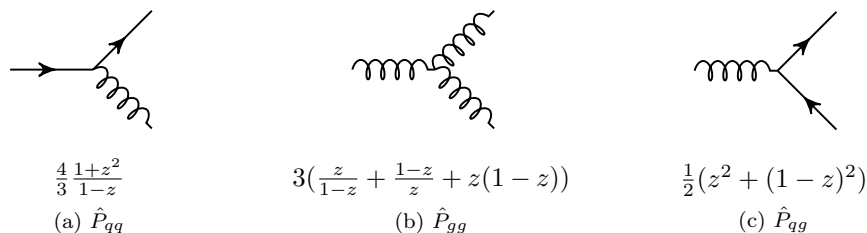


Figure 2.1: Fundamental parton splittings occurring in a parton shower: The given leading order expressions depend on the energy fraction z of the out-going parton.

parton shower can be formulated with different evolution parameters, most commonly virtuality Q^2 and transverse momentum p_\perp . The probabilistic nature of the description is well-suited for the implementation in Monte Carlo event generators and a variety of realizations exist, e.g. PYTHIA [101], Herwig++ [102], and Sherpa [103]. They differ in the parton shower formulation but also in other areas, e.g. the treatment of the hard interaction and the hadronization model.

While the parton shower language as such has no notion of time evolution, the involved scales translate to times comparable to those of the medium evolution. Thus, the presence of a medium can be expected to alter the evolution of a parton shower, on average leading to a loss of energy. Different modifications accounting for this energy loss have been proposed and implemented [78, 79, 80]. The realization used by JEWEL shall be explained in more detail in the next section.

2.1 Jet Evolution With Energy Loss (JEWEL)

For the study of in-medium jet fragmentation, JEWEL implements a virtuality-ordered parton shower similar to the implementation in PYTHIA 6, i.e. the evolution parameter is the parton virtuality Q^2 . JEWEL is implemented as a FORTRAN program linked to PYTHIA 6. Besides the use of PYTHIA for the production of the initial partons and the hadronization, as explained above, its event record and corresponding methods are used to keep track of the particles. An initial hard parton is taken from a hard scattering provided by PYTHIA. For each sufficiently virtual parton, i.e. above the hadronization scale, a shower is started. Therein, the non-branching probability of a parton a from a scale Q_i^2 to a lower Q^2 is calculated from the Sudakov form factor [100]:

$$S_a(Q_i^2, Q^2) = \exp \left\{ - \int_{Q^2}^{Q_i^2} \frac{dQ'^2}{Q'^2} \int_{z_-}^{z_+} dz \frac{\alpha_s(z(1-z)Q'^2)}{2\pi} \sum_b \hat{P}_{ba}(z) \right\} \quad (2.1)$$

where z refers to the energy fraction kept by the parton. The allowed z range is constrained by kinematics such that the daughters remain above the hadronization scale Q_0 . The leading order splitting functions \hat{P}_{ba} corresponding to the diagrams in Figure 2.1 are used according to the parton being a quark or gluon. In the Monte Carlo implementation the scale of the next branching above the hadronization scale, if any, is distributed as the derivative of Equation 2.1. After every branching the kinematics of the splitting is fixed, i.e. the two daughters are assigned four-momenta. For the pure shower evolution this step would not be required at this stage (and is not made e.g. in PYTHIA). If the virtuality of the daughters is still high enough they can undergo further splittings in the same way, thus leading to a shower.

For the interaction with a non-trivial medium a space-time structure must be imposed on the parton shower. This is accomplished by fixing the time between two branchings as:

$$\tau = \frac{E}{Q^2}, \quad (2.2)$$

which is motivated by the uncertainty principle [80]. As the kinematics of the involved partons is known, the parton position at a time t_0 after its production at t_0^s can be calculated as:

$$\vec{x}_1 = \vec{x}_0 + (t_0 - t_0^s) \cdot \frac{\vec{p}_0}{E_0}. \quad (2.3)$$

The positions are tracked in the lab frame and this path is also used for the evaluation whether a scattering with the medium occurs. The scattering probability per path length is determined by

a cross section σ and the corresponding density of potential scattering centres. The cross section is calculated by integrating the leading term of the leading order t -channel cross section:

$$\frac{d\sigma}{dt} = \frac{\pi\alpha_s^2}{s^2} C_R \frac{s^2 + u^2}{|t|^2} \simeq \pi\alpha_s^2 C_R \frac{1}{|t|^2} \quad (2.4)$$

over the range $[|t|_{\min}, |t|_{\max}]$ which is kinematically allowed for a given projectile energy [80]. To mitigate the divergence for $t \rightarrow 0$, the cross section is regularized by the Debye mass. With a quark/gluon as projectile and a quark/gluon as scattering centre the processes: $qq \rightarrow qq$, $qg \rightarrow qg$, $gg \rightarrow gg$ have to be considered. The cross sections for different combinations of projectile and target species are related by a colour factor:

$$\sigma_{gg} = \frac{9}{4}\sigma_{qg}, \quad \sigma_{qq} = \frac{9}{4}\sigma_{qg}. \quad (2.5)$$

An effective density n_{eff} comprising all possible scatterings can be used by noting [58]:

$$\begin{aligned} n_g\sigma_{gg} + n_q\sigma_{qg} &= \frac{3}{2}n_g \cdot \frac{2}{3}\sigma_{gg} + \frac{2}{3}n_q \cdot \frac{3}{2}\sigma_{qg} \\ &= \underbrace{\left(\frac{3}{2}n_g + \frac{2}{3}n_q\right)}_{n_{\text{eff}}} \cdot \underbrace{\frac{3}{2}\sigma_{qg}}_{\sigma_g}, \end{aligned} \quad (2.6)$$

$$\begin{aligned} n_g\sigma_{gq} + n_q\sigma_{qq} &= \frac{3}{2}n_g \cdot \frac{2}{3}\sigma_{gq} + \frac{2}{3}n_q \cdot \frac{3}{2}\sigma_{qq} \\ &= \underbrace{\left(\frac{3}{2}n_g + \frac{2}{3}n_q\right)}_{n_{\text{eff}}} \cdot \underbrace{\frac{3}{2}\sigma_{qq}}_{\sigma_q}. \end{aligned} \quad (2.7)$$

Then, the probability for no scattering between x_0 and x_1 is given by:

$$P_{\text{no scatt.}} = \exp \left\{ - \int_{x_0}^{x_1} dl \sigma_{q/g}(x(l)) n_{\text{eff}}(x(l)) \right\} \quad (2.8)$$

which is sampled in the Monte Carlo implementation. If a scattering is encountered the relative contribution of gluons as scattering centres is given by:

$$r = \frac{n_g\sigma_{gg}}{n_g\sigma_{gg} + n_q\sigma_{qg}} = \frac{n_g\sigma_{qg}}{n_g\sigma_{qg} + n_q\sigma_{qq}} = \frac{3}{2} \frac{n_g}{n_{\text{eff}}}. \quad (2.9)$$

Because of interference effects there is a non-trivial interplay between the shower evolution and scatterings off medium recoil centres. Earlier versions of JEWEL treated elastic scatterings explicitly and inelastic ones by an enhancement factor in the splitting function. In the current version (2.0.x), a sufficiently hard scattering can result in further splitting by setting the parton shower to a higher scale. Thus, a scattering off a parton in the medium modifies the projectile virtuality, which affects the shower evolution [80]. In other words, the scatterings are dressed with initial and final state radiation. This also allows for a consistent treatment of the interference between vacuum and medium-induced radiation, which are treated on the same footing. In the probabilistic formulation of the LPM effect [104], a parton cannot undergo a splitting instantaneously, but only with a finite formation time. The decision on the scale of the potentially next branching is taken according to the Sudakov form factor. If no scattering occurs during the formation time, the radiation is realized. Otherwise, the momentum transfer of the scattering

is added coherently to the one from the previous scattering (which can be the primary hard one) and the new starting scale is calculated. At this point, the probability for radiation has to be re-evaluated. If the updated scale is lower, the emission might be rejected; if it is higher, radiation might be added or assigned a different scale. If the update results in a formation such that the scattering is outside the formation time, it is rejected. This evolution must interact with the medium implementation in a well-defined way and the medium must provide all the required information.

When all partons have reached the hadronization threshold they are handed over to PYTHIA where the Lund string model is used for the hadronization to arrive at the final state particles. The final state comprises only the particles from the parton shower, i.e. there is no underlying event from medium hadronization. However, the recoiling scattering centres can be included in the shower evolution. If enabled, they undergo the same shower evolution as the original projectile parton.

2.2 Medium implementation

Conceptually, the algorithm outlined above allows for any medium with partonic scattering centres. To make use of this flexibility and compare the behaviour of the same parton shower formulation in the presence of different media, a clear separation of the shower from the medium implementation is desirable. In order to use different media evolutions, it must be ensured that the evolution of the parton shower with all interference effects remains intact. Therefore, a first step was to identify and separate the components that should be attributed to the medium into an exchangeable code with a well-defined interface to the main parton shower. The implementation of the latter must properly interact through this interface wherever medium properties are required. Technically, JEWEL can be linked to different modules for the medium evolution.

The general sequence of a JEWEL simulation now consists of a run initialization, during which configuration parameters for the shower and the medium are read in, and an event loop. The latter comprises an event initialization producing the initial partons and the medium (e.g. the impact parameter can be different per event), the parton shower with branchings and scatterings, and the hadronization. Of course, the medium implementation must still allow for a vacuum shower as benchmark and baseline for comparison. For this purpose, a dummy implementation is used which just provides the required interface but leads to no interactions.

Besides obvious medium parameters such as local temperature and density some more information is best attributed to the medium. The impact parameter b , see Figure 1.3, is assigned to the medium because it is strongly related to the resulting overlap region. At the same time the probability for an impact parameter in some range depends on the assumptions made for the nuclei. The evolution of the parton shower is completely ignorant of the impact parameter and only senses it through the resulting medium. Depending on the medium, b can be fixed or generated randomly in the per-event initialization. The next ingredient is the position of the hard interaction vertex. While it fixes the generation of the hard partons, its location is again determined from the collision geometry and, thus, picked in the medium implementation.

The calculation of the next scattering point must be done in the shower code since it is closely intertwined with the handling and rejection of parton splittings. It must, however, only rely on properties provided by the medium to evaluate the scattering probability. For this purpose the corresponding method in the shower code was modified to numerically integrate over the locally evaluated scattering probability:

$$dl \sigma(x) \cdot n_{\text{eff}}(x) \tag{2.10}$$

along the parton trajectory with the effective density n_{eff} taken from the medium implementation.

While the dependence of n_{eff} on the position is obvious, it enters also to the cross section through the kinematically accessible phase space and the regularization (temperature-dependent Debye mass). The former is determined by the relative motion of the projectile and a scattering centre and fixes the boundaries for the integration over $dt \frac{d\sigma}{dt}$. For the target the average velocity at a given position is used. The integration over $n_{\text{eff}}\sigma$ along the path is carried out in the lab frame and, thus, the effective density n_{eff} in a fluid rest cell must be boosted accordingly if the medium flows (collective motion):

$$n_{\text{eff}}^{\text{lab}} = \frac{3}{2}n_g\gamma + \frac{2}{3}n_q\gamma = \gamma \cdot n_{\text{eff}} \quad (2.11)$$

where γ is the Lorentz factor¹. The probability for no interaction within some time t_{max} after a parton was produced is then given by:

$$P_{\text{no int}}(t_{\text{max}}) = \exp \left\{ - \int_0^{t_{\text{max}}} dt \underbrace{\beta \cdot n_{\text{eff}}^{\text{lab}}(t) \sigma(t)}_{=:f(t)} \right\} \quad (2.12)$$

where $n_{\text{eff}}^{\text{lab}}(t)$ and $\sigma(t)$ refer to the evaluation at the position $\mathbf{x}_0 + \beta \cdot t$. β is the particle velocity as a fraction of c .

Whenever a scattering is encountered a recoil parton from the medium has to be generated. For a microscopic calculation of the $2 \rightarrow 2$ scattering, the recoil centre must be assigned a parton species, a mass, and a four-momentum. At this point, also flow enters by an average velocity of the partons in a fluid cell at a given location. This information must clearly be provided by the medium since both species and kinematic variables depend on the medium composition and evolution. The species is picked according to the relative gluon and quark density. The mass is derived from the local temperature as $m_s = 3T/\sqrt{2}$. And the momentum is constructed by sampling a thermal distribution in the rest-frame of the fluid cell and boosting it accordingly by the cell velocity, i.e. flow.

A list of the FORTRAN functions and subroutines required for a JEWEL medium implementation can be found in Appendix A.

2.2.1 Bjorken medium

As an example, a medium following Bjorken expansion shall be discussed first since can be treated analytically. The boost-invariant hydrodynamic evolution, introduced in Section 1.2, describes the longitudinal evolution for given initial conditions. Here, the transverse profile is taken from a Glauber calculation. First, the impact parameter for the collision is chosen. For the nuclear density a Woods-Saxon profile is assumed [105]:

$$\rho(r) = \frac{n_0}{1 + \exp \left\{ \frac{r-R}{D} \right\}} \quad (2.13)$$

where n_0 is the saturated nuclear density, R the nuclear radius and D the thickness of the edge². The corresponding nuclear radius is calculated from the atomic number by the requirement that $A = \int dV \rho(\vec{r})$ [105]:

$$R = 1.12 \cdot A^{\frac{1}{3}} - 0.86 \cdot A^{-\frac{1}{3}}. \quad (2.14)$$

Now the probability of the two nuclei passing each other without interaction can be calculated for a given impact parameter b in an optical Glauber model. The event plane is always considered

¹For a boost-invariant longitudinal expansion $\gamma = \cosh \eta_s$.

²Alternatively, a homogeneous sphere can be assumed as an even simpler geometry

to be in the x direction. For convenience we define the nuclear thickness function, i.e. the longitudinally integrated density:

$$T_A(x, y) = \int dz \rho(x, y, z). \quad (2.15)$$

The nuclear thickness functions obtained for the Woods-Saxon profile of Au and Pb nuclei are shown in Figure 2.2a as a function of the radius. Then, the probability for no interaction at a given impact parameter can be written as:

$$P_{\text{no int}}(b) = \exp \left\{ -\sigma_{\text{NN}} \int dx dy T_A(x + \frac{b}{2}, y) \cdot T_A(x - \frac{b}{2}, y) \right\} \quad (2.16)$$

where σ_{NN} is the inelastic nucleon-nucleon cross section, taken to be 42 mb for the top RHIC energy $\sqrt{s_{\text{NN}}} = 200$ GeV/ c . This leads to the differential cross section:

$$\frac{d\sigma}{db} = 2\pi b \cdot (1 - P_{\text{no int}}(b)), \quad (2.17)$$

which is used to pick an impact parameter during event initialization. Figure 2.2b shows the cross sections for Au–Au and Pb–Pb collisions. It should be noted here that the collision geometries for the two systems are very similar.

At this stage, also the position of the hard vertex is chosen according to binary collision scaling, i.e. proportional to:

$$T_A(x - \frac{b}{2}, y) \cdot T_A(x + \frac{b}{2}, y). \quad (2.18)$$

The initial temperature $T_i(x, y)$ is derived from scaling with the number of participants:

$$T_i(x, y) \propto T_A(x - \frac{b}{2}, y) \left(1 - \exp \left\{ -\sigma_{\text{NN}} \cdot T_A(x + \frac{b}{2}, y) \right\} \right) + T_A(x + \frac{b}{2}, y) \left(1 - \exp \left\{ -\sigma_{\text{NN}} \cdot T_A(x - \frac{b}{2}, y) \right\} \right) \quad (2.19)$$

with an externally provided average temperature. For comparison of the N_{part} and N_{coll} scaling Figures 2.3a and 2.3b show the distribution of the hard vertices and the initial temperature, respectively.

The initial time also has to be fixed externally, at top RHIC energy typically $\tau_i = 0.6$ fm/ c is used. Then, the temperature evolution with proper time is given by:

$$T(x, y) = T_i(x, y) \cdot \left(\frac{\tau}{\tau_i} \right)^{-\frac{1}{3}} \quad (2.20)$$

as explained in Section 1.2. The effective medium density is calculated under the assumption of an ideal relativistic parton gas with N_f active quark flavours:

$$n_{\text{eff}} = \left(-g_3(-1) \cdot 12 \cdot N_f \cdot \frac{2}{3} + g_3(1) \cdot 16 \cdot \frac{3}{2} \right) \cdot \frac{T^3}{\pi^2} \quad (2.21)$$

with the polylogarithmic function $g_\nu(z)$.

For any given space-time point in the medium, a scattering centre can be sampled with an isotropic momentum and an absolute value according to Fermi-Dirac (+) or Bose-Einstein (–) statistics:

$$\frac{dN}{dp} \propto \frac{p^2}{\exp \left\{ \frac{\sqrt{p^2 + m^2}}{T} \right\} \pm 1}. \quad (2.22)$$

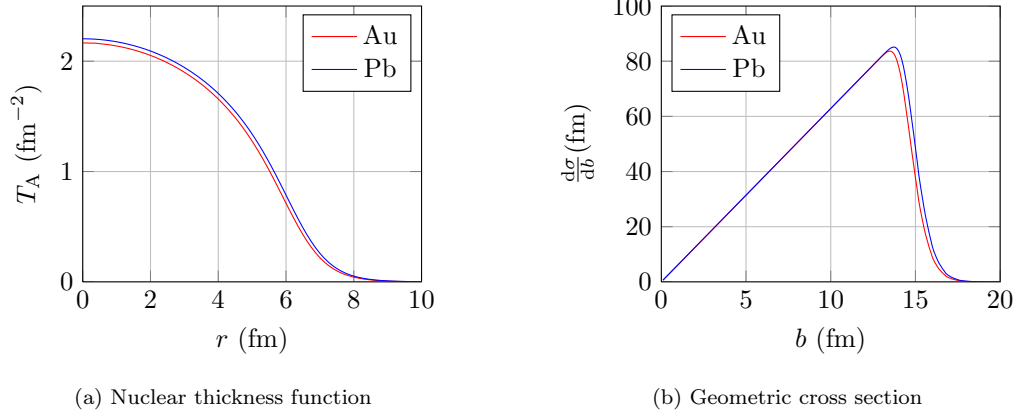


Figure 2.2: Nuclear thickness functions and geometric cross sections for Au and Pb nuclei as obtained from a Woods-Saxon density distribution and a nucleon-nucleon cross section $\sigma_{\text{NN}} = 42$ mb.

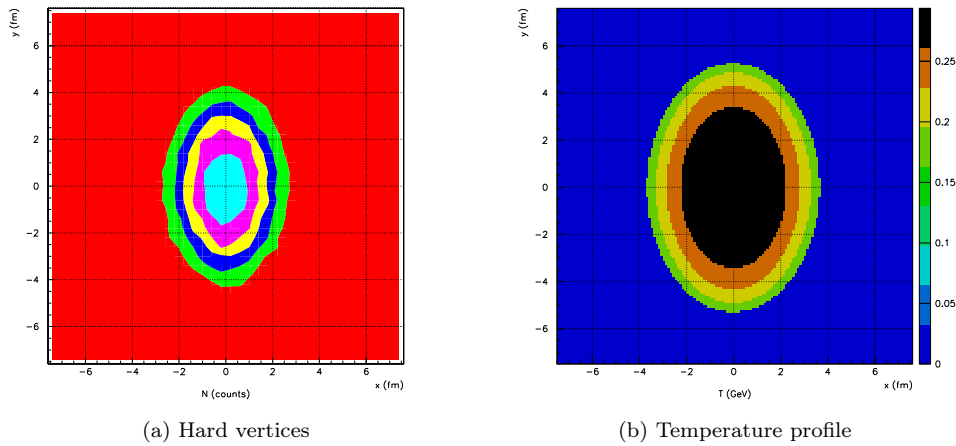


Figure 2.3: Distribution of hard interaction vertices and temperature profile ($t = 0.9$ fm/c): Both quantities are derived from the nuclear thickness function, the former from scaling with the number of binary collisions, the latter from scaling with the number of participants. A Au–Au collision with fixed impact parameter of $b = 8.87$ fm was assumed.

A boost from the rest frame of the fluid cell to the lab frame has to be applied to account for the flowing fluid. In the case of the Bjorken evolution, it is purely longitudinal. The non-zero mass arises from using a thermal scattering centre from the medium.

2.3 Interface to hydro-dynamical calculations

Having separated the medium implementation, it is appealing to use the output of realistic numerical relativistic hydrodynamic evolutions. By now several groups have codes for a full evolution in 2+1 or 3+1 space-time dimensions [106]. The calculations differ e.g. in the initial conditions, the equation of state, the inclusion of dissipative effects (viscosity), and the technical realization (e.g. the type of grid used for space-time discretization). Within the work of TECHQM, a common exchange format for the output was proposed under the name OSCAR2008H [107]. Because of the differences of the hydro models, the OSCAR standard allows for a variety of data formats. In fact, a header specifies details about the structure of the subsequent data. This includes the type of coordinates (2+1, 3+1, Cartesian, cylindrical), the used type of grid (Eulerian or Lagrangian), the start time of the hydrodynamical evolution, the assumed equation of state, and whether the full history of the evolution or only the final status before hadronization is stored. Two types of space-time grids are commonly used in hydrodynamical codes. Fixed cells as used in a Eulerian grid can be difficult because of the drastic expansion of the medium during the evolution. This requires a very fine-grained, yet large grid to describe the full evolution accurately. Therefore, Lagrangian grids with co-moving and expanding fluid cells are often preferred.

In the main data, local variables are provided for every fluid cell (in the following capital letters are used for the variables from the OSCAR data file, derived quantities are written in lower case). They comprise the energy density E , the temperature T , the pressure P , the fraction R of the density in the plasma phase (relevant for an equation of state with a first order phase transition), the transverse flow velocities $V_{x,y}$, and others which are not relevant for the parton shower evolution.

A corresponding interface was implemented as a JEWEL medium to allow for the use of arbitrary medium evolution. The treatment of the output from a hydrodynamical calculation must provide the same information to the shower simulation as in the case of the Bjorken medium, but much fewer implicit assumptions can be made, e.g. the life time of the medium at a given transverse position is only known numerically. For the OSCAR implementation of JEWEL the full history in 3-dimensional coordinates in a Lagrangian or Eulerian grid is required. Only if those conditions are met the actual data will be read.

Typical OSCAR data files can be large (few 10 GB) if they contain all details of the evolution. For the shower evolution in JEWEL, information about the medium is required at space-time points in the lab frame. Thus, the natural choice for handling numerical information is a discretized grid in these coordinates. The granularity must be sufficiently fine to contain the characteristics of the medium densities. But it does not drive the hydro-dynamical evolution, i.e. errors from averaging do not propagate in time. Therefore, a grid much coarser than for the hydrodynamical calculation itself can be used, which helps to reduce the memory requirement and to speed up the shower simulation. Therefore, an intermediate representation is used which is filled on first reading and then cached for subsequent runs. This avoids the time costly reading of the potentially large OSCAR files. This is also beneficial because of the different allowed grids. In the actual implementation for JEWEL a grid of up to 80^3 bins for the time and transverse space coordinates is used for the internal representation while longitudinal information is currently limited around mid-rapidity.

If the OSCAR file contains data in a Eulerian grid the reading process is straight-forward

as the data can be filled directly into the internally used grid, possibly with averaging over and removing unnecessary regions of rapidity.

For data in a Lagrangian grid a translation to the internal Eulerian grid is necessary. Only the data around mid-rapidity are read at the moment. The reading routine calculates the position of each Lagrangian cell in the Eulerian grid, averages over multiple values assigned to the same bin, and interpolates any occurring gaps as a final step³. This results in the following sequence:

1. allocate a Eulerian grid with a given granularity
2. loop over all Lagrangian grid cells
 - (a) skip cell if $|z| > z_{\max}$
 - (b) calculate time in lab frame:

$$t_i = t_{i-1} + (\tau_i - \tau_{i-1}) \cdot \gamma, \quad \gamma = \frac{1}{\sqrt{1 - V_x^2 - V_y^2}} \quad (2.23)$$

(In the first iteration the time is initialized with the starting time from the header.)

- (c) calculate Eulerian (x, y, z) bin from the Lagrangian cell
 - (d) add data to bin and increase fill counter for the bin
3. loop over all Eulerian cells and calculate the average
4. run interpolation to bridge gaps in the Eulerian grid

Some complications arise from the limited information available compared with a fully known evolution model. For example, the effective density is not directly available from the OSCAR file and must be calculated from other values. For every cell it is known which fraction R of the energy density E is in the plasma phase. For the evaluation of n_{eff} the composition of quarks and gluons is needed. The energy density in the plasma phase:

$$\varepsilon(x) = E(x) \cdot R(x) \quad (2.24)$$

must fulfil:

$$\varepsilon(x) = \varepsilon_q(x) + \varepsilon_g(x). \quad (2.25)$$

As this information is not available from the OSCAR data the gluon energy density is calculated assuming an ideal relativistic gas:

$$\varepsilon_g(x) = \frac{16\pi^2}{30} \cdot T(x)^4 \cdot R(x). \quad (2.26)$$

The factor $R(x)$ is added to account for a possible two-phase mixture. Then it follows for the quark density:

$$\varepsilon_q(x) = \max(\varepsilon(x) - \varepsilon_g(x), 0). \quad (2.27)$$

The corresponding number densities are then calculated as:

$$n_q = \frac{8}{7} \cdot \frac{-g_3(-1) \cdot 30}{\pi^4} \cdot \frac{\varepsilon_q}{T} \simeq \frac{\varepsilon_q}{3.15 \cdot T}, \quad n_g = \frac{g_3(1) \cdot 30}{\pi^4} \cdot \frac{\varepsilon_g}{T} \simeq \frac{\varepsilon_g}{2.7 \cdot T}, \quad (2.28)$$

yielding the effective density:

$$n_{\text{eff}}(x) = \frac{2}{3}n_q + \frac{3}{2}n_g. \quad (2.29)$$

³For data with fluctuating initial conditions, the interpolation should be avoided.

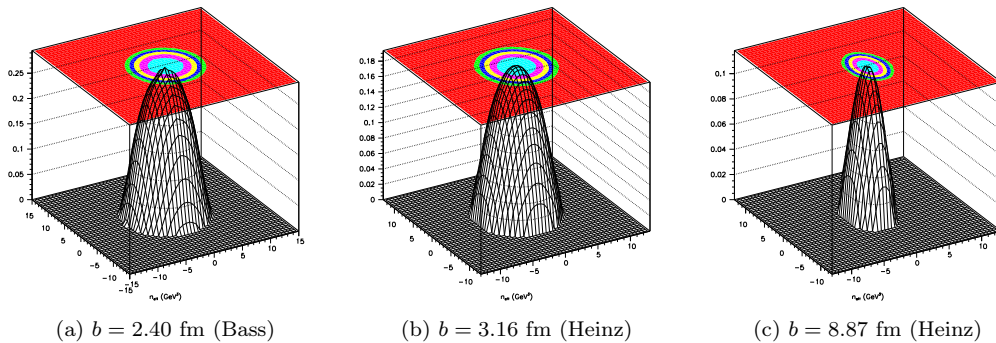


Figure 2.4: Effective density of media from relativistic hydrodynamics: In all cases, the shape of the effective density (in GeV^3) at the beginning of the hydrodynamical evolution is determined from Glauber models for a given impact parameter.

The hydrodynamic evolution only starts at a given time and the behaviour before has to be added by hand. By default, a linear rise of temperature is implemented up to the start time of the hydrodynamic data, for the effective density the rise is assumed to be proportional to T^3 . The primary vertex of the interaction is chosen according to binary collision scaling. The remaining implementation is analogous to the Bjorken case. The above discussion made evident that the calculation of the derived quantities is not uniquely determined but some choices, e.g. the calculation of the effective density, had to be made. However, it has been considered most crucial that the features of the hydrodynamical evolution are kept.

2.4 Impact on observables

To judge the influence and the relevance of the medium implementation for the energy loss modelling, we shall look at observables which can also be measured experimentally. However, it should be stressed that the focus of this discussion is on differences arising from the medium evolution. The direct comparison with experimental data using Bjorken evolution has been studied elsewhere [80]. In the following, we compare results obtained from JEWEL+PYTHIA [81] with identical energy loss prescriptions but with different medium evolutions. For this purpose, the HepMC output from JEWEL was processed with analyses implemented for Rivet [108, 109].

Before discussing the actual observables, an overview of the scenario under study is due. Because of the availability of hydrodynamic calculations with output in the OSCAR2008H format, we consider Au–Au collisions at the top RHIC energy, i.e. $\sqrt{s_{\text{NN}}} = 200$ GeV. Within this scope, we shall consider three medium evolutions with different impact parameters (which will be used together with the author as identifier in the following). They are based on two implementations of relativistic hydrodynamics. The hydrodynamic calculations also differ in the assumed initial conditions and the equation of state. In each case, we shall compare the results with those obtained for the previously explained boost-invariant Bjorken evolution following Glauber initial conditions for the same impact parameter.

The most central collision with an impact parameter of $b = 2.40$ fm (comparable to the 0 - 6 % most central events) was calculated in 3+1 ideal (i.e. non-viscous) relativistic hydrodynamics by the group of Steffen Bass [110, 111]. The hydrodynamic evolution is seeded with initial conditions from a Glauber wounded nucleon model. A first-order equation of state (Bag model, 3 fermions)

is assumed and results in the existence of a mixed phase⁴. The calculation and the output use a Lagrangian grid.

Another similarly central collision with $b = 3.16$ fm (comparable to 0 - 10 % most central collisions) was provided from a boost-invariant 2+1 viscous relativistic hydrodynamic evolution, in the group of Ulrich Heinz [112, 113]. The initial conditions were calculated from an optical Glauber model. The used equation of state (s95p-PCE) interpolates between a hadron resonance gas and the plasma equation of state from QCD simulations on a discretized space-time lattice [114]. The viscosity to entropy ratio η/s is assumed to be constant. A sudden transition to final state hadrons is implemented by the Cooper-Frye mechanism [115]. However, the particle abundances are fixed at the chemical freeze-out temperature $T_{\text{chem}} \simeq 165$ MeV as obtained from thermal model fits. This is realized by temperature-dependent chemical potentials below T_{chem} . In this case, output for other impact parameters is available as well and we shall consider a semi-central event with $b = 8.87$ fm (comparable to 30 - 40 % most central collisions). The output from this implementation is provided in a Eulerian grid.

Figure 2.4 shows the local effective density n_{eff} of the different media described above at the beginning of the hydrodynamic evolution as used for JEWEL (read from the OSCAR data). With averaged initial conditions from optical Glauber modelling, all density distributions are smooth. The two central collisions are very similar in shape, the peak density being a bit higher for $b = 2.40$ fm. The semi-central collision exhibits a significant eccentricity in the initial density as expected for the large impact parameter $b = 8.87$ fm. In Figure 2.5, we show the temporal evolution of temperature and effective density at three different points in the transverse plane. We compare it with the evolution from the purely longitudinal Bjorken expansion. For the Bjorken medium, we use the same initial time and fix the centrality to achieve the same impact parameter. The initial temperature is chosen such that the effective density n_{eff} (at the centre) evolves similar to the one from the hydrodynamic calculation. The configured values are listed in Table 2.1.

In the $b = 2.40$ fm case, the evolution of the density at the considered space points is similar but the values are higher than in the Bjorken case. The medium ceases to exist at similar times. The temperature, drops more quickly in the data from full hydrodynamics. With transverse expansion, the cooling can be more effective while the relation to the density is given by the equation of state. The full hydrodynamic evolution used a first order phase transition, which is visible as a plateau in T . The effective density drops rapidly to 0 at this critical temperature.

The picture for the $b = 3.16$ fm evolution is a bit different. While the effective density at the centre of the collision evolves similarly to the Bjorken description, it is lower at space points farther away from the centre. The lifetime of the media are similar. The temperature drops more slowly and, at the centre, is higher most of the time.

Being based on the same implementation of hydrodynamics and the same equation of state, a similar picture arises for the $b = 8.87$ fm case. The density and lifetime are very close at the centre, and the cooling is slower.

A qualitative difference of the hydrodynamic data to the purely longitudinal Bjorken expansion is the presence of transverse flow, see Figure 2.6. Driven by the pressure gradients, the fluid cells are pushed outwards. The eccentricity of the initial conditions results in an anisotropy of this flow pattern. Besides the average velocity of the scattering centres, it results in the medium reaching farther out in the transverse plane at late times.

⁴Recent results from lattice QCD show a cross-over instead of a first-order phase transition for the physical quark masses.

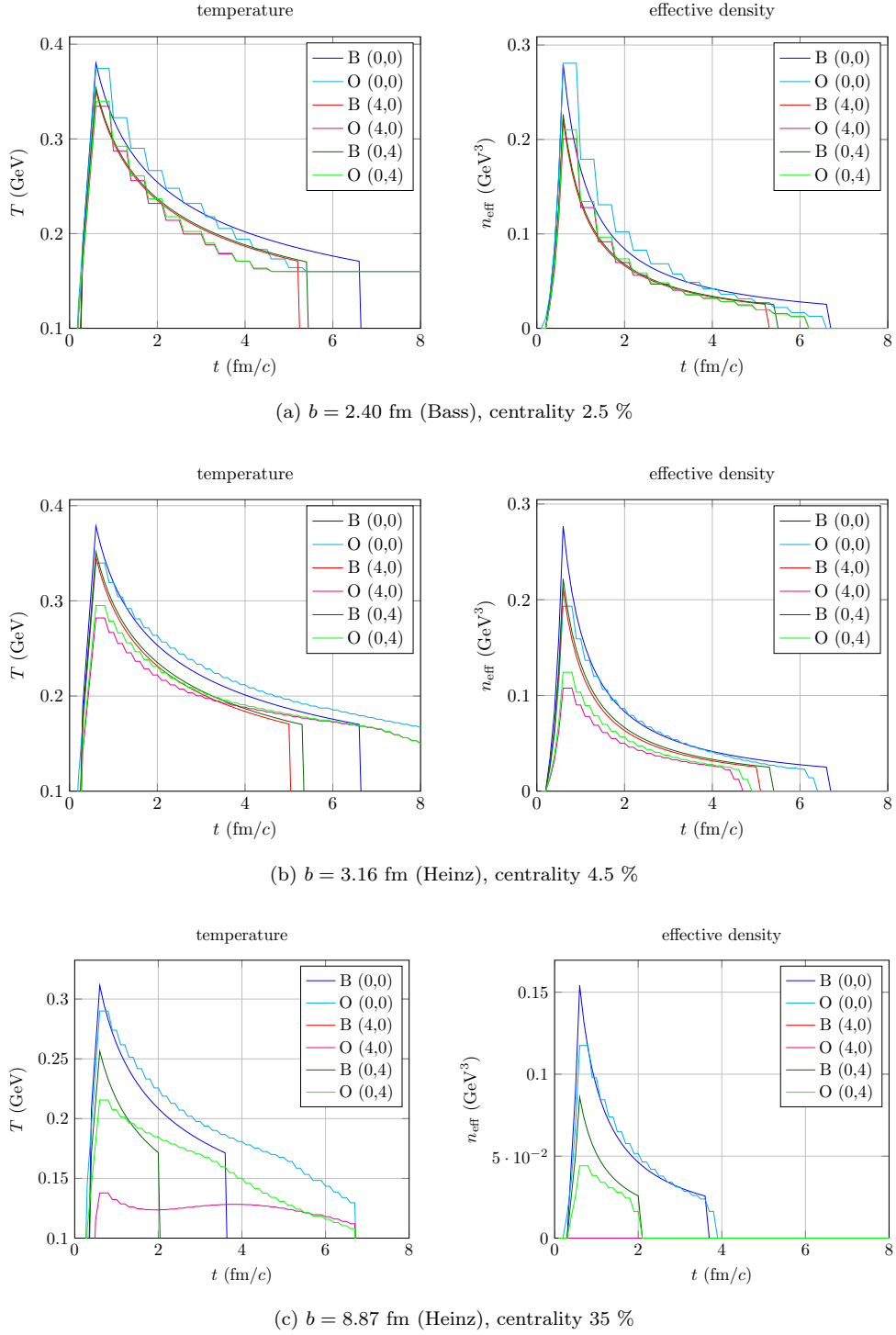


Figure 2.5: Comparison of medium evolution for various centralities: The temporal evolution of temperature and effective density at mid-rapidity is shown for the Bjorken (B) and OSCAR (O) data at different transverse positions (x, y) , values in fm. An explanation of the different media is given in the text.

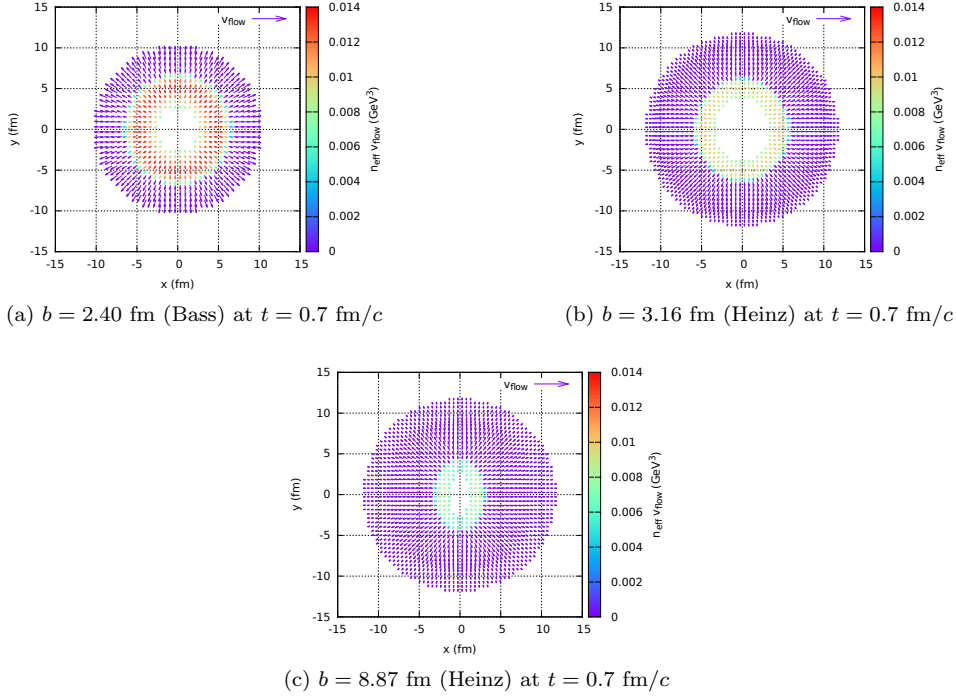


Figure 2.6: Transverse flow in hydrodynamical evolution: In contrast to the purely longitudinal expansion of the Bjorken medium, the hydrodynamical simulations show significant flow also in the transverse plane. The length of the arrows indicate the flow velocity, the colour the flow velocity weighted with the local effective density.

impact parameter	b	2.40	3.16	8.87	fm
centrality		2.5	4.5	35	%
Woods-Saxon		yes	yes	yes	
initial temperature	T_i	0.28	0.28	0.25	GeV
initial time	τ_i	0.6	0.6	0.6	fm/c
critical temperature	T_c	0.17	0.17	0.17	GeV
active flavours	N_f	3	3	3	

Table 2.1: Parameters used for the Bjorken medium: The values were chosen such that the effective density n_{eff} resembles the one from the hydrodynamical simulation.

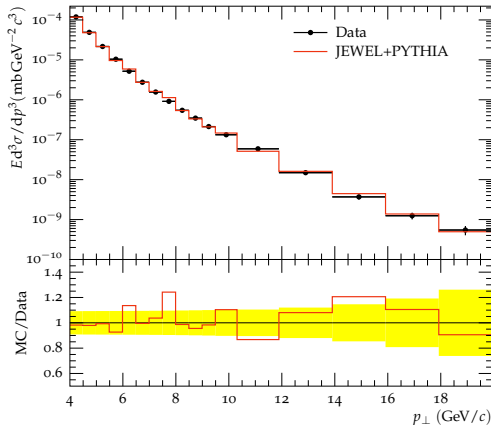


Figure 2.7: Transverse momentum spectrum of pions in pp collisions at $\sqrt{s} = 200$ GeV: With vacuum evolution JEWEL+PYTHIA reproduces the pion p_{\perp} spectrum measured by PHENIX [117]. Since the jet quenching observables are sensitive to the shape of the initial hard spectrum, this is an important benchmark.

2.4.1 Nuclear modification factor

A standard observable for the study of jet quenching is the nuclear modification factor R_{AA} , introduced in Section 1.4. It is used to characterize the suppression of a number of objects, e.g. particles (possibly identified) or reconstructed jets, relative to the expectation from incoherent scaling of the hard interactions. It is interesting to compare the effect of different medium evolutions on R_{AA} to judge how important an accurate description of the medium is for the modelling of jet energy loss. From an experimental perspective, it shows how sensitive measurements of R_{AA} are to differences in the medium evolution.

In the JEWEL framework, there is exactly one hard interaction per event. Thus, no normalization to the number of binary collisions is required. R_{AA} can simply be obtained by dividing the spectrum found in the presence of a medium by the one with vacuum evolution. For single particles, the suppression is often measured as a function of transverse momentum, i.e.:

$$R_{AA}(p_{\perp}) = \left(\frac{1}{N_{ev}} \frac{dN(p_{\perp})}{dp_{\perp}} \right)_{med} / \left(\frac{1}{N_{ev}} \frac{dN(p_{\perp})}{dp_{\perp}} \right)_{vac}. \quad (2.30)$$

Arising from partonic energy loss, the observed nuclear modification factor strongly depends on the p_{\perp} spectrum of partons from hard interactions. Its slope is a crucial difference between collisions at LHC and RHIC energies [80] and we must be sure to reproduce the p_{\perp} spectrum in vacuum for $\sqrt{s_{NN}} = 200$ GeV. We use the π^0 spectrum measured by PHENIX as benchmark [116], see Figure 2.7. The initial partons are taken from PYTHIA with a leading order perturbative matrix element⁵. The comparison with the measured spectrum shows good agreement. All values used for the parameters determining the shower evolution are given in Table A.3 in Appendix A.

First, we look at the suppression of charged particles as a function of p_{\perp} . The left column in Figure 2.8 shows the nuclear modification factors obtained for the different media. They

⁵PYTHIA contains only the leading order matrix element but the difference to a next-to-leading calculation is mostly the total cross section.

were obtained from the p_{\perp} spectra of all charged particles in the final state with pseudo-rapidity $|\eta| < 0.4$. As the modelling can only be expected to work for reasonably high transverse momenta results are shown only above 4 GeV/ c . It should be further noted that the recoiling scattering centres were not included in this simulation. This allows for the consistent comparison of the different media. But comparisons with data should be taken seriously only at larger transverse momenta since the recoiling partons contribute to the particle yield at lower transverse momenta. For every impact parameter, the Bjorken evolution (with corresponding parameters) is shown for direct comparison.

Secondly, we also look at the suppression of jets reconstructed by the FastJet anti-kt algorithm with a resolution parameter $R = 0.2$ [52], see the right column of Figure 2.8. We constrain the jet axis to $|\eta| < 0.4$ and their constituents to $|\eta| < 0.6$. The advantage of R_{AA} for jets as observable is its better resilience to fluctuations in the hadronization. Again, we compare the results using the full hydrodynamic evolution with the Bjorken approximation. As argued above, results are shown only above a minimum p_{\perp} , here 10 GeV/ c .

For $b = 2.40$ fm (Bass), we find a strong suppression for both charged hadrons and jets over a large p_{\perp} range. For the former, a small increase with p_{\perp} is visible, for jets the suppression is independent of p_{\perp} in the considered range. With the medium evolution from the hydrodynamic calculation, the suppression is stronger but does not differ in its p_{\perp} dependence. Looking back at the medium evolution, we see that the effective densities from the full hydrodynamical calculation are higher in most sampling points. At the same time, the temperature is similar or lower, especially away from the centre of the collision. The latter has an impact on the regularization of the cross section and the masses assumed for the scattering centres. In fact, such a difference can be accounted for by increasing the regularization Debye mass by 10 - 20 %.

For $b = 3.16$ fm (Heinz), we find an R_{AA} which differs slightly in absolute value between Bjorken and the OSCAR data, but again agrees in its p_{\perp} dependence. Compared to the previous scenario, the difference in geometry is small which is reflected by the suppression for the Bjorken evolution. Now, the suppression is weaker for the evolution from full hydrodynamics. This can be explained from the lower effective densities away from the collision centre and the higher temperature. As the difference is already visible at the beginning of the hydrodynamic evolution, this can be partially attributed to the determination of the initial conditions.

For $b = 8.87$ fm (Heinz), the suppression is considerably weaker, now for both hadrons and jets about a factor 2. This is expected for the much larger impact parameter, which results in lower energy density in a smaller volume. Otherwise, we find the behaviour similar to the previous cases.

In general, we do not observe a significant impact of the medium evolution on the nuclear modification factor for either hadrons or reconstructed jets. The absolute value of the suppression changes in a way expected from the differences in the medium evolution. The observed differences are small compared to the uncertainties. On the modelling side, a small change of the Debye mass, which is to be considered as a systematic uncertainty, results in R_{AA} changes of similar size. On the experimental side, the reconstruction of jets on top of the high-multiplicity heavy-ion background is difficult, in particular at RHIC energies, and the resulting jet R_{AA} carries large uncertainties [118]. The background must be subtracted to compare the yield of jets from the same original p_{\perp} . In this situation, we can conclude that the simpler Bjorken evolution is adequate for the simulation of the nuclear modification factors for inclusive hadrons and jets.

2.4.2 Azimuthally sensitive R_{AA}

Having found the global R_{AA} rather insensitive to the medium evolution, we continue by looking at more differential observables. With the non-trivial transverse shape of peripheral events, it is

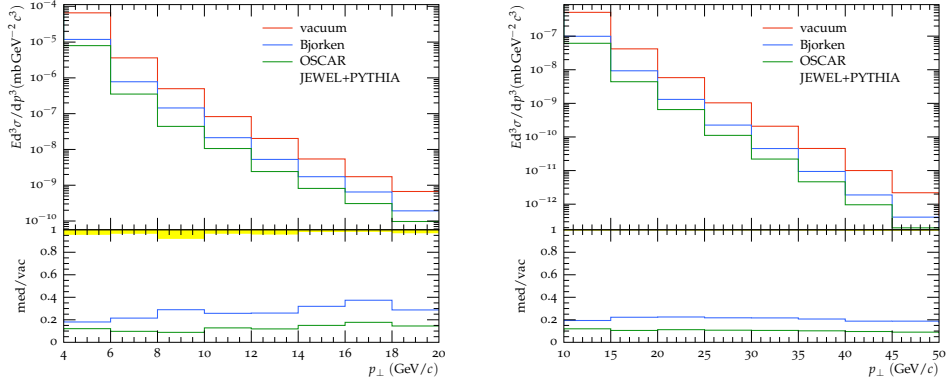
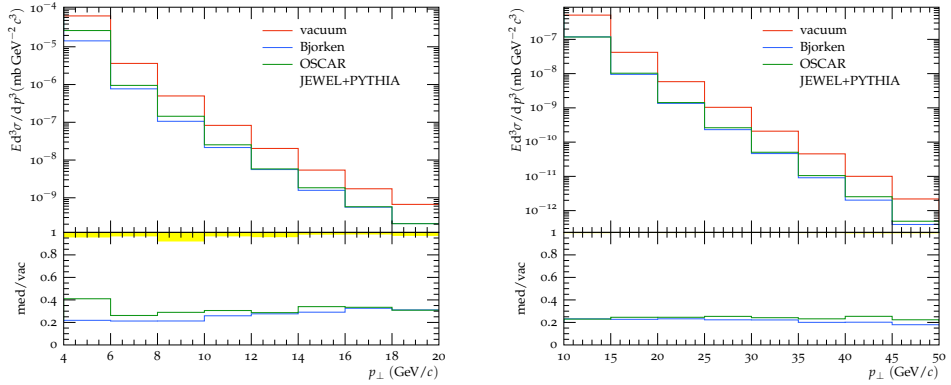
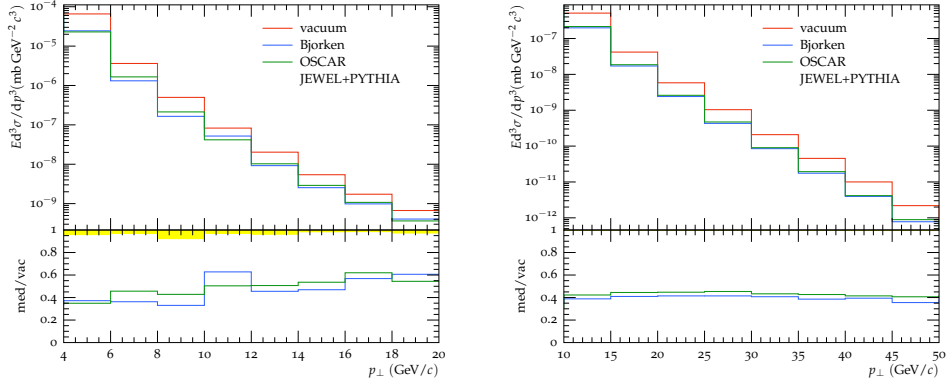
(a) $b = 2.40$ fm (Bass), centrality 2.5 %(b) $b = 3.16$ fm (Heinz), centrality 4.5 %(c) $b = 8.87$ fm (Heinz), centrality 35 %

Figure 2.8: Comparison of nuclear modification factors (Au–Au at $\sqrt{s_{NN}} = 200$ GeV): The suppression is shown for a medium evolution from relativistic hydrodynamics (OSCAR) and compared with Bjorken expansion (Bjorken). Left: charged particles ($|\eta| < 0.4$), right: anti-kT jets with $R = 0.2$ and $|\eta| < 0.4$.

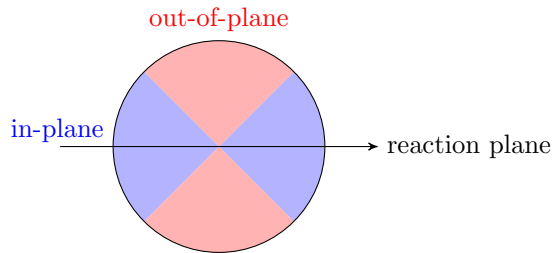


Figure 2.9: Azimuthal distinction of particles in- and out-of-plane: The azimuthal distribution around the collision vertex is considered. Particles oriented along the reaction plane (direction of the impact parameter) are said to be in-plane, those in perpendicular direction out-of-plane.

interesting to look at azimuthal differences, e.g. in R_{AA} . The particle yield at high p_{\perp} originates from hard interactions which intrinsically lead to isotropic particle production. However, the different path length in the medium is expected to result in a direction-dependent energy loss. The comparison of the Bjorken and full hydrodynamical medium is even more interesting now because of transverse flow.

The R_{AA} analysis discussed before can be repeated in azimuthal bins with respect to the reaction plane. The latter is known to be always in x direction for the medium scenarios under study⁶. For simplicity, we choose the two orientations along and perpendicular to the reaction plane, i.e. the so-called in- and out-of-plane regions, sketched in Figure 2.9. Thus, we simply select particles in the corresponding intervals of azimuthal angle and calculate R_{AA} as before, but separately for the two bins.

Figure 2.10 shows the nuclear modification factor for jets (anti-kt, $R = 0.2$) in- and out-of-plane. We limit ourselves to the case $b = 8.87$ fm, for which we expect the strongest effect because the asymmetry is largest. As expected from a path-length dependent energy loss and the collision geometry, we see a stronger suppression out-of-plane than in-plane. The difference between the two directions is small. Comparing the medium evolutions, we find a change in absolute value as before but no further impact. And the experimental discrimination is even more challenging here, since the proper measurement of the jet R_{AA} requires the subtraction of the heavy-ion background to account for the anisotropy of the underlying event. Of course, it helps to consider jets at higher transverse momentum, but then the statistics is very limited. This makes these studies very difficult at RHIC energies – at LHC, the high- p_{\perp} yields are significantly higher because of the higher centre-of-mass energy.

2.4.3 High- p_{\perp} v_2

Another way of looking at the influence of the anisotropic medium is the resulting modulation in the azimuthal distribution of the probe, usually quantified by the coefficients of a Fourier expansion in φ , see Equation 1.10. For low transverse momenta (below ~ 4 GeV/ c), this modulation arises from the pressure gradient varying with direction, which translates the spatial anisotropy to momentum space. For high- p_{\perp} particles (above ~ 5 GeV/ c), it can be generated by a direction-dependent in-medium path length. This modulation has the same phase as the

⁶In experimental data, the event plane must be reconstructed from the event anisotropy.

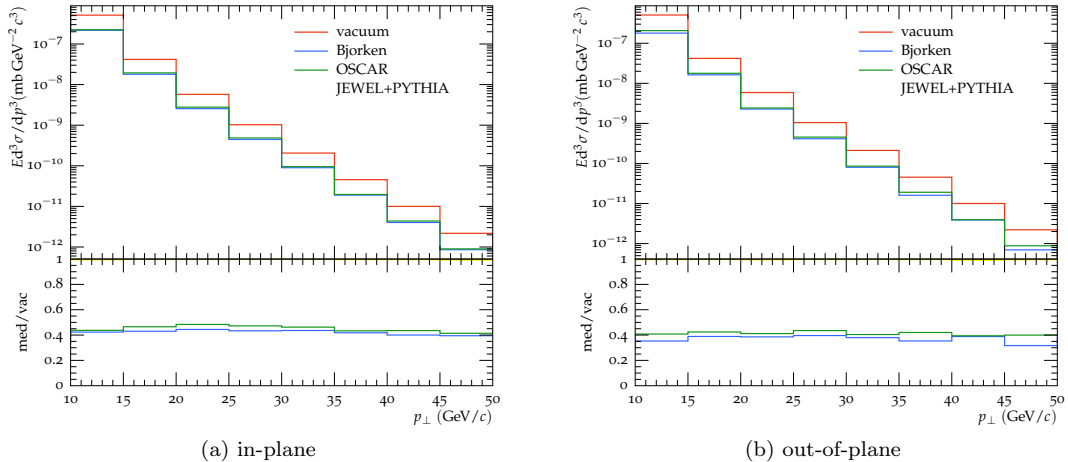


Figure 2.10: In- and out-of-plane R_{AA} : The nuclear modification factor is calculated separately for jets pointing in- and out-of-plane for a medium with $b = 8.87$ fm (Heinz) or a centrality of 35 %. A difference arises from the initial eccentricity of the overlap region which results in different quenching.

one at lower momenta but arises from a different mechanism⁷.

We look for such a modulation in the azimuthal distribution of reconstructed jets. Since the effect is small and difficult to see directly as a modulation in φ , we show instead $\langle \cos(2\varphi) \rangle$ as a function of jet p_{\perp} , see Figure 2.11. This extracts the v_2 component of the Fourier decomposition. For the central events, we find values close to 0. This is expected because of the small anisotropy of the collision such that the traversed path lengths are relatively independent of direction. For the more peripheral scenario, we find a significant deviation from 0. The effect is about 5 % for both medium evolutions. The positive sign of v_2 shows that more particles are emitted in-plane than out-of-plane. In fact, the value is directly related to the yields in- and out-of-plane by:

$$v_2 = \frac{\pi}{4} \cdot \frac{N_{\text{in}} - N_{\text{out}}}{N_{\text{in}} + N_{\text{out}}} = \frac{\pi}{4} \cdot \frac{R_{AA}^{\text{in}} - R_{AA}^{\text{out}}}{R_{AA}^{\text{in}} + R_{AA}^{\text{out}}}. \quad (2.31)$$

Measurements of v_2 for jets are difficult for the same reasons explained above for the separation of in- and out-of-plane yields. And the dependence which we see on the medium evolution is again so small that the simple evolution can be considered good enough.

2.5 Conclusions

A meaningful comparison of observables from jet quenching Monte Carlo event generators and data requires a realistic description of the medium evolution or the confidence that a simpler model is sufficiently precise. Therefore, we have studied the impact of the medium evolution on the simulation of partonic energy loss in JEWEL. For this purpose, we have compared results obtained with a purely longitudinal Bjorken expansion to those with medium evolutions from full hydrodynamic calculations.

⁷At low $\sqrt{s_{NN}}$ around 3 GeV/c, the elliptic flow goes out-of-plane and, thus, v_2 becomes negative.

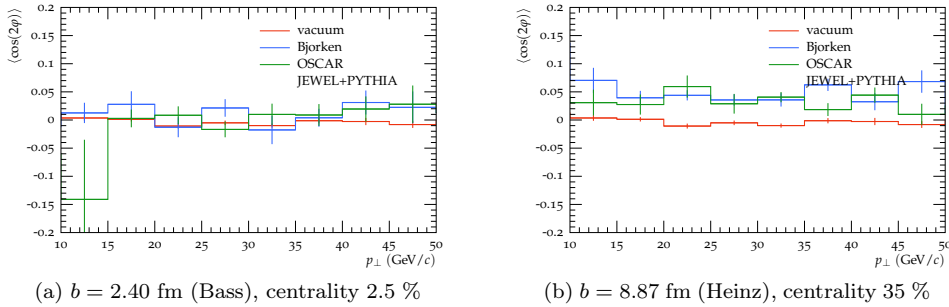


Figure 2.11: High- p_{\perp} v_2 of jets: The p_{\perp} dependence of the azimuthal anisotropy is shown as $v_2 = \langle \cos(2\varphi) \rangle$.

The OSCAR interface implemented for JEWEL gives the flexibility to use the output from hydrodynamic calculations as underlying medium for the parton shower evolution. Here, we have used three different Au–Au scenarios at the top RHIC energy $\sqrt{s_{NN}} = 200$ GeV (with impact parameters of 2.40, 3.16, and 8.87 fm) from two different groups. For each of them, we have compared the suppression of charged hadrons and jets with the one obtained for a medium following the longitudinal Bjorken expansion. We observe small differences in the absolute strength of the suppression. The changes can be explained from the comparison of the initial conditions and the medium evolution, e.g. the usage of different equations of state. In all cases, the impact of the precise medium evolution is small compared with experimental errors or systematic uncertainties of the model, e.g. variation of the Debye mass. We have not observed different trends in p_{\perp} or azimuthal patterns. Thus, we can conclude that, within the investigated scope, the usage of the analytic Bjorken expansion is indeed adequate for the modelling of high- p_{\perp} suppression.

The higher collision energy of $\sqrt{s_{NN}} = 2.76$ TeV in Pb–Pb collisions at the LHC results in much more abundant production of high- p_{\perp} particles and jets. This allows us to significantly extend the reach of measurements and facilitates the separation of jets from the underlying background. Respective studies of energy loss in Pb–Pb collisions are on-going. The JEWEL-OSCAR interface lays the foundations for more systematic studies using results from modern hydrodynamic calculations in these settings – provided that more output of relativistic hydrodynamical simulations will be released in the OSCAR2008H format. It is also interesting to apply the longitudinal Bjorken expansion on initial conditions read from an OSCAR input file, which shall allow to study changes from the evolution alone.

A recent trend of hydrodynamic calculations is to include fluctuations in the initial state. In this way, triangular flow (v_3) and higher harmonics can be described quantitatively. It is also conceivable to use such event-by-event output for the study of the impact of initial density fluctuations on the energy loss modelling. The medium would be much less homogeneous and exhibit hot spots of high density. The flexibility of using (almost) arbitrary medium evolutions as input for JEWEL clearly opens a wide field of possible applications. In particular, it allows to systematically check the energy loss for a given medium evolution without changes in the shower prescription. It further allows to confirm results obtained with the simpler Bjorken evolution. In the end, we should mention that also the impact of the jets on the medium evolution has been studied by the JEWEL author and collaborators [119].

Chapter 3

Experimental access

Particle accelerators have become an important tool for nuclear and particle physics. While they cannot achieve energies as high as observed in cosmic rays (the measured spectrum extends beyond 10^{20} eV [10]), they provide controlled collisions at a well-constrained point in an experimental setup. Together with high beam intensities, this allows for the detailed measurement of fully reconstructed events, also for rare processes.

3.1 Large Hadron Collider

Already when the construction of the Large Electron-Positron Collider (LEP) at CERN had just started in 1984, synchrotron radiation was known to put a fundamental limit on the collision energy achievable in electron rings. To overcome this limitation a Large Hadron Collider (LHC) was discussed to supplement LEP [120, 121]. Besides the increase in energy, the small cross sections expected for interesting processes called for high luminosities and high beam intensities.

Within this general framework the ideas matured and lead to the LHC conceptual and technical design reports [122, 123, 124, 125]. The LEP tunnel consisting of eight arcs and eight straight sections – the latter required for radio-frequency cavities compensating the energy losses by synchrotron radiation – was to be reused for the installation of the LHC. With the given circumference of 26.7 km and the charge over mass ratio of the proton, a target beam energy of 7 TeV translated to the requirement for dipole magnets with $B \simeq 8.33$ T, which in turn required super-conducting technology. The need for high beam intensities ruled out the use of protons and anti-protons, which would allow to use the same magnetic fields to bend the opposing beams. With the limited space available in the LEP tunnel, super-conducting twin-bore magnets were chosen despite their technical challenges and the fixed coupling of the fields. Besides protons, also heavy ions, in particular fully stripped lead nuclei, were considered already during the conceptual design.

The injection chain required to feed the LHC should make use of available resources and was built from existing accelerators at CERN, see Figure 3.1. The protons are accelerated in Linac2, transferred to the Proton Synchrotron Booster (PSB), the Proton Synchrotron (PS), and the Super Proton Synchrotron (SPS) before they are injected at 450 GeV into the LHC. Lead beams are produced from a different source and go through the Linac3, to the Low Energy Ion Ring (LEIR), the PS, and the SPS.

The radio-frequency for the LHC cavities was chosen as 400 MHz to match the injection. This results in 35,640 radio frequency buckets over the full LHC ring, of which every tenth can be populated with a bunch of particles. Both rings are equipped with independent RF systems.

The large number of bunches cannot be filled by the injection of individual bunches into the LHC. Instead trains of up to 72 bunches are used. For every beam a part of the ring is left empty (abort gap) to allow for a safe beam dump. A limitation on the maximum number of protons per bunch from non-linear beam-beam interactions and the available aperture amounts to about $1.15 \cdot 10^{11}$ protons. This also puts limits on the achievable luminosity. The design values are listed in Table 3.1. An important constraint in view of beam lifetime and experimental background comes from the vacuum conditions in the beam pipe which have to stand the deterioration from synchrotron radiation and the build up of electron clouds.

Only in four straight sections, the two beams are fed into a common beam pipe for roughly 130 m and brought to collision, see Figure 3.1. Crossing angle orbit bumps are setup to avoid parasitic collisions before and after the intended primary Interaction Points (IP). The straight sections not occupied by experiments are used for other purposes, such as the radio frequency for acceleration, beam cleaning, and the instrumentation for dumping.

An early filling scheme with a few populated bunches only is shown in Figure 3.2 for illustration. It has to accommodate for different optimization criteria at the different interaction points – ATLAS and CMS should get the highest possible luminosity, LHCb lower but constant luminosity, and ALICE even lower luminosity with the beam background as low as possible.

For the p-Pb operation – which was not part of the original design and is often considered as the first LHC upgrade – an additional complication arises as the revolution frequencies of the beams on the on-momentum orbits are different. With the independent RF systems for the two beams, they can be injected and accelerated on-momentum. Before colliding the beams, they are moved to off-momentum orbits, at which the revolution frequencies match, such that the RF systems can be locked¹. In a cogging step the beam crossings are moved to the nominal interaction points.

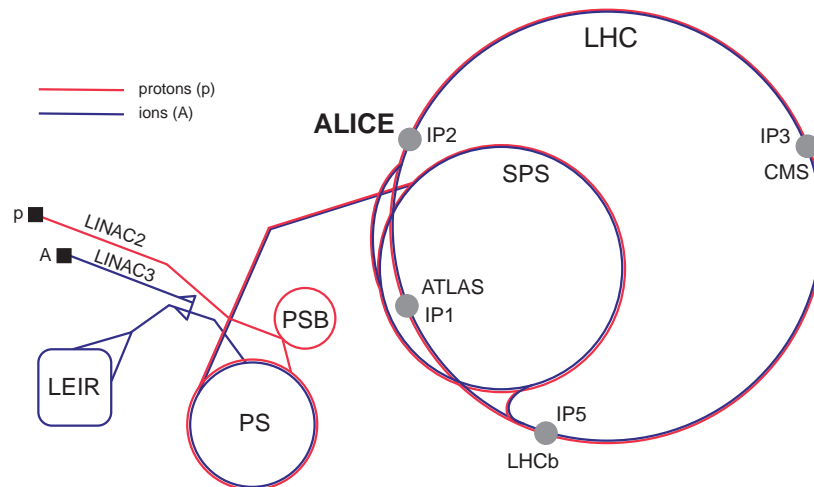


Figure 3.1: LHC injector chain and interaction points: The LHC requires a set of pre-accelerators to reach the injection energy of 450 GeV. The opposing beams intersect in four interaction points which are equipped with experiments.

¹At lower energy the aperture is too small for the off-momentum operation.

beam species	$\sqrt{s_{NN}}$ (TeV)	L ($\text{cm}^{-2}\text{s}^{-1}$)	N_{bunch}	β^* (m)	bunch spacing (ns)
pp	14	10^{34}	$1.15 \cdot 10^{11}$	0.55	25
Pb-Pb	5.52	10^{27}	$7 \cdot 10^7$	0.5	100

Table 3.1: LHC design values [126]: The LHC was designed for both pp and Pb-Pb collisions from the beginning. p-Pb collisions were only considered later.

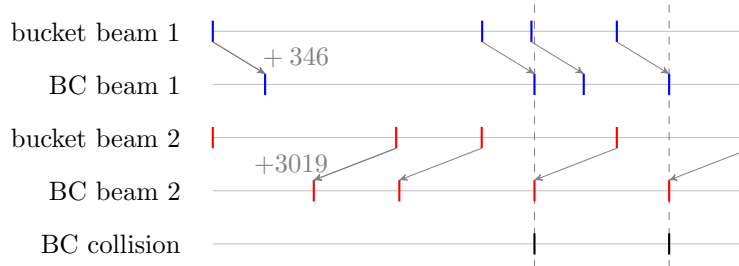


Figure 3.2: LHC filling scheme and resulting collisions: The filled RF buckets are shown for the two beams. A given bucket passes the ALICE interaction point at a certain value of the Bunch Crossing counter (BC). A collision occurs if two bunches pass at the same time.

3.1.1 Experiments at the LHC

The LHC is used by several experiments installed around the interaction regions. Among the four large experiments, there are two multi-purpose detectors, ATLAS and CMS, one specialized on B physics, LHCb, and a dedicated heavy-ion experiment, ALICE. In addition, there are three smaller experiments.

ATLAS (A Toroidal LHC Apparatus for Spectroscopy) is a general purpose detector installed at IP 1 [127]. It was designed to search for the Higgs boson and physics beyond the Standard Model, e.g. supersymmetric particles, extra dimensions, and black holes. The particle trajectories are observed in the magnetic field of a solenoid close to the beam pipe and a toroid farther out. The inner tracking system comprises silicon pixels and a transition radiation tracker. The need for calorimetry is served by liquid argon technology, both in the central barrel and the end caps, as well as hadronic calorimeters. Furthermore, there is an extensive muon system.

CMS (Compact Muon Solenoid) is a multi-purpose detector installed at IP 5 with similar objectives as ATLAS [128]. It differs in the used detector technologies. The detector is installed within a large super-conducting solenoidal magnet. The inner tracking system consists of silicon pixel detectors. It is followed by electromagnetic and hadronic calorimeters. Muon chambers are embedded in the return yoke of the magnet.

LHCb is dedicated to heavy-flavour physics with the objective to search for new physics in CP violation and rare decays of beauty and charmed hadrons [129]. The detector at IP 8 is built as a single arm spectrometer because pairs of b and \bar{b} quarks are predominantly produced both forward or backward. A warm dipole magnet produces a field of 4 Tm. A vertex locator allows for the precise reconstruction of secondary vertices. Both silicon microstrip detectors and straw tubes are used for tracking.

run	system	$\sqrt{s_{NN}}$ (TeV)	L_{max} ($\text{cm}^{-2}\text{s}^{-1}$)	integrated luminosity		
				ATLAS/CMS	LHCb	ALICE
2009	pp	0.90	n/a	$10 \mu\text{b}^{-1}$	$6.8 \mu\text{b}^{-1}$	$19.6 \mu\text{b}^{-1}$
2009	pp	2.36	n/a	$0.4 \mu\text{b}^{-1}$	n/a	$0.87 \mu\text{b}^{-1}$
2010	pp	7.00	$2.1 \cdot 10^{32}$	48pb^{-1}	42pb^{-1}	0.5pb^{-1}
2011	pp	7.00	$3.5 \cdot 10^{33}$	5.3fb^{-1}	1.2fb^{-1}	4.9pb^{-1}
2012	pp	8.00	$7.6 \cdot 10^{33}$	23.3fb^{-1}	2.2fb^{-1}	9.8pb^{-1}
2010	Pb-Pb	2.76	$3.0 \cdot 10^{25}$	$9.5 \mu\text{b}^{-1}$	n/a	$9.5 \mu\text{b}^{-1}$
2011	pp	2.76	$5.0 \cdot 10^{27}$	330nb^{-1}	540nb^{-1}	46nb^{-1}
2011	Pb-Pb	2.76	$4.7 \cdot 10^{26}$	$160 \mu\text{b}^{-1}$	n/a	$144 \mu\text{b}^{-1}$
2013	p-Pb	5.02	$1.2 \cdot 10^{29}$	31nb^{-1}	2nb^{-1}	32nb^{-1}
2013	pp	2.76	$1.4 \cdot 10^{32}$	5.2pb^{-1}	4.2pb^{-1}	129nb^{-1}

Table 3.2: The LHC running conditions in the runs from 2009 to 2013 [135, 136, 137, 138, 139]: Collisions were achieved with all combinations of proton and lead beams at different energies. The integrated luminosities at the interaction points were optimized according to experimental requirements.

ALICE (A Large Ion Collider Experiment) was built as a specialized heavy-ion experiment [130]. It is installed at IP 2 and will be explained in detail in the next section.

LHCf has the goal to measure the production cross section and energy spectra at very forward rapidities [131]. For this purpose, sampling calorimeters are installed in the Target Neutral Absorbers, where the common beam pipe splits into two. The detectors are installed on both sides of IP 1.

TOTEM aims at a luminosity-independent measurement of the total pp cross section based on the optical theorem [132]. In addition, studies of diffractive events are planned. The detector is installed around IP 5 and comprises two telescopes for the detection of charged particles and Roman pots.

MoEDAL (Monopole and Exotics Detector At the LHC) was built for the direct search of magnetic monopoles and other highly ionizing massive particles directly [133]. It is installed around IP 8.

All experiments face the challenge that the processes of interest have very small cross sections compared to the total inelastic pp cross section, about 73 mb at $\sqrt{s} = 7$ TeV [134]. The high luminosity required to produce the rare probes results in very high interaction rates. This implies that the detectors have to cope with pile-up, i.e. multiple overlapping events per bunch-crossing, and have to rely on a significant online rejection by a fast trigger system. An overview of the beam conditions at the interaction points is given in Table 3.2.

3.2 ALICE at the LHC

A Large Ion Collider Experiment was proposed and designed to study the properties of strongly interacting matter and the Quark-Gluon Plasma (QGP) [140, 141, 142, 143]. This led to design requirements which are different from the other LHC experiments. In central heavy-ion collisions, the charged particle multiplicities are very high and yet all tracks should be reconstructed to allow for event-by-event analyses. The detector was designed to allow for track reconstruction with pseudo-rapidity densities of charged particles up to $dN_{ch}/dy \sim 8000$ [143]. The detector must

allow for global event characterization, e.g. the determination of centrality and event plane. For the measurement of total (p_{\perp} -integrated) particle yields, tracking down to very low transverse momenta, where particles are produced most abundantly, is required. On the other hand, high p_{\perp} probes, e.g. jets, require good tracking resolution up to high momenta. In addition, Particle IDentification (PID) is of crucial importance to study e.g. the chemical composition of the produced particles. The experiment focuses on physics at or close to the mid-rapidity region and in forward direction.

An almost symmetrical central barrel is installed in the solenoidal magnet inherited from the L3 experiment at LEP. It produces a modest longitudinal field of about 0.5 T. Furthermore, a muon spectrometer is installed behind an absorber in forward direction. It consists of a warm dipole magnet with an integrated horizontal field of 3 Tm, six tracking stations, and additional trigger stations behind further iron shielding.

An overview of the detector setup is shown in Figure 3.3. In the following, only the detectors relevant to the further discussion in this thesis will be described.

3.2.1 Detector setup

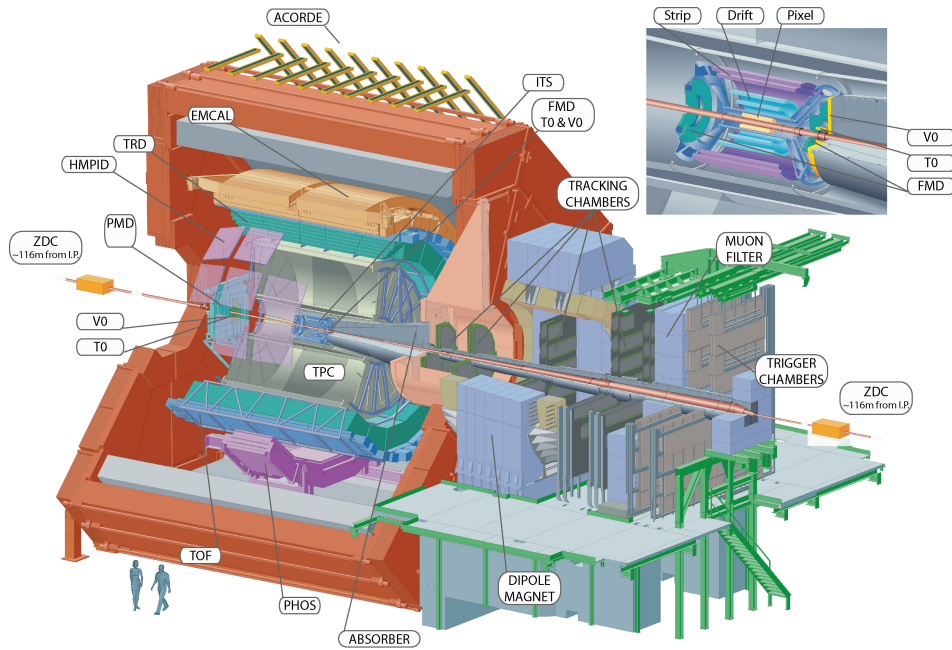
To cope with the high track densities, a cylindrical Time Projection Chamber (TPC) fully covering a pseudo-rapidity interval of $[-0.9, 0.9]$ was chosen as the major tracking device [144]. It has an inner and outer diameter of 0.85 and 2.5 m, respectively. The field cage holds a drift voltage of 100 kV between the central electrode and the end plates. The latter are equipped with multi-wire proportional chambers with analogue pad read-out. This allows for the measurement of the specific energy loss dE/dx and thereby the identification of particles. The TPC was operated with Ne-CO₂-N₂ as drift and counting gas until 2011, and with Ne-CO₂ from 2012 on. This resulted in a drift time of about 95 μ s, a momentum resolution of about 7 % at 10 GeV and a dE/dx resolution of about 5 %. This makes particle identification possible even for momenta in the relativistic rise of the specific energy loss. Figure 3.3c shows the specific energy loss as a function of rigidity p/z . The different particles are visible as bands. The latter are described well by the ALEPH parameterization [145].

To allow for low- p_{\perp} tracking and to improve the pointing resolution towards the interaction point a silicon-based Inner Tracking System (ITS) was installed around the beam pipe inside the TPC. The pointing is of importance for p_{\perp} resolution and secondary vertexing as used for the reconstruction of decays of heavy-flavour mesons. The ITS consists of Silicon Pixel (SPD), Silicon Strip (SSD) and Silicon Drift Detectors (SDD), with two layers of each (ordered with increasing radius). The SPD can be used for triggering. SSD and SDD feature analogue read-out and allow the measurement of specific energy loss.

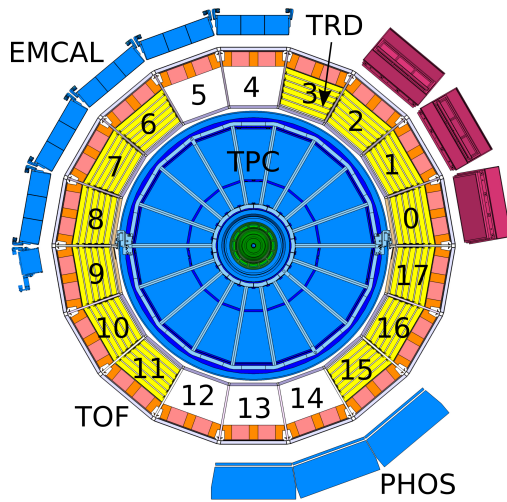
Towards larger radii, the TPC is followed by the Transition Radiation Detector (TRD), which allows for the identification of electrons by the detection of specific energy loss and transition radiation. Furthermore, it increases the lever arm for charged particle tracking and, thus, improves the momentum resolution. It also provides a variety of triggers. The TRD will be discussed in the dedicated Section 3.3.

A Time Of Flight (TOF) detector covers the full central barrel just outside of the TRD [146]. It is based on Multigap Resistive Plate Chambers (MRPC) and provides a timing resolution better than 100 ps at an occupancy below 10 %. This allows for good K/p separation up to ~ 4 GeV/c.

Only part of the central barrel acceptance is equipped with electromagnetic calorimeters. The PHOton Spectrometer (PHOS) is based on scintillating PbWO₄ crystals and provides high granularity and energy resolution. It has no overlap with the TRD. The ElectroMagnetic CALorimeter (EMCAL) is composed of Pb scintillator sandwiches [147]. A major incentive was to extend the



(a) Overview of the ALICE detector



(b) 2012/13 installation status

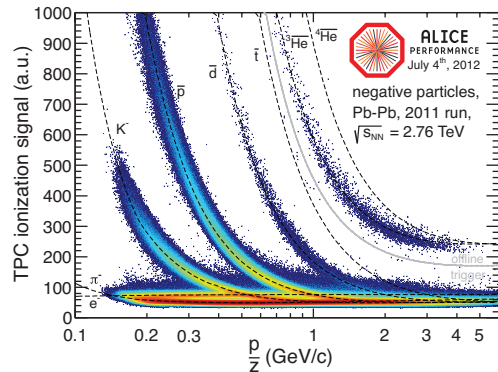
(c) TPC dE/dx

Figure 3.3: ALICE detector setup (top): The central barrel is located in the solenoidal field of $B = 0.5$ T. The Time Projection Chamber (TPC) forms the main tracking device, supplemented towards the interaction point by a silicon-based Inner Tracking System (ITS) for improved vertex resolution, towards large radii by the Transition Radiation Detector (TRD) for electron/pion separation, and a Time-Of-Flight detector (TOF) for additional particle identification. Electromagnetic calorimeters (EMCAL and PHOS) cover part of the central barrel acceptance. A muon spectrometer is installed in forward direction. The cross-sectional view (bottom left) shows the installation status for the data taking with TRD triggers in 2012 and 2013. The measurement of the specific energy loss in the TPC (bottom right) allows for good particle identification over a large momentum range.

jet measurement capabilities of the experiment. Both calorimeters can be used for triggering.

Detectors in the forward direction are used for triggering and event characterization. Two wheels of scintillator panels on each side of the interaction point build the V0 detector. It provides the minimum bias trigger for the experiment and allows for centrality and event plane estimates in Pb–Pb collisions. The T0 detector is based on 12 quartz Cerenkov counters on either side of the interaction point. It can be used for a very accurate event time measurement and as a minimum bias trigger with a reduced efficiency as compared to V0. Zero-Degree Calorimeters (ZDC) at about 100 m from the interaction point also allow for the determination of the centrality and the event plane in Pb–Pb collisions. They also contributed a trigger to reject electromagnetic background in Pb–Pb operation.

3.2.2 Triggering and read-out

During Run 1 all detectors were operated with triggered read-out, i.e. a global start signal was provided for every event to a set of detectors that should be read out. Such a group of commonly read out detectors is referred to as trigger cluster. For the read-out, each detector sends its data to the Data Acquisition (DAQ) where global event building takes place. For some detectors the read-out results in a dead time while others implement multi-event buffering and are dead time free at typical read-out rates. Thus, the spread of busy times upon read-out ranges from 0 to 1 ms (a few 100 μ s for the TPC²). Therefore, the hardware trigger generation is split into multiple levels at which the read-out can be aborted. The two fast decisions at level-0 and level-1 are taken at a fixed time with respect to the interaction, in Run 1 after about 1.2 μ s and 8 μ s. The timing of the level-2 trigger, about 100 μ s after the interaction, was chosen to allow for past-future protection of the TPC since events with pile-up of central Pb–Pb collisions were considered to be non-reconstructable. In addition to the hardware triggers, a High-Level Trigger (HLT) receives the data in copy from the DAQ. This allows to partially or fully reconstruct events and decide whether they should be recorded or not. It was also foreseen to select regions of interest for storage but this mode of operation has not been used yet.

The contributions to the level-0 trigger must be provided by detectors which are fast and continuously live, e.g. V0, T0, SPD, and TOF. The decisions that are not available within the low latency requirement of the level-0 trigger are used at level-1. It can be based on the information read out upon a level-0 trigger. An example are the TRD triggers, which evaluate the data sampled after a level-0 trigger was received; they will be discussed in detail in Chapter 4.

The global trigger decisions are taken in the Central Trigger Processor (CTP). It receives the inputs from various detectors at the different levels. Trigger classes can be defined to require a set of fired inputs. Each trigger class can trigger the read-out of multiple trigger clusters (if not busy). The trigger decisions are sent to the affected detectors over optical Trigger Timing and Control (TTC) links. Dedicated TTCex and TTCrx modules take care of the transcoding between electrical and optical signals [148]. The protocol allows for the distribution of the LHC-synchronized 40 MHz clock and two time-encoded data channels. The A-channel is used with simple pulses for level-0 and level-1 triggers, the B-channel for the distribution of level-2 triggers and additional messages with information for event identification and read-out cluster encoding.

Depending on the accelerator operation and the physics goals, different trigger scenarios were set up. Every read out event is marked with all trigger classes that lead to the read-out. The class names comprise the information on the trigger input requirements, the bunch crossing mask, the status of past-future protection, and the trigger cluster. As trigger classes can be downscaled, e.g. to limit the bandwidth used for minimum bias data taking, an event can fulfil the input

²For the TPC the dead time had an artificial lower bound to limit the trigger rate and, thus, space charge effects.

requirements for a certain class but not be marked with that class. The relevant classes are explained as needed in the following discussion.

3.3 Transition Radiation Detector in ALICE

The measurement of electrons in heavy-ion collisions gives access to the di-lepton continuum, light and heavy vector meson resonances, as well as hadrons with open charm and beauty in semi-electronic decays. With the much more abundant pions as background, the clean identification of electrons is a crucial ingredient for a high-significance measurement. From the study of signal to background ratios for a J/Ψ measurement with $p_{\perp} \gtrsim 3$ GeV/ c , it was concluded that a rejection of pions by a factor 100 at an electron efficiency of 90 % is required in addition to the identification from the TPC and ITS in central Pb–Pb collisions.

In general, particles are identified by measuring their mass in some way. For example, the specific energy loss depends on $\beta\gamma$ and thus for fixed momentum on the mass. However, the mass dependence becomes small at momenta in the relativistic rise. Similarly, time of flight measurements provide a good separation as long as the velocities are significantly below the speed of light. An appealing feature unique to electrons (at momenta relevant for accelerator experiments) is the production of Transition Radiation (TR) at an interface between materials of different refractive index, predicted by Ginzburg and Frank in 1946 [149]. It becomes relevant only for Lorentz factors $\gamma \geq 1000$. The production probability for transition radiation at a single surface is very low and many boundaries are needed to produce a sizeable effect. Therefore, a typical radiator consists either of a stack of foils in which coherence is of importance, or an unstructured material with many interfaces, e.g. foam, in which the TR production is incoherent.

A Transition Radiation Detector (TRD) was proposed to add good electron/pion separation from 1 GeV/ c up to high momenta to the central barrel and to provide information for a trigger contribution with low latency [150]. For combination with the information from TPC and ITS, the matching to individual tracks is required to work in the high-multiplicity environment of central heavy-ion collisions. Therefore, the matching requires pointing information towards the TPC and, thus, 3-dimensional reconstruction instead of 2-dimensional hits. With the TRD installed outside the TPC, it has to cover a large area (over 600 m²). This favours the use of gas detectors which detect both ionization from a traversing charged particle and the possibly associated TR photon. At the same time, the radiation length from the used material must be as small as possible to avoid imprecise p_{\perp} reconstruction and additional occupancy from bremsstrahlung. These considerations lead to a six-layered design of Xe/CO₂-filled tracking chambers with short drift time and extensive online processing in detector-mounted Front-End Electronics (FEE). To arrive at manageable chamber sizes a segmentation into 18 sectors with 5 stacks each was chosen. The chambers of one sector are mounted in a super-module. An overview of the TRD architecture is shown in Figure 3.4a, the layout of an individual chamber in Figure 3.4b.

The material and thickness of the radiator had to be chosen as a compromise of TR efficiency and mechanical properties. In the final design, a 48 mm thick Rohacell/polypropylene fibre sandwich is used as radiator. Its coated back-side also serves as electrode for the drift region. On average, it results in the production of ~ 1.45 TR photons for a charged particle with $\gamma \geq 1000$. The drift region had to be long enough to allow for correct track matching and PID but short enough to meet the latency requirements for the trigger contribution. With a drift velocity of 1.5 cm/ μ s, 2 μ s suffice for the 3 cm in the final design. The anode wires used for gas amplification are separated from the drift region by cathode wires. Pad read-out is used with pad sizes of about 1 cm times 10 cm. The $r\varphi$ width is chosen to achieve the required p_{\perp}

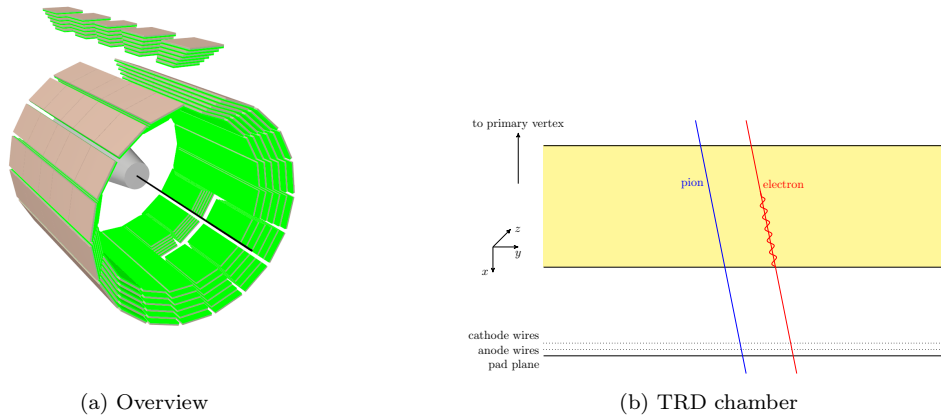


Figure 3.4: Overview of the TRD installation. Left: The TRD consists of 6 layers of tracking chambers and is segmented into 18 sectors in azimuth with 5 stacks in longitudinal direction each. The picture shows the full installation with the holes in front of PHOS for three super-modules. Right: The cross-sectional view of one TRD chamber shows the radiator, the drift region separated by the cathode wires from the amplification region.

parameter	value
gas	Xe (85 %) / CO ₂ (15 %)
drift velocity	1.5 cm/ μ s
gas gain	~ 4000
PASA gain	12 mV/fC
ADC depth	10 bit
sampling frequency	10 MHz
total number of pads	$1.15 \cdot 10^6$
total number of MCMs	$6.9 \cdot 10^5$
material budget	$\sim 25 \% X_0$

Table 3.3: Overview of TRD parameters: The stated numbers refer to the detector operation during physics data taking in Run 1 (2009-2013).

resolution by exploiting charge sharing over adjacent pads. The z direction only has to allow for matching between layers and other detectors. As a compromise, the pads are tilted by $\pm 2^\circ$, which improves the z resolution during global tracking with only marginal deterioration in y direction. The cathode pads are connected to the front-end electronics mounted directly on the detector. An overview of detector parameters is shown in Table 3.3.

3.3.1 Front-end electronics

The Front-End Electronics (FEE) has to serve for the raw data read-out but also for triggering [151, 152]. The latter puts stringent constraints on the latency and requires massively parallel processing already on the detector instead of just shipping raw data. For this purpose Multi-Chip Modules (MCM) composed of two ASICs, a PreAmplifier and ShAper (PASA) and a TRackett Processor, were designed. The FEE is highly configurable to be adaptable to the changing needs of data taking and especially triggering. For the configuration a Slow Control Serial Network (SCSN) is used, which forms a ring of individual chips in a fault-tolerant way [153]. More details on the processing will be discussed in the next Chapter. The read-out is organized in one tree per half-chamber. It is operated in two modes: one latency-optimized and handshake-free for shipping a limited amount of trigger information, another one for bulk raw data read-out. One Optical Read-out Interface (ORI) per half-chamber ships the data at 2.5 Gbit/s [154]. To limit the average power consumption, most parts of the circuit are not clocked when idle (sleep mode). Therefore, an external wake-up signal is needed to initiate the acquisition and processing.

For the control and monitoring of the FEE, a DCS³ board hosting an Altera Excalibur EPXA1 (ARMv4 core + FPGA fabric) is mounted on every chamber [155]. It receives the trigger information on the optical TTC link and passes it on electrically to the FEE. This also includes the distribution of the LHC clock. The DCS board can be accessed through Ethernet and is used to configure the FEE through SCSN. The communication is handled by a DIM-based FEEserver with a TRD-specific control engine [156]. Some parameters are only calculated on the DCS board as will be discussed later. In addition, it provides monitoring of environmental parameters but it is not directly involved in the actual data taking. It also features general purpose I/O lines, a JTAG link to the neighbouring chamber, and an I²C interface.

The data read out from all chambers are processed in the Global Tracking Unit (GTU) [157], see Figure 3.5. It consists of one Track Matching Unit (TMU) per stack which performs the stack-wise tracking for the trigger contribution and the raw data buffering. The tracking, which shall be explained in the next section, relies on a fixed geometrical read-out order on every link. The five TMUs of one super-module are installed in one crate with an additional SuperModule Unit (SMU) combining the information from the stacks to form a trigger decision. In addition, it builds and buffers the events before shipping them to the DAQ. A Trigger Unit (TGU) builds the interface to the CTP.

3.4 Reconstruction, simulation, and analysis

The raw data read out from the detectors need extensive processing to extract physics results from them. For this purpose the ROOT-based AliRoot framework has been developed and is continuously adapted to arising needs [158, 159, 160]. It comprises interfaces to Monte Carlo event generators and detector simulation, detector-specific reconstruction code, and physics analyses.

Figure 3.6 shows the different levels of processing. During data taking raw data are accumulated. They can be translated to so-called digits, i.e. the digitized detector responses. The

³Detector Control System

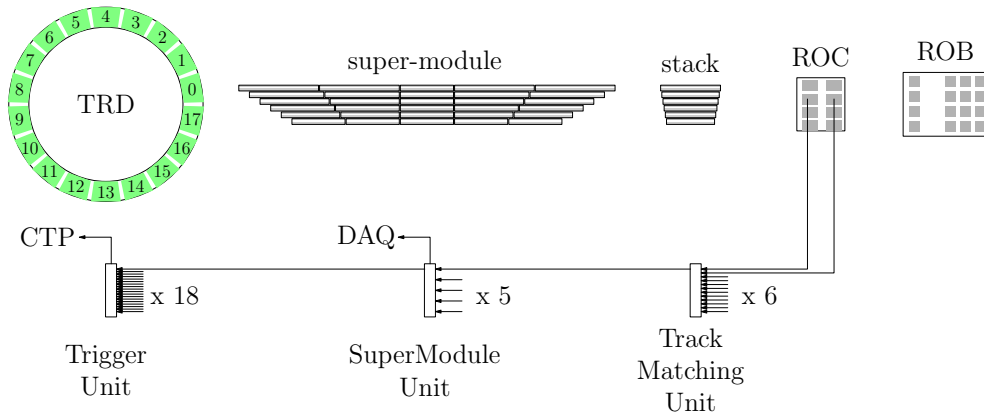


Figure 3.5: Overview of the TRD read-out: The top row shows the detector structure, from the coarse sectors on the left to the individual Read-Out Boards (ROB) on the right. Every Read-Out Chamber (ROC) sends its data over two optical links at 2.5 Gbit/s to the Global Tracking Unit (GTU). A Track Matching Unit (TMU) performs stack-wise tracking and raw data buffering. It has an uplink to a SuperModule Unit (SMU) which hosts the trigger logic and the uplink to DAQ. A global trigger unit (TGU) builds the interface to the Central Trigger Processor (CTP).

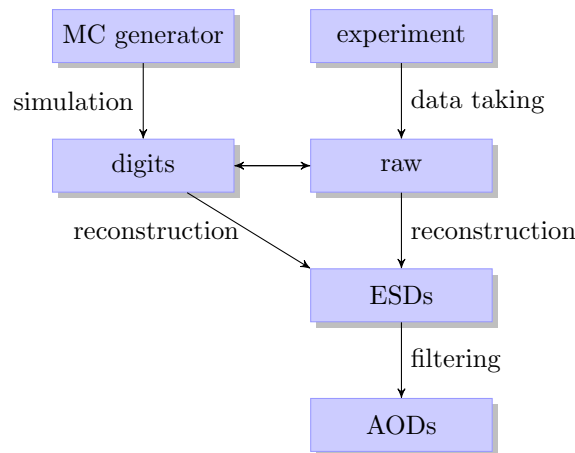


Figure 3.6: Simulation and reconstruction chain: During data taking in the experiment raw data are recorded. In a reconstruction step more abstract entities such as tracks are found and stored in the Event Summary Data (ESD). To further reduce the data volume a filtering procedure to Analysis Object Data (AOD) can be used. A parallel branch exists for the treatment of data from Monte Carlo simulations.

digits can be used for prompt quality assurance or for the full reconstruction. Digits can also be produced from events obtained from a Monte Carlo event generator by means of detector simulation. In this case, they can be translated into raw data to produce as realistic initial input for the reconstruction chain as possible⁴. The reconstruction can either run on digits or directly on raw data. In the latter case the raw data parsing is done on-the-fly which avoids an intermediate I/O step.

For a Monte Carlo simulation, a variety of event generators is available for different physics scenarios. The detector simulation uses a virtual Monte Carlo interface such that Geant3, Geant4, and Fluka can be used with the ALICE geometry. In addition to the energy deposit in the material, the full Monte Carlo information is retained for subsequent analysis. The detector response depends on many parameters which have to be known for simulation but also during the reconstruction. Some of the values are configured or measured during the data taking. Others must be extracted from data in calibration steps. They are stored as ROOT files in the Off-line Condition DataBase (OCDB). It is used both for detector simulation (to reproduce the detector responses of actual operation) and for reconstruction.

A major part of the reconstruction is the tracking in the central barrel [139]. After local cluster finding in the individual detectors, seeding clusters are searched at the outer radius of the TPC. If possible further clusters at smaller radii are attached to the track in a Kalman filtering process. If present, hits in the inner tracking system are attached. Then, the track is Kalman-propagated outwards to TRD, TOF, and HMPID. A last inwards refit is used to obtain ultimate precision. In analyses quality cuts are used to select usable tracks, often so-called global tracks, i.e. TPC tracks with ITS contributions. In other cases TPC stand-alone tracks are used to avoid the loss in acceptance or efficiency. The set of cuts is often optimized for a specific analysis but standard sets have emerged.

Eventually, the output of the reconstruction are Event Summary Data (ESD), which contain e.g. tracks with their parameters and PID information, detector amplitudes used for centrality determination, etc. They can be used as input for analyses. A more condensed format is realized with Analysis Object Data (AOD). They are produced in a filtering process which includes only tracks passing certain cuts. In addition, they can contain more advanced objects, e.g. reconstructed jets, which avoids re-running a jet finder with every analysis. Analyses are implemented as so-called analysis tasks. They can be combined in a train which loops over all events from a given data set. The latter can consist of ESDs or AODs from real data or Monte Carlo productions. The advantage of combining the tasks is to reduce the I/O overhead from reading the event data.

3.5 Jet finding in ALICE

The reconstruction of jets is often based on calorimetric measurements, which provide good energy resolution at high energies. With ALICE being only partially equipped with an electromagnetic calorimeter and having no hadronic calorimeter, the approach to jet reconstruction is different and shall be explained shortly. Within the central barrel, tracks reconstructed from charged particles form the basis for jet reconstruction. In the areas covered by calorimetry the information can be combined but we shall limit ourselves to charged jets, which can be reconstructed over the full azimuthal angle. The available tracks allow for the use of various jet algorithms, of which the k_{\perp} family is now most widely used at the LHC experiments. These algorithms sequentially recombine tracks according to a distance measure to form a jet [51]. The

⁴This was mostly relevant before real data taking had started.

measure:

$$d_{ij} = \min \left(p_{\perp,i}^{2p}, p_{\perp,j}^{2p} \right) \frac{\Delta R_{ij}^2}{R^2} \quad \text{with } \Delta R_{ij}^2 = \Delta \eta_{ij}^2 + \Delta \varphi_{ij}^2 \quad (3.1)$$

yields the k_{\perp} and anti- k_{\perp} algorithm for $p = 1$ and $p = -1$, respectively. The former starts the clusterization around soft, the latter around hard particles. R serves as a resolution parameter determining to what level jets shall be further subdivided. A jet is formed when an object is associated with the beam, for which the distance $d_{iB} = p_{\perp,i}^{2p}$ is used. While the k_{\perp} algorithm was used for a long time, the anti- k_{\perp} version was introduced in view of large underlying event contributions as expected for a high-energy hadron collider as the LHC. Its main advantage are the more regular jet shapes with a narrow distribution in area, typically a cone of radius R . Here, the jet area refers to the area in η - φ in which particles would be assigned to the jet. It can be determined by filling the event with many very soft (ghost) particles, which do not change the structure of the event, and checking which ones are attributed to which jet during the jet reconstruction. The uniformity of the jet area becomes important when contributions from the underlying event are subtracted. Already in pp collisions, the underlying event is visible but it is much more so in Pb–Pb collisions.

As jet finders impose a geometrical structure on the event, they are affected by non-uniform tracking efficiencies and, in particular, by sharp edges. The standard primary track cuts, which require a contribution in the SPD, are disfavoured because of dead areas in this detector. Instead a hybrid approach is used. If available, a track with SPD contribution is used, otherwise a TPC-only track is constrained to the primary vertex to mitigate the loss in p_{\perp} resolution. This procedure results in a much flatter φ distribution. This set will be referred to as hybrid tracks, the selection criteria as hybrid track cuts.

For the actual jet reconstruction the algorithms implemented in the Fastjet package [52] are used. They are fed with the tracks and comprise the determination of the jet area. Mostly, the anti- k_{\perp} algorithm with a resolution parameter $R \in \{0.2, 0.3, 0.4\}$ is used for signal jets. The jet p_{\perp} is calculated according to The p_{\perp} -boost-invariant recombination scheme.

In central Pb–Pb collisions, the contribution from the underlying event amounts, on average, to a summed transverse momentum of about 140 GeV per unit area in η - φ (for constituents above 150 MeV/ c). The effect becomes weaker in non-central events. However, this is not a constant offset in jet energy but fluctuates, both event-by-event and from region to region. In order to assign a meaningful and comparable jet energy, a background subtraction procedure is desirable. This is usually implemented by assigning the transverse momentum of the jet as:

$$p_{\perp}^{\text{jet}} = p_{\perp}^{\text{jet,rec}} - \rho \cdot A^{\text{jet}} \quad (3.2)$$

where A^{jet} is the jet area and ρ an estimate of the background energy density. To take fluctuations into account, the background is estimated from the same event. For this purpose the event is clustered using a k_{\perp} algorithm and the density is then taken as:

$$\rho = \text{median}_{i \in I} \left\{ \frac{p_{\perp,i}^{\text{jet}}}{A_i^{\text{jet}}} \right\} \quad (3.3)$$

where i runs over all found clusters (excluding the leading and sub-leading ones). The median is used instead of the arithmetic mean since it is more resilient to a few outliers, which can arise from true high- p_{\perp} jets in the event.

The quality of this subtraction procedure can be studied by randomly placing cones of a given radius R into a background event and calculating the background-subtracted p_{\perp} :

$$\delta p_{\perp} = p_{\perp}^{\text{RC}} - \pi R^2 \cdot \rho. \quad (3.4)$$

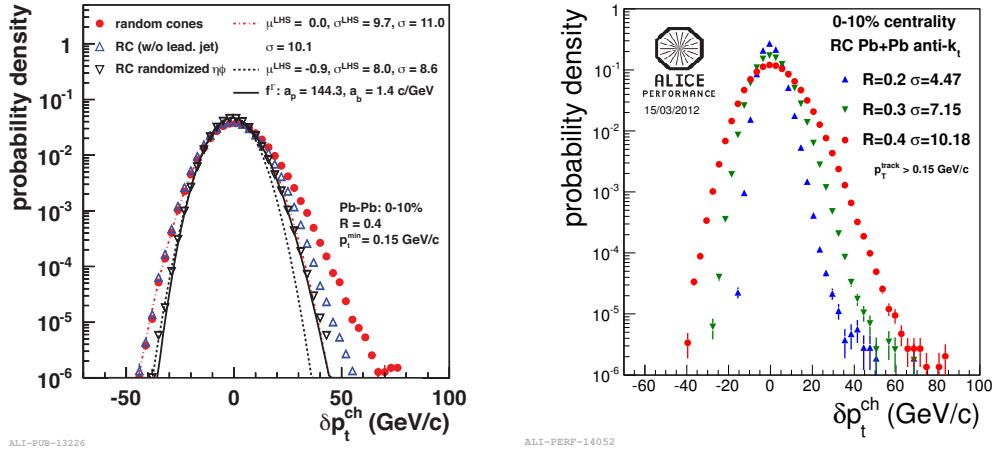


Figure 3.7: Distribution of $\delta p_{\perp}^{\text{ch}}$ for random cones: The quality of the background subtraction is characterized by the distribution of the background-subtracted p_{\perp} in random cones [161]. Left: The distribution is shown for all random cones, those excluding the leading jet, and after full randomization of the event. Right: The background fluctuations are reduced by lowering the cone radius.

Here, the focus is on the characterization of the background subtraction procedure. Therefore, this test can be performed on the track level without full embedding in the detector simulation. The δp_{\perp} distribution in Figure 3.7 shows that the distribution is centred around zero, i.e. on average the correct amount of underlying event contribution is subtracted. However, the width is sizeable and limits the access to the true jet momentum. For a radius of $R = 0.4$, the width of the distribution is about 10 GeV/c. By decreasing the radius and, thus, the area covered in η - φ , the background contribution and its fluctuations become smaller. For $R = 0.2$ the width is about 4.5 GeV/c. This shows that the jet energy derived by the described subtraction procedure is indeed a useful quantity and that smaller jet radii are favourable to reduce the contribution from background fluctuations. With larger jet radii more constituents of the jet are caught and can be used to study the jet substructure.

In what follows, signal jets shall be reconstructed by the anti- k_{\perp} algorithm with radii $R = 0.4$ and $R = 0.2$. For Pb–Pb events the background shall be subtracted with the background density ρ estimated as the median of clusters from a k_{\perp} algorithm with $R = 0.4$.

Chapter 4

Triggering with the TRD

The Transition Radiation Detector (TRD) has two points of contact with the central ALICE trigger. The integration of the TRD with the global system is sketched in Figure 4.1 and will be explained in the following.

The latency of the global level-0 trigger issued by the Central Trigger Processor (CTP) is such that it arrives too late at the TRD Front-End Electronics (FEE) to record the full signal of a traversing particle. Therefore, a dedicated PreTrigger system (PT) is installed inside the L3 magnet which receives direct copies of the signals from the minimum bias trigger detectors, i.e. V0 and T0, and TOF [130]. Because of the reduced cable lengths, a significant reduction in latency is achieved. The system is used to generate a wake-up signal for the TRD electronics which starts the sampling of the data. These data can only be read out if a global level-0 trigger is issued by the CTP for the same event. Thus, the pretrigger condition should mimic the level-0 logic as close as possible. On the other hand, events for which no wake-up signal was generated cannot be read out in a meaningful way either. This should be taken into account by the CTP by triggering the TRD only if a wake-up signal was sent before. Therefore, the wake-up signal is sent in copy to the CTP as a level-0 contribution. This allows to limit the read-out of the TRD to those events having a wake-up signal – the corresponding trigger classes are marked by the suffix WU (Wake-Up). Non-WU classes are used to trigger clusters without the TRD.

The second role of the TRD in the trigger scheme is the selection of events at level-1, for which

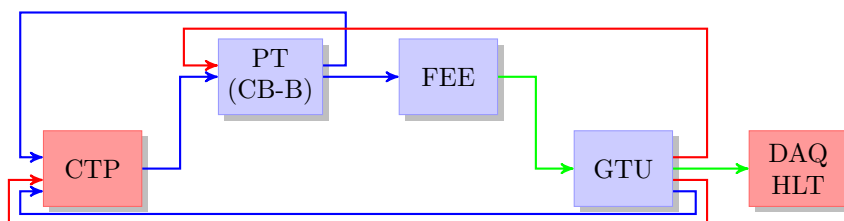


Figure 4.1: Overview of TRD triggering. The TRD enters the trigger scheme with level-0 and level-1 contributions by the PreTrigger system (PT) and the Global Tracking Unit (GTU), respectively. In both cases, the components receive and contribute trigger and busy signals. The lines show the signals transmitted between the components (trigger in blue, busy in red, data in green).

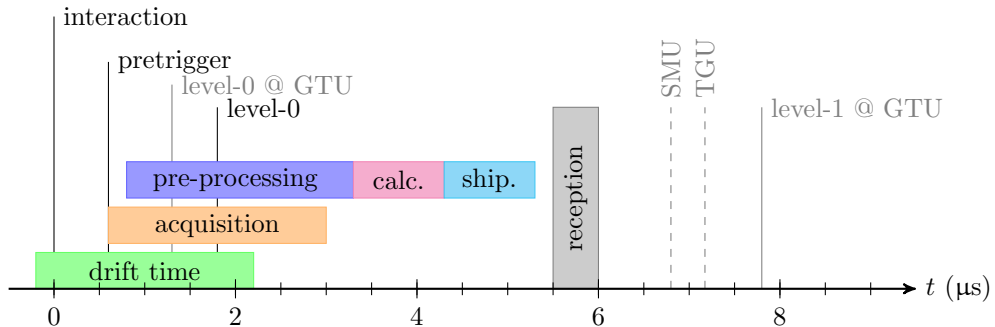


Figure 4.2: Trigger timing relative to the interaction. All FEE timings are determined by the pretrigger and configured with respect to it. The latency of the pretrigger determines the position of the sampling window (green). The acquisition (orange) of the delayed signals starts with the pretrigger. The pre-processing (blue), tracklet calculation (magenta), and tracklet shipping (cyan) start with a small offset. The GTU-related timings are shown in grey.

the TRD was designed to contribute several physics triggers¹. The contributions are derived from TRD-only (online) tracks in the Global Tracking Unit (GTU) and sent to the CTP. The GTU also receives back the global trigger decision because it is the upstream connection to the DAQ, (multi-event) buffering the FEE data and forwarding them. It further contains the busy logic protecting the TRD from being triggered during read-out [162]. In fact, the situation is more involved by the need for a separate busy logic for the CTP and the pretrigger system. While the signal to the CTP may only be deasserted when the GTU buffers can receive new data, the PT system can already fire a pretrigger as soon as the FEE has completed the data transfer of the previous event to the GTU. Not doing this results in an unnecessary loss of efficiency because the CTP busy can still be cleared in the time between the wake-up signal and the level-0 trigger. The FEE supports this operation by expecting a wake-up signal to start the read-out which can be followed by confirmation signals for the global level-0 and level-1 triggers at fixed times after the wake-up signal. When the read-out is not confirmed, the FEE enters into sleep mode again after a short clear sequence and waits for the next wake-up pulse. The timing sequence is shown in Figure 4.2. The signals from the pad plane are continuously sampled, digitized, filtered, and delayed (a more detailed discussion follows in Section 4.2.1). The acquisition of data only starts with a pretrigger. Because of the delaying pipeline stages, the pretrigger can initiate the processing for a time window beginning before its arrival at the FEE. Both the level-0 and level-1 parts of the TRD trigger system will be discussed in more detail in the following sections.

The trigger rates at the individual stages have different limits. The pretrigger system itself could trigger continuously but a maximum rate of about 300 kHz arises from the power consumption of the FEE. The level-1 trigger is limited to about 100 kHz which is close to the dead time limit. For the level-2 trigger, a limit arises from the read-out bandwidth and typically saturation is reached for rates around 5 kHz (depending on the detector occupancy and the resulting data volume).

¹While during normal data taking the pretrigger system provides the wake-up signal, it can also be used for other triggers, e.g. with TOF back-to-back conditions in cosmics data taking.

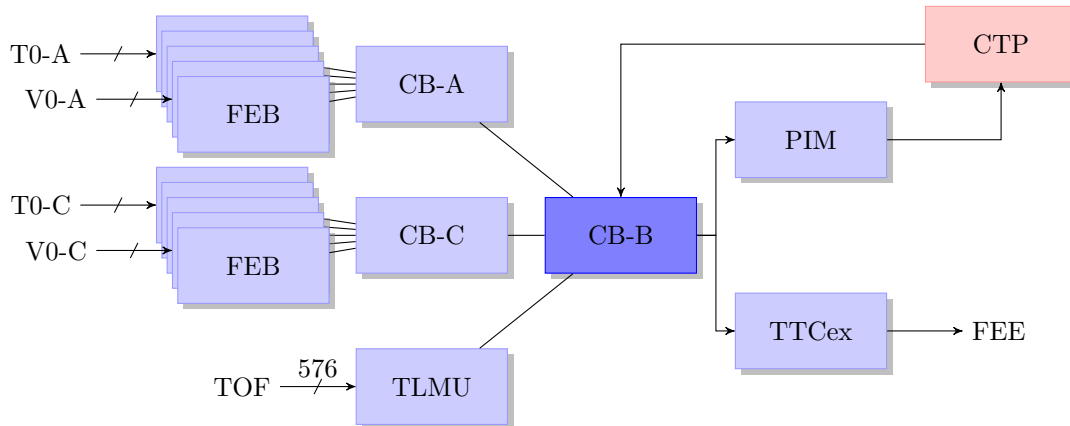


Figure 4.3: Overview of the TRD pretrigger system. The components are shown as blue boxes, the CB-B serves as the main processing unit and interface to all other components.

4.1 Pretrigger system

The TRD pretrigger system was designed and implemented with several components [163], see Figure 4.3. Several Front-End Boxes (FEB) collect and discriminate the signals from the V0 and T0 detectors. They are installed on both sides of the interaction region (A- and C-side). The information is merged and processed in the Control Boxes on the A- and C-side (CB-A/C). The data from the TOF detector are processed in a dedicated unit (TLMU). The central CB-B control box constitutes the interface to FEE, GTU, CTP, and the individual components. The control boxes are equipped with a DCS board for monitoring, control, and TTC reception. Optical transceivers are used for the interconnects between the components. The digital logic is implemented in Xilinx Spartan-3 XC3S500E FPGAs [164] to allow for flexibility. The large number of channels from the TOF detector required the use of a Xilinx Virtex-4 LX40 [165] in the TLMU. The pretrigger system had been installed for the LHC start-up in 2008 and integrated in the control system of the experiment [163, 166].

The CB-B is particularly critical for stable detector operation since the FEE behaviour under improper trigger sequences is not well-defined. And for the first data taking with the TRD (with collisions) in 2009, a fully efficient pretrigger was sought for. With only a few colliding bunches per orbit in the early LHC filling schemes it was affordable and attractive to issue a pretrigger for each of them and, thus, operate at full efficiency. This also allowed for thorough testing of the V0- and T0-based pretrigger before they were needed in filling schemes with many bunches. Issuing a pretrigger for every possible collision requires a bunch crossing counter (BC) synchronized to the LHC counting, such that the bucket to local BC mapping is constant and known. Later on, this feature has been continuously used to accept contributions from the detectors only for bunch crossings with two colliding bunches. To accommodate all required features and achieve stable operation, a previous implementation of the CB-B FPGA design [163] was replaced by a more robust version with additional features.

The CB-B logic is controlled through a dedicated DCS board. The communication to the FPGA is realized with the same interface as for the FEE, i.e. SCSN (see Chapter 3). The DCS board also receives the central TTC signal, which is then decoded in a module re-used from the GTU implementation (in the FPGA) [162]. The inputs from the other components are sampled using (double data rate) input cells with adjustable input delays for synchronization.

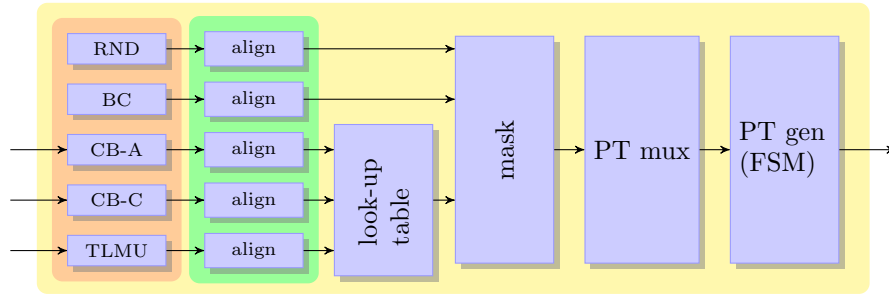


Figure 4.4: Overview of CB-B: The central processing unit receives the trigger contributions from different sources. Besides the sampled input signals, which can be delayed to accommodate for different latencies, random (RND) and BC-derived signals are used. The inputs from T0, V0, and TOF are fed into a look-up table. The final trigger output is generated in a state machine reflecting the FEE.

The adjustment can be made statically since all components use the same phase-stable clock.

An overview of the CB-B design as used since the beginning of physics data taking in 2009 is shown in Figure 4.4. It is mostly implemented in VHDL and was simulated using Xilinx tools and Modelsim. The system operates synchronously with the LHC beam by using the clock derived from the TTC link (40 MHz). The central task is to ensure the provision of valid trigger signals to the FEE. Therefore, the trigger generation is steered by a state machine which reflects the FEE requirements, see Figure 4.5. Starting from the idle state, a pretrigger can be issued based on a request from the input conditions. After sending a pretrigger, a level-0 trigger from the CTP is awaited in a configurable time interval. Depending on its reception, a level-0 pulse is sent to the FEE or a wait state is entered to enforce the dead time required for the FEE clear sequence. After a level-0 trigger was sent, the same procedure is used for the level-1 trigger. After issuing a level-1 trigger a dead time is enforced which can be used to prevent further triggers being issued during the read-out of the FEE. The output to the CTP is formed in an interface module (TIN) according to CTP requirements [167]. It also contains test modes such as toggling or sending of a signature. An intermediate Pretrigger Interface Module (PIM) converts optical to electrical signals, which are then fed to the CTP. Normally, a copy of the pretrigger sent to the FEE is issued to the CTP to indicate the presence of a wake-up signal; for monitoring it is also possible to send the pretrigger requests instead (independent of whether they do not result in a wake-up signal because of busy).

The pretrigger system must ensure not to start a new trigger sequence while the read-out is still on-going. This can be achieved by a fixed dead time after a level-1 trigger covering the maximum read-out time. To avoid this worst-case scenario, the GTU asserts a busy signal to the CB-B as long as the data transfer from the FEE is in progress. It is used in the trigger generation state machine to veto the start of a new sequence.

A pretrigger can be derived from various sources, see also Figure 4.4. A random signal (RND), useful for testing, is provided by the comparison of a random number from an implementation of a Mersenne twister [168] and a configurable threshold. A BC mask (stored in a RAM block) can be used to generate a pretrigger for fixed bunch crossings. The inputs from CB-A/C and the TLMU provide the actual physics triggers. All inputs can be delayed and stretched to 50 ns to allow for the alignment of the different contributions. They also enter a look-up table which allows for the implementation of arbitrary logical combinations. For the final decision whether to issue a pretrigger, a configurable mask allows to limit the contributions depending on the

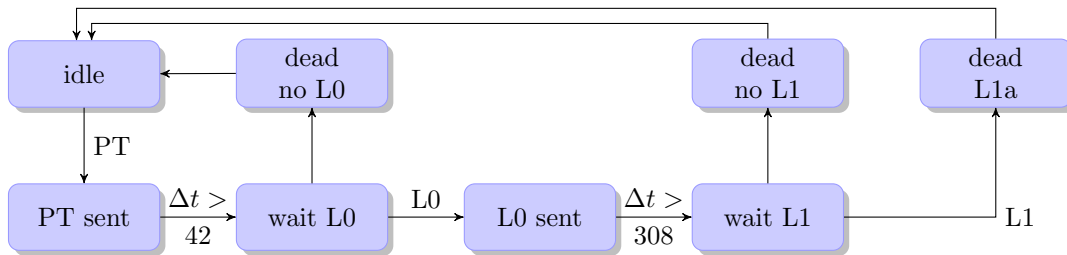


Figure 4.5: Pretrigger state machine: To ensure the production of valid trigger sequences a state machine reflecting the FEE requirements is used. It steps through the sequence of pretrigger, level-0, and level-1 pulses with proper timing if the sequence is confirmed at level-0 and level-1. If the sequence is aborted dead times are ensured to protect the FEE from unexpected triggers.

mode of operation of the experiment. If any non-masked contribution is active a pretrigger is requested. Whether it is actually issued, still depends on the state machine explained above.

A difficulty arises for non-physics data taking, so-called technical runs for testing of the data taking, when artificial (e.g. random) triggers are used. No corresponding pretrigger can be derived for them. As the purpose of this mode of operation are technical tests, the timing of the pretrigger is not crucial. On the other hand, the pretrigger generation should stay as simple as possible. Therefore, an emulation stage was introduced in front of the state machine. Upon reception of a level-0 trigger without corresponding pretrigger, it generates a pretrigger and delays the level-0 and level-1 contributions accordingly. The actual state machine can then be either fed with the raw signals or with the emulated signals. The latter is also referred to as level-0 expansion and is only enabled for technical runs.

In order to generate a pretrigger for a fixed set of bunch crossings, a BC counter was implemented in the CB-B design. It is a simple counter from 0 to 3563 which is reset by the TTC bunch counter reset signal. However, there is a constant offset between the internal BC and the CTP counting. Therefore, the BC of a level-0 reception is compared with the BC contained in a subsequent level-2 trigger message. This allows to observe the offset and adjust the value used for resetting the internal counter. Once adjusted, this value should not change as long as no hardware modifications are made.

Already during early data taking an automatic procedure was implemented to create the BC masks: The LHC filling scheme is taken from the LHC DIP publication [169], the buckets are translated to BCs at the ALICE collision point (beam 1: $1 \rightarrow 346$, beam 2: $1 \rightarrow 3019$), colliding bunches are then selected by the intersection of beam 1 and beam 2 bunches. Then, the pretrigger is issued 42 bunch crossings before the collision BCs to wake up the electronics in time.

For monitoring, counters for a set of internal signals are implemented in the FPGA. They are realized with fast counters in registers, and slow counters in RAM to fit a large number of wide counters in the device. They can be captured synchronously (without stopping them) in order to read out consistent values.

In addition, a simple integrated logic analyser can be used e.g. for the alignment of the input signals by adjusting compensatory delays. After arming, it writes the values of a set of signals to a ring buffer (block RAM) until a configurable trigger condition is fulfilled. Then it continues for a configurable number of clock cycles such that the firing of the trigger can be placed anywhere in the recorded time interval. An example of the alignment of the T0 inputs is shown in Figure 4.6.

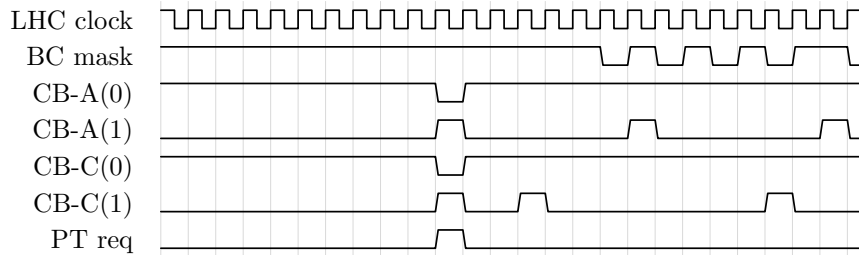


Figure 4.6: Pretrigger alignment: The inputs need to be aligned to compensate for different detector and cable latencies. An example from the alignment of the T0 inputs is shown, recorded with the logic analyser implemented in the CB-B design. The information of the A- and C-side instances of V0 and T0 is encoded in the two bits from both CB-A and CB-C as active high and low, respectively.

The signals CB-A(1) and CB-C(1) indicate if the V0 trigger condition was fulfilled on the A- and C-side in active-high logic. The signals CB-A(0) and CB-C(0) show the T0 trigger condition in active-low logic. For the V0 contributions, after-pulses can be seen (photomultiplier tubes). Triggering on an isolated bunch² with a coincidence of V0-A and V0-C and checking the relative position of the T0 signals allowed to adjust the delays to achieve coincidence between T0 and V0. T0 provides much cleaner trigger signals but with lower efficiency than V0 because of its smaller acceptance.

At a later stage, the design was extended by an additional output to the CTP to allow for monitoring or the contribution of a trigger. The design was made device independent to allow the synthesis for an upgraded version of the CB-B board using an Actel ProASIC3E [170] and allowing for read-out through a Detector Data Link (DDL).

For the production data taking the pretrigger condition was chosen as close as possible to the ALICE interaction trigger setup, i.e. either a coincidence of the two sides (A and C) of V0 or T0. The actual performance of the TRD pretrigger is affected by several contributions. On the one hand, the efficiency of the individual detectors depends on the discrimination thresholds. On the other hand, there is an impact from the dead time requirements. This is particularly important when the collisions occur in trains, i.e. subsequent collisions are very close in time. The implementation of this system leads to an inherent dead time for the time between pretrigger and abort or end of the read-out. In low luminosity running conditions, the pretrigger efficiency is above 99 %. For higher interaction rates, it is determined by the colliding bunch structure in the filling scheme. The design developed within this thesis was used throughout the production data taking of Run 1.

4.2 On-line tracking

The level-1 contributions from the TRD are based on individual tracks with information on transverse momentum p_{\perp} and Particle IDentification (PID). The tracks are reconstructed in two online stages. An overview of an event as seen at the level of the trigger is shown in Figure 4.7. First, chamber-wise track segments (tracklets) are (straight-line) fitted in the FEE and sent to the GTU. Then, tracklets within a TRD stack are matched to form tracks, which contain references to the contributing tracklets. The p_{\perp} of the track is extracted from the intercept a

²In the LHC filling schemes, there often are a few collision bunch crossings with no others surrounding them.

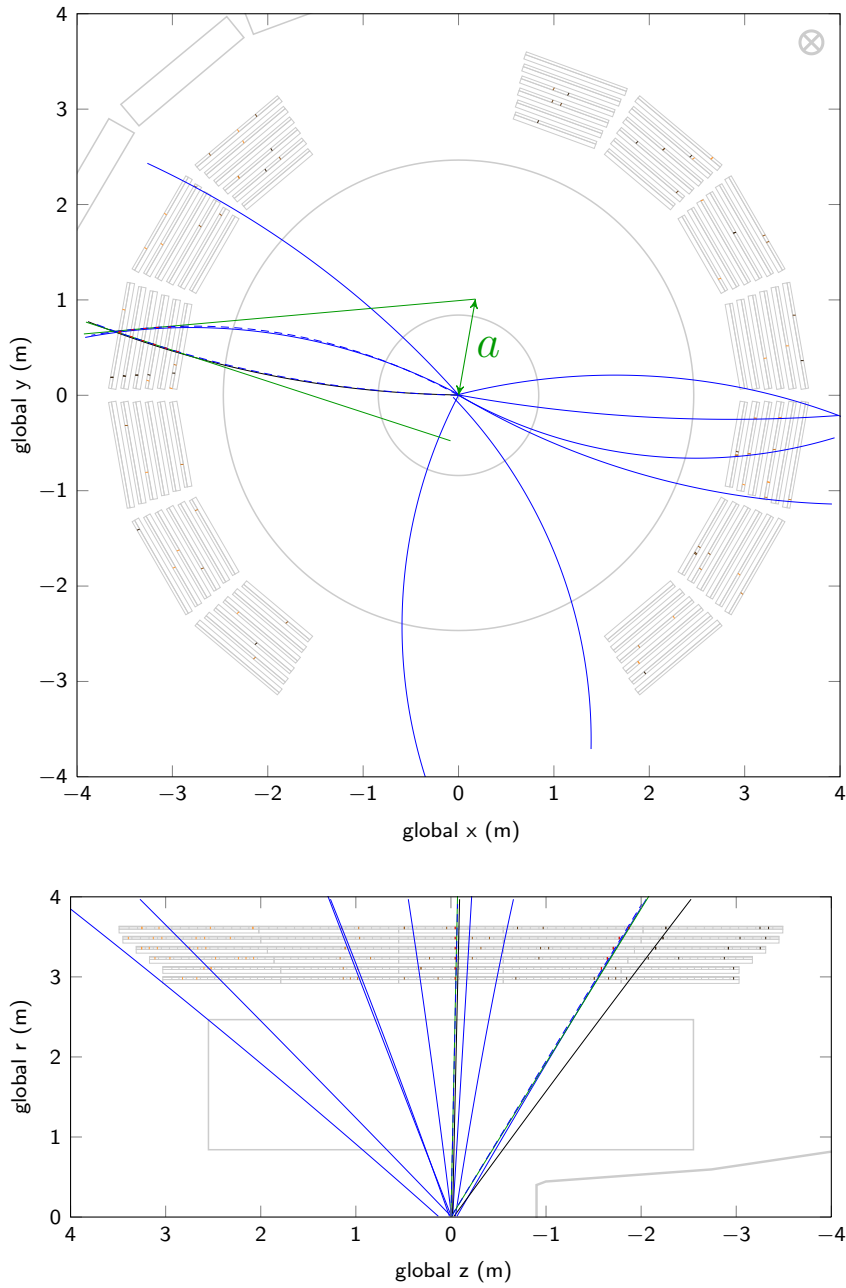


Figure 4.7: TRD online reconstructed event together with global off-line tracks. Top: The chamber-wise tracklets (red) are matched to tracks for which a straight line fit (green) is calculated. The transverse momentum is extracted from the transverse offset a to the nominal vertex position. Bottom: In the longitudinal plane, groups of tracklets consistent with a primary track are considered for matching.

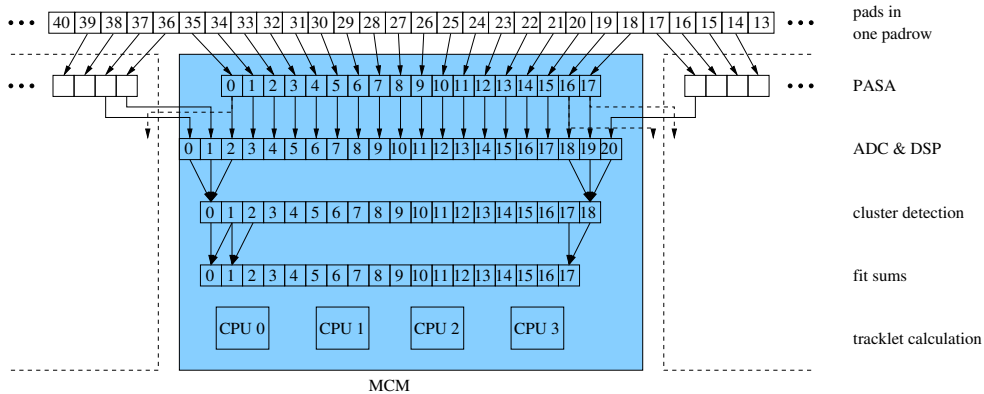


Figure 4.8: Data processing in one MCM [171]: The pad-plane signals are fed into a charge-sensitive amplifier, digitized, and processed to find local track segments (tracklets). The border channels are shared with neighbouring MCMs to avoid inefficiencies at the boundaries.

of a straight line fit through the tracklet positions in the transverse plane, see the event display. The track PID is calculated as the average of the values from the contributing tracklets. The tracks with p_{\perp} and PID information are used for jet and electron triggers.

4.2.1 Local tracking

The local, i.e. chamber-wise tracking, is based on primary ionization in the active volume, electron drift towards the amplification region, and gas amplification, see Section 3.3. The signals from 18 pads are connected to the charge-sensitive PreAmplifier and ShAper (PASA) inputs on one Multi-Chip Module (MCM). The differential outputs are fed into the ADCs in the TRAcklet Processor (TRAP) on the same MCM. The TRAP comprises cycling 10-bit ADCs for 21 channels, a digital filter chain, a hardware preprocessor, four two-stage pipelined CPUs with individual single-port, Hamming-protected instruction memories (IMEM, 4k x 24 bit), about 400 configuration registers usable by the hardware components, a quad-port Hamming-protected data memory (DMEM, 1k x 32 bit), and an arbitrated Hamming-protected data bank (DBANK, 256 x 32 bit) [151]. Three excess ADC channels are fed with the amplified analogue signal from the two adjacent MCMs to avoid tracking inefficiencies at the MCM boundaries. The signals of all 21 channels are sampled in timebins of 100 ns. An overview of the connections is shown in Figure 4.8.

The digitized data are processed in a chain of configurable digital filters as shown in Figure 4.9 [172]. During the filtering two additional binary digits are appended to reduce rounding errors from the intermediate calculations. The non-linearity filter, foreseen to correct for non-linearities in detector response or electronics, was not used for data taking in Run 1. Neither is the cross-talk filter needed³. The pedestal filter is of crucial importance for the online processing to remove offsets which differ channel by channel. It extracts the low frequency components from the signal by a relaxation process; the slow component is then subtracted and replaced by the configured nominal pedestal:

$$P'_n(t+1) = P'_n(t) + (I_n(t) - \beta \cdot P'_n(t)), \quad O_n(t) = I_n(t) - P'_n(t) + P_{\text{nom}}. \quad (4.1)$$

³It is used in a no-operation configuration to delay the signal in addition to the dedicated pipeline stages.

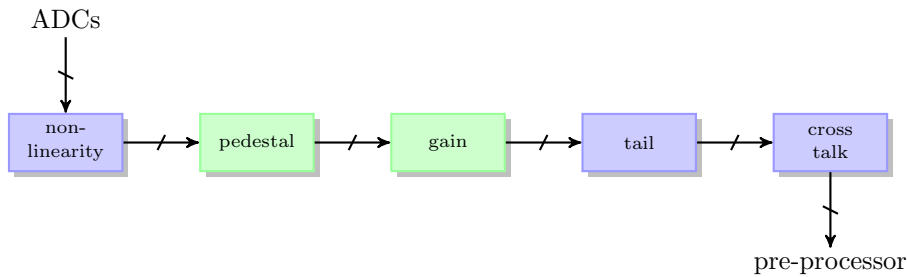


Figure 4.9: Digital filter chain: The digitized signals are propagated through a chain of digital filters. For the intermediate stages, the 10-bit data are extended by 2 additional binary digits. Only the pedestal and gain filters were used in the production data taking during LHC run 1.

P_{nom} should be small to limit its impact in the following filter stages, but positive to allow for the propagation of undershoots below the baseline. The gain filter is used to correct for non-uniform gain channel-by-channel:

$$O_n(t) = \gamma_n \cdot I_n(t) + \alpha_n. \quad (4.2)$$

The multiplicative and additive constants γ_n and α_n are obtained from special calibration runs with metastable $^{83\text{m}}\text{Kr}$, which is fed into the gas system of the detector where it decays [173, 174]. The dominant modulations arise from chamber non-uniformities resulting in slight changes of the distance between anode wires and pad plane. The impact on the online tracking is limited since it relies on local properties only. However, the corrections are important for the online PID.

The double exponential tail cancellation filter can be used to suppress the ion tails in later timebins in order to improve the angular resolution. Due to constraints by the online PID calculation, it was used for test runs only but not in production data taking. Its use is under study for Run 2.

For the choice of filter settings, an important constraint arises from the storage of either completely unfiltered or completely filtered data in the event buffer for read-out. Here, also the zero-suppression based on ADC values is applied which requires a well-defined common baseline⁴. This implies that all filtering applied online affects the data available for the off-line reconstruction.

After the filtering stage, a hardware preprocessor searches timebin-wise for clusters as the data arrive as the channel-wise charge values Q_i arrive. Figure 4.10 shows the data processed in one MCM. The primary condition for the detection of a cluster in a given channel is a local maximum with respect to the adjacent channels, i.e. $Q_{i-1} \leq Q_i < Q_{i+1}$. In addition, a configurable charge threshold Q^{thr} must be reached, i.e. $Q_{i-1} + Q_i + Q_{i+1} \geq Q^{\text{thr}}$. A trade-off between the quality of the clusters (high threshold) and their number (low threshold) has to be made. For up to four clusters (per timebin), the approximate position y^{cog} is calculated from the pedestal-subtracted charges on three adjacent pads as the centre-of-gravity and corrected with values from a look-up table $C(y_{\text{cog}})$:

$$y_i^{\text{cog}} = \frac{(Q_{i+1} - Q^{\text{ped}}) - (Q_{i-1} - Q^{\text{ped}})}{Q_i - Q^{\text{ped}}}, \quad y_i = \frac{1}{2}y_i^{\text{cog}} + C(y_i^{\text{cog}}). \quad (4.3)$$

⁴Otherwise, the baseline subtraction could be done during off-line processing.

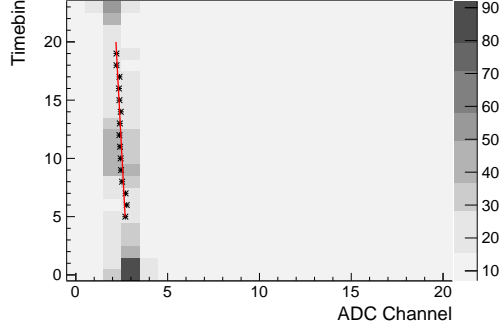


Figure 4.10: Local tracking in one MCM [175]: Every MCM processes the ADC data from 21 channels, finds clusters (asterisks), and calculates a straight line fit parameterized by position y and deflection d_y in transverse direction. Together with the longitudinal chip position and a PID value calculated from the deposited charge, the information is shipped as one 32-bit tracklet word.

The correction is required to compensate for a distortion from the simplified position calculation [176]. The look-up table was filled with values calculated from the pad response function $p(y)$ as:

$$C(y^{\text{cog}}) = y(y^{\text{cog}}) - y^{\text{cog}}, \quad y^{\text{cog}} = \frac{p(y+1) - p(y-1)}{2 \cdot p(y)}. \quad (4.4)$$

The inversion of the latter equation was done numerically. For this purpose, the same pad response function as for the off-line processing was used.

The fit sums needed for a linear regression are accumulated timebin-wise for every channel i , $\mathbf{1}_i(t)$ being the indicator variable for the detection of a cluster in channel i and timebin t :

$$N_i = \sum_{t=t_{\text{fs}}}^{t_{\text{fe}}} \mathbf{1}_i(t), \quad (4.5)$$

$$X_i = \sum_{t=t_{\text{fs}}}^{t_{\text{fe}}} \mathbf{1}_i(t) \cdot t, \quad X_i^2 = \sum_{t=t_{\text{fs}}}^{t_{\text{fe}}} \mathbf{1}_i(t) \cdot t^2, \quad (4.6)$$

$$Y_i = \sum_{t=t_{\text{fs}}}^{t_{\text{fe}}} \mathbf{1}_i(t) \cdot y_i(t), \quad XY_i = \sum_{t=t_{\text{fs}}}^{t_{\text{fe}}} \mathbf{1}_i(t) \cdot t \cdot y_i(t), \quad (4.7)$$

$$Q_{0,i} = \sum_{t=t_{\text{qs0}}}^{t_{\text{qe0}}} \mathbf{1}_i(t) \cdot Q_i, \quad Q_{1,i} = \sum_{t=t_{\text{qs1}}}^{t_{\text{qe1}}} \mathbf{1}_i(t) \cdot Q_i, \quad (4.8)$$

where t_{fs} and t_{fe} mark the range of timebins used for the linear fit. The two charge sums Q_0 and Q_1 can be used for the PID calculation and can cover different timebin ranges than the ones for tracking. An overview of the configuration settings relevant to the local online tracking is given in Table 4.1.

Based on the fit sums, the preprocessor selects up to four channels with tracklet candidates. For this purpose, two conditions on the number of clusters are checked, considering clusters centred over two adjacent pads i and $i+1$:

$$N_i \geq N_{\text{CL}}^{\text{thr}}, \quad N_i + N_{i+1} \geq N_{\text{CT}}^{\text{thr}}. \quad (4.9)$$

parameter	register	description	value
P_{nom}	FPNP	nominal pedestal	32
β	FPTC	time constant for pedestal filter	0 (0.82 ms)
γ_n	FGFn	gain factor	channel-wise
α_n	FGAn	gain addition	channel-wise
t_{fs}	TPFS	fit start	1
t_{fe}	TPFE	fit end	24
Q^{thr}	TPHT	hit threshold (charge, incl. pedestal)	200
Q^{ped}	TPFP	effective pedestal (charge)	40
$N_{\text{CL}}^{\text{thr}}$	TPCL	min. number of clusters (left)	2
$N_{\text{CT}}^{\text{thr}}$	TPCT	min. number of clusters (total)	10
t_{qs0}	TPQS0	charge sum start	0
t_{qe0}	TPQE0	charge sum end	23
t_{qs1}	TPQS1	charge sum start	23
t_{qe1}	TPQE1	charge sum end	22
n_{drift}		no. of timebins corresponding to l_{drift}	19.4
$\omega\tau$		tangent of Lorentz angle, sign according to B -field	± 0.16133

Table 4.1: Relevant parameters for local online tracking: A set of parameters controls the digital filtering, hit detection, fitting, and charge accumulation. The given values were used for the production data taking in LHC Run 1.

If more than four channels fulfil the criteria, those with the highest number of hits are chosen. The restriction to form a tracklet from clusters of two adjacent pads poses a limit on the maximal deflection of a tracklet if the full track segment is required to be captured. It leads to a position-dependent lower bound in transverse momentum. This is illustrated in Figure 4.11 which shows the local deflection of tracklets over the 3 cm drift region for different track p_{\perp} . Because of the Lorentz drift in the magnetic field the local deflection is asymmetric around $y = 0$. With a pad width between ~ 6 mm in layer 0 and ~ 8 mm in layer 5, the requirement results in a position-dependent lower cut on the transverse momentum, which is below the p_{\perp} range of interest for the TRD trigger.

The final calculations are performed in the CPUs of the TRAP, each of which handles one tracklet candidate. While the CPUs could access the information from the event buffers, the processing time would be much longer than using the parallel hardware preprocessor⁵. For a tracklet candidate, i.e. a pair of adjacent channels with a sufficient number of clusters, the fit sums are merged. For the $i + 1$ -th channel, the shift by one pad width is accounted for. All positions are in fix-point arithmetic (in units of $\frac{1}{256}$ pad width). From the combined values, a straight line fit can be calculated as:

$$y = \frac{X^2 \cdot Y - X \cdot (XY)}{N \cdot X^2 - X \cdot X}, \quad b = \frac{N \cdot (XY) - X \cdot Y}{N \cdot X^2 - X \cdot X} \quad (4.10)$$

with the transverse offset y relative to the pad centre of the i -th channel and the slope b . The transverse position, in units of a pad width, has to be understood at the virtual radial position corresponding to timebin 0, i.e. at a slightly larger radius than the anode wire plane. It is scaled by the pad width and a channel-dependent offset is added to arrive at a global coordinate. The

⁵Yet this might become relevant for non-triggering operation in the LHC Run 3 to circumvent limitations, e.g. in transverse momentum.

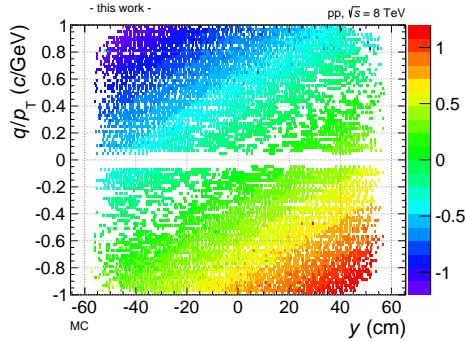


Figure 4.11: Geometrical tracklet deflection: The local deflection of a tracklet over the 3 cm drift length is shown (in cm) as a function of the transverse position y in the chamber and q/p_{\perp} . The Lorentz drift results in an additional offset to these values (about 0.5 cm for $|B| = 0.5$ T).

slope (in units of pads per timebin) is multiplied by the pad width w_{pad} and the number of timebins n_{drift} corresponding to the drift length l_{drift} :

$$d_y = b \cdot w_{\text{pad}} \cdot n_{\text{drift}} \qquad n_{\text{drift}} = \frac{l_{\text{drift}}}{v_{\text{drift}}} \quad (4.11)$$

to arrive at the deflection d_y over the drift length l_{drift} . The longitudinal position is derived from the pad row of the MCM. Based on Q_0 and Q_1 , a PID value is looked up from a configurable table. It is usually filled to translate the accumulated charge to an electron likelihood. The tracklet parameters in the bending plane are illustrated in Figure 4.12.

The tracklet parameterization by the straight-line fit is subject to corrections and possibly additional cuts. The longitudinal magnetic field results in a Lorentz drift of the electrons from primary ionization. Using the Lorentz angle Ψ_L the effect can be corrected by subtracting a fixed length from the deflection. In addition, the tilted pads result in a systematic shift of the apparent deflection when the track enters and leaves the chamber at different z positions, which is the case for primary particles at $\eta \neq 0$. Also this effect can be corrected solely based on the assumption that the tracks relevant for the online tracking point to the primary vertex in the xz plane. As the length of a track segment in the active volume depends on the incident angle of the track, also the accumulated charge is affected. Therefore, geometric correction factors are used for normalization to the tracklet length before entering the look-up table. At last, the number of shipped tracklets can be reduced by the restriction to those which are consistent with a p_{\perp} in excess of a given threshold. This condition translates to a position-dependent cut on the deflection d_y . For the tracklets passing the cuts, the corrected parameters are assembled in a 32-bit word and transferred to the GTU. The word contains (from LSB to MSB) the y -position (13 bits signed, 160 μm bins), the deflection (7 bits signed, 140 μm bins), the z row (4 bits unsigned), and the PID value (8 bits unsigned):

$$pppp : pppp : zzzz : dddd : dddy : yyyy : yyyy : yyyy. \quad (4.12)$$

The GTU uses the positional information in the tracklets for the track matching. For this, it relies on a fixed read-out order increasing with pad row and y . The read-out tree of the detector was configured accordingly, see also Appendix C.1.

The corrections and cuts explained above must be configured locally and, thus, vary for individual MCMs. In order to send common configurations to all chambers and avoid excessive

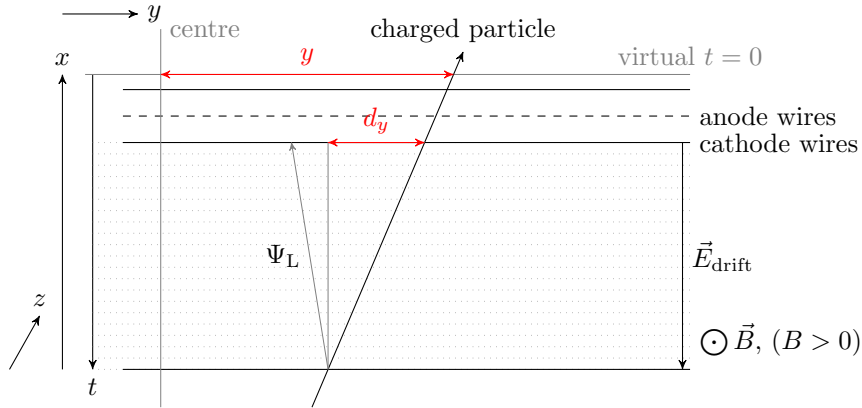


Figure 4.12: Tracklet reconstruction and correction: The primary ionization electrons from a traversing charged particle are deflected by the Lorentz angle Ψ_L . This results in an offset of the apparent deflection which is corrected. The y position with respect to the chamber centre holds for the virtual $t = 0$ radial position.

network traffic, the position dependence is handled by the DCS boards on each chamber. The common parameters, e.g. the p_{\perp} threshold, are sent only once and identical to all chambers. The actual calculations were encapsulated in the class `AliTRD1tuParam`, which receives a few configuration settings and outputs the resulting settings for each pad position. It contains an implementation of the detector geometry and was written for usage in identical form on the DCS board and in AliROOT such that the values can also be used in the off-line code. Thus, it is contained in both libTRD and AliRoot. The following calculations are performed within this class:

Tilt correction The correction for the pad tilting angle α_{tilt} is calculated based on the position of each MCM as:

$$\Delta y = l_{\text{drift}} \cdot \frac{z}{x_0} \cdot \tan \alpha_{\text{tilt}}, \quad (4.13)$$

where x_0 is the distance from the primary vertex in the direction normal to the chamber.

Lorentz correction The correction of the Lorentz drift is calculated based on a configured value for $\tan \Psi_L = \omega\tau$ as:

$$\Delta y = -l_{\text{drift}} \cdot \omega\tau \cdot \text{sgn}(B). \quad (4.14)$$

Deflection range The range in deflection corresponding to a transverse momentum above a configured threshold p_{\perp}^{min} depends on the position of the channel and is calculated as:

$$d_{\pm} = l_{\text{drift}} \cdot \tan \left(\varphi \pm \text{asin} \left(\frac{R}{2} \cdot \frac{0.3 \cdot B/T}{p_{\perp}^{\text{min}} / (\text{GeV}/c)} \right) \right), \quad \varphi = \text{atan} \frac{y}{x}. \quad (4.15)$$

Drift velocity The drift velocity is transformed into the required fix-point representation.

PID correction factors The correction factors for charge normalization do not affect the pure tracking and are discussed elsewhere [177].

4.2.2 Local tracking simulation

The local tracking in the TRAP can be simulated on different levels. Except for very specific checks, a full simulation from the HDL implementation of the TRAP (e.g. using ModelSim) is too computing intensive and unnecessary. A faster C++ model, implemented for AliRoot in the class `AliTRDmcmSim`, allows for a complete simulation of the processing of the digitized ADC data in the TRAP. It replaced a previous implementation [178]. For performance reasons, the TRAP CPU programs were translated to C++ instead of emulating the CPUs to execute native TRAP instructions. It was considered crucial to obtain results as identical to the hardware as possible, which in particular requires the use of identical configurations. Therefore, the TRAP configuration for the simulation was encapsulated in a streamable ROOT object `AliTRDtrapConfig`. It holds the values of all configuration registers and potentially the DMEM and DBANK content. With almost 70,000 MCMs on the full detector, it is not desirable to store all values individually since most of them are identical for certain groups of chips. Thus, the granularity of storage is configured such that global parameters are stored only once, and the more specific ones once per chamber, half-chamber, layer, etc. Even then, the configuration objects have a considerable size and instead of storing the used object in the OCDB for every run, a list of commonly used configurations is stored once. For every run only a reference in the form of the configuration name (identifier) and version is stored. A list of configurations relevant for the data taking with flagging and triggering during Run 1 is given in Appendix C.2. To ensure that these configuration objects really correspond to the settings in the detector, they are filled from the very same data sent to the DCS board, on which still some processing is done as explained above. The required calculations are performed by the implementation in `AliTRDltuParam` discussed above. For validation of the configurations stored in the OCDB, verification files can be produced. These contain SCSN commands that can be executed on the real detector to read back and compare the settings. Hereby, a direct comparison of the actual configuration on-chip and the expectation is achieved.

The ultimate test for the simulation of the local tracking is to compare the result with the online tracklets found by the real hardware in standard data taking (in the following referred to as raw tracklets). This is possible because the tracklet calculation is based on the ADC data, which are also read out. However, a dedicated reconstruction is required since normally the ADC data are used for clusterization but not stored for further processing. The MCM simulation can then be run on these ADC data. The simulated tracklets are added to the ESDs (with a different label to allow for the distinction of raw and simulated tracklets). By default, the identical TRAP configuration as used for a given run is retrieved from the OCDB.

For a comparison of raw and simulated tracklets they are first matched based on their geometrical information (the raw tracklets do not contain the information from which MCM they originate). The matching is implemented as a loop over all raw tracklets in which for each of them the closest simulated tracklet is searched. Only tracklets in the same detector and within a window of 100 and 20 bins in y and d_y , respectively, are considered. Raw and simulated tracklets remaining unmatched after this procedure show a discrepancy of the simulation and the real tracklet finding. A small deviation is expected because of the additional binary digits for the filtered signals, which are not available for the re-simulation. Deviations in the reconstructed properties, i.e. y , d_y , and PID, are extracted. Figure 4.13 shows results of such a comparison. In most cases, the parameters of the two tracklets agree within ± 1 bin. Larger deviations occur when there is a difference in the contributing clusters. Close to the threshold for the cluster charge, the different rounding can lead to this effect. Since the description of the additional digits in simulation is correct on average, the performance studies are not affected by these deviations.

Despite the required computing time a full hardware simulation of the TRAP HDL imple-

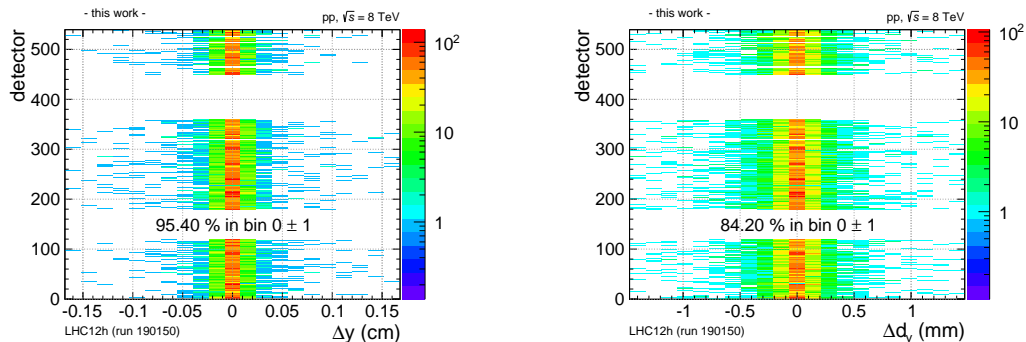


Figure 4.13: Comparison of raw and simulated tracklets. The vertical axis shows the detector number, i.e. $30 \cdot \text{sector} + 6 \cdot \text{stack} + \text{layer}$. The gaps arise from sectors which were not equipped with super-modules in Run 1. Left: Deviations in the transverse position y . Right: Deviations in the deflection d_y .

mentation is useful for more thorough checks on individual input vectors. Such a simulation gives access to every signal within the TRAP and, thus, allows to fully follow the internal processing. Again, the problem of identical configurations arises. Therefore, a test bench design was set up which reflects the SCSN layout of a chamber, see Appendix C.1. This allows to use the exact sequence of SCSN commands which is sent from the DCS board to the TRAPs. Such a sequence can be dumped on the DCS board when receiving a configuration. For a full simulation of the local tracking in the TRAP, the configuration is read in before input ADC data is read from a file and processed. The configuration for one SCSN link pair takes about 200 ms, which results in several hours of total computing time. The actual tracking, which in reality takes only a few microseconds, is simulated much faster then. Such HDL simulations were used to debug the TRAP implementation and identify possible work-arounds in the CPU code. Another use is to check the behaviour for certain (unforeseen) configuration settings. For any analysis beyond that, the C++ model must be used for performance reasons.

4.2.3 Global tracking

The global tracking operates on the tracklets within a TRD stack. An optimized algorithm is used to cope with the high multiplicities of Pb–Pb collisions [179, 180]. Starting from the prototype implementation, an extended version was brought to operation and commissioned in the GTU during Run 1 [181]. Groups of tracklets whose longitudinal positions are consistent with a track from the primary vertex are considered in parallel instances of a track matching logic. Using their transverse position and deflection, the tracklets are projected onto a virtual yz plane in the middle of the TRD stacks ($R = 3.32$ m). If tracklets from at least 4 layers fall into windows of configurable size in the projected position y and the angle α relative to a track with infinite p_{\perp} , a track is formed. By exploiting the fixed read-out order of the tracklets, the actual algorithm achieves linear scaling of the tracking time with tracklet multiplicity [180]. Per track, only one tracklet per layer can contribute, and every tracklet can be part of at most one track. Thus, a track can consist of four to six tracklets.

For all found tracks, a straight line fit through the contributing tracklets is performed. Then, the p_{\perp} of the track can be estimated from the offset of the fit to the nominal vertex position in the transverse plane, see Figure 4.7. The value of the track PID is calculated as the arithmetic

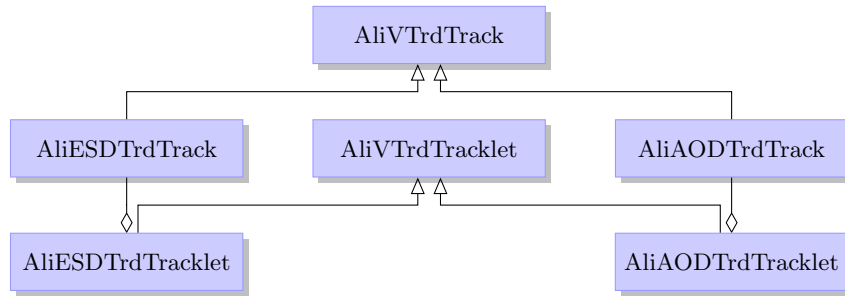


Figure 4.14: TRD online tracking class hierarchy: The abstract base classes `AliVTrdTrack` and `AliVTrdTracklet` provide the interface to the TRD online tracking information for the use in analyses. The realizations in ESDs and AODs vary in the level of detail.

average over the tracklet values [177].

Also for the global tracking, a full simulation based on raw or simulated tracklets is available [171]. Again, care was taken to achieve results identical to the hardware implementation. The simulation was extensively used for mutual validation of the implementations in simulation and hardware. Furthermore, it was used for detailed studies of the global tracking performance [181]. The GTU simulation can also be run on-the-fly as an analysis task on ESD data since all tracklets are contained therein. This allows for the easy use of the 2011 Pb–Pb data for which the hardware tracks are not directly usable, or for the study of changed window settings or improved algorithms.

4.2.4 Integration into the computing framework

The ADC data, tracklets, and tracks are not only used during triggering but are also stored in the recorded raw data. Thus, they can be made available for analyses in order to evaluate the trigger performance or study possible signatures for new triggers. The reconstruction uses a raw stream to parse the data. Within this thesis, it evolved from an online data integrity checker [171] and was extended to serve the general purpose in reconstruction, i.e. decoding ADC data and trigger-related information. The online tracklets and tracks are filled in ESD structures together with the global reconstruction output. The ADC data are normally discarded after clusterization in the reconstruction. However, they can also be written to a dedicated file, which then allows the re-simulation of the local tracking on real data (possibly with different settings).

For analyses based on ESDs and AODs (see Section 3.4) the information from the TRD online processing is made available with different structures and level of detail. At first, the tracklets are written to the ESDs as `AliESDTrdTracklet`, the tracks as `AliESDTrdTrack` and extended with the references to the contributing tracklets. This assignment requires that the tracklets are sorted after reading in the same way as in the GTU input units. In addition, the status of trigger conditions is stored per sector (`AliESDTrdTrigger`). In an AOD production the tracks are copied as `AliAODTrdTrack` together with the contributing tracklets. Tracklets not contributing to any track are discarded in this step. To allow for analyses handling both ESD and AOD input, the abstract base classes `AliVTrdTrack` and `AliVTrdTracklet` were introduced. An overview is shown in Figure 4.14, more details are provided in Table C.4.

The exact simulation of all online tracking and trigger stages available in AliRoot [160] is particularly useful since it can also be run on real recorded data. Using identical configurations, this allows for mutual validation, using different configurations for testing of new settings on real

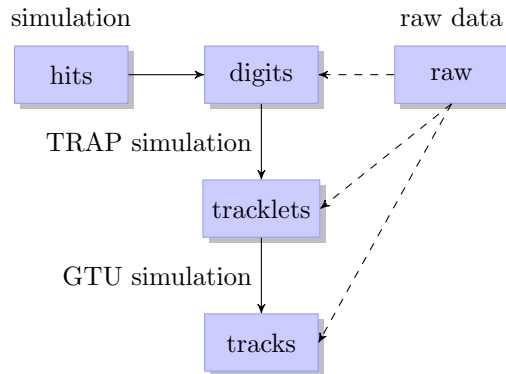


Figure 4.15: On-line tracking simulation: Digits, tracklets, and tracks can be extracted from recorded raw data. The digits can also originate from a Monte Carlo detector simulation, with tracklets and tracks being simulated from them. The tracklet and tracking simulation can also be used for re-simulation on raw data.

data, e.g. for improvements on the tracking performance or the development of new triggers. The possible processing steps are sketched in Figure 4.15. The global tracking is based on tracklets, which themselves are based on the ADC data from a TRD chamber. The local tracking simulation operates on digits, the structures containing the ADC data. The latter can either be extracted from raw data or produced from a Monte Carlo detector simulation. The global tracking simulation operates on tracklets, which can either originate directly from raw data, from a re-simulation on raw data, or from a Monte Carlo simulation. The origin of the data is transparent for the online tracking simulation. The only difference arises from the assignment of Monte Carlo labels by a majority decision on the cluster or tracklet labels. During Monte Carlo simulations also the trigger contributions from the TRD are calculated and stored in the event data in the same way as for real data.

The data from online tracking allow for self-contained quality checks without the need for global tracking, which is not available e.g. in the online Quality Assurance (QA) framework [182]. In Monte Carlo simulations, also comparisons with track references are possible and such results will be discussed in the next section.

4.2.5 Performance and quality assurance

In the following, we will discuss the performance of the online tracking in the TRD, focusing on the local tracking. Having verified that the online tracking simulation reproduces the results from the real detector, Monte Carlo simulations are a good way to study the achievable performance of the local tracking method. Here, the found tracklets can be compared easily to the Monte Carlo truth to extract e.g. efficiencies and shift distributions or to tune the look-up tables for particle identification. The Monte Carlo comparison is also well-suited to study how the performance changes depending on the configuration settings. The TRAP simulation explained above has been used in various such studies [176, 183, 184, 185, 177]. Here, the main objective is to point out general features and limitations of the online tracking.

First, we shall look at an ideal Monte Carlo simulation (without mis-alignment or gain variations) for minimum bias pp collisions. Consequently, an ideal TRAP configuration with only the pedestal filter enabled is used. To determine tracklet efficiencies, a set of findable tracklets

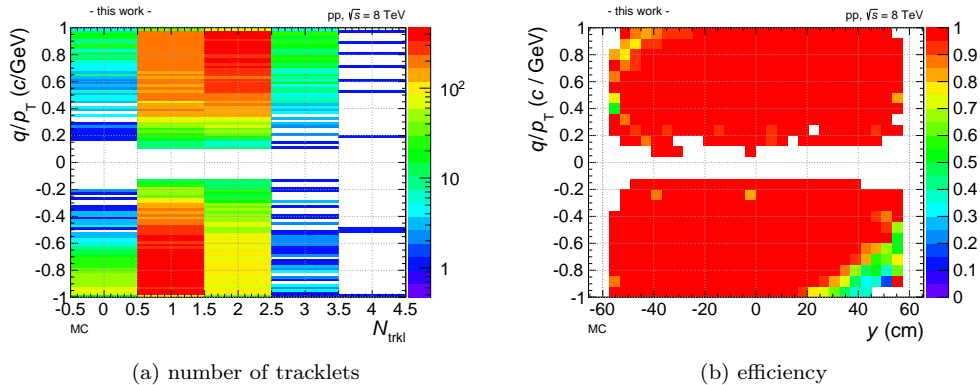


Figure 4.16: Tracklet efficiencies in Monte Carlo. Left: The number of tracklets found per expected one (from Monte Carlo track references) clearly shows that tracklets are found multiple times. Right: The efficiency slightly depends on the transverse position and the transverse momentum.

is defined from the Monte Carlo track references, i.e. the first and last point of energy deposit of a particle in the active volume of a TRD chamber during the detector simulation. Since such track references are produced by all particles traversing the active volume, we have to apply cuts to consider only those of interest to the online tracking. For the trigger, we are interested in tracklets only from primary tracks above a minimum p_{\perp} threshold of 1 GeV/ c and we only consider corresponding track references. For a pair of track references (position of entering and leaving the chamber), we count how many tracklets are found. The matching is based on spatial proximity and the Monte Carlo labels. The obtained distribution is shown in Figure 4.16a as a function of q/p_{\perp} . The fact that tracklets are found more than once is expected from the local tracking algorithm outlined before. The reason behind is that the requirement for a tracklet candidate can be fulfilled in more than one channel if the clusters are spread over more than one pad. For tracks from negatively charged particles the most probable value is one, tracklets are found twice much more often for positive q/p_{\perp} . For such tracklets, the apparent inclination angles are larger because of the Lorentz drift. Another effect is visible in the tracklet efficiency, see Figure 4.16b. It is determined as the fraction of track reference pairs for which at least one tracklet was found. The efficiency is close to unity except for large y and negative q/p_{\perp} . Negative tracklets, being bent in the same direction as the Lorentz drift, can be shifted out of the accepted deflection range by the Lorentz correction. The behaviour depends on the settings in the TRAP configuration.

Next, we compare the simulated tracklets to the track references and extract shift distributions for their position and deflection. For a meaningful comparison, the position of the track references is propagated to the radial position of the tracklets. In addition, the tilting of the pads must be taken into account. While the reconstructed tracklet has no notion of its z position other than the pad row, the position of the track references can be updated to obtain the apparent position, which is then used for the comparison, see Figure 4.17. Of course, this is not the achievable position resolution of a single tracklet but since the z information can be recovered in a global fit, it is relevant to judge the tracklet quality. We extract a resolution from a double-Gaussian fit and find the narrow peak to have a width of about 300 μm . The deflection from the track references is scaled to the 3 cm drift length. Here, the effect of the pad tilting is already taken

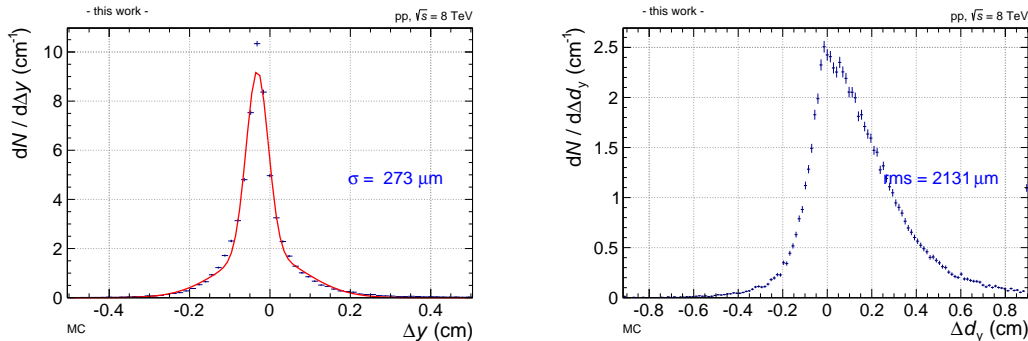


Figure 4.17: Shifts of tracklets with respect to Monte Carlo truth. Left: The shift distribution for the transverse position y . Right: The shift distribution for the deflection d_y .

into account during the local tracking such that no further adjustment is required. The resulting shifts are shown in Figure 4.17. The asymmetry is caused by the combination of the Lorentz drift and the ion tails. The former results in a shift of the deflections of about ~ 0.5 cm for the standard magnetic field of $B = 0.5$ T. The reconstructed deflection is, however, biased to smaller values by the ion tails from preceding clusters. This results in an over-correction of the Lorentz drift. The effect can be counter-acted by understanding the configured drift velocity as an effective quantity, which is tuned to minimize the width of the deflection residuals.

Next, we look at a standard Monte Carlo production, which takes into account mis-alignment and gain variations. The latter are corrected by the enabled gain filter in the TRAP. Now, we show the results for shifts in transverse position and deflection for different detector chambers, see Figure 4.18. The y shifts show distributions with chamber-wise offsets of up to about 2 cm. This is caused from the so-far uncorrected mis-alignment. However, the change between neighbouring chambers is small and the impact of the mis-alignment on the global tracking is limited. Therefore, it could be neglected for the triggering during Run 1. Since the deflection is a purely local property, the shifts show the same distribution as we have seen before without a dependence on the detector position.

For performance studies, also real data from different running periods are available and listed in Table 4.2. First test runs with the TRD triggers were taken with pp collisions at $\sqrt{s} = 7$ TeV, but the configuration settings were still evolving. For Pb–Pb running in 2011, the triggers were not used since the timing requirement for the level-1 contribution could not be met and the trigger implementation was not ready for production operation. In addition, a GTU bug for high multiplicity events prohibits the direct usage of the online tracks from these data. However, the tracking can be redone based on the tracklets available from the ESDs. By that re-simulation, these data are valuable for the study of future trigger signatures. The high-multiplicity bug was fixed for the data taking in 2012. Triggered data are available for pp collisions at $\sqrt{s} = 8$ TeV and $\sqrt{s} = 2.76$ TeV as well as p–Pb/Pb–p collisions at $\sqrt{s_{NN}} = 5.02$ TeV.

For real data, we cannot rely on a known particle trajectory. Instead, we calculate residuals of tracklets to tracks. To do so in a self-contained way, which is also usable for online monitoring without relying on information from other detectors, the GTU tracks can be used as a basis. Thus, we take the matching of tracklets to tracks from the GTU tracking. Fits for such a set of tracklets were implemented in `AliTRDtrackOnline`. Herein, the radial propagation can be based on different track models. For direct comparison to the algorithm in the GTU, a straight line fit

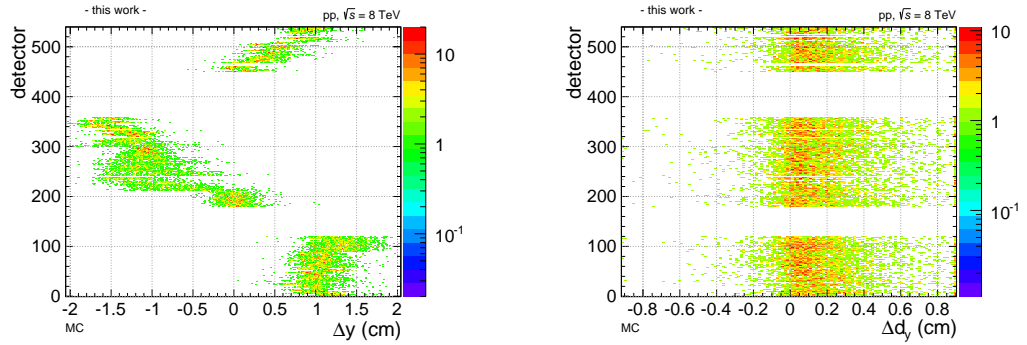


Figure 4.18: Shifts of tracklets with respect to Monte Carlo truth for different detector chambers. The gaps correspond to super-modules which were not yet installed in Run 1. Left: The shift distribution for the transverse position y . Right: The shift distribution for the deflection.

system	$\sqrt{s_{NN}}$	comment
pp	2.76 TeV	2013 run only
pp	7 TeV	test runs only
pp	8 TeV	production running
p-Pb, Pb-p	5.02 TeV	production running
Pb-Pb	2.76 TeV	requires re-simulation of GTU tracking

Table 4.2: Available data from TRD triggers: Data from running periods with different collisions systems and energies are available and can be used for the study of future possibilities.

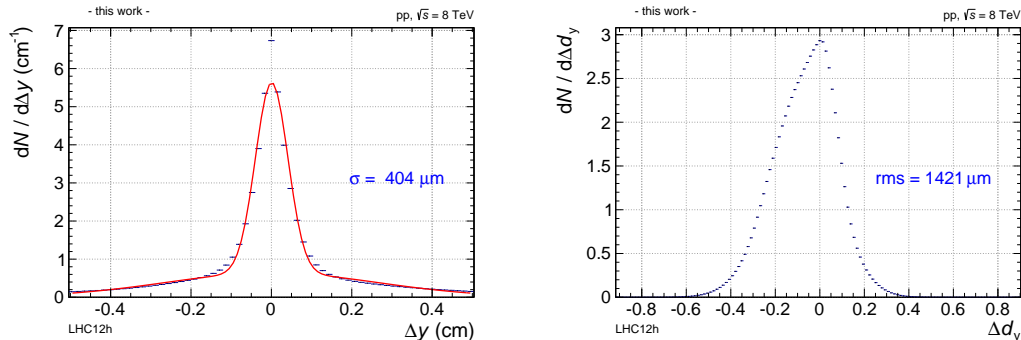


Figure 4.19: Tracklet residuals in y and d_y : The residuals are extracted from the comparison to a helix fit through the tracklets from GTU tracks. The correction on d_y for the Lorentz drift in the magnetic field is negative here.

is appropriate. For a more thorough comparison with the tracklet positions, a helix fit through the nominal vertex is used. It is parameterized by y_1 at a fixed radial position $x_1 = 3$ m, the tangent c of the polar angle, and the inverse bending radius $1/R$. For given parameters, other points on the trajectory can then be calculated by solving:

$$(x - x_0)^2 + (y - y_0)^2 = R^2, \quad z = c \cdot x, \quad (4.16)$$

with the centre point (x_0, y_0) fixed by the required radius $(x_1 - x_0)^2 + (y_1 - y_0)^2 = R^2$. The parameters are determined by minimizing the deviations of the tracklets from the parameterized track. Again, the pad tilting must be taken into account, with the z position now taken from the track extrapolation. The correlation of the y and z residuals allows the fit to achieve sub-pad resolution in z .

With the track parameterization available, residuals of the individual tracklets can be calculated with respect to the track fit, both in position and deflection, see Figure 4.19. Again, we fit two Gaussians to the distribution and extract the width of the central peak. It is a bit wider than in Monte Carlo. It should be noted that the track description is not as perfect as the Monte Carlo reference and also no correction of mis-alignment was done. The stack-internal mis-alignment enters while shifts of the complete stack do not show up in the residuals (only indirectly by invalidating the track model). With the tracking algorithm assigning the first matching tracklet to a track, it is not always the closest in y , which can broaden the resolution. For the deflection, we see a very similar shape as in the Monte Carlo comparisons, the opposite orientation is caused by the opposite sign of the magnetic field. The stated width is smaller but it should be noted that only tracklets matched to tracks enter to this distribution. By looking at distributions for individual chambers or certain groups of chambers, e.g. even and odd layers, it is possible to separate different effects on the residuals. A wrong Lorentz correction results in a common shift of the d_y residuals. A problem with the tilt correction results in opposite shifts in adjacent layers. And scaling of the drift velocity changes the shape and width of the distribution, as we can see here. With a good effective setting the distribution can be made much more Gaussian.

While additional online tracklets, which are not matched to a track, do not affect the result of the global tracking⁶, they deteriorate the latency. And high multiplicities can lead to the

⁶If the excess multiplicities get high enough, the assignment of random tracks also deteriorates the p_{\perp} reconstruction [181].

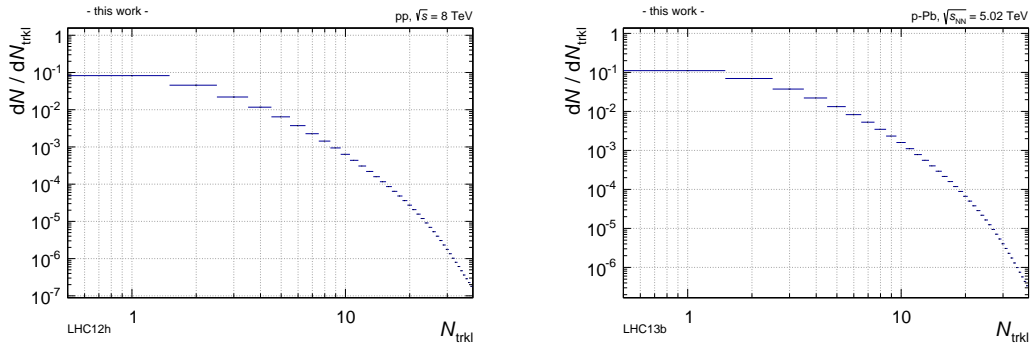


Figure 4.20: Tracklet multiplicities per chamber as observed in pp collisions at $\sqrt{s} = 8$ TeV (left) and p-Pb collisions at $\sqrt{s_{NN}} = 5.023$ TeV (right). The values are low enough for the online tracking to finish in time for the trigger contribution.

tracking not finishing in-time for the trigger contribution. The tracklet multiplicities observed without applying an explicit tracklet-level p_{\perp} cut beyond the restriction the allowed deflection range are shown in Figure 4.20 for different collision systems. They are low enough to allow for proper operation of the global tracking and triggering, see also [181].

The performance of the global tracking with respect to timing, resolution, and efficiency has been studied elsewhere using the software infrastructure discussed here [181]. In real data, the p_{\perp} resolution in the range of interest for the trigger (2 - 8 GeV/c) is confirmed to be better than 20 %. The efficiency rises quickly between 0.6 and 1.5 GeV/c, reaching its plateau around 2 GeV/c. About 95 % of the primary tracks with at least four tracklets in the TRD are found by the global online tracking. Here, we should further note that the sample of TRD online tracks has a significant contribution from the conversion of photons to electron-positron pairs in the material in front of and within the TRD. Those tracks are likely to be correctly identified as an electron and look like high- p_{\perp} tracks if the conversion occurred at a large radius. The track sample can be cleaned up by requiring the existence of a corresponding TPC track which can be matched geometrically [181]. This track matching also allows to correlate information from the online TRD tracks and from the full off-line tracking. It can even be run with the tracking information available in the HLT to recalculate the trigger decision with only those tracks having a global match (clean-up).

Within this thesis, we have established the local tracking with a performance allowing for the proper operation of the TRD triggers. Further optimization of the parameters relevant for the local online tracking are possible. In particular, the impact of the magnetic field through the Lorentz drift is significant, and e.g. resolutions for $B = 0$ are significantly better [176]. However, the changes would have also affected the accumulated charge used for electron identification, which would have required the re-generation of the PID look-up tables for the new settings [177]. Therefore, no further tuning was done during the operation of the triggers in Run 1. For Run 2, several improvements are in preparation. The channel-wise constants added to the reconstructed y positions shall contain the correction for the detector mis-alignment. Furthermore, the linear regression shall take into account the time offset t_0 of the signal at the position of the anode wires. This decouples the position reconstruction from the deflection. For the tail cancellation filter the impact on the tracking and PID has to be studied carefully. As the filter reduces the signal, a trade-off between tracking and PID performance must be found within the possible configuration settings. The ultimate choice will also depend on the priorities from the ALICE-

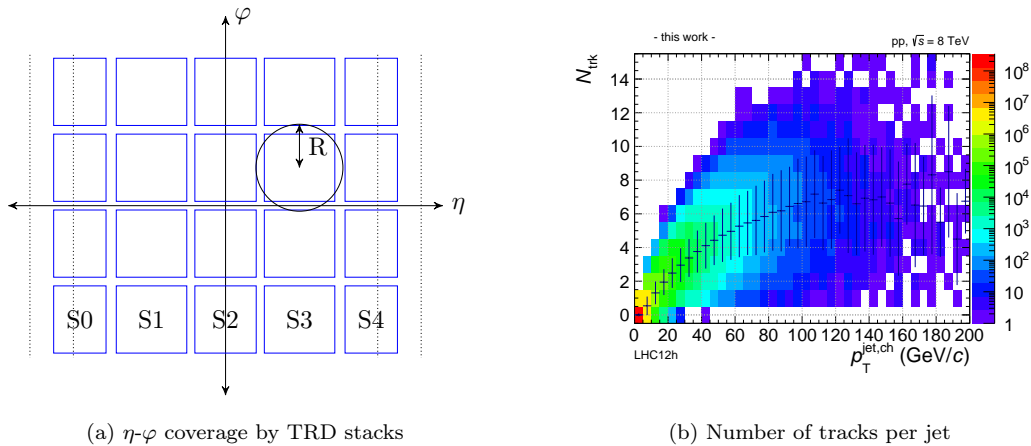


Figure 4.21: Left: The η - φ coverage of a TRD stack is comparable to the area of a jet cone with $R = 0.2$. Right: For jets the number N_{trk} of constituent tracks from charged particles above a p_{\perp} threshold of 3 GeV/ c motivates a trigger condition of a minimum number of tracks in any TRD stack. The markers show the mean and spread in a given p_{\perp} bin.

wide trigger strategy. With the full simulation chain established, these performance studies can be done both on Monte Carlo and existing data in such a way that the found configurations can later be directly used for the real detector.

4.3 Level-1 trigger

Having access to reconstructed tracks allows the implementation of much more flexible trigger conditions than just a single high- p_{\perp} track or electron candidate. However, one must keep in mind that the tracking is run stack-wise. Considering the η - φ coverage of a TRD stack one finds it similar in area to a typical jet cone of radius $R \simeq 0.2$, see Figure 4.21a. This opens the possibility for a jet trigger since most of the transverse momentum of a high- p_{\perp} jet is contained at small radii around the jet axis [186]. Using a moderate track p_{\perp} threshold is attractive to reduce the overall bias to hard fragmentation patterns. In order to still achieve sufficient rejection, the presence of a minimum number of tracks above this p_{\perp} threshold in any TRD stack can be required. Figure 4.21b motivates such a condition by showing that charged jets with transverse momenta above ~ 50 GeV/ c are indeed likely to have many contributing tracks. Here, a single track p_{\perp} cut at 3 GeV/ c has been used.

This argumentation had led to the idea of implementing a jet trigger on a minimum number of tracks above a p_{\perp} threshold within one TRD stack [187]. Both the p_{\perp} threshold and the number of required tracks must be chosen such that the trigger becomes efficient in the jet p_{\perp} range of interest while strongly suppressing events without high- p_{\perp} jets. Monte Carlo studies had been carried out to check different combinations of p_{\perp} and number thresholds [188, 171, 184, 189]. They also confirmed that such a condition can indeed be used meaningfully on only the charged part of a jet since the energy of neutral particles is invisible to the TRD. Figure 4.22a shows the inclusive p_{\perp} spectrum of reconstructed charged jets from a PYTHIA jet-jet production in p_{\perp} hard bins. While high- p_{\perp} jets are produced, they cannot be recorded in sufficient number

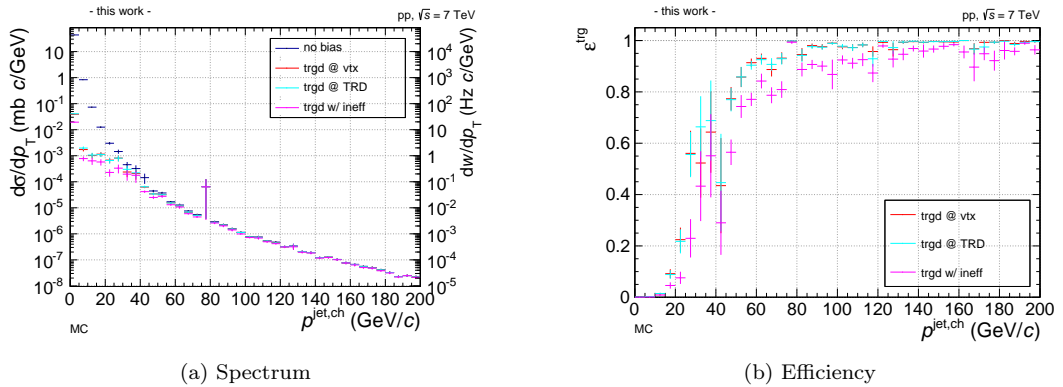


Figure 4.22: Left: Jet (anti-kt, $R = 0.4$) p_{\perp} spectra from a PYTHIA simulation ($\sqrt{s} = 7$ TeV, merged from p_{\perp}^{hard} bins) before and after event selection. The rates are given for a luminosity of 1 kHz/mb. Right: Ratio of triggered over untriggered spectra.

during minimum bias data taking. In addition, the respective spectra from only those events having at least 3 tracks above 3 GeV/c (as an example) in any of the η - φ windows corresponding to a TRD stack are shown. Once the track properties are evaluated at the vertex, once at the inner radius of the TRD, and once a global tracking efficiency of 80 % is assumed. The resulting efficiencies are shown in Figure 4.22b. They show that such a trigger condition is indeed feasible and becomes efficient for charged jets above ~ 100 GeV/c.

The rejection of unwanted events also depends on the beam conditions including beam background and pile-up. This is more difficult to extract from Monte Carlo simulations but easy to derive from real data as the statistics requirements are low. During actual triggering the rejection is available as the ratio of accepted events (level-1) over the number of inspected events (level-0) from the monitoring in the CTP. The rejection depends on the pre-selection by the level-0 trigger used as input to the TRD trigger and has to be studied separately for different choices. Before actually using the trigger, the rejection can be extracted from a recorded minimum bias sample since all information on the online tracks is available in data. And for checks on the rejection factors over a sufficiently wide range of thresholds the statistics was already sufficient at an early stage – in contrast to the requirements for efficiency estimates which require a sample with a sufficient number of signal events.

In order to extract the rejection for a recorded sample of input events the number of tracks above a p_{\perp} threshold must be counted stack-wise and compared to the number threshold. For every event the GTU tracks are sorted with descending p_{\perp} and iteratively assigned to the stacks, counting the number of tracks per stack. Whenever a new maximum number n of tracks is found in any stack, the p_{\perp} of this last track is used to increment a histogram bin $N(n, p_{\perp})$. Thus, for a given entry the p_{\perp} is the maximum threshold at which n tracks are reached. For a given n the number of accepted events can then be extracted as a function of p_{\perp} from the histogram alone:

$$N_{\text{ev}}(n, p_{\perp}) = \int_{p_{\perp}}^{\infty} dp'_{\perp} \frac{dN}{dp_{\perp}}(n, p'_{\perp}) \quad (4.17)$$

and the rejection is obtained by division by the number of sampled events. This avoids fixing thresholds when the analysis is run over a large data sample. The average rejections observed for different n and p_{\perp} are shown in Figure 4.23 for data taking periods with pp, p-Pb, and Pb-Pb

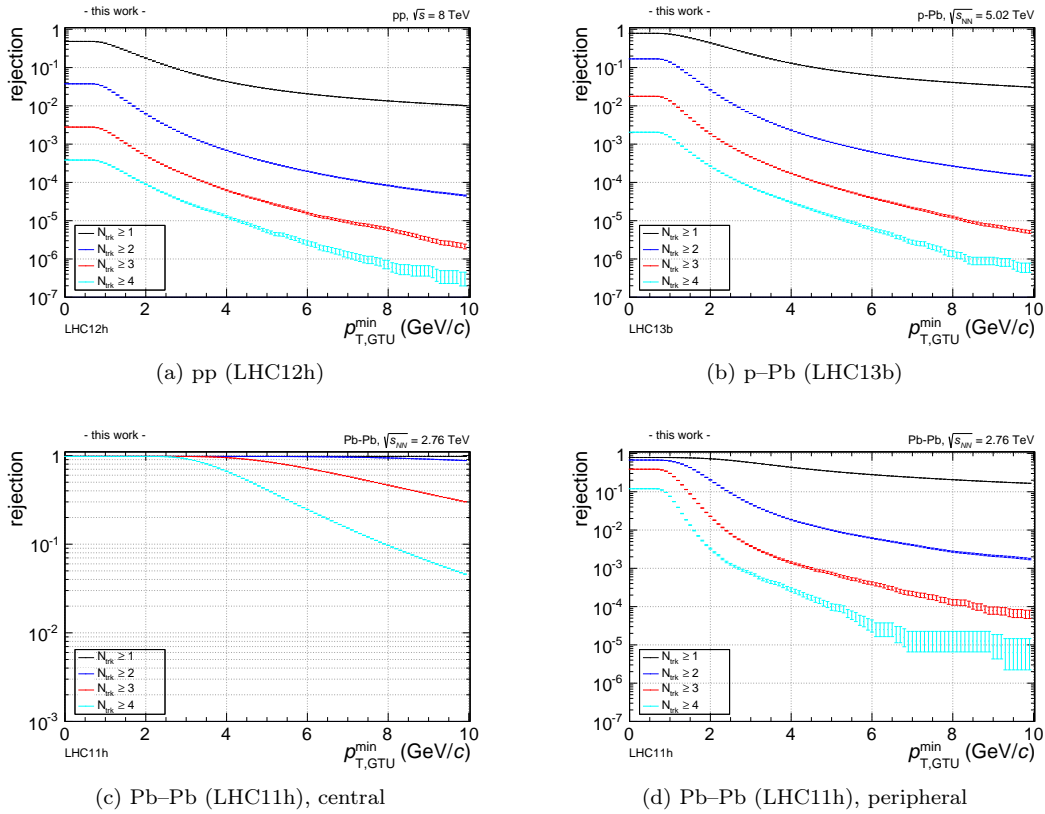


Figure 4.23: Rejection factors of the TRD jet trigger in different collision systems: The fraction of accepted events is shown for different combinations of the required minimal number of tracks and the minimal p_{\perp} . For pp and p-Pb, the rejection refers to the minimum bias input. For Pb-Pb the rejection was extracted from a re-simulation of the global tracking and two centrality classes are distinguished.

collisions. The plots show some common features. The plateau at low p_{\perp} arises from the pure requirement of any track. Then, its p_{\perp} typically exceeds ~ 1 GeV/ c because the GTU tracking is inefficient below. Thus, most tracks which are found also reach the p_{\perp} threshold then. The suppression by a one-track condition even with a high p_{\perp} threshold remains below a factor of 100 in pp and p-Pb, and well below a factor of 10 in central Pb-Pb collisions. For a jet trigger, this encourages the use of conditions with more than one track per stack to avoid very high p_{\perp} thresholds while retaining the rejection power.

For the ultimate choice of thresholds, the jet- p_{\perp} range interesting for ALICE must be taken into account. The lower bound is given by what is sufficiently covered by minimum bias data taking, the upper threshold is determined by how far the p_{\perp} reconstruction of individual tracks is considered precise enough. By these considerations, the target p_{\perp} range for an ALICE trigger on charged jets was considered to be 100 – 200 GeV/ c . Based on these considerations the condition of 3 tracks above 3 GeV/ c within any TRD stack was chosen as a compromise between efficiency and rejection. It results in a rejection of about 10^{-4} for pp collisions at $\sqrt{s} = 8$ TeV. This configuration was used throughout the production running of the TRD jet triggers in LHC

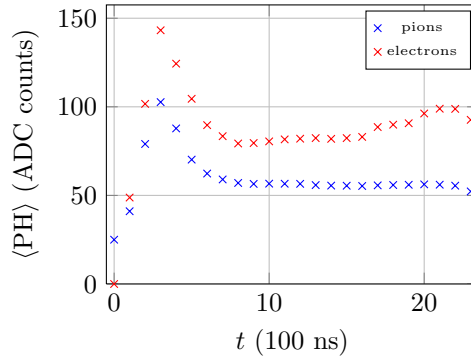


Figure 4.24: Average pulse height distribution for electrons and pions with momentum of 2 GeV/c.

Run 1.

4.3.1 Commissioning

Before taking the TRD triggers into operation a series of checks had to be performed. Some important steps towards production operation are listed in chronological order in Table 4.3. For the interaction with the CTP, we had to make sure that the trigger contribution was correctly transmitted from the GTU to the CTP, which expects it at a fixed time with respect to the level-0 trigger. This was accomplished by comparing event counters in the GTU and the CTP. Next, we confirmed that the trigger fired exactly when the condition was fulfilled. This was done based on recorded minimum bias data by evaluating the trigger condition (3 tracks above 3 GeV/c in any TRD stack) based on the track information contained in data. For events in which the online tracking had finished in time for the trigger contribution agreement was found. For other events discrepancies occurred because tracks were not taken into account for the online decision. To control this problem the tracks were marked by a flag indicating whether it was in time for the trigger decision [181]. In addition, it was made sure that the tracking is not aborted immediately after the trigger decision is due such that all tracks are still processed even if they are too late for the trigger contribution [181]. This update allowed us to consider only in-time tracks for the off-line evaluation of the trigger condition. We could now also check how the trigger behaviour changed when counting all tracks. Of course, the underlying problem, the too long latency of the tracking, was not solved by these measures. Instead, the number of timebins sampled by the FEE had to be reduced in order to start the tracklet transfer earlier after a level-0 trigger. This was possible because of the meanwhile established pretrigger timing and a good knowledge of the detector signal. Since the processing in the TRAP waits for the end of the sampling (to reduce noise in the data), the reduction from 27 to 24 timebins directly translated into a gain of 300 ns. After measures for the stabilization of the drift velocity were taken, the sampling window was further reduced to 22 timebins. This had not been possible before because with 22 timebins the signal just fits into the sampling window, see Figure 4.24. With the reduced latency of the tracklet arrival, the tracking finished well in time in pp and p-Pb conditions.

After the first checks in 2011, the TRD trigger contribution was permanently connected to the CTP and the decisions recorded in the event headers. Data with flagged events could then be used for further studies even though the TRD trigger was not yet included in the global trigger

date	action
2011/05	fix read-out order for tracklets
2011/08	first triggered test runs
2011/09	27 \rightarrow 24 timebins
2011/10	tests at high level-0 input rate
2011/11	Pb–Pb run with flagging
2011/12	patches for tracklet finding
2012/07/12	start production running of jet trigger (run 185465)
2012/09/26	start production running of electron triggers (run 189122)
2012/10/12	layer-0 and 5-tracklet requirement for HSE
2012/10/25	layer-0 and 5-tracklet requirement for HQU
2012/10/30	24 to 22 timebins (run 191128)

Table 4.3: Timeline of TRD trigger commissioning and operation: Before the production running of the TRD triggers started in July 2012, optimization and extensive tests were performed.

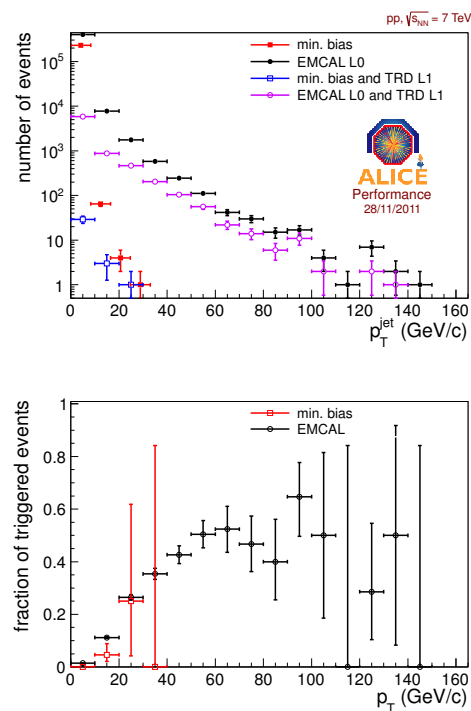


Figure 4.25: Fraction of jet-triggered events in test runs [175]: The first evaluation of the TRD jet trigger was based on a few runs with pp collisions at $\sqrt{s} = 7$ TeV in 2011. The jet- p_{\perp} spectra in a minimum bias and an EMCAL-triggered sample are shown without and with requiring the TRD trigger. The resulting fraction of accepted events as a function of p_{\perp} gave a first impression on the performance of the trigger.

identifier	condition
HCO	at least one track (cosmics)
HJT	at least 3 tracks above 3 GeV/ c in any stack
HSE	any track with $p_{\perp} \geq 3$ GeV/ c , PID ≥ 144 , at least 5 tracklets, tracklet in first layer
HQU	any track with $p_{\perp} \geq 2$ GeV/ c , PID ≥ 164 , at least 5 tracklets, tracklet in first layer
HEE	as HSE but limited to sectors 6 – 8 (EMCAL overlap)

Table 4.4: Trigger contributions by the TRD. The conditions are referred to by the given identifier, which follows the ALICE naming scheme.

decision⁷. But with minimum bias data alone, it was not possible to address the interesting jet- p_{\perp} range where the TRD condition could be expected to become efficient. However, the partial geometrical overlap with the ElectroMagnetic CALorimeter (EMCAL) allowed us to use a jet-enriched sample from an EMCAL level-0 trigger. While still not covering the full p_{\perp} range, this allowed to check the fraction of events which the TRD would have triggered up to reasonably high p_{\perp} , see Figure 4.25. The results showed a saturating ratio in agreement with expectations. The trigger could not be expected to be fully efficient with the incomplete EMCAL-TRD overlap. Furthermore, test runs with the TRD triggers activated were taken to check for stable operation with high level-0 but low level-1 rates. In fact, with the TRD trigger high rejection at level-1 was used for the first time in global data taking. The list of recorded test runs is given in Appendix C.5. For most of them the level-1 threshold was reduced to 2 tracks above 3 GeV/ c in order to achieve a reasonable accept rate and actually record data. Here, the focus was on testing the performance on the technical side. As the level-0 input rates were increased during the test runs ($\gtrsim 15$ kHz), an instability in the GTU was discovered. It blocked the read-out and prevented operation at high input rates at this stage. After this was fixed, the TRD trigger operation was stable also at high rates. This is crucial because the TRD can only inspect those events for which a level-0 trigger was issued before and, thus, the sampled luminosity depends on this rate.

While initially having planned to use the TRD triggers for the 2011 Pb–Pb run, the experience from the commissioning showed that the timing requirements for the tracking and level-1 contribution were too tight for the high-multiplicity environment of Pb–Pb collisions. For a significant fraction of the events the tracking data for the trigger decision would have been incomplete and the trigger condition would have depended on the event multiplicity. While the level-1 time can be (and already was) adjusted in ALICE, this was prohibitively involved shortly before the heavy-ion run. During the analysis of the online tracking results in the data recorded during the 2011 Pb–Pb run, it was found that the GTU did not correctly handle events with a very high number of tracklets from any half-chamber. Also this would have prevented the meaningful operation of a trigger. This bug was fixed for subsequent data taking periods [181]. While the TRD level-1 triggers were not used in the 2011 Pb–Pb run, all trigger-related information is available in the recorded data. In order to have the most general information available for future studies, the PID look-up tables were filled such that the tracklet PID value contains the (scaled) accumulated charge.

At the beginning of the data taking campaign in 2012, a dedicated test sample was recorded with the TRD trigger. Later, further tests were performed for the electron triggers [177].

⁷For the level-0 contributions not all possible inputs might be connected because of a preceding switch board.

4.3.2 Trigger requests

Based on Monte Carlo studies and the analysis of the flagged and triggered data recorded during the test runs, proposals were formulated for multiple trigger contributions and eventually requests were made by the respective physics working groups. An overview of the used TRD contributions is given in Table 4.4. Here, we shall further discuss only the jet trigger (HJT).

From the evaluation of Monte Carlo simulations, the fraction of jet-triggered pp events which contain a jet above 100 GeV/ c was estimated to be $2.4 \cdot 10^{-3}$. This led to the proposal of inspecting $5 \cdot 10^{10}$ events in order to populate the charged jet p_{\perp} interval between 100 and 200 GeV/ c . In the end, $1.25 \cdot 10^{10}$ inspected events were agreed as goal for the 2012 run. With an effective running time of $\sim 10^6$ seconds in the rare trigger configuration, this led to an average input rate requirement of 12.5 kHz. With a rejection of 10^{-4} , the read-out rate for the jet trigger was expected to be around 12.5 Hz. In addition, requests for the electron triggers were made. The TRD trigger inspects all events for all possible trigger conditions such that the same input sample can be used for the different TRD level-1 contributions. The electron triggers were put into operation a bit later than the jet trigger. Then, they used the same input events for inspection.

4.3.3 Data taking

For the data taking with the TRD triggers, a few constraints must be kept in mind. Firstly, the trigger requires an input sample from a level-0 trigger. This implies a contribution from the level-0 to level-1 time to the dead time of the experiment, which depends on the rate. A compromise must be found between the TRD need to sample as many events as possible and the impact on other level-0 triggers which loose luminosity. Furthermore, a suitable level-0 trigger must be compatible with the TRD pretrigger in the sense that the TRD pretrigger must be efficient for the used condition. At the same time the pretrigger has to allow for minimum bias data taking and, thus, also be efficient there. After a pretrigger was issued, an intrinsic dead time is enforced until the event is either rejected or accepted by a level-0 trigger. Together with the short-spaced collision trains this leads to a situation in which the first bunch crossings of a bunch train are most likely triggered, and subsequent bunch crossings are hidden by the intrinsic pretrigger busy time. A level-0 trigger more restrictive than minimum bias would trigger equally likely on any bunch crossing (assuming it is restrictive enough) and the combination with the pretrigger would be very inefficient. Given these boundary conditions, mostly the minimum bias triggers were used as input to the TRD level-1.

Different minimum bias conditions have been used depending on the mode of operation. For the pp data taking mostly the INT7 condition was used. It requires a coincident activity in V0-A and V0-C. However, the V0 detector is based on photo-multiplier tube read-out of scintillators suffers from ageing. Hence, it could not be used at high rates in pp operation. When the interaction rate was considered too high for the operation of the V0 detector, a condition based on the T0 detector was used instead. This INT8 requires coincident activity in T0-A and T0-C. The Cerenkov counters can stand the high rates but sample only about half of the cross section of the INT7 condition because of their smaller acceptance. Thus, the data taking in a typical fill started with INT8 as minimum bias trigger and was switched to INT7 when the rates had decreased sufficiently. In either case, a bunch crossing mask was used to select a part of the bunch crossings and reduce background. This mask was derived from the respective LHC filling scheme⁸. Both of the minimum bias conditions can be reproduced in the TRD pretrigger system, see Section 4.1. Thus, they were used as level-0 input condition for the TRD

⁸Coincidences with the BPTX beam monitors were used only in early data taking.

triggers. Furthermore, an EMCAL-based level-0 trigger was used as input for TRD. It was used in combination with the aforementioned INT7 and INT8 conditions and restricted by a suitable BC mask.

For the jet trigger, the following combinations of level-0 and level-1 HJT were used. They are given here with their respective trigger class name:

CINT7WUHJT V0 coincidence, TRD pretrigger, TRD level-1 jet trigger

CINT8WUHJT T0 coincidence, TRD pretrigger, TRD level-1 jet trigger

CEMC7WUHJT V0 coincidence, EMCAL level-0, TRD pretrigger, TRD level-1 jet trigger

CEMC8WUHJT T0 coincidence, EMCAL level-0, TRD pretrigger, TRD level-1 jet trigger

These classes were used to read out different trigger clusters, i.e. combinations of detectors. The choice depended on boundary conditions from the running strategy of ALICE. The following clusters were of relevance for the TRD-triggered data taking:

ALL all detectors

CENT central barrel detectors,
i.e. without the muon arm

FAST central barrel detectors at least as fast as the TPC,
i.e. without SSD, PHOS, ...

Depending on the analysis, not all clusters are usable because they lack the information of certain detectors. For example, the lack of SSD affects the resolution of the reconstructed transverse momentum. For the jet reconstruction we consider all clusters in the following.

Another parameter of the event selection is the previously mentioned bunch crossing mask. In ALICE, we distinguish bunch crossings with beam-beam (B), main-satellite (S), and isolated (I) collisions. Without collisions, we use those with beam only from the A-/C-side (A, C) and with no beam from either side (E). The last three masks were usually combined to ACE at the level of the CTP. Those events can be used for studies of beam-induced background.

In the end, a certain set of events is referred to by the class name, the bunch crossing mask, and the cluster of read out detectors, e.g. **CINT7WUHJT-S-NOPF-CENT**⁹. All classes used with the TRD jet trigger are listed with their accumulated statistics in Appendix C.6.

Having discussed the boundary conditions for the operation of the TRD trigger, we can describe the actual running conditions. After the minimum bias data taking in the beginning of 2012, rare triggers were operated from the period LHC12d onwards. This included the TRD jet trigger (HJT), which continued to run until the end of the pp data taking at $\sqrt{s} = 8$ TeV. An overview of the accumulated statistics is shown in Figure 4.26. The dominant part of the statistics was collected in the combination with the V0-based level-0 trigger although the number of events based on EMCAL has to be weighted differently in terms of jet content. The figure also shows the grouping into data taking periods, during which operational conditions, e.g. magnetic field polarity, were kept stable. For a detailed overview of the available statistics see Appendix C.6.

Figure 4.27 shows the level-0 inspection rate and the fraction of events accepted at level-1 for the LHC12h and LHC12i data taking periods. The inspection rate at the beginning of this interval was low and was ramped up later. Later, it was automatically adjusted to be low at the beginning of the fill and increase towards the end. This minimizes the dead time during the high luminosity at the beginning of a fill. The fraction of events accepted at level-1 is stable

⁹NOPF indicates the lack of past-future protection which was not used in Run 1 and this marker appears for all classes

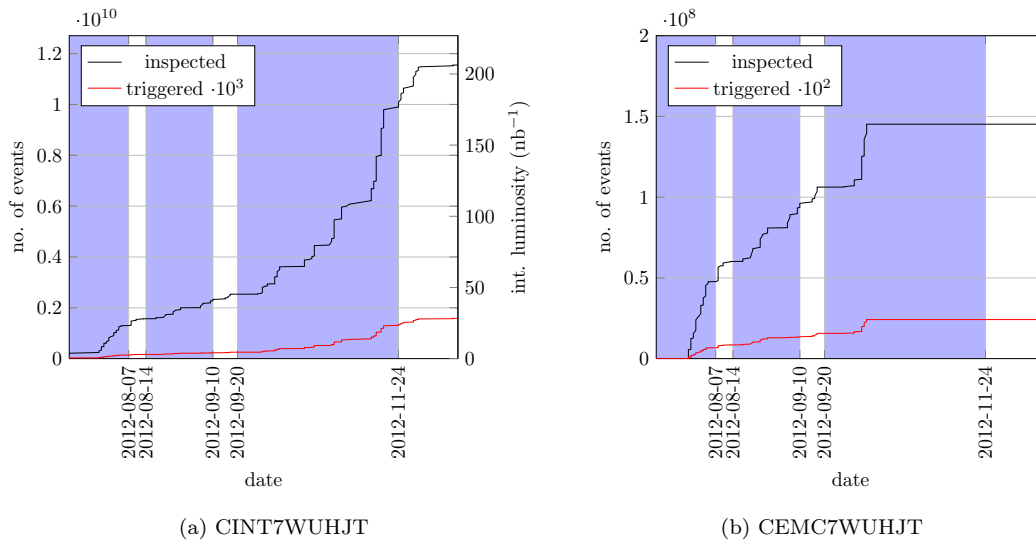


Figure 4.26: Statistics accumulated with the TRD jet trigger in pp collisions at $\sqrt{s} = 8$ TeV (2012). The black curve indicates the inspected events, the red curve the triggered events. The shaded areas mark the grouping into data taking periods. Left: V0-based level-0 trigger. Right: EMCAL-based level-0 trigger.

around $1.6 \cdot 10^{-4}$ and consistent with the expectation discussed before. It still depends a bit on beam-induced background conditions. In principle, we could compare the observed rejection run-wise with the expectation from the recorded minimum bias data. However, the statistics of the minimum bias sample in each run is too limited to judge the high rejection and the resulting errors are too large for a meaningful comparison.

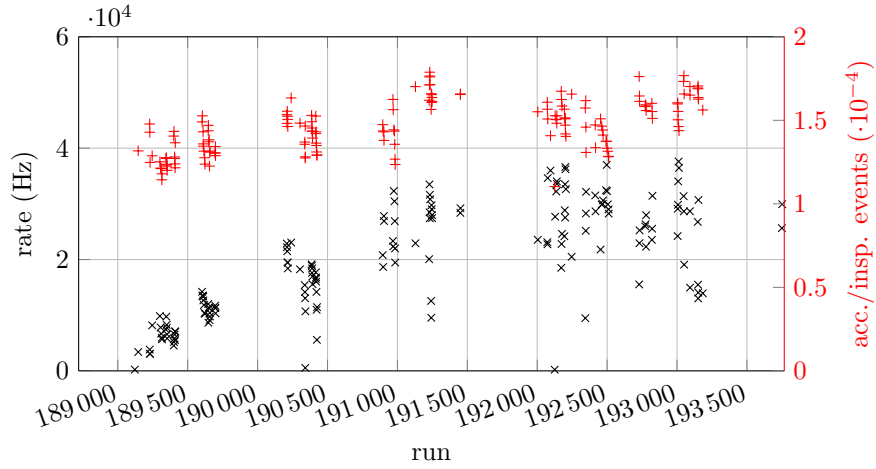
In p-Pb running the trigger was continued to be used in very similar conditions. An overview of the accumulated statistics is shown in Figure 4.28a. Finally, the trigger was also active during the pp run at intermediate energy, which serves as reference for the Pb-Pb runs. An overview of the available statistics is shown in Figure 4.28b. In all cases, the figures contain only events from runs usable for analysis as explained in the next section.

4.3.4 Performance of the jet trigger

In the following, we discuss the performance of the TRD jet trigger with a focus on the triggered data from pp collisions at $\sqrt{s} = 8$ TeV. First, we define the set of input data. In general, the following requirements were imposed on runs to be used for the analysis:

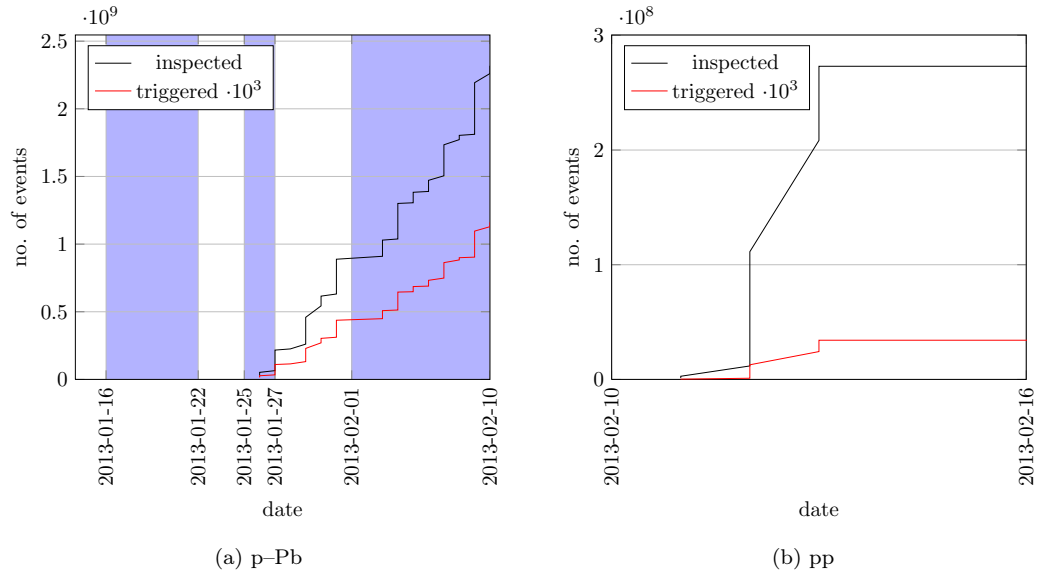
- physics run with stable beams
- data migrated
- minimum 10 minutes duration
- read-out of at least SPD, TPC, TRD
- SPD, TPC, TRD not marked as bad

In addition, individual runs with known issues were removed. A detailed list of usable runs is given for the relevant periods in Appendix C.7.



(a) CINT7WUHJT

Figure 4.27: Inspection rate (black) and fraction of accepted events (red) for the periods LHC12h and LHC12i: The input rate was increased at the beginning and continuously adjusted. The observed rejection of $\sim 1.6 \cdot 10^{-4}$ is stable and consistent with the expectation from the analysis of minimum bias data.



(a) p-Pb

(b) pp

Figure 4.28: Statistics accumulated with the TRD jet trigger in 2013. The black curve indicates the inspected events, the red curve the triggered events. The shaded areas mark the grouping into data taking periods. Left: p-Pb at $\sqrt{s_{NN}} = 5.02$ TeV. Right: pp at $\sqrt{s} = 2.76$ TeV.

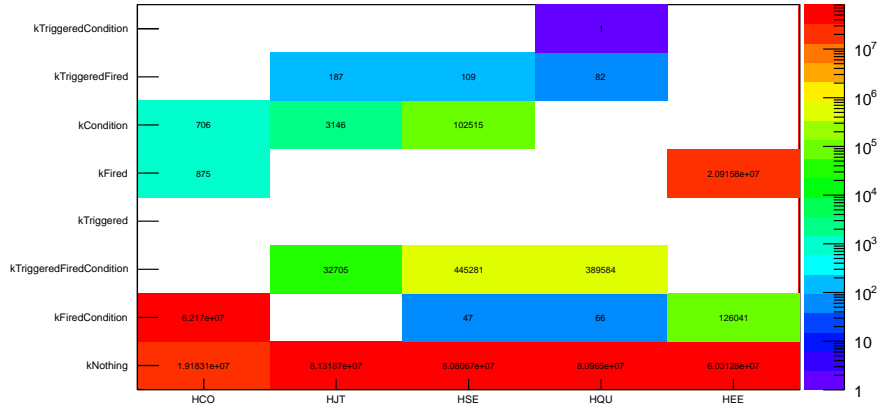


Figure 4.29: Consistency checks for TRD triggers: To ensure the proper operation of the TRD triggers we check for all TRD triggers the respective condition, the state of the trigger input, and the trigger class. In the example here, the behaviour is inconsistent, i.e. the firing of the trigger and the fulfilment of the condition are not identical. Such a run should not be used for analysis. The TRD trigger contributions are listed in Table 4.4.

We shall first look at the raw jet p_{\perp} spectra in triggered and untriggered events. In the analysis, we are interested in a minimum bias sample for which we use events triggered by the previously explained V0 coincidence (kTrgInt7). The read-out of this class was down-scaled but in combination with WU it also served as input to the TRD level-1 trigger. We shall also look at the resulting jet-triggered events (kTrgInt7WUHJT). We can also require the presence of the WU and level-1 condition retroactively on the minimum bias events (kTrgInt7_WUHJT). Then, we have the flexibility to evaluate modified trigger conditions. An analogue situation arises for the EMCAL level-0 input to the TRD trigger. However, we shall instead study the sample triggered by the combination of an EMCAL level-0 and level-1 trigger (kTrgEMCEJE) for comparison. Again, we impose off-line the additional conditions for WU and the jet trigger (kEMCEJE_WUHJT). Table 4.5 shows an overview of the described selections.

The evaluation of the various TRD conditions was encapsulated in `AliTRDTriggerAnalysis` such that it can also be used by other analyses [190]. An additional analysis task was developed which simply checks the consistency of the TRD trigger condition, the trigger input sampled at the CTP, and the trigger class. Normally, the fulfilment of the trigger condition and the activity of the CTP input should be equivalent. If true, an event can be read out in the corresponding trigger class but does not have to, e.g. because of down-scaling. If the condition was not fulfilled, the event must not be read out for this class. An example of the QA output, which shows inconsistencies, is shown in Figure 4.29. It resulted from a run during which tests on the GTU firmware were performed. Such runs have to be excluded from the analysis, of course.

From the selected runs, only events with at least one of the trigger flags discussed above (see Table 4.5) and passing the following event cuts are analysed further:

- collision candidate according to physics selection
- primary vertex with at least 3 contributors and $|z| < 10$ cm

flag	description
kTrgInt7	min. bias events from V0 coincidence (CINT7)
kTrgInt7WUHJT	min. bias events from V0 coincidence (CINT7) with TRD wake-up and jet trigger
kTrgInt7_WUHJT	min. bias events from V0 coincidence (CINT7) with off-line requirement of TRD wake-up and jet trigger
kTrgEMCEJE	events from EMCAL level-0 and jet level-1 trigger
kTrgEMCEJE_WUHJT	events from EMCAL level-0 and jet level-1 trigger with off-line requirement of TRD wake-up and jet trigger

Table 4.5: Trigger flags for the jet trigger analysis: Events fulfilling the listed criteria are flagged and then used for comparison.

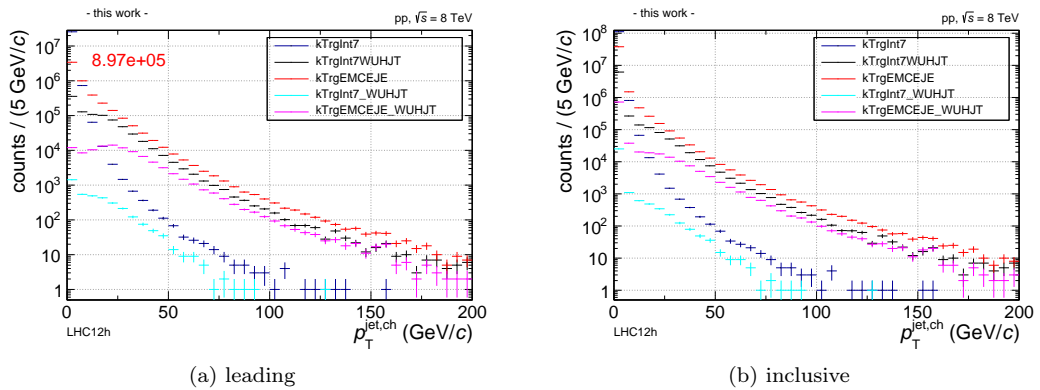


Figure 4.30: Raw leading and inclusive jet p_{\perp} spectra: The jet (anti-kt, $R = 0.4$, $|\eta^{\text{jet}}| < 0.5$) p_{\perp} spectra are shown for different sets of events.

For the events that passed the above selection, jets are reconstructed by an anti-kt jet finder with $R = 0.4$ based on hybrid tracks as explained in Section 3.5. Figure 4.30 shows the leading (highest p_{\perp} in the event) and inclusive jet p_{\perp} spectra for the different event flags. Intentionally, the raw counts are shown to convey the picture of the available statistics. As the dominant part of the statistics was accumulated in the period LHC12h, the plots are shown for that period only. This reduces changes of running conditions and facilitates later comparisons.

The spectra show that the goal to cover the jet- p_{\perp} range from 100 to 200 GeV/ c was achieved. The leading jets are expected to show the largest effect of a trigger bias. Except for very low p_{\perp} , the leading and inclusive spectra agree since a high- p_{\perp} jet is likely to be also the leading jet in the event. It should be further noted that the statistics from the EMCAL and TRD jet triggers are comparable within a factor of two. This allows for cross-checks of trigger biases. The two curves with the off-line requirement of WU and HJT lie below their respective input distribution. In both cases, there are two effects. The dominant one arises from the limited TRD acceptance which is not equivalent to the one covered in the minimum bias or EMCAL case. The second one is the necessity of a pretrigger for the events, which is not fully efficient either.

To judge the purity of the samples, we can normalize the spectra per triggered event as shown in Figure 4.31. As expected we can see the minimum bias sample lowest. Next, we find the EMCAL sample, followed by the TRD trigger based on minimum bias input. It is worth

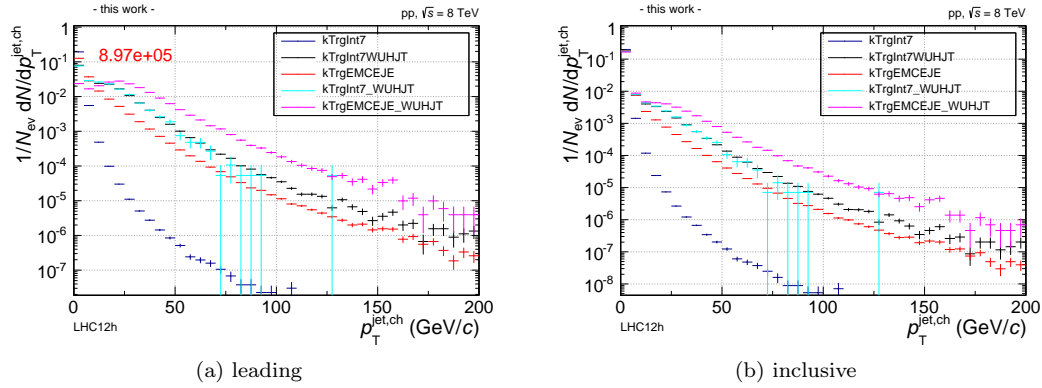


Figure 4.31: Raw leading and inclusive jet p_{\perp} spectra: The jet p_{\perp} spectra normalized per event are shown for different sets of events.

noting that the off-line requirement on top of the minimum bias data results in a consistent spectrum as expected. As the highest curve, we find the combination of EMCAL and TRD, which benefits from both rejections. We should also take note that the spectra are very similar in shape for high p_{\perp} but differ for low p_{\perp} , where the triggers are not yet fully efficient. And even without an efficiency correction, we can compare the shape of the spectra by looking at the ratio after normalization in some p_{\perp} window, here 60–80 GeV/ c . Figure 4.32 shows the comparison of the minimum bias and EMCAL-triggered spectra with the TRD-triggered spectrum. Within the available statistics, we find the EMCAL/TRD ratio consistent with a saturated trigger efficiency above ~ 100 GeV/ c .

Another interesting check concerns the geometrical distribution of jets in the TRD-triggered sample. Figure 4.33 shows the distributions of the (leading) jet axis in φ and η depending on the jet p_{\perp} . The stack boundaries of the TRD are clearly visible. To get a two-dimensional impression the η - φ distribution of the jets above 50 GeV/ c is shown as well. Here, also regions of inefficiency in the TRD can be identified. Since the trigger requires only a single entity, the non-homogeneity of the jet axis is not harmful by itself. However, the boundaries result in a loss of efficiency, which is caused by the limitation to count tracks only within a stack. For future runs, an extension is under study to count over the area of a stack but crossing stack and sector boundaries. This requires position information on the tracks that goes beyond the stack. Even though not used in the GTU during Run 1, the calculation of an approximate track position is foreseen. And it is available in the simulation model such that the upgraded trigger condition can be easily tested on existing data.

Finally, to judge the trigger bias, one should also look at the fragmentation patterns. The most direct way is to plot the p_{\perp} distribution of tracks contained in a jet. For this purpose the tracks assigned to a given jet by the jet finder are used. Figure 4.34 shows the distributions for (leading) jets from different p_{\perp} bins in TRD-triggered events. Since a jet cannot contain a track with p_{\perp} higher than its own, the spectra end depending on the jet p_{\perp} bin. As expected, they also get harder for a higher transverse momentum of the jet. For the lower jet p_{\perp} bins a bump at the trigger threshold is clearly visible. This is expected since we explicitly require tracks of 3 GeV/ c to select the event.

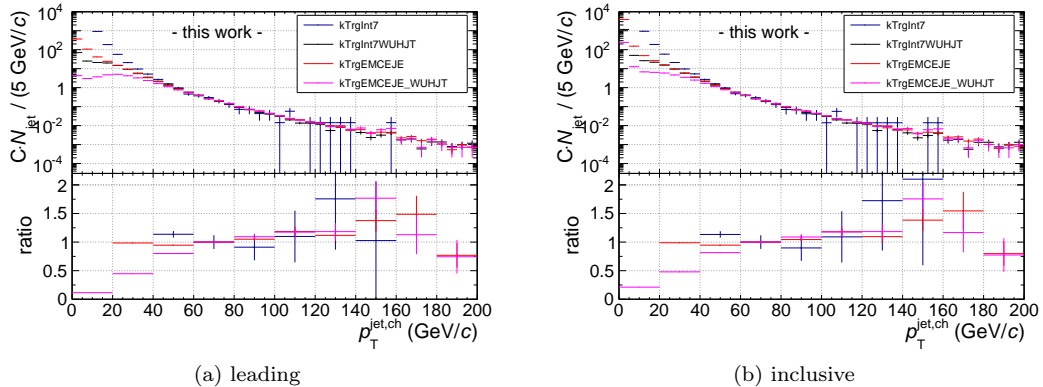


Figure 4.32: Comparison of leading and inclusive jet p_{\perp} spectra: The spectrum from TRD-triggered events is compared with other sets of events by scaling to the same yield between 60 and 80 GeV/c.

A better way to compare the fragmentation for different jet p_{\perp} is to normalize the track p_{\perp} as:

$$z := \frac{p_{\perp}^{\text{trk}}}{p_{\perp}^{\text{jet}}}. \quad (4.18)$$

Then, a commonly used variable to plot the fragmentation function is:

$$\xi := -\log \frac{p_{\perp}^{\text{trk}}}{p_{\perp}^{\text{jet}}}, \quad (4.19)$$

which emphasizes the low- p_{\perp} part of the fragmentation. Figure 4.34 shows the corresponding distributions for leading and inclusive jets in TRD-triggered events. In both representations, the track- p_{\perp} cut at 3 GeV/c is visible for soft jets. For higher p_{\perp} , the bias vanishes and the data can be used to study the fragmentation, also with identified particles. The conclusion becomes even clearer by comparing the fragmentation function for jets from a TRD-triggered sample with the one obtained from an EMCAL-triggered sample, see Figure 4.35.

4.4 Conclusions

Besides its use for tracking and particle identification, the TRD plays an important role in the trigger setup of ALICE. It needs a dedicated low-latency wake-up signal to sample the full signal and provides contributions to the global level-0 and level-1 decisions. We have first discussed the implementation of the FPGA design for the core pretrigger component to generate the wake-up signal. Based on a bunch counter synchronized to the LHC clock and corresponding masks of bunch crossings with beam from both sides, it allowed for a fully efficient pretrigger from the first day of LHC operation with stable beams. When the interaction rates became higher, the wake-up signal was derived from signals of the V0 and T0 detector. The bunch crossing masks were then used to restrict the triggering to a defined set of beam-beam bunch crossings. We have also discussed some limitations on the operation of the TRD and, in particular, its use for level-1 triggers. The most stringent limitation arises from the inherent dead time after a wake-up

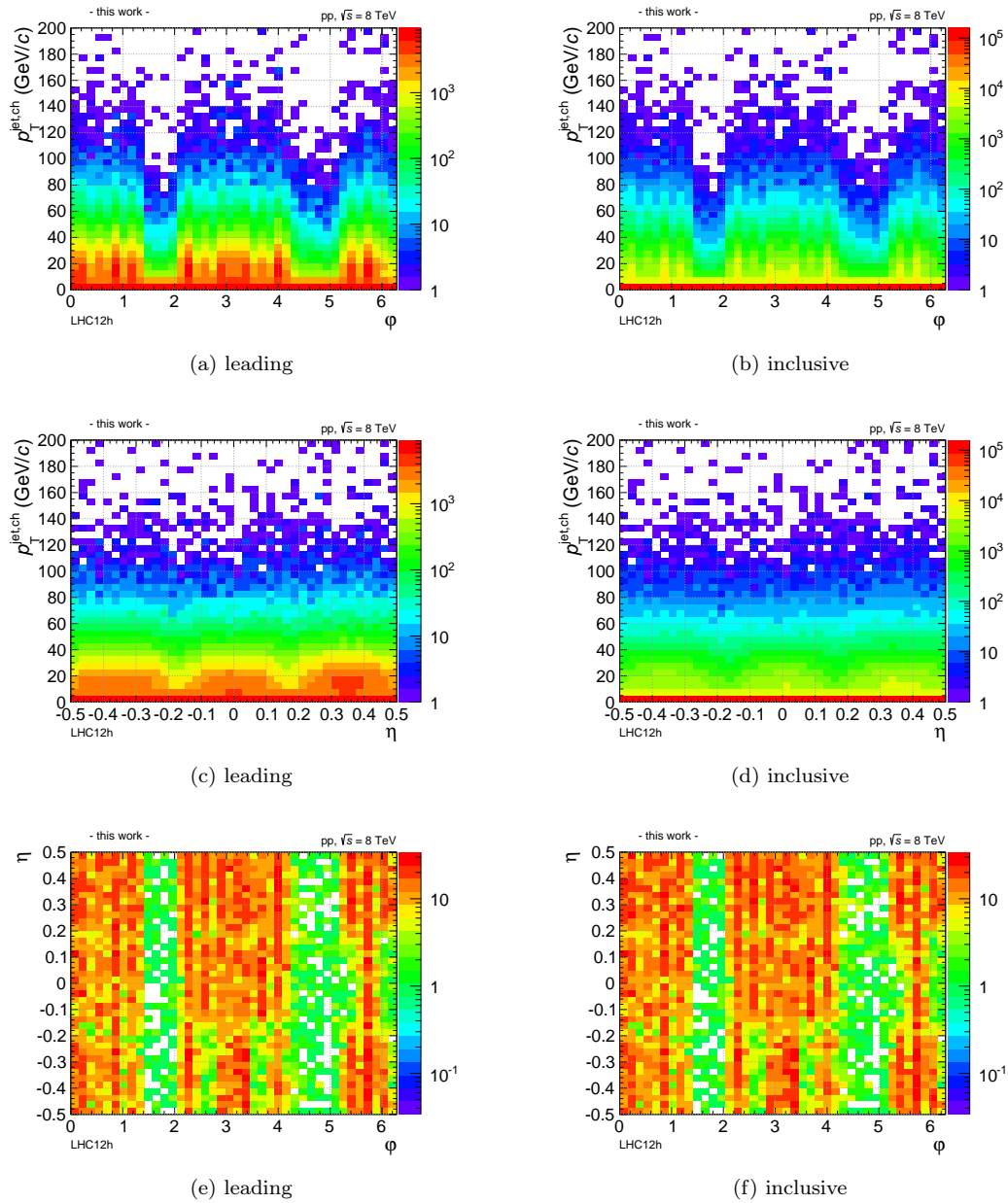


Figure 4.33: Distribution of the axis of the leading (left) and the inclusive (right) jets in η and φ : In $r\varphi$ direction the sector boundaries of the TRD, in longitudinal direction the stack boundaries in each supermodule are visible. The effect of the TRD acceptance is less pronounced for the inclusive jets as also jets enter which have not triggered the event.

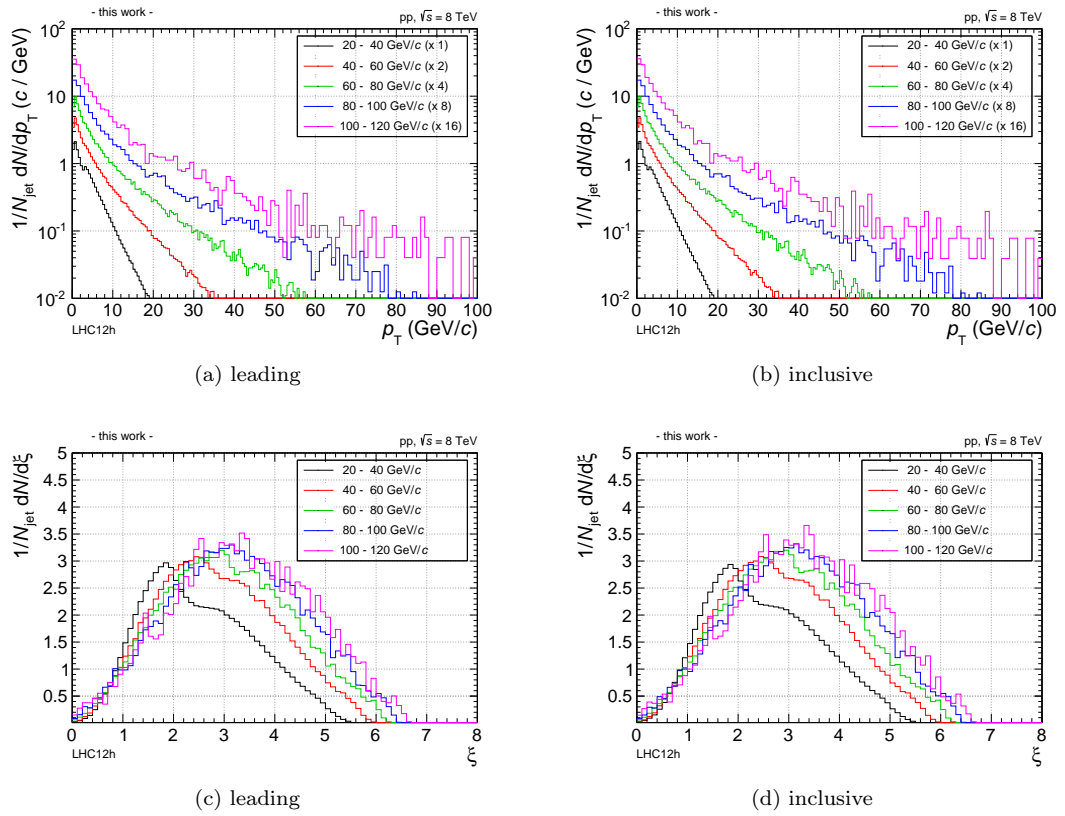


Figure 4.34: Jet fragmentation. Left: The p_{\perp} spectra for tracks in jets of different transverse momentum are shown for TRD-triggered events. Right: The fragmentation is well characterized by the fragmentation functions in $\xi = -\log(p_{\perp}^{\text{trk}}/p_{\perp}^{\text{jet}})$.

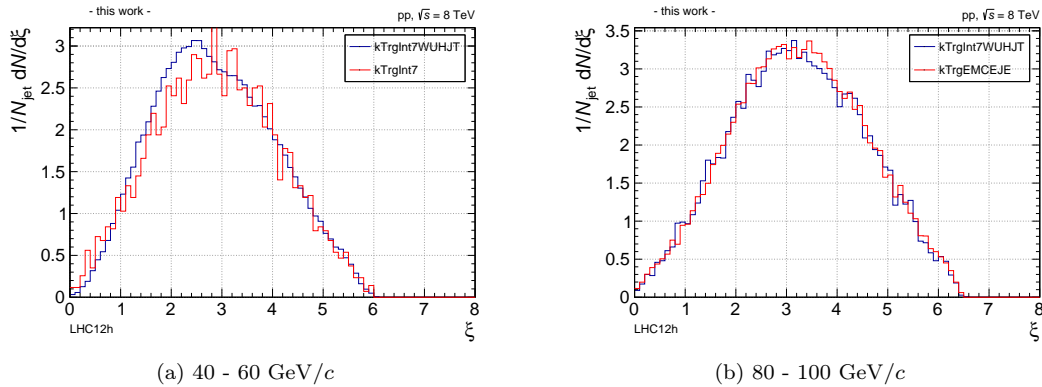


Figure 4.35: Comparison of the fragmentation in TRD-triggered data: The fragmentation functions for leading jets with a p_{\perp} between 40 and 60 GeV/ c are compared with a minimum bias sample. The distortion from the trigger is clearly visible. Between 80 and 100 GeV/ c the distributions from TRD- and EMCAL-triggered samples are compared and show good agreement with each other.

signal was issued in combination with the derivation of the pretrigger decision on only V0, T0, and TOF. The limitations had to be taken into account for the running scenario with level-1 triggers from the TRD. The pretrigger design as discussed here was successfully used throughout the production data taking of Run 1.

Next, we have discussed the online tracking of the TRD. First, chamber-wise tracklets are searched in the detector-mounted front-end electronics. Then, global tracks are found in the FPGA-based GTU. In the ALICE software framework, all information from the online tracking is propagated during reconstruction from raw data to the ESDs and AODs, which are the input to analyses. Furthermore, for all stages of the online tracking software models have been implemented, which reproduce the hardware results. They can be used either in full Monte Carlo simulations or on recorded data. Within this thesis, we have focused on the local tracking, for which reliable operation was established during Run 1. We discussed the relevant parameters and the control software for their configuration. In the end, we have discussed the performance of the local online tracking based on Monte Carlo simulations and recorded data.

Last, we have shown how the TRD was operated in LHC Run 1 to provide physics triggers. After a period of commissioning and validation, the TRD jet trigger, on which the focus of this thesis lies, was brought to productive operation. Shortly afterwards, the TRD contributed also two electron trigger conditions, which have been used to enhance the statistics for the measurement of quarkonia and to extend the p_{\perp} reach for the analysis of heavy-flavour mesons in semi-electronic decays. In pp collisions at $\sqrt{s} = 8$ TeV, the TRD has sampled the anticipated integrated luminosity of about 200 nb^{-1} from minimum bias level-0 input. The jet trigger condition resulted in a rejection of minimum bias events by a factor $1.6 \cdot 10^4$, and the event-normalized jet p_{\perp} spectrum is enhanced by three orders of magnitude. With this the charged jet p_{\perp} spectrum covers the anticipated range from 100 - 200 GeV/ c in the triggered data. The TRD triggers continued to run in the 2013 data taking with p-Pb ($\sqrt{s_{NN}} = 5.023$ TeV) and pp ($\sqrt{s} = 2.76$ TeV) collisions.

For low jet p_{\perp} , the triggered raw spectra and fragmentation functions show a bias at the track p_{\perp} threshold (3 GeV/ c). It disappears for higher transverse momenta of the jet, for which the

trigger becomes interesting. The recorded data sample can be used to extend studies on charged jets to significantly higher p_{\perp} than with the previously existing minimum bias data. This is particularly interesting in physics areas, in which ALICE offers unique possibilities, e.g. the measurement of fragmentation functions down to low transverse track momenta or of identified particles. The analysis of the triggered data is on-going.

We have also discussed some limitations and possible improvements. The separate pretrigger system puts constraints on the possible use of level-0 input conditions. For Run 2, it shall be replaced by a system fully integrated with the CTP such that more advanced pre-selections at level-0 become efficient. Several improvements at the tracking stage are under investigation, e.g. the correction of misalignment at the local tracking stage, the local tracking parameters, the tail cancellation filter, and also reduced window settings for the global track matching. The optimization criteria depend on the application of the tracks for actual trigger decisions. And the level-1 trigger itself could be extended by more advanced signatures. The discussion of the data taking strategy of ALICE for Run 2 is currently on-going and includes several level-1 contributions from the TRD. For the jet trigger the avoidance of stack boundaries, the combination of two pairs of p_{\perp} and number thresholds, or the evaluation of a stack-wise p_{\perp} sum could be useful. Using data from the LHC12h period, it could already be shown that the extension of the track counting to a stack-sized window that can move by half a stack in longitudinal and azimuthal direction improves the efficiency by about 40 % (the rejection only scales accordingly). A new trigger is studied to enhance the sample of light nuclei, e.g. $\text{He}^{3/4}$ or hyper-triton, based on the higher charge deposit of multiply charged particles. During Run 1, the TRD triggers have allowed to accumulate interesting data samples. With its flexibility, many more options exist for Run 2.

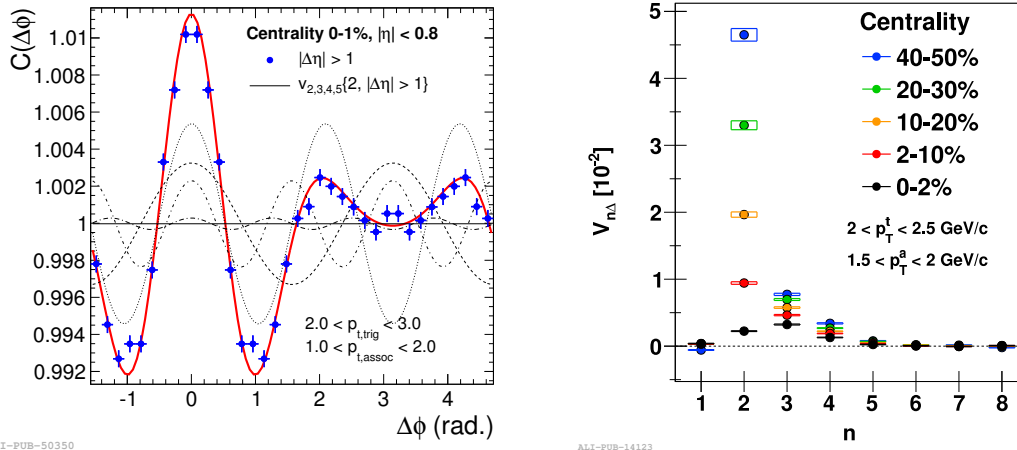
Chapter 5

Jet-hadron correlations

Already shortly after the first RHIC measurements, the results were interpreted in terms of a strongly coupled Quark-Gluon Plasma (sQGP) [88, 89, 90, 91]. The strong coupling explains the observed collective, fluid-like behaviour, e.g. strong elliptic flow in non-central collisions. It should be noted that this situation differs from the weakly coupled system expected at ultimately high temperatures from the asymptotic freedom of QCD and came as a surprise.

The fluid-like behaviour calls for the measurement of thermodynamical and hydrodynamical properties, such as the energy density, equation of state, viscosity, and velocity of sound. These questions are addressed from many sides, foremost by the study of jet quenching and the comparison of measurements to hydrodynamical models [191, 193, 194]. Such comparisons show that the viscosity is close to the lower bound conjectured from AdS/CFT duality [99, 195]. Furthermore, the measurements of non-zero odd harmonics v_n in the azimuthal particle distributions (see Figure 5.1), in particular the triangular flow component v_3 , have shown the presence of initial density fluctuations which survive a hydrodynamical evolution [192]. The important point is that the odd harmonics, in contrast to the even ones, cannot arise from averaged geometrical properties because of the collision symmetry. And a dissipative hydrodynamic evolution can only dampen these components but not generate them. Instead, they must be driven by fluctuations before the hydrodynamic evolution. The weak dependence of e.g. v_3 on the impact parameter further confirms the hypothesis of an origin other than averaged overlap regions. The sources of these fluctuations are supposedly initial processes before local thermalization. This suggests that also any other density fluctuations in the early stage survive throughout the hydrodynamic evolution.

Many measurements of jet quenching have shown significant energy loss, most recently the measurements of the nuclear modification factors R_{AA} and the di-jet asymmetry at the LHC [97, 196, 197]. The energy lost by the jet must be absorbed by the medium which is the only interaction partner (or there would have to be a drastic change in fragmentation such that the energy is not attributed to the jet any longer). This led to the idea of a Mach cone being produced by a parton traversing a dense medium at the super-sonic speed of light [198]. For some time this was thought to be the effect behind a double peak structure on the away-side of di-hadron correlations [199]. By now, this phenomenon has been fully explained by fluctuations in the initial phase of the collision [192]. Nevertheless, this explanation does not rule out the presence of a Mach cone-like emission but only avoids its necessity to explain the higher harmonics in the azimuthal correlation functions.



ALI-PUB-50350

ALI-PUB-14123

Figure 5.1: Harmonic decomposition of two particle angular correlations in Pb–Pb collisions. Left: The azimuthal di-hadron correlation of trigger and associated particles – separated in pseudo-rapidity by $|\Delta\eta| > 1$ – is decomposed into its Fourier components [191]. Right: The higher harmonics contribute with different strength depending on the collision centrality [192].

5.1 Analysis motivation from theory

A lot of work has gone into the study of the mechanisms responsible for partonic energy loss, see the previous discussion in Chapter 2 and reviews [62, 63]. The details are not sorted out but the general features are medium-induced gluon radiation and collisional energy loss. In either case, one can imagine that the lost energy is thermalized if the process is soft enough. This results in a local increase of entropy and energy density. Such a perturbation would propagate through the medium as a shock wave since the hard parton is faster than the speed of sound in the medium. Besides this very simple picture much more detailed models for the medium response exist [200, 201, 202, 203]. One result is the Mach cone, i.e. the conical emission of additional hadrons.

It was argued by Shuryak that the additional shock front is boosted by radial flow and, thus, should be sufficiently pronounced to be measurable [204, 205]. An observable signature would result from a quenched jet with additional particles being emitted around it. The experimental challenge is to identify this jet axis since a fully quenched jet is often not reconstructed in the final state accessible by the experiment. Thus, those events in which most energy is deposited in the medium do not contain the corresponding jet in the reconstructed final state. However, the lowest order Feynman diagrams for jet production in a hard scattering lead to two jets, which are back-to-back in their rest-frame. Even though at a hadron collider the parton centre-of-mass system is usually longitudinally boosted with respect to the lab frame, the two jets remain back-to-back in azimuth, see Figure 5.2. Thus, one can use one jet as a trigger and correlate other particles with it. Then, the correlation with a fully quenched jet is still measurable as the other (reconstructed) jet is used as reference.

A Mach-cone like emission would lead to additional particle production around the quenched jet. Thus, the main focus of this analysis is to look for signs of a medium response on the away-side of a trigger jet. The particles detected in such a way can originate from two sources. One is the fragmentation of a jet as it also happens in vacuum. The second process is the

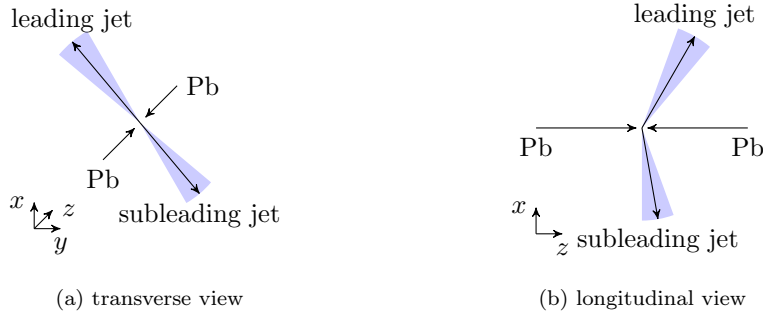


Figure 5.2: Di-jet production in Pb–Pb collisions: Because of momentum conservation pairs of jets are produced back-to-back in azimuth (transverse view). There is no fixed orientation in the longitudinal direction since the Bjorken x of the participating partons can be different.

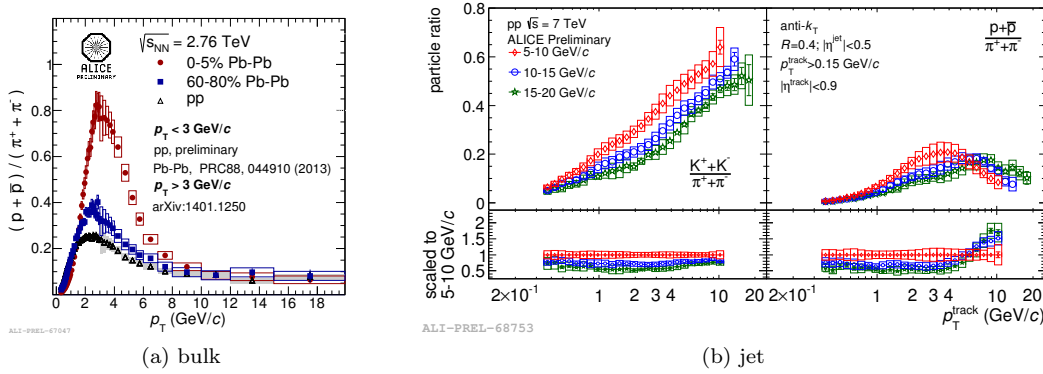


Figure 5.3: Particle ratios and fractions in jets and bulk. In the p_{\perp} range around 3 GeV/c, the proton fraction is significantly enhanced in central Pb–Pb collisions (left) and considerably higher than in jets (right).

medium hadronization which is also studied in bulk properties. A distinction of the two sources would be appealing. We want to exploit the different particle composition and in particular the different proton abundance in jets and in the bulk, see Figure 5.3 [206, 207]. This motivates the study of jet-hadron correlations with identified associates. In the following, we shall look for a difference between associated hadrons and protons. The presented analysis has the goal to look for signatures of additional particle emission on the away-side of a jet, and is not a precision measurement at the current stage.

5.2 Analysis outline

Based on the description above, the following analysis was designed for the data collected by ALICE in the 2010 and 2011 Pb–Pb runs [139]. The first data set comprises minimum bias triggered events, the latter includes central and semi-central triggers which results in increased

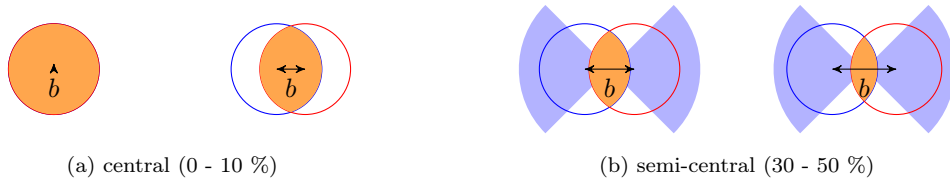


Figure 5.4: Centrality classes: The events are classified according to their centrality in order to select certain geometrical arrangements for a possible medium response. The sketches show the change in geometry from minimum to maximum impact parameter in the stated centrality range.

statistics for the respective centrality classes. An overview of the analysis shall be given here before the details of the individual steps are discussed in the subsequent sections.

After a cut-based selection of usable events from appropriate trigger classes, the event is classified according to its centrality. This is done because the geometrical properties depend strongly on the impact parameter. Figure 5.4 shows the overlap regions in the transverse plane for central and semi-central events. We use 0 – 10 % and 30 – 50 % most central events, respectively. The hard interactions leading to jet production scale with the number of binary collisions. In the case of a central event, the hard vertices are distributed more or less evenly over the overlap region. However, by requiring a high- p_{\perp} jet as trigger the hard vertex of those events is biased towards the surface of the medium. The jet in the opposite direction can have a long path length through the medium. But very different geometries arise depending on the hard vertex position. The advantage of central events is the large statistics, both from the high number of binary collisions and the use of a centrality trigger in the 2011 Pb–Pb run.

For semi-central events, the overlap region is much smaller and very asymmetric. However, by using jets pointing in the direction of the impact parameter more uniform geometries can be achieved. This comes at the price of lower statistics.

Because the sensitivity to the searched-for effect in the two cases is not clear a priori, both geometries shall be considered. Thus, every event is classified as either central or semi-central. Another interesting class would be di-jet events, for which two jets back-to-back in azimuth are reconstructed. This would allow a correction for the longitudinal boost of the parton centre-of-mass system. However, the statistics requirements are higher and this case shall not be further discussed here.

In the next step of the analysis, the potential trigger jets are selected. For central events, all jets in a given p_{\perp} range are allowed. For semi-central events, only those pointing in a window of $\pm 45^{\circ}$ around the event plane are accepted. The latter has to be reconstructed from the event itself as the impact parameter is not directly accessible. This is done based on the azimuthal anisotropy of particles arising from elliptic flow. In addition to jets, single high- p_{\perp} hadrons are also considered as triggers since they can be seen as proxies for jets. Not only is more statistics available for the individual particles but this also allows for comparisons to previous analyses.

Associated particles are selected from the event based on a set of track cuts, once inclusively and once with additional particle identification cuts to select protons. We use the p_{\perp} interval from 2 to 4 GeV/ c , for which we expect the highest proton enhancement. The hadrons are correlated with every trigger in the event in pseudo-rapidity ($\Delta\eta$) and azimuth ($\Delta\varphi$). In technical terms, the number of pairs is counted in bins of $\Delta\eta$ and $\Delta\varphi$. This is also done with the associated particles identified as protons. A distribution corrected for the contamination by non-protons is extracted using the probabilities for protons and non-protons to pass the particle identification cuts. To

allow for the correction of detector effects, associated particles are also used from other events (mixed event technique). This distribution contains the trivial effects which are not related to the presence of jets. Ultimately, we can compare the correlation functions for associated protons and inclusive hadrons. Before going through the steps of the correlation analysis in detail, it shall be discussed on a conceptual level in the following section. The abstract formulation might help some readers to follow the later discussion of the analysis steps.

5.3 Correlation analysis

In order to better understand the procedures of the correlation analysis, we can simplify the situation and consider tracks from primary charged particles to be characterized by an element from the set:

$$\Gamma := \underbrace{\mathbb{R}}_{\eta} \times \underbrace{S^1}_{\varphi} \times \underbrace{\overline{\mathbb{R}}}_{q/p_{\perp}}, \quad (5.1)$$

i.e. pseudo-rapidity η , azimuthal angle φ , and charge over transverse momentum q/p_{\perp} . A complete event can then be seen as an element of the sample space¹:

$$\Omega := \bigcup_{n \in \mathbb{N}} \Gamma^n, \quad (5.2)$$

i.e. an aggregate of n tracks. A probability measure on a suitable σ -algebra \mathcal{A}_{Ω} contains the physics describing the outcome of a collision in a statistical way. An event-wise observable O can be defined as a random variable, i.e. as a mapping from an element ω of the sample space (an event) to a measurable quantity:

$$O: \Omega \rightarrow \mathbb{R}, \quad \omega \mapsto O(\omega). \quad (5.3)$$

Accordingly, the event multiplicity is:

$$N: \Omega \rightarrow \mathbb{N}, \quad \omega \mapsto \#\omega, \quad (5.4)$$

where $\#\omega$ denotes the cardinality of the set ω . We can define more differential observables, e.g. for the azimuthal angle we map a measurable subset $A_{\varphi} \subset S^1$ to the random variable of the number of contained particles:

$$N_{\varphi}: \mathcal{A}_{S^1} \rightarrow (\Omega \rightarrow \mathbb{R}), \quad A_{\varphi} \mapsto \left(\omega \mapsto \sum_{i=1}^{\#\omega} 1_{A_{\varphi}}(\omega_{i,\varphi}) \right). \quad (5.5)$$

where $\omega_{i,\varphi}$ is short for the projection $\text{pr}_{\varphi} \circ \text{pr}_i(\omega)$ to the φ component of the i -th track. The indicator variable $1_{A_{\varphi}}$ is one if the argument is contained in A_{φ} . The generalization to the two-dimensional case of η and φ yields:

$$N_{\eta,\varphi}: \mathcal{A}_{\mathbb{R} \times S^1} \rightarrow (\Omega \rightarrow \mathbb{R}), \quad A_{\eta,\varphi} \mapsto \left(\omega \mapsto \sum_{i=1}^{\#\omega} 1_{A_{\eta,\varphi}}(\omega_{i,\eta}, \omega_{i,\varphi}) \right). \quad (5.6)$$

Now, we can also map a given A_{φ} (or $A_{\eta,\varphi}$) to the expectation value:

$$\langle N_{\varphi} \rangle: \mathcal{A}_{S^1} \rightarrow \mathbb{R}, \quad A_{\varphi} \mapsto \langle N_{\varphi}(A_{\varphi}) \rangle \quad (5.7)$$

¹We impose some ordering prescription to achieve uniqueness.

and find the average azimuthal particle density to be:

$$\frac{dN}{d\varphi} : S^1 \rightarrow \mathbb{R}, \quad \varphi \mapsto \left. \frac{d\langle N_\varphi([0, \varphi']) \rangle}{d\varphi'} \right|_{\varphi'=\varphi}. \quad (5.8)$$

The generalization to the two dimensional case is straight-forward. If we wanted to actually calculate the expectation values, we would need to know the underlying law to observe a given element ω of the sample space Ω .

Next, we look at correlations between trigger (trg) and associated (ass) particles in η and φ . We start by defining the pair distribution in $\Delta\eta := \eta_{\text{ass}} - \eta_{\text{trg}}$ and $\Delta\varphi := \varphi_{\text{ass}} - \varphi_{\text{trg}}$:

$$N_{\text{pair}} : \mathcal{A}_{\mathbb{R} \times S^1} \rightarrow (\Omega \times \Omega \rightarrow \mathbb{R}), \quad (5.9)$$

$$A_{\Delta\eta, \Delta\varphi} \mapsto \left((\omega, \omega') \mapsto \sum_{i=1}^{\#\omega} 1_{\text{trg}}(\omega_i) \sum_{j=1}^{\#\omega'} 1_{\text{ass}}(\omega_j, \omega'_j) 1_{A_{\Delta\eta, \Delta\varphi}}(\omega'_{j,\eta} - \omega_{i,\eta}, \omega'_{j,\varphi} - \omega_{i,\varphi}) \right). \quad (5.10)$$

where $1_{\text{trg/ass}}$ are indicator variables encoding which tracks to use as trigger and associate, respectively. Different selections based on the kinematic variables will be used later. The meaning is that we count the number of pairs for a given set of values of $\Delta\eta$ and $\Delta\varphi$. We can also write this as:

$$\int d\eta_{\text{trg}} d\varphi_{\text{trg}} d\eta_{\text{ass}} d\varphi_{\text{ass}} 1_{A_{\Delta\eta, \Delta\varphi}}(\eta_{\text{ass}} - \eta_{\text{trg}}, \varphi_{\text{ass}} - \varphi_{\text{trg}}) \cdot \sum_{i=1}^{\#\omega} 1_{\text{trg}}(\omega_i) \delta(\eta_{\text{trg}} - \omega_{i,\eta}) \delta(\varphi_{\text{trg}} - \omega_{i,\varphi}) \sum_{j=1}^{\#\omega'} 1_{\text{ass}}(\omega_j, \omega'_j) \delta(\eta_{\text{ass}} - \omega'_{j,\eta}) \delta(\varphi_{\text{ass}} - \omega'_{j,\varphi}) \quad (5.11)$$

to show the connection to the single particle distributions. With $\omega = \omega'$ we arrive at the so-called same event distribution:

$$N_{\text{pair}}^{\text{same}} : \mathcal{A}_{\mathbb{R} \times S^1} \rightarrow (\Omega \rightarrow \mathbb{R}), \quad A_{\eta, \varphi} \mapsto (\omega \mapsto N_{\text{pair}}(A_{\eta, \varphi})(\omega, \omega)) \quad (5.12)$$

with the average distribution:

$$\frac{d^2 N_{\text{pair}}^{\text{same}}}{d\Delta\eta d\Delta\varphi} : \mathbb{R} \times S^1 \rightarrow \mathbb{R}, \quad (\Delta\eta, \Delta\varphi) \mapsto \left. \frac{d\langle N_{\text{pair}}^{\text{same}}([0, \Delta\eta'] \times [0, \Delta\varphi']) \rangle}{d\Delta\eta' d\Delta\varphi'} \right|_{\Delta\eta'=\Delta\eta, \Delta\varphi'=\Delta\varphi}. \quad (5.13)$$

After dividing by the average number of trigger particles per event:

$$\langle N_{\text{trg}} \rangle = \left\langle \sum_{i=1}^{\#\omega} 1_{\text{trg}}(\omega_i) \right\rangle. \quad (5.14)$$

we obtain the so-called per-trigger yield:

$$\frac{1}{\langle N_{\text{trg}} \rangle} \cdot \frac{d^2 N_{\text{pair}}^{\text{same}}}{d\Delta\eta d\Delta\varphi}. \quad (5.15)$$

It tells how many particles are produced on average in a given $\Delta\eta$ and $\Delta\varphi$ window in association with a trigger hadron or jet. However, it cannot be extracted as such in an experiment because the detection probability of a track is in general non-homogeneous in phase space and does not

extend to infinite rapidities. Thus, the true distribution is distorted. To see how that affects the analysis we extend the definition of Γ to:

$$\Gamma' := \Gamma \times \{\text{detected, not detected}\}, \quad (5.16)$$

i.e. we add to the track the information whether it was detected in a given experimental setup. Then, we can define the projection on this sample space to retain only detected tracks:

$$\text{pr}_{\text{det}}: \Omega' \rightarrow \Omega', \quad \omega \mapsto \{\gamma \in \omega \mid \gamma \text{ detected}\} \quad (5.17)$$

for the evaluation of observables. Instead of deriving an observable O from a full event ω , we must only use the projected one, i.e. $O^{\text{det}} := O(\text{pr}_{\text{det}}(\omega))$ to describe what can be reconstructed from experimental data. Often, a detector is characterized by single particle efficiencies as a function of the kinematic variables²:

$$\epsilon: \Gamma \rightarrow [0, 1], \quad \gamma \mapsto \frac{\langle N_\gamma(B_\epsilon(\gamma)) \circ \text{pr}_{\text{det}} \rangle}{\langle N_\gamma(B_\epsilon(\gamma)) \rangle}. \quad (5.18)$$

This averages over all event and track topologies and does not reflect that the efficiency can be lower for (locally) high multiplicities. In particular, if two tracks get very close in a tracking detector, they might not be reconstructed properly (or at least not both of them). Such an effect is not contained in the single track efficiency, and is instead taken care of by explicitly removing pairs of very close tracks (pair cut) from the same event distribution.

5.3.1 Event mixing

We now consider the expectation value for the measurable pair distribution for which we shall use the notation $\bar{\omega} := \text{pr}_{\text{det}}(\omega)$:

$$\langle N_{\text{pair}}^{\text{same}} \circ \text{pr}_{\text{det}} \rangle = \quad (5.19)$$

$$\left\langle \int d\eta_{\text{trg}} d\varphi_{\text{trg}} d\eta_{\text{ass}} d\varphi_{\text{ass}} 1_{A_{\Delta\eta, \Delta\varphi}}(\eta_{\text{ass}} - \eta_{\text{trg}}, \varphi_{\text{ass}} - \varphi_{\text{trg}}) \right. \quad (5.20)$$

$$\left. \sum_{i=1}^{\#\bar{\omega}} 1_{\text{trg}}(\bar{\omega}_i) \delta(\eta_{\text{trg}} - \bar{\omega}_{i,\eta}) \delta(\varphi_{\text{trg}} - \bar{\omega}_{i,\varphi}) \sum_{j=1}^{\#\bar{\omega}'} 1_{\text{ass}}(\bar{\omega}'_j) \delta(\eta_{\text{ass}} - \bar{\omega}'_{j,\eta}) \delta(\varphi_{\text{ass}} - \bar{\omega}'_{j,\varphi}) \right\rangle \quad (5.21)$$

The two sums are linked by the possibility that the choice of the associated particles can depend on the trigger particle. From this we can read off several contributions which determine the pair distribution. The detected single particle distributions enter and induce a correlation if they are non-homogeneous. The most important reason for this is the finite detector acceptance which sharply cuts the efficiency. The pair cut adds an additional correlation. Finally, a physical correlation also enters. The correlation including the trivial effects induced from the single particle distributions is of limited use, especially since it depends on the details of the detector.

The event mixing technique now exploits that all but the non-trivial correlation are still contained if we consider the expectation value for the pair distribution with tracks from different events:

$$\langle N_{\text{pair}}^{\text{mixed}} \circ \text{pr}_{\text{det}} \rangle. \quad (5.22)$$

²We consider the combination of efficiency times acceptance.

Except for the pair cut, this is just a convolution of the single particle distributions. For the pair densities we obtain:

$$\frac{dN_{\text{pair}}^{\text{same}}}{d\Delta\eta d\Delta\varphi} : \mathbb{R} \times S^1 \rightarrow \mathbb{R}, \quad (\Delta\eta, \Delta\varphi) \mapsto \langle N_{\text{pair}}^{\text{same}} \circ \text{pr}_{\text{det}} \rangle, \quad (5.23)$$

$$\frac{dN_{\text{pair}}^{\text{mixed}}}{d\Delta\eta d\Delta\varphi} : \mathbb{R} \times S^1 \rightarrow \mathbb{R}, \quad (\Delta\eta, \Delta\varphi) \mapsto \langle N_{\text{pair}}^{\text{mixed}} \circ \text{pr}_{\text{det}} \rangle. \quad (5.24)$$

Then, we can also construct the change in the correlation by taking the ratio of the two maps which is referred to as correlation function:

$$C : \mathbb{R} \times S^1 \rightarrow \mathbb{R}, \quad (\Delta\eta, \Delta\varphi) \mapsto \frac{N_{\text{mixed}}}{N_{\text{same}}} \cdot \frac{\frac{dN_{\text{pair}}^{\text{same}}}{d\Delta\eta d\Delta\varphi}(\Delta\eta, \Delta\varphi)}{\frac{dN_{\text{pair}}^{\text{mixed}}}{d\Delta\eta d\Delta\varphi}(\Delta\eta, \Delta\varphi)} \quad (5.25)$$

where the individual distributions are normalized by their integrals:

$$N_{\text{same}} := \int d\Delta\eta d\Delta\varphi \frac{dN_{\text{pair}}^{\text{same}}}{d\Delta\eta d\Delta\varphi}(\Delta\eta, \Delta\varphi), \quad N_{\text{mixed}} := \int \frac{dN_{\text{pair}}^{\text{mixed}}}{d\Delta\eta d\Delta\varphi}(\Delta\eta, \Delta\varphi). \quad (5.26)$$

The correlation function describes the change in probability to observe a pair of a given $(\Delta\eta, \Delta\varphi)$ in the same and mixed event samples. Thus, it shows the non-trivial correlation of the associates with the trigger.

5.3.2 Experimental realization

In the experiment, the number of particles or pairs are counted in histograms with finite bins. To study the correlation in $\Delta\eta$ and $\Delta\varphi$ we count the number of pairs and estimate the pair density in same and mixed events by normalizing to the bin size:

$$\frac{d^2 N_{\text{pair}}}{d\Delta\eta d\Delta\varphi}(\Delta\eta, \Delta\varphi) \simeq \frac{N_{\text{pair}}([\eta_{\text{lo}}, \eta_{\text{hi}}], [\varphi_{\text{lo}}, \varphi_{\text{hi}}])}{(\eta_{\text{hi}} - \eta_{\text{lo}})(\varphi_{\text{hi}} - \varphi_{\text{lo}})}. \quad (5.27)$$

Then, we calculate the correlation function as explained above. The results in the following are not corrected for single track efficiencies.

We will later restrict ourselves to the measurement of azimuthal correlations for trigger jets because of statistics. Having discussed the two-dimensional case here, it should be noted that this restriction can be achieved in different ways. Even if we do not measure η , the effect from the limited acceptance remains present. The effect can be seen in the mixed event distributions and we will show it later. If we take the ratio of the same and mixed event distributions in $\Delta\varphi$:

$$C : S^1 \rightarrow \mathbb{R}, \quad \Delta\varphi \mapsto \frac{N_{\text{mixed}}}{N_{\text{same}}} \cdot \frac{\frac{dN_{\text{pair}}^{\text{same}}}{d\Delta\eta}(\Delta\varphi)}{\frac{dN_{\text{pair}}^{\text{mixed}}}{d\Delta\eta}(\Delta\varphi)} \quad (5.28)$$

we assign different weights to contributions for different regions of $\Delta\eta$. This is a valid and meaningful procedure but the outcome depends on the pseudo-rapidity ranges used for the trigger and associated particles. If the same/mixed correction is done in $\Delta\eta$ - $\Delta\varphi$ and the corrected result then projected to $\Delta\varphi$, different $\Delta\eta$ regions contribute equally.

	2010	2011
min. bias triggers	$5.6 \cdot 10^7$	$9 \cdot 10^6$
central triggers	n/a	$2.9 \cdot 10^7$
semi-central triggers	n/a	$3.4 \cdot 10^7$

Table 5.1: ALICE Pb–Pb data samples [139]. In the 2010 run, data were collected with a minimum bias trigger. For 2011, central (0 - 10 %) and semi-central (0 - 50 %) events were enhanced by two additional multiplicity triggers.

flag	description
kStatSeen	seen by analysis task
kStatTrg	collision candidate from accepted trigger: min. bias, central, or semi-central
kStatVtx	primary vertex information available
kStatCent	centrality information available
kStatEvPlane	event plane information available
kStatPID	PID response available
kStatUsed	considered for analysis, i.e. all required information available
kStatEvCuts	event cuts passed
kStatCentral	flagged as central (0 - 10 %)
kStatSemiCentral	flagged as semi-central (30 - 50 %)

Table 5.2: Event statistics flags: The listed flags are used to mark the events which have passed certain cuts or were marked for a certain event class. Further details are given in the text.

5.4 Event selection and classification

The data samples for which this analysis was designed were recorded with the ALICE detector in the Pb–Pb runs of the LHC in 2010 and 2011 [139]. In 2010, a minimum bias trigger based on V0-A, V0-C, and SPD was used, see Section 3.2.1 for the detector description. At least two of the three had to be active to fire the trigger. In 2011, an additional V0-based multiplicity trigger was activated with two thresholds to enhance central (0 - 10 %) and semi-central (0 - 50 %) events. In the 2011 run, unwanted electromagnetic interactions were suppressed by requiring signals in both ZDCs. An overview of the available statistics is given in Table 5.1, a detailed list of runs used for the analysis can be found in Appendix D.1. In the following, results obtained with the data from the 2010 run will be shown.

5.4.1 Event selection

The selection of events to be analysed is implemented as a series of checks. For the book-keeping of the statistics, the events are marked by the flags listed in Table 5.2. From all inspected events (kStatSeen) only those from hadronic collisions are of interest for this analysis. They are selected using the standard ALICE physics selection which implements a re-evaluation of the hardware trigger condition on reconstructed data and a suppression of events from bunch crossings without colliding bunches [139]. For this analysis, events are further limited to the minimum bias, central, and semi-central triggers (kStatTrg).

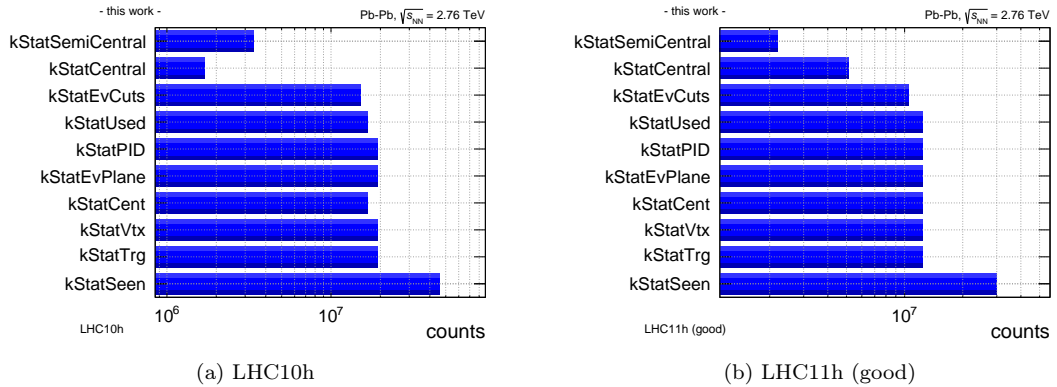


Figure 5.5: Statistics from the 2010 and 2011 Pb–Pb data. For 2011, only good runs with homogeneous TPC acceptance are included. More statistics is available from runs in which some TPC chambers were not at nominal settings. The used flags are listed in Table 5.2.

For the further processing, we check the presence of the information on centrality (kStatCent), the event plane (kStatEvPlane), the primary vertex (kStatVtx), and particle identification (kStatPID). Only events with all information available are further considered (kStatUsed).

In addition, the events are required to have a primary vertex reconstructed from at least 3 contributing tracks longitudinally within 10 cm of the nominal primary vertex position, and to have a centrality below 90 % (kStatEvCuts). Figure 5.5 shows the analysed statistics and the effect of the various event selection cuts. In addition, the events recognized as central (kStatCent) and semi-central (kStatSemiCentral) are indicated, for which we use the previously mentioned ranges 0 - 10 % and 30 - 50 %, respectively.

5.4.2 Centrality

Because the impact parameter is not amenable to direct measurement, we have to estimate the centrality from an observable. Different choices are possible within the analysis framework (AliRoot). In general, they rely on Glauber Monte Carlo simulations to relate experimental observables to the impact parameter [208]. In this analysis, we use the forward multiplicity measured by the V0 detector for the centrality estimation since it is separated from the phase space used for the actual analysis around mid-rapidity. As a cross check, we compare with the estimate using the track multiplicity in the central barrel (TPC-only tracks, $|\eta| < 0.8$, $p_{\perp} > 150$ MeV/ c). Figures 5.6a and 5.6b show the distribution of centrality as determined from the multiplicity measured in the V0 detector and from the number of tracks in the central barrel, respectively. In addition, the ranges selected by V0 for central (0 - 10 %) and semi-central (30 - 50 %) events are marked. We can see good agreement of the two centrality estimators.

5.4.3 Event plane

For semi-central events, we want to enforce an azimuthal orientation between a trigger particle and the reaction plane, which is not amenable to direct measurement either. However, a non-zero impact parameter leads to an anisotropic overlap region in the transverse plane. With a dense medium produced therein, the pressure gradient is different in- and out-of-plane and leads to

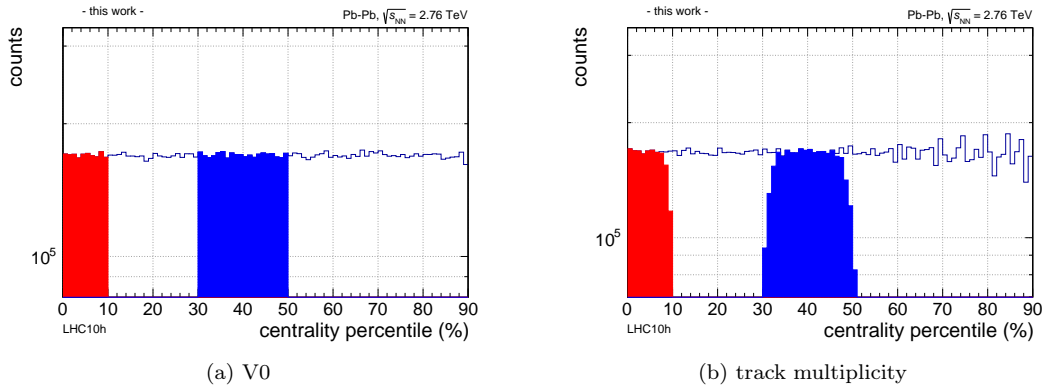


Figure 5.6: Centrality estimates for events from the 2010 Pb–Pb data. They are obtained from the multiplicity measured in the V0 detector (left) and from the number of tracks in the central barrel (right). Central and semi-central events determined from V0 are marked in red and blue, respectively.

enhanced particle emission in the event plane. One should keep in mind that fluctuations in the initial conditions lead to a different symmetry axis which is usually referred to as participant plane.

The reconstruction of an event plane can be based on any observable which carries along the anisotropy. In the following, we use the second-order event plane calculated from tracks in the central barrel by the calculation of the so-called Q -vector (of order n), as implemented in the commonly used event-plane selection task [139]:

$$\vec{Q}_n = \begin{pmatrix} Q_x \\ Q_y \end{pmatrix} = \sum_i w(p_{\perp,i}, \varphi_i) \begin{pmatrix} \cos(n\varphi_i) \\ \sin(n\varphi_i) \end{pmatrix} \quad (5.29)$$

where w is a weighting function:

$$w(p_{\perp}, \varphi) = \min\left(2, \frac{p_{\perp}}{\text{GeV}/c}\right) \cdot \frac{1}{\langle dN/d\varphi \rangle}. \quad (5.30)$$

It enhances the sensitivity by using p_{\perp} -dependent weights and flattens the event plane angle by correcting for detection efficiencies varying with the azimuthal angle [139]. The resulting distribution of the event plane angle Ψ obtained from the Q -vector as:

$$\Psi_n = \frac{1}{n} \text{atan} \frac{Q_y}{Q_x} \quad (5.31)$$

is shown in Figure 5.7a. The distribution is sufficiently flat for the purposes of this analysis, namely the selection of the direction of a trigger jet in semi-central events.

Later on, it will become important that the event plane reconstruction from a finite number of tracks is not perfect. For example, the azimuthal modulation of particle yields, when measured relative to the event plane, appears smaller than the true value by a factor R . This correction factor is also called event plane resolution – even though it is not really a resolution and $R = 1$ for perfect knowledge of the event plane. We follow commonly used procedures [209] to determine this resolution by randomly splitting the set of tracks in two and calculating the correlation:

$$R_{\text{sub}}^2 = \langle \cos(n \cdot (\Psi_1 - \Psi_2)) \rangle. \quad (5.32)$$

where Ψ_1 and Ψ_2 are the event plane angles calculated from the two sub-events. Then, R_{sub} measures the sub-event resolution under the assumption that they are equivalent. To arrive at the resolution for the full event, we have to note that the resolution depends on the 'visible signal', i.e. the strength of the modulation v_n and the track multiplicity M . In fact, it scales with the so-called dispersion $\chi = v_n \cdot \sqrt{M}$. The exact connection for the resolution of the second order event plane is given by [209]:

$$R(\chi) = \frac{\sqrt{\pi}}{2} \frac{\chi}{\sqrt{2}} \exp\left(-\frac{\chi^2}{4}\right) \left(I_0\left(\frac{\chi^2}{4}\right) + I_1\left(\frac{\chi^2}{4}\right) \right) \quad (5.33)$$

$$\simeq 0.626657 \cdot \chi - 0.09694 \cdot \chi^3 + 0.02754 \cdot \chi^4 - 0.002283 \cdot \chi^5 \quad (5.34)$$

with the modified Bessel functions I_0 and I_1 . The given polynomial approximation is accurate for $\chi \lesssim 3$. It allows to extract the resolution for the full event plane as:

$$R_{\text{full}} = R(\sqrt{2} \cdot \chi_{\text{sub}}), \quad \chi_{\text{sub}} = R^{-1}(R_{\text{sub}}). \quad (5.35)$$

The factor $\sqrt{2}$ arises from twice the number of tracks in the full event as compared to the sub-events. The resulting resolution is shown in Figure 5.7b as a function of centrality. For very central events, it is limited by the magnitude of elliptic flow, for very peripheral events by the reduced track multiplicity.

The tracks assigned to the reconstructed jet are also in the central barrel region and, thus, enter the calculation of the event plane. This effect can be quantified by removing these tracks from the calculated Q vector:

$$\vec{Q}'_n = \vec{Q}_n - \sum_J \sum_{i \in J} w(p_{\perp,i}, \varphi_i) \begin{pmatrix} \cos(n\varphi_i) \\ \sin(n\varphi_i) \end{pmatrix}, \quad (5.36)$$

where the sums are over the (trigger) jets and the assigned tracks. As can be seen in Figure 5.8, the contribution from the jet-assigned tracks is small. In the following, we thus use the event plane angle calculated from the full event.

5.5 Track selection

For the correlation analysis, we use individual tracks as triggers and associates in the pseudorapidity interval $|\eta| < 0.8$. Two different sets of track cuts are used. For the associate tracks we want to reliably use particle identification. Therefore, the cuts for them are chosen to resemble those used for the parameterization of the PID responses. Thus, we use the ALICE standard ITS-TPC track cuts (2011) for primary particles. First, we consider only tracks for which TPC and ITS information was used for the track fit and which have at least one hit in the SPD. Daughters from kinks are rejected. We further require every track to have crossed 70 out of 159 radial pad rows in the TPC. In addition, the ratio to the number of findable clusters (based on the particle trajectory) must be above 80 %. For the track fit, the χ^2 per TPC cluster must be below 4, the χ^2 per ITS cluster below 36. The distance of closest approach to the primary vertex must be below 2 cm in the longitudinal direction, for the transverse cut the requirement is p_{\perp} dependent: $0.0105 \text{ cm} + \frac{0.0350 \text{ cm}}{(p_{\perp}/(\text{GeV}/c))^{1.1}}$. In addition to these standard cuts, we enforce for the associates:

- $2 \text{ GeV}/c \leq p_{\perp} \leq 4 \text{ GeV}/c$
- PID status ok for TPC and TOF

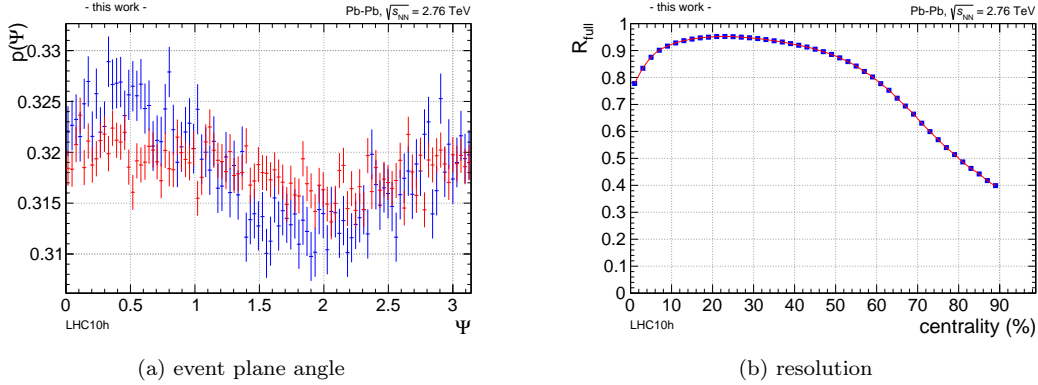


Figure 5.7: Left: Event plane angle distribution for central (blue) and semi-central (red) events reconstructed from tracks in the central barrel for events from the 2010 Pb–Pb run. Right: The blue markers show the event plane resolution as determined from two sub-events in bins of centrality, the red curve shows a spline interpolation which is well-suited to describe the curve and will be used in the analysis.

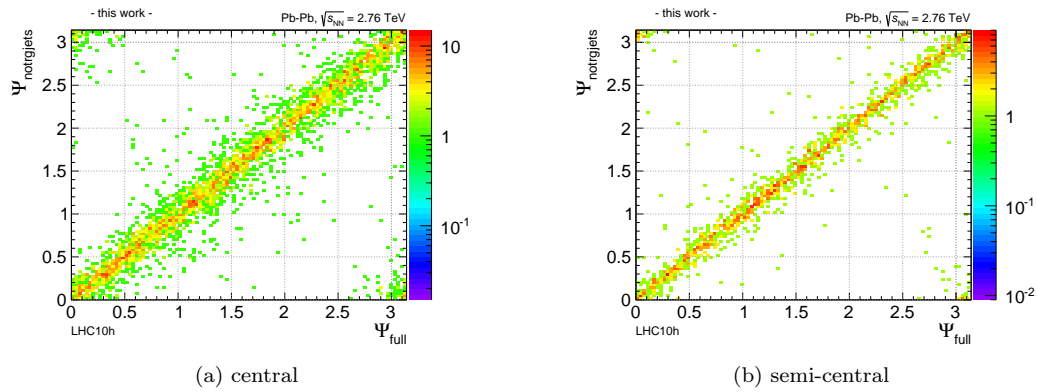


Figure 5.8: Correlation of the event plane angle before and after subtraction of the trigger jets ($R = 0.2$) from the Q vector in central (0 - 10 %) and semi-central (30 - 50 %) events. Only events containing a trigger jet are shown.

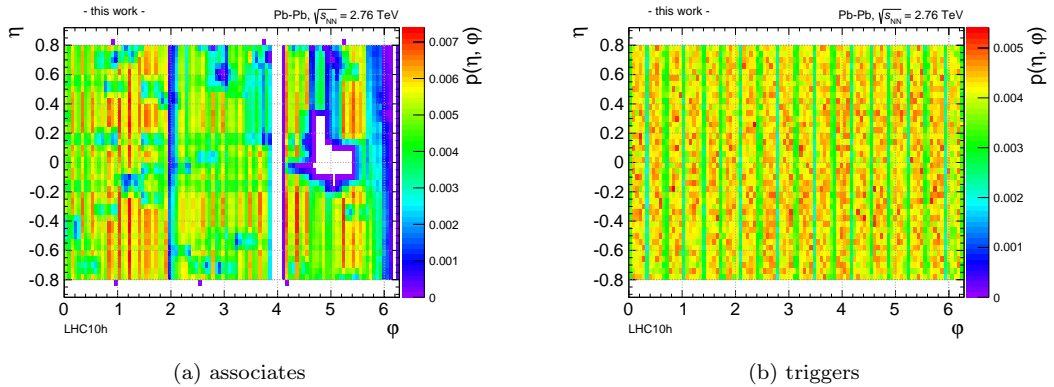


Figure 5.9: The η - ϕ distributions for associate candidates (left) and triggers (right) in the 2010 Pb–Pb data which arise from the used track cuts. The inhomogeneities in efficiency are taken into account for the correlation functions by the event mixing technique.

- at least 60 TPC PID clusters
- TPC signal at least 10 arb. units

The η - ϕ distribution resulting from these cuts are shown in Figure 5.9a. The azimuthal gaps extending over the full η range are caused by inoperational SPD ladders. The additional hole originates from a dead area in the TOF detector during the Pb–Pb data taking in 2010. These anisotropic distributions are treated by the correction of the pair distributions.

A strong inhomogeneity for both trigger and associate particles results in large mixed events corrections. In addition, jet finders react rather sensitively to edges in detector efficiency or acceptance. Therefore, we use hybrid tracks for trigger hadrons and jet finding to achieve better homogeneity in azimuth. These cuts use TPC-only tracks constrained to the primary vertex if no global track is available, see also Section 3.5. Here, we require a p_{\perp} between 6 and 8 GeV/ c for the single particle triggers. The remaining azimuthal structure for the trigger particles arises from the TPC sector boundaries, see Figure 5.9b.

For comparability with other analyses, we also impose a common ALICE track pair cut on the minimal distance for a radius R within the TPC in azimuth and pseudo-rapidity:

- $\Delta\varphi_{\min}^* := \min\{\Delta\varphi^*(R) \mid 0.8 \text{ m} < R < 2.5 \text{ m}\} > 0.02$,
with $\Delta\varphi^*(R) := \varphi_1 - \varphi_2 + \arcsin\left(\frac{q_1 BR}{2p_{T,1}}\right) - \arcsin\left(\frac{q_2 BR}{2p_{T,2}}\right)$
- $\Delta\eta > 0.02$

It results in the rejection of track pairs which are close at some radius in the TPC and cannot be reconstructed with full efficiency. The cut ensures a consistent rejection in the same- and mixed-event distributions. Otherwise, close pairs of tracks would contribute for mixed events but not for the same event where they suffer from the reconstruction inefficiency.

5.6 Jet reconstruction

The general jet finding procedure in ALICE was explained in Section 3.5. The purpose of the jet reconstruction in this analysis is to reconstruct the jet axis. The jet energy is used only for the

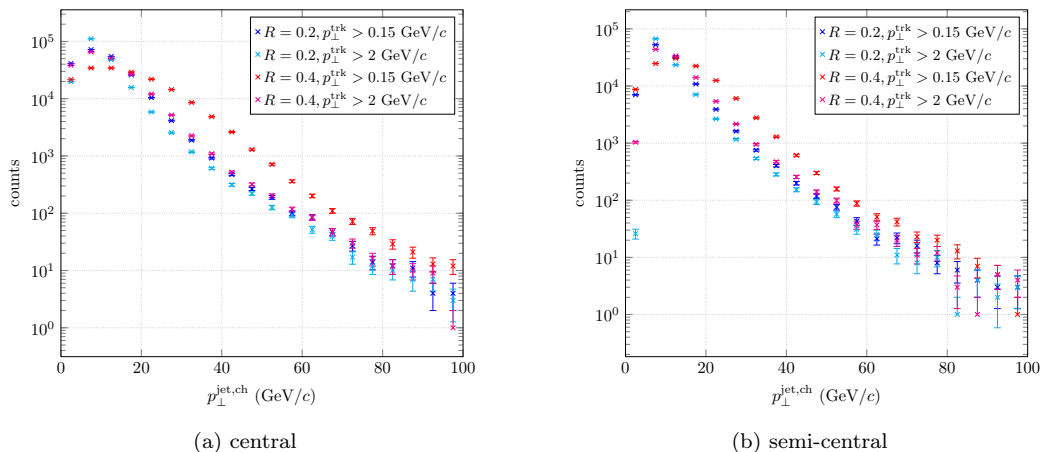


Figure 5.10: Jet p_{\perp} spectra: The plots show the p_{\perp} spectra for jets ($R = 0.2$) after background subtraction for central (left) and semi-central (right) events. In the latter case, only the jets oriented along the event plane are included.

selection of suitable trigger jets. Therefore, we want to use the anti-kt algorithm with a small resolution parameter of $R = 0.2$ and subtract the background estimated from clusterization by a kt algorithm with $R = 0.4$. For comparisons, we will also look at $R = 0.4$ jets. To suppress purely combinatorial jets from the background, we require the leading track to have a p_{\perp} above $6 \text{ GeV}/c$ (leading track bias) and a jet area larger than $0.6 \cdot \pi R^2$. To avoid edge effects from the jet finders, only jets fully contained in the acceptance of the central barrel are considered, i.e. $|\eta^{\text{jet}}| < 0.45$.

Figures 5.10a and 5.10b show the measured jet p_{\perp} spectra in central and semi-central events. For the p_{\perp} interval of the jets to be used as trigger a compromise has to be found. A higher threshold in p_{\perp} results in a smaller contamination by fake jets. On the other hand, the statistics at large p_{\perp} , where the jets are well above the background, is rather limited. In the spectra, we can see an extended bump at low p_{\perp} which arises from the background contributions. To avoid this region, we have to use a p_{\perp} interval above $\sim 30 \text{ GeV}/c$ for $R = 0.2$ and above $\sim 40 \text{ GeV}/c$ for $R = 0.4$. The background contributions can also be reduced by the introduction of a minimum constituent p_{\perp} but this also results in a smaller fraction of the jet p_{\perp} being reconstructed. The fluctuations can also be judged from the width of the δp_{\perp} distributions discussed in Section 3.5. In the following, we will use the lowest sensible p_{\perp} threshold for maximum statistics and discuss the impact of this choice later as a systematic effect.

5.7 Proton identification

Among all potential associates we want to identify the protons. In the considered p_{\perp} range between 2 and 4 GeV/c , both the specific energy loss dE/dx in the TPC and the time of flight from the TOF array are suitable for such a selection. However, crossings of different species occur in the dE/dx measurement at low p . On the other hand, the separation in the time of flight gets smaller for larger momenta. Therefore, the two measurements are combined. We follow a cut-based approach in which a track is either considered as a proton or not. Within ALICE, a common cut variable for a track is defined as the deviation of the measured signal $S(\text{trk})$ from

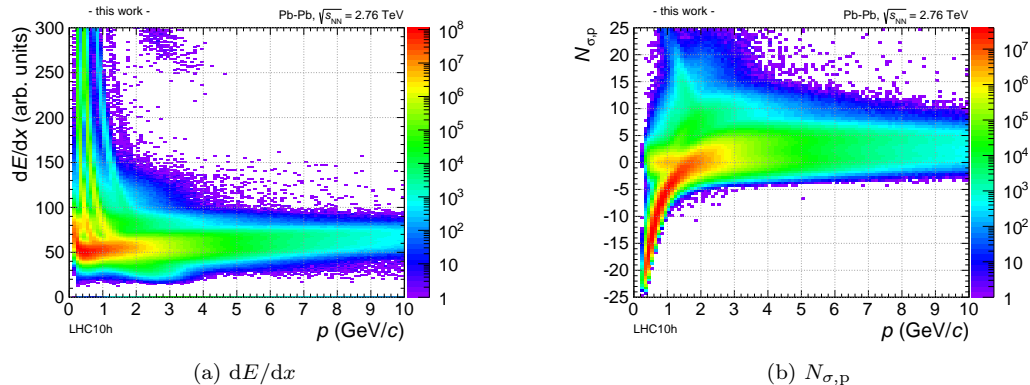


Figure 5.11: Measured specific energy loss dE/dx in the TPC (truncated to 60 %) and resulting $N_{\sigma,p}$ as a function of momentum. $N_{\sigma,p}$ is calculated according to Equation 5.37.

the expectation for a given particle species $\langle S \rangle_p(\text{trk})$, here protons, normalized to the expected resolution $\langle \sigma \rangle_p(\text{trk})$:

$$N_{\sigma,p} := \frac{S(\text{trk}) - \langle S \rangle_p(\text{trk})}{\langle \sigma \rangle_p(\text{trk})} \quad (5.37)$$

where the expectation values depend on the properties of the track, e.g. momentum and the number of TPC clusters. The defined variable $N_{\sigma,p}$ allows for constant cut values for all tracks. The actual signal used depends on the detector. For the TPC it is the specific energy loss dE/dx , for TOF it is the time of flight t_{flight} .

In this analysis, we extract a proton-enhanced sample by cutting on $|N_{\sigma,p}| < 2$ for TPC and TOF. It contains a residual contamination from non-protons. To correct for this, we need to know the efficiencies for protons and other particles to pass the cuts. Details will be discussed in the following.

5.7.1 Specific energy loss

For the TPC, the measured signal is the specific energy loss dE/dx averaged over the contributing clusters (truncated to the lower 60 %). Through geometrical effects and imperfections of the detector, the average $\langle dE/dx \rangle$ and width $\langle \sigma \rangle$ for a given species depend not only on the track momentum but also on η , φ , the number of reconstructed clusters, and the event multiplicity. The measured value is partially corrected for the η and multiplicity dependence [210]. The remaining dependencies are parameterized in the expectation values separately for each data taking period.

The measured dE/dx for all tracks passing the cuts for associated particles (except the p_{\perp} cut) is shown in Figure 5.11a as a function of momentum. Figure 5.11b shows the corresponding distribution of $N_{\sigma,p}$. As expected, the protons are visible as a band around 0. At the lower end of the momentum range of interest to this analysis, i.e. close to 2 GeV/c, a clean separation of protons is complicated with the TPC alone because of the line crossings of other particle species.

While the goal of the N_{σ} approach is to have stable cut conditions, the shape of the distributions resulting for each species is not known a priori since track properties enter in a non-trivial way. For example the expected resolution used for normalization in Equation 5.37 varies track-by-track. Because the respective shapes are needed to extract efficiencies and contamination

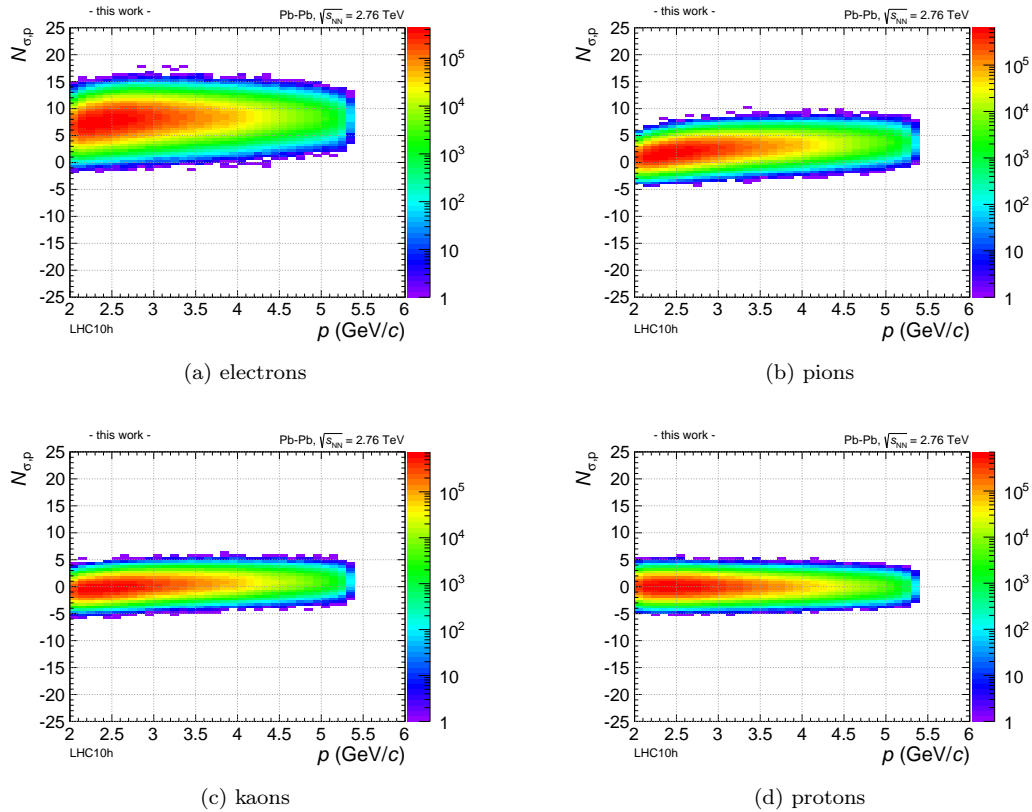


Figure 5.12: TPC $N_{\sigma,p}$ templates for central events. The templates shown are generated according to Equation 5.38, based on all associate candidates.

for the chosen selection cuts they were checked by generating templates. Assuming a correct parameterization of the expected mean and width, a template for the particle species x can be generated as:

$$N_{\sigma,p}^x = \frac{\mathcal{N}(\langle dE/dx \rangle_x(\text{trk}), \langle \sigma \rangle_x(\text{trk})) - \langle dE/dx \rangle_p(\text{trk})}{\langle \sigma \rangle_p(\text{trk})} \quad (5.38)$$

where \mathcal{N} denotes a normally distributed random variable. The required expectation value and width are taken from the parameterization which is already used for the $N_{\sigma,p}$ calculation. It should be noted here that they depend on the properties of the tracks. We use all tracks considered as associate candidates to evaluate the track-dependent parameters. The templates produced for electrons, pions, kaons, and protons in central events are shown in Figure 5.12. Even though the electrons are negligible in the total yield, which is dominated by the other three species, we include them as a benchmark for the method. Because of the limitation to possible associates only the p_{\perp} interval between 2 and 4 GeV/c is populated. This also affects the η distribution in bins of momentum which is used for the $N_{\sigma,p}$ distributions. It should be clarified here that the goal of this procedure was not to extract the expectation values for the dE/dx signal but to check the resulting $N_{\sigma,p}$ variable which is used to cut on.

For the subsequent analysis, we consider momentum slices of 0.5 GeV/c width. The projections of the templates for one slice are shown in Figure 5.13. Because of the multiplicity

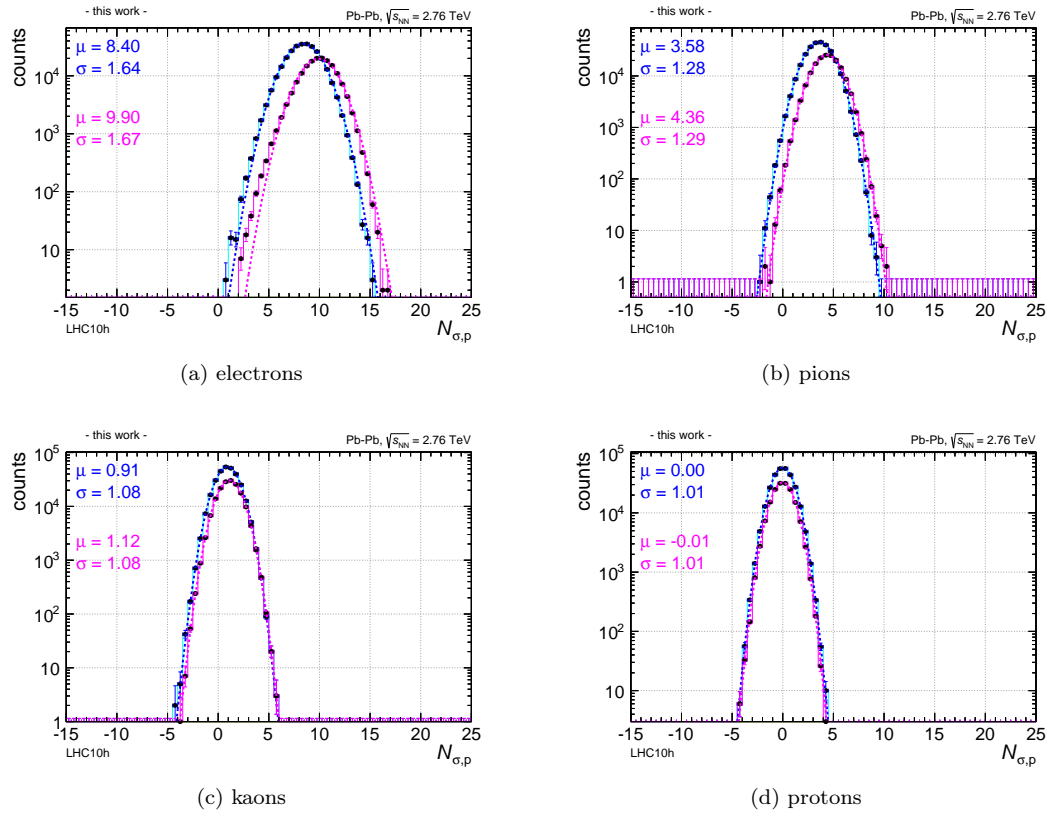


Figure 5.13: TPC $N_{\sigma,p}$ templates projected onto a momentum bin of $4.5 - 5.0 \text{ GeV}/c$. The distributions observed in central (blue) and semi-central (magenta) events deviate and are fitted separately by Gaussians. The resulting Gaussian parameterizations in terms of mean μ and width σ are given in the plots.

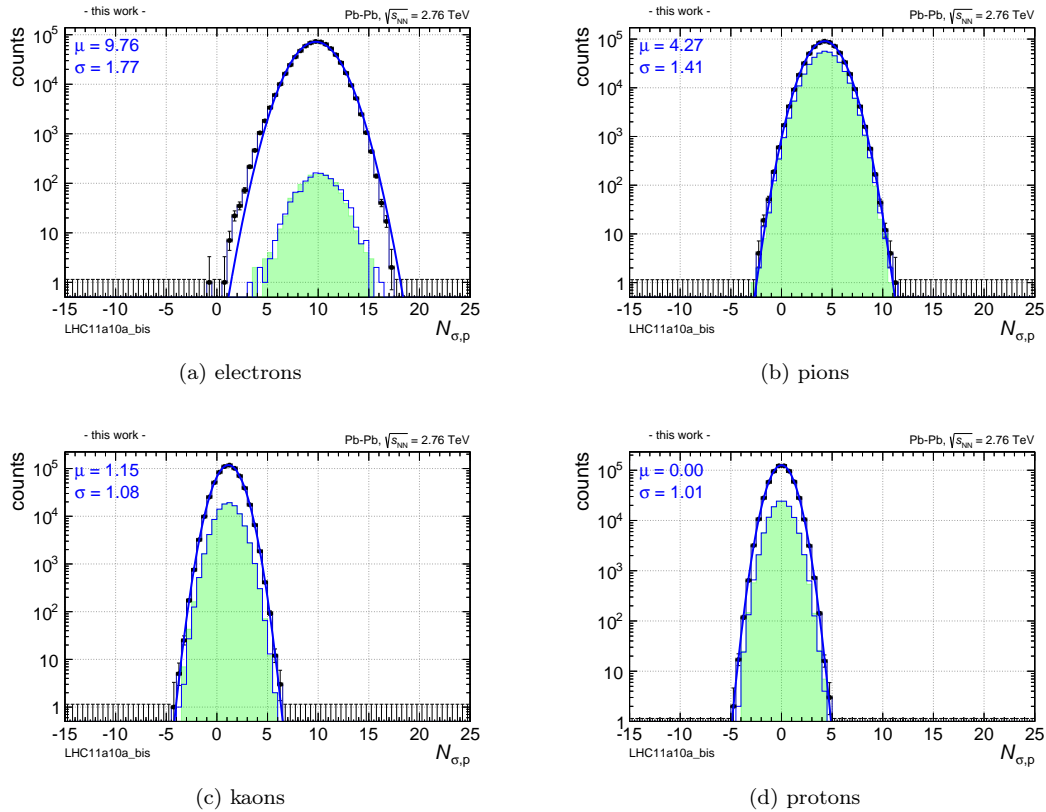


Figure 5.14: Comparison of templates generated from all tracks (data points + blue fit) or only tracks of the same species (thin blue line) to Monte Carlo truth (green), projected to a momentum bin of $4.5 - 5.0$ GeV/c. We find good agreement between the generated templates and the true distribution using Monte Carlo information. The strongest deviations appear for electrons which are rare in number.

dependence of the dE/dx signal we show the projections for central and semi-central events in comparison. Both are fitted by Gaussians which describe the data well. It should be noted here that the distribution for protons is indeed centred at 0 and has a width of 1 which confirms the intended behaviour that cutting on a certain value for N_σ results in an efficiency according to a Gaussian distribution. As the distributions derived for central and semi-central events are not identical, we will treat the event classes separately.

An important question is how these templates are affected by using all tracks, irrespective of species, for their generation. To judge this influence the analysis was run on a Monte Carlo data set (LHC11a10a_bis) for which a comparison of the true signal with templates for all particles and with those restricted to tracks of identical species (Monte Carlo truth) can be performed. Figure 5.14 shows that the templates are very similar for the two cases and also agree with the true Monte Carlo distribution. Therefore, no track pre-selection, other than the track cuts explained above, was applied for the template generation.

Two limitations of this procedure should be mentioned. In sampling a normal distribution with $\mu = \langle dE/dx \rangle_x$ and $\sigma = \langle \sigma \rangle_x$ it is assumed that the signal (after truncation) is Gaussian. It

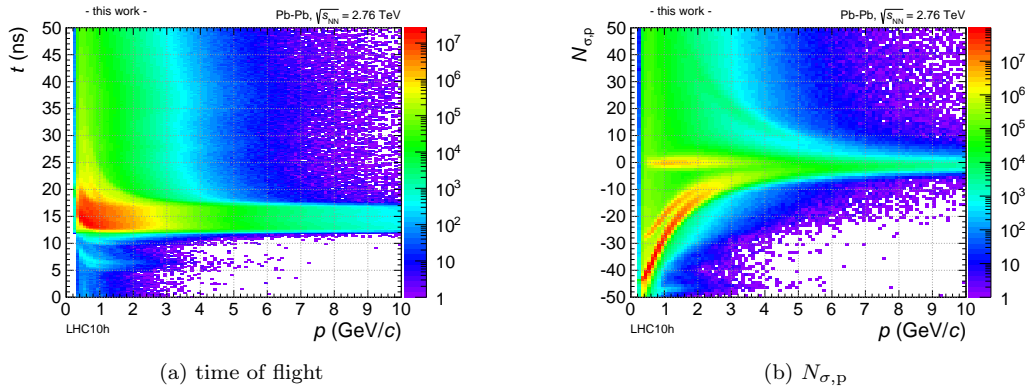


Figure 5.15: The time of flight measured by TOF and the resulting $N_{\sigma,p}$ as a function of momentum. $N_{\sigma,p}$ is calculated according to Equation 5.37.

is known, however, that with very high statistics a tail appears [211, 210]. This could be taken into account by sampling a more complicated probability distribution for the signal generation. The second constraint is that one already needs to have a parameterization for the mean and width of the signals. Given that, the method provides a good check since deviations from the perfect parameterization lead to inconsistencies with the observed distributions (see below).

The efficiency for a given track to pass the 2σ cut depends on the shape of the $N_{\sigma,p}$ distribution and the particle species. For protons, the 2σ cut on the Gaussian distribution around 0 results in the centrality-independent efficiency:

$$\varepsilon_p^{\text{TPC}} = 95 \%. \quad (5.39)$$

For non-protons the probability to pass the cut depends on the relative abundances of the various particle species. Therefore, we will use fits to the measured $N_{\sigma,p}$ distributions in momentum bins to extract the contamination in Section 5.7.3.

5.7.2 Time of flight

The procedure for TOF is very similar to the TPC treatment and the discussion focuses on the differences. The measured signal is the arrival time of a particle relative to the interaction time (with some offset), see Figure 5.15a. The expected signal depends via β on the momentum of a track but also on its trajectory. The path length integrated during the tracking is used to include possible effects of energy loss. Thus, also the expected resolution comprises contributions from the time measurement (σ_{TOF}), the time offset determination (σ_{t_0}), and the track length (σ_{trk}). They are added quadratically:

$$\sigma = \sigma_{\text{TOF}} \oplus \sigma_{t_0} \oplus \sigma_{\text{trk}}. \quad (5.40)$$

For the template generation the signal is sampled around the expectation value with three different components for smearing:

$$N_{\sigma,p} = \frac{\langle \text{TOF} \rangle_{\text{X}}(\text{trk}) + \mathcal{F}(\sigma_{\text{TOF}}) + \mathcal{N}(\sigma_{t_0}) + \mathcal{N}(\sigma_{\text{trk}}) - \langle \text{TOF} \rangle_{\text{P}}(\text{trk})}{\langle \sigma \rangle_{\text{P}}(\text{trk})} \quad (5.41)$$

The signal itself is not symmetric and sampled from a parameterized function \mathcal{F} comprising a Gaussian and a tail towards positive values. We generate templates for pions, kaons, protons,

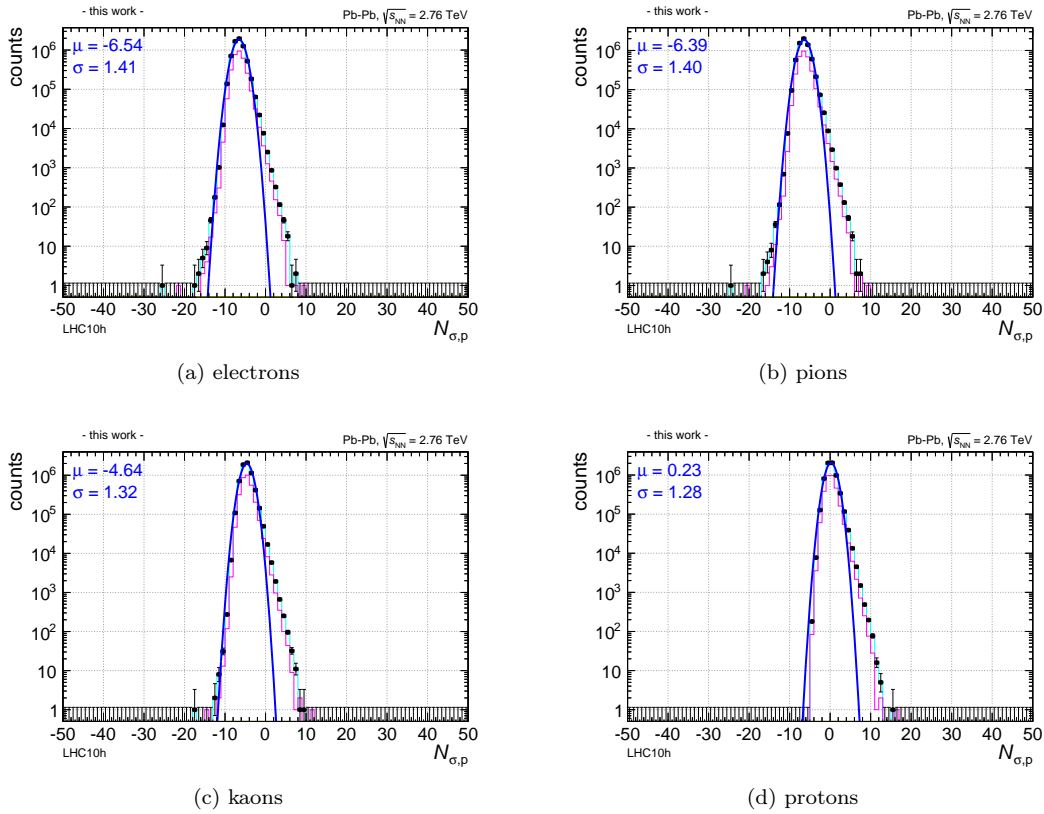


Figure 5.16: TOF $N_{\sigma,p}$ templates projected onto a momentum bin of $3 - 3.5$ GeV/ c . In contrast to the TPC case, the distributions observed in central (cyan) and semi-central (magenta) events agree. The Gaussian fit (blue line) is not suitable to describe the data, instead the distributions are used as templates for the further analysis.

and deuterons, the latter again as benchmark. Also here, a comparison to Monte Carlo was performed and lead to the same conclusion that no pre-selection of tracks is required³.

The templates for one momentum slice are shown as an example in Figure 5.16. In contrast to the measured signal of the TPC no centrality dependence of the templates is observed. The shown Gaussian fits do not describe the distribution well. Consequently, we keep the full templates for later fits. Not being Gaussian, the fraction of protons ending up in the 2σ range is different from 95 %. From integrating over the extracted distribution we obtain an efficiency:

$$\varepsilon_p^{\text{TOF}} = 87 \% \quad (5.42)$$

which is lower than for the TPC because of the tail in the distribution.

In addition to the contributions from different particle species, signals from mismatches in TOF have to be taken into account. These arise from TOF hits which are wrongly assigned to global tracks. We also generate a template for this distribution by randomly sampling from a

³The Monte Carlo data is only used to validate the method. The actual positions of the peaks are different than in data.

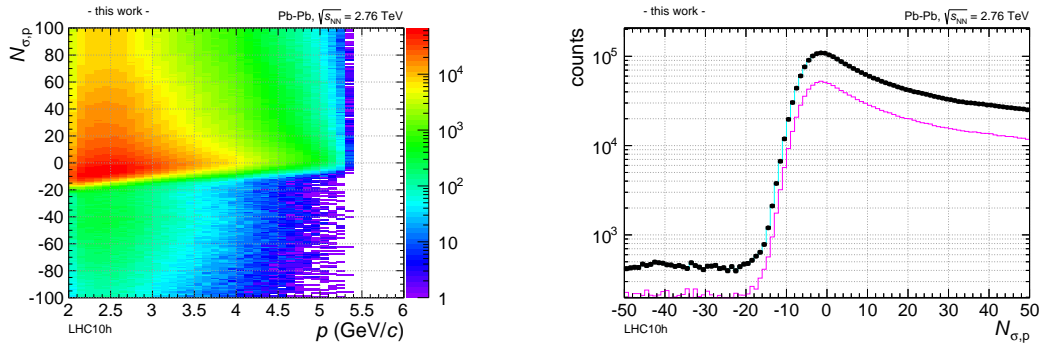


Figure 5.17: TOF mismatches. Left: The template for wrongly assigned TOF hits shows a long tail to large values of $N_{\sigma,p}$. Right: The projection to the momentum bin from 3.0 - 3.5 GeV/ c shows a similar shape for central (black, cyan) and semi-central (magenta) events but the probability is multiplicity dependent.

distribution of t_{flight} measurements, see Figure 5.17. We find the fraction of mismatched tracks in the 2σ interval to be:

$$\varepsilon_{\text{mismatch}}^{\text{TOF}} \simeq 5 \%. \quad (5.43)$$

We will extract the fraction of mismatches from fits to the total $N_{\sigma,p}$ distribution. For this we have to distinguish central and semi-central events because of their difference in multiplicity which changes the probability to assign a wrong hit.

5.7.3 Efficiency and contamination

In order to verify the expected proton efficiencies for the TPC and TOF particle identification cuts, to extract the mismatch fraction in TOF, and to determine the efficiencies for non-protons, we shall use the templates explained before (Gaussians for TPC, full templates for TOF) to fit the measured $N_{\sigma,p}$ distributions in momentum slices of 0.5 GeV/ c width. In every slice, we extract yields for the different particles from Gaussian (TPC) or template (TOF) fits. Only the yields are free parameters for these fits.

To establish the method, we shall first look at results obtained from Monte Carlo simulations, for which the true yields are known. Figure 5.18 shows the fits to the TPC and TOF $N_{\sigma,p}$ distributions in different momentum slices together with those from true Monte Carlo identification. As expected, we find that the separation of species is good in the TPC for large momenta (≥ 3.5 GeV/ c), in TOF for low momenta (≤ 4.0 GeV/ c). We can distinguish the contributions from the considered species. In case of TOF, we see a deviation between the particle templates and the true Monte Carlo distributions. The differences are accounted for by the mismatch contribution which is also fitted and used to determine the mismatch probability (values given in the plots). The values in Monte Carlo do not reproduce the data precisely⁴. For the extraction of yields, we must consider that a certain fraction of the particles is not contained in the respective template but in the mismatch distribution. Therefore, we will introduce corrected yields. We shall denote the fitted yields for a component x , representing a given particle species, by Y_x^{TPC} and Y_x^{TOF} , those restricted to $\pm 2\sigma$ by an additional hat, and those after the 2σ cut on the other

⁴The detector occupancy in Monte Carlo and data is not identical.

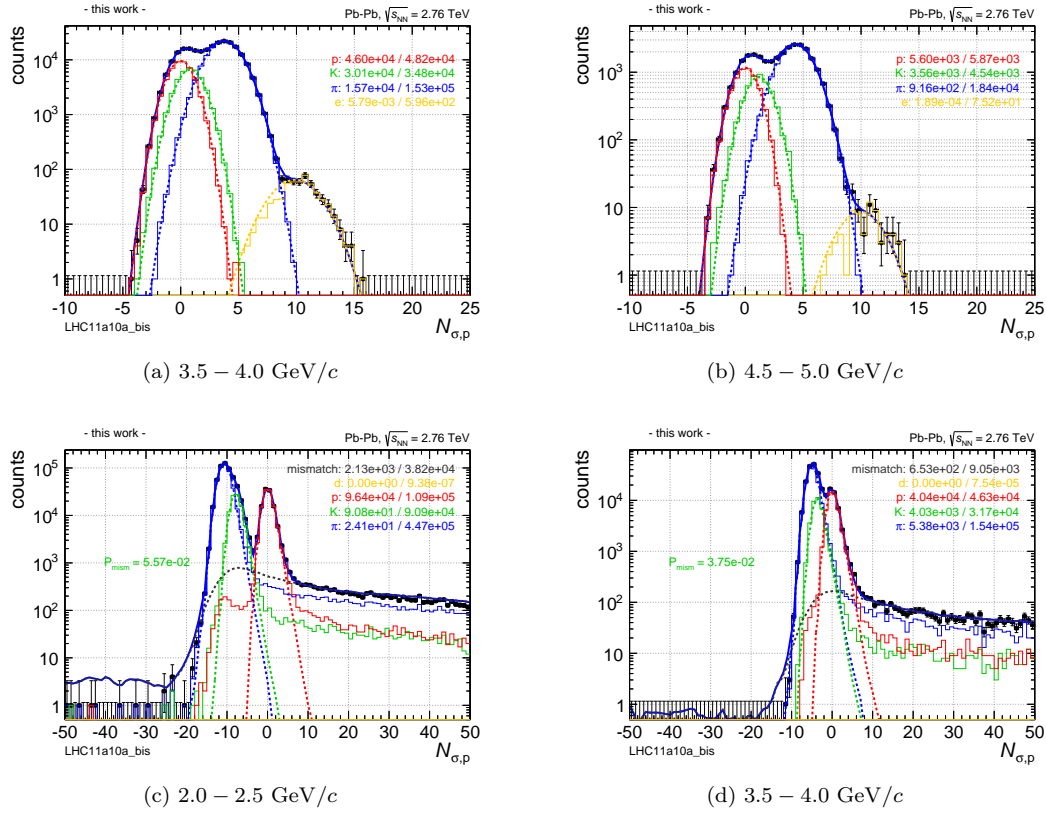


Figure 5.18: Fits of the templates to the observed $N_{\sigma,p}$ distributions in TPC (top) and TOF (bottom). The fits (dashed) are shown for different momentum bins and compared to the true Monte Carlo distributions (solid). The fitted yields for the considered particle species are given in the plot, once within the $\pm 2\sigma$ interval and once inclusively.

detector by Z_x^{TPC} and Z_x^{TOF} . Then, we further introduce for proton (p) and non-proton (np) yields:

$$\Upsilon_p^{\text{TPC}} := Y_p^{\text{TPC}} \quad (5.44)$$

$$\Upsilon_p^{\text{TOF}} := Y_p^{\text{TOF}} + Y_{\text{mismatch}}^{\text{TOF}} \cdot f_p \quad f_p := \frac{Y_p^{\text{TOF}}}{\sum_x Y_x^{\text{TOF}}} \quad (5.45)$$

$$\Theta_p^{\text{TPC}} := Z_p^{\text{TPC}} \quad (5.46)$$

$$\Theta_p^{\text{TOF}} := Z_p^{\text{TOF}} + Z_{\text{mismatch}}^{\text{TOF}} \cdot f'_p \quad f'_p := \frac{Z_p^{\text{TOF}}}{\sum_x Z_x^{\text{TOF}}} \quad (5.47)$$

$$\Upsilon_{\text{np}}^{\text{TPC}} := \sum_{x \neq p} Y_x^{\text{TPC}} \quad (5.48)$$

$$\Upsilon_{\text{np}}^{\text{TOF}} := \sum_{x \neq p} Y_x^{\text{TOF}} + Y_{\text{mismatch}}^{\text{TOF}} \cdot f_{\text{np}}, \quad f_{\text{np}} := \frac{\sum_{x \neq p} Y_x^{\text{TOF}}}{\sum_x Y_x^{\text{TOF}}} \quad (5.49)$$

$$\Theta_{\text{np}}^{\text{TPC}} := \sum_{x \neq p} Z_x^{\text{TPC}} \quad (5.50)$$

$$\Theta_{\text{np}}^{\text{TOF}} := \sum_{x \neq p} Z_x^{\text{TOF}} + Z_{\text{mismatch}}^{\text{TOF}} \cdot f'_{\text{np}}, \quad f'_{\text{np}} := \frac{\sum_{x \neq p} Z_x^{\text{TOF}}}{\sum_x Z_x^{\text{TOF}}} \quad (5.51)$$

where we have added the yields from the mismatch distribution in TOF according to the observed particle fractions. The corresponding hatted versions refer to the yields in the $\pm 2\sigma$ interval. Now, we can use these quantities to calculate the required efficiencies. Before doing so for the data fits, we conclude that the extraction of particle yields by the template fits works well in the p_\perp ranges considered for either detector. The components for the various species are properly recovered by the fits and the method is well-suited for the determination of the required PID efficiencies.

The global fits from data are shown in Figure 5.19 for one momentum slice, the remaining ones are given in Appendix D.3. The yields, as introduced above, are extracted from the fits and listed in Tables D.1 and D.2 for central and semi-central events, respectively. Also in data, we extract the probability for TOF mismatches from these fits and find:

$$P_{\text{mismatch}}^{\text{cent}} \simeq 7.5 \%, \quad P_{\text{mismatch}}^{\text{semi}} \simeq 2.5 \%. \quad (5.52)$$

The average mismatch probability for the considered sample of associates in the given p_\perp range is used.

With the determined mismatch fraction in TOF, we now expect the efficiency of the combined cuts for the protons to be:

$$\varepsilon_p^{\text{cent}} = \varepsilon_p^{\text{TPC}} \cdot ((1 - P_{\text{mismatch}}^{\text{cent}}) \cdot \varepsilon_p^{\text{TOF}} + P_{\text{mismatch}}^{\text{cent}} \cdot \varepsilon_{\text{mismatch}}^{\text{cent}}) \simeq 77 \%, \quad (5.53)$$

$$\varepsilon_p^{\text{semi}} = \varepsilon_p^{\text{TPC}} \cdot ((1 - P_{\text{mismatch}}^{\text{semi}}) \cdot \varepsilon_p^{\text{TOF}} + P_{\text{mismatch}}^{\text{semi}} \cdot \varepsilon_{\text{mismatch}}^{\text{cent}}) \simeq 81 \%. \quad (5.54)$$

To check these efficiencies in data we compare to results from the extracted yields (the values for semi-central events will be given in parentheses). In fact, we can fit the $N_{\sigma,p}$ distributions before and after applying the cut on the other detector. This allows to verify the efficiencies by comparing to the value from the detector-internal fits. For the TPC cut for protons, we compare the yield in the TOF proton template after and before the TPC cut was applied, i.e.

$$\varepsilon^{\text{TPC}} = \frac{\Theta_p^{\text{TOF}}}{\Upsilon_p^{\text{TOF}}} \simeq 95.5 \text{ (94.5) } \% \quad (p \leq 4 \text{ GeV}/c). \quad (5.55)$$

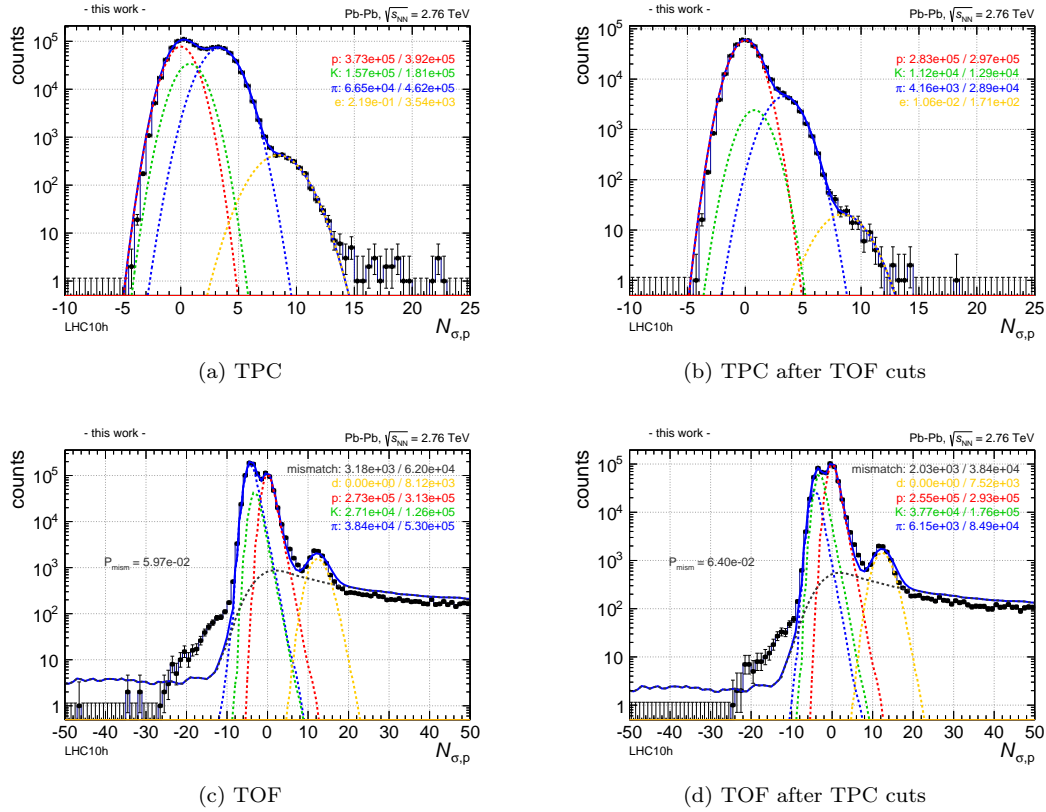


Figure 5.19: Global fits to the TPC (top) and TOF (bottom) $N_{\sigma,p}$ distributions in the momentum range of $4.0 - 4.5$ GeV/ c in central collisions before (left) and after (right) the 2σ -cut around the proton hypothesis of the other distribution (TOF/TPC). In all cases the yields in the interval $[-2, 2]$ and over the full range are calculated and listed in the plots.

which is consistent with the value of 95 % expected for a Gaussian distribution within 1 %. The other way around we can check the TOF cut and find:

$$\varepsilon^{\text{TOF}} = \frac{\Theta_{\text{p}}^{\text{TPC}}}{\Upsilon_{\text{p}}^{\text{TPC}}} \simeq 75 \text{ (78) \%} \quad (p \geq 3.5 \text{ GeV}/c). \quad (5.56)$$

This value should be compared to the fraction of the TOF template lying within $\pm 2\sigma$ while taking into account the mismatch probability, i.e. 81 (85) % for central (semi-central) events. So, the extracted values are below the expectation by 6 – 7 %.

We can also compare the overall efficiencies:

$$\varepsilon_{\text{p}} = \frac{\widehat{\Theta}_{\text{p}}^{\text{TOF}}}{\Upsilon_{\text{p}}^{\text{TOF}}} \simeq 78.2 \text{ (81.2) \%} \quad (p \leq 4.0 \text{ GeV}/c), \quad (5.57)$$

$$\varepsilon_{\text{p}} = \frac{\widehat{\Theta}_{\text{p}}^{\text{TPC}}}{\Upsilon_{\text{p}}^{\text{TPC}}} \simeq 71.4 \text{ (74.2) \%} \quad (p \geq 3.5 \text{ GeV}/c). \quad (5.58)$$

Consistent with the previous findings, the value obtained from the TPC fits is a bit lower than the expectation of 77 (81) %. We assign conservative uncertainties to the efficiencies for protons to pass the TPC and TOF cuts:

$$\Delta\varepsilon_{\text{p}} = \pm 10 \text{ (10) \%}. \quad (5.59)$$

For non-protons the efficiency depends on the particle composition and we cannot start from a simple expectation. Instead, we must count how many non-protons end up in the 2σ interval around 0 in every momentum bin. We can again calculate the values in multiple ways:

$$\varepsilon_{\text{np}}^{\text{TPC}} = \frac{\Theta_{\text{np}}^{\text{TOF}}}{\Upsilon_{\text{np}}^{\text{TOF}}} = 63.5 \text{ (52.6) \%} \quad (p \leq 4.0 \text{ GeV}/c), \quad (5.60)$$

$$\varepsilon_{\text{np}}^{\text{TPC}} = \frac{\widehat{\Upsilon}_{\text{np}}^{\text{TPC}}}{\Upsilon_{\text{np}}^{\text{TPC}}} = 36.8 \text{ (29.0) \%} \quad (p \geq 3.5 \text{ GeV}/c). \quad (5.61)$$

We can also use the fits from one detector while cutting on the other one. With the mismatch probability unaffected by the TPC cut, we do not have to explicitly include the mismatch component here:

$$\varepsilon_{\text{np}}^{\text{TOF}} = \frac{\widehat{\Upsilon}_{\text{np}}^{\text{TOF}}}{\Upsilon_{\text{np}}^{\text{TOF}}} = 1.0 \text{ (0.9) \%} \quad (p \leq 4.0 \text{ GeV}/c), \quad (5.62)$$

$$\varepsilon_{\text{np}}^{\text{TOF}} = \frac{\Theta_{\text{np}}^{\text{TPC}}}{\Upsilon_{\text{np}}^{\text{TPC}}} = 4.4 \text{ (6.6) \%} \quad (p \geq 3.5 \text{ GeV}/c). \quad (5.63)$$

We could use the two ways for cross-checking but we have to keep in mind that the separation and, thus, rejection changes with momentum. For the efficiency of the simultaneous cuts we obtain:

$$\varepsilon_{\text{np}} = \frac{\widehat{\Theta}_{\text{np}}^{\text{TOF}}}{\Upsilon_{\text{np}}^{\text{TOF}}} = 0.7 \text{ (0.6) \%} \quad (p \leq 4.0 \text{ GeV}/c), \quad (5.64)$$

$$\varepsilon_{\text{np}} = \frac{\widehat{\Theta}_{\text{np}}^{\text{TPC}}}{\Upsilon_{\text{np}}^{\text{TPC}}} = 1.4 \text{ (3.2) \%} \quad (p \geq 3.5 \text{ GeV}/c). \quad (5.65)$$

Finally, we find the weighted average values over all momentum bins:

$$0.8 \text{ (0.8) \%}. \quad (5.66)$$

We assign the uncertainties as:

$$\Delta\varepsilon_{\text{np}} = \pm 1 \text{ \%}. \quad (5.67)$$

These efficiencies give the probability for a non-proton with the kinematic and species distributions as in the candidate sample to pass the proton cuts⁵.

5.8 Correlation functions

Having discussed all the ingredients, we can finally look at the actual measurement. We shall go through all the steps for the hadron-triggered correlations first. In this case, we have sufficient statistics resulting in less fluctuating data points which facilitates the explanations.

In the analysis, we accumulate pair distributions $N_{\text{pair}}(\Delta\eta, \Delta\varphi)$ with $\Delta\eta$ and $\Delta\varphi$ calculated for each considered combination of a trigger ($p_{\perp} \in [6, 8]$ GeV/ c) and associate ($p_{\perp} \in [2, 4]$ GeV/ c) particle. In a second case, we restrict the associates to those identified as protons. The same particles are used as triggers. Dividing the pair distributions by the number of triggers we arrive at the so-called per-trigger yields, however, uncorrected for detector acceptance and efficiency. Figure 5.20 shows the inclusive and proton-identified data for the events classified as central (0 - 10 %) and semi-central (30 - 50 %) events. The distributions exhibit some clear structures. In all cases, the distribution has a triangular shape in $\Delta\eta$. This arises from the limited η -acceptance of the detector. Another distinct feature is the peak around (0,0) which arises as the so-called near-side peak of a jet as we shall discuss later. For the central events, the distribution is fairly flat otherwise — which was the motivation to choose cuts yielding a flat azimuthal distribution for the trigger particles. For the semi-central events, we see an additional azimuthal modulation which is caused by flow and the requirement for the trigger particle to be oriented along the event plane.

Before addressing the unwanted trivial correlations (from single particle inhomogeneities) in the pair distributions we have to consider that the sample for identified protons contains some contamination from non-protons. Using the suppression factors determined in Section 5.7.3, we can extract the pair distributions for clean protons as:

$$N_{\text{p}}(\Delta\eta, \Delta\varphi) = \frac{N_{\text{pid}}(\Delta\eta, \Delta\varphi) - \varepsilon_{\text{np}}N_{\text{inc}}(\Delta\eta, \Delta\varphi)}{\varepsilon_{\text{p}} - \varepsilon_{\text{np}}} \quad (5.68)$$

Here, we have assumed the suppression factors to be constant in $\Delta\eta$ and $\Delta\varphi$. The extracted proton distributions are shown in Figure 5.21. We see the same structures as discussed above for the inclusive case.

We could also extract the non-proton pairs:

$$N_{\text{np}} = \frac{N_{\text{pid}} - \varepsilon_{\text{p}}N_{\text{inc}}}{\varepsilon_{\text{np}} - \varepsilon_{\text{p}}} \quad (5.69)$$

for comparison with the proton pairs. However, we will prefer comparing the distribution for identified protons to the inclusive one to avoid having PID uncertainties in both distributions.

⁵Extracting the values only for the non-protons which are used as associate would be more correct but also more involved.

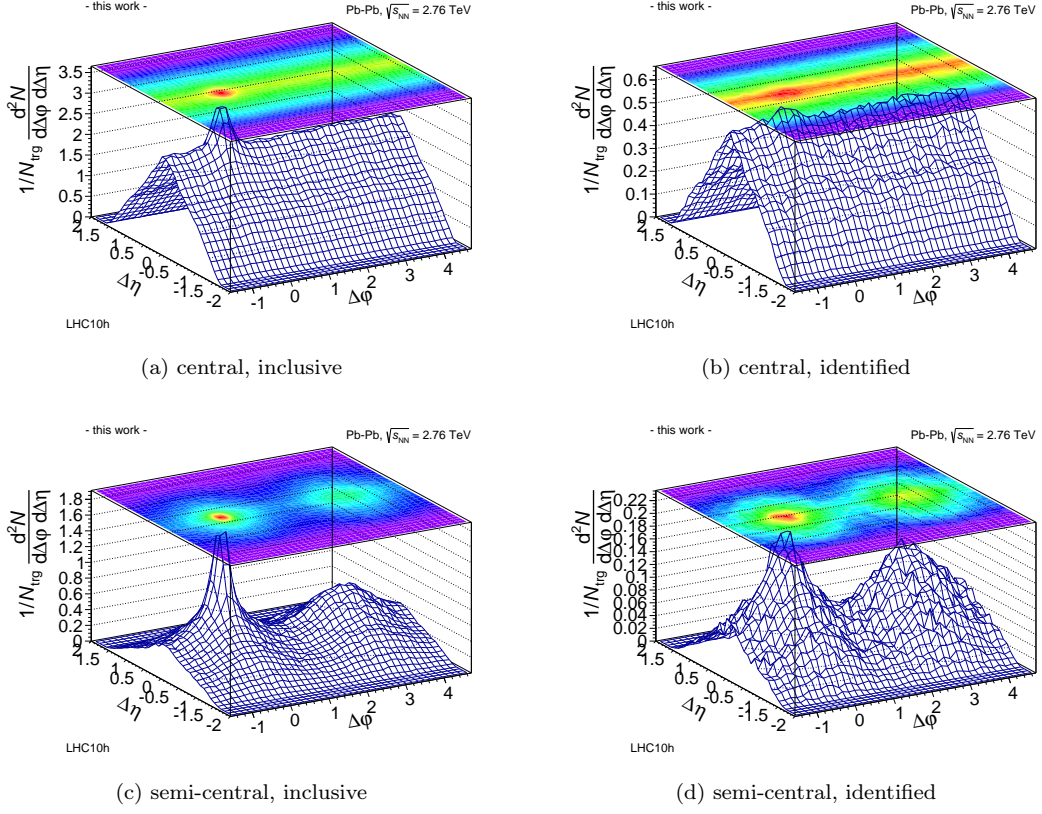


Figure 5.20: Raw per-trigger yields for hadron triggers and inclusive or identified associates: The transverse momentum is required to be between $6 - 8$ GeV/ c for the trigger and between $2 - 4$ GeV/ c for the associate particles.

In order to remove the correlations due to detector imperfections, we also accumulate the pair distributions for triggers and associates from different events. Every trigger particle is combined with associates from a number of different events which are similar in global parameters. We classify events according to centrality and the z -position of the primary vertex:

- centrality: (0, 2, 4, 6, 8, 10, 30, 32, 34, 36, 38, 40, 42, 44, 46, 48, 50, 90) %
- z -position primary vertex: (-10, -8, -6, -4, -2, 0, 2, 4, 6, 8, 10) cm

In every mixing class we store up to 10 000 tracks from previous events in a ring buffer. The distribution from event mixing contains the correlations induced by inhomogeneities of acceptance and efficiency but none from true physics. We extract the mixed event distributions for protons in the same way as discussed above. Indeed, Figure 5.22 shows the same triangular shape in $\Delta\eta$, hardly any modulation in $\Delta\phi$, and no near-side jet peak. In fact, a small dip at $(0, 0)$ is caused by the two track cut.

Finally, we can divide the same and mixed event distributions. We impose a fixed normal-

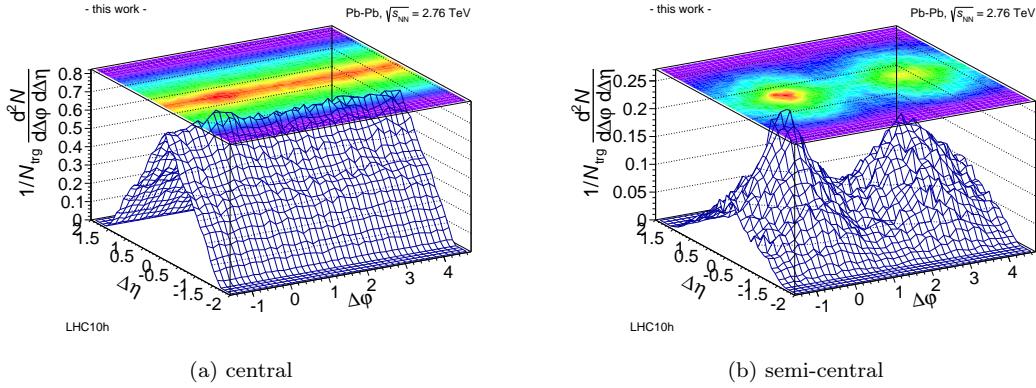


Figure 5.21: Raw per-trigger yields for hadron triggers and associated protons: The transverse momentum is required to be between 6 – 8 GeV/ c for the trigger and between 2 – 4 GeV/ c for the associate particles.

ization to arrive at the correlation function:

$$C(\Delta\eta, \Delta\varphi) := \frac{N_{\text{mixed}}}{N_{\text{same}}} \cdot \frac{N_{\text{pair}}^{\text{same}}(\Delta\eta, \Delta\varphi)}{N_{\text{pair}}^{\text{mixed}}(\Delta\eta, \Delta\varphi)}. \quad (5.70)$$

If we had corrected the individual distributions for single track efficiencies, we could extract per-trigger yields. For the extraction of the shape, which was our primary interest, this is not required. The correlation function is shown in Figure 5.23 for the two event classes and associates. Most notably, the triangular shape in $\Delta\eta$ was turned flat by the same/mixed correction. In all cases, we can now clearly see a peak at $(0, 0)$. It is caused by particles produced in association with the trigger. This is exactly the expectation for a jet which consists of a spray of particles close in η and φ . For the central events, it is difficult to make out further features in this view. In the semi-central case, we still see a modulation in $\Delta\varphi$, which is not due to detector effects and survives the same/mixed correction.

For the further discussion, we shall limit ourselves to azimuthal correlations because of the statistics limitation in the jet-triggered case. To arrive at the azimuthal correlation function, we project the same and mixed pair distributions for inclusive and proton associates to $\Delta\varphi$ and divide them. As before we impose a normalization:

$$C(\Delta\varphi) := \frac{N_{\text{mixed}}}{N_{\text{same}}} \cdot \frac{N_{\text{pair}}^{\text{same}}(\Delta\varphi)}{N_{\text{pair}}^{\text{mixed}}(\Delta\varphi)}. \quad (5.71)$$

Figure 5.24 shows the same and mixed event distributions together with the extracted correlation function. In the plots, we show the statistical uncertainties arising from the bin-wise counting for the pair distributions.

In the azimuthal view, some more features become visible. Compared with the inclusive case, the near-side peak is less pronounced for protons. This is expected from the lower proton fraction in jets as compared to the bulk properties. On the away-side (azimuthally opposite to the trigger jet) there is a broad peak. It has contributions from the away-side jet and flow. It is very similar for the inclusive and the proton case.

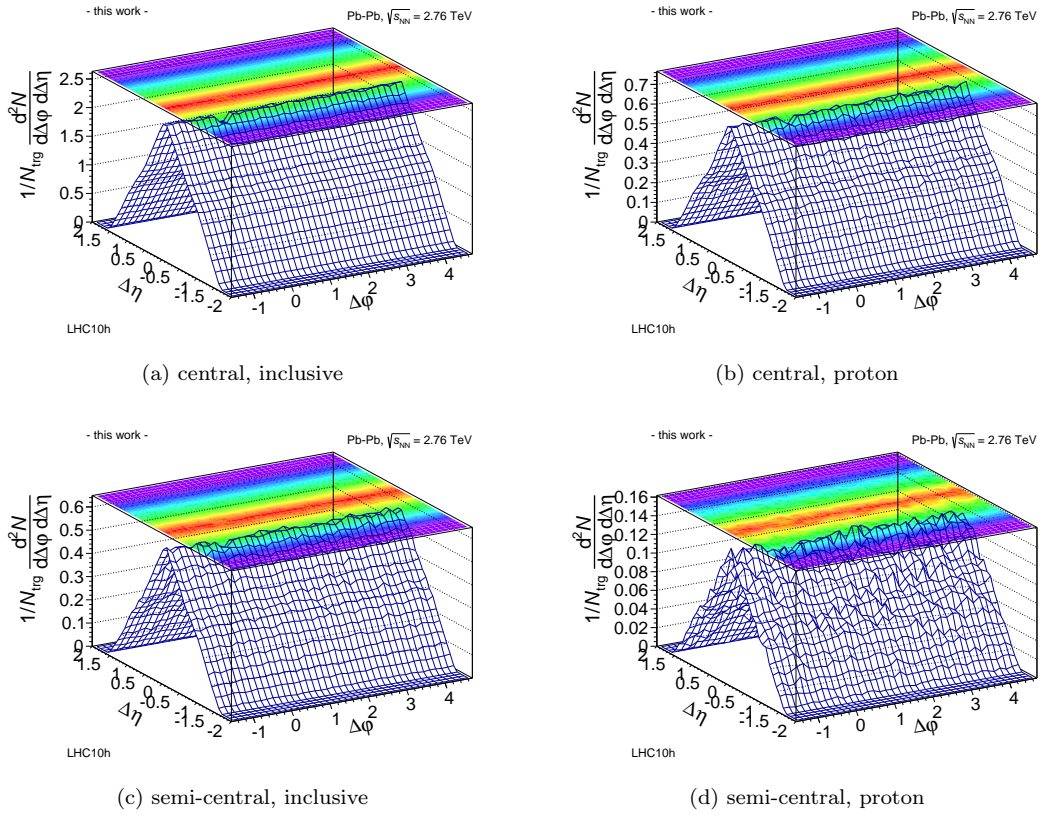


Figure 5.22: Raw per-trigger yields for hadron triggers and inclusive or proton associates from mixed events: The transverse momentum is required to be between $6 - 8 \text{ GeV}/c$ for the trigger and between $2 - 4 \text{ GeV}/c$ for the associate particles. The trigger particle is combined with associates from a number of other events in the same mixing class.

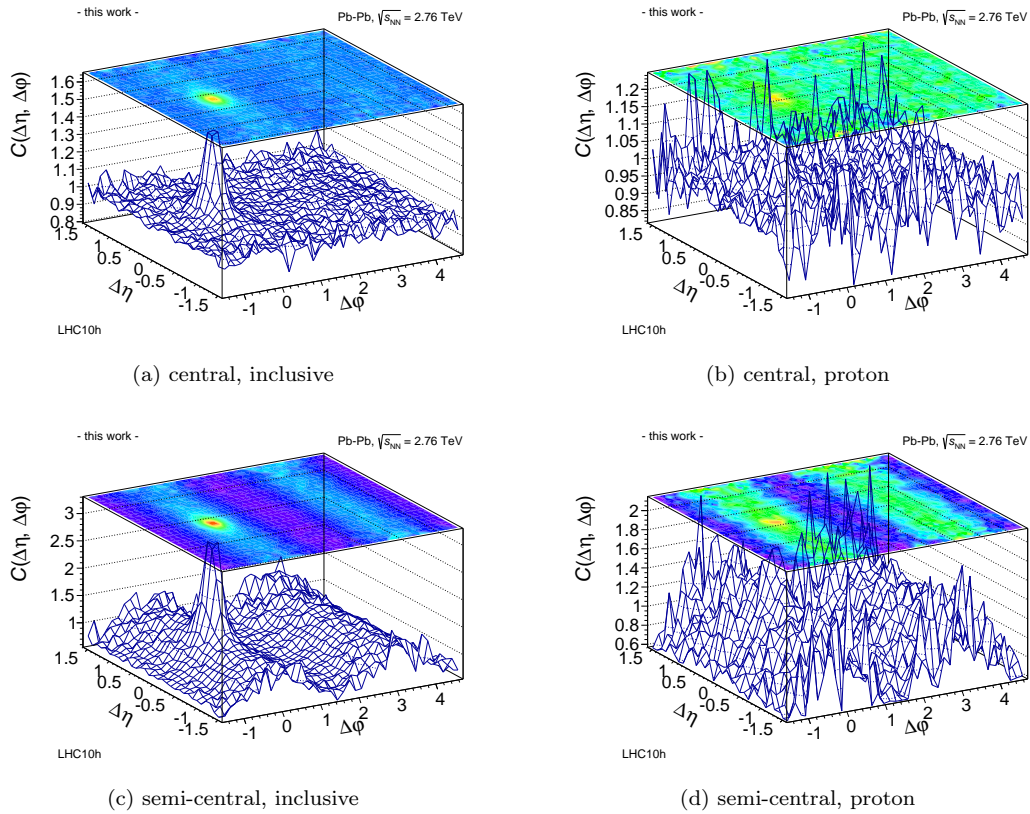


Figure 5.23: Correlation functions $(\Delta\eta, \Delta\phi)$ for hadron triggers and inclusive or proton associates: The transverse momentum is required to be between $6 - 8 \text{ GeV}/c$ for the trigger and between $2 - 4 \text{ GeV}/c$ for the associate particles.

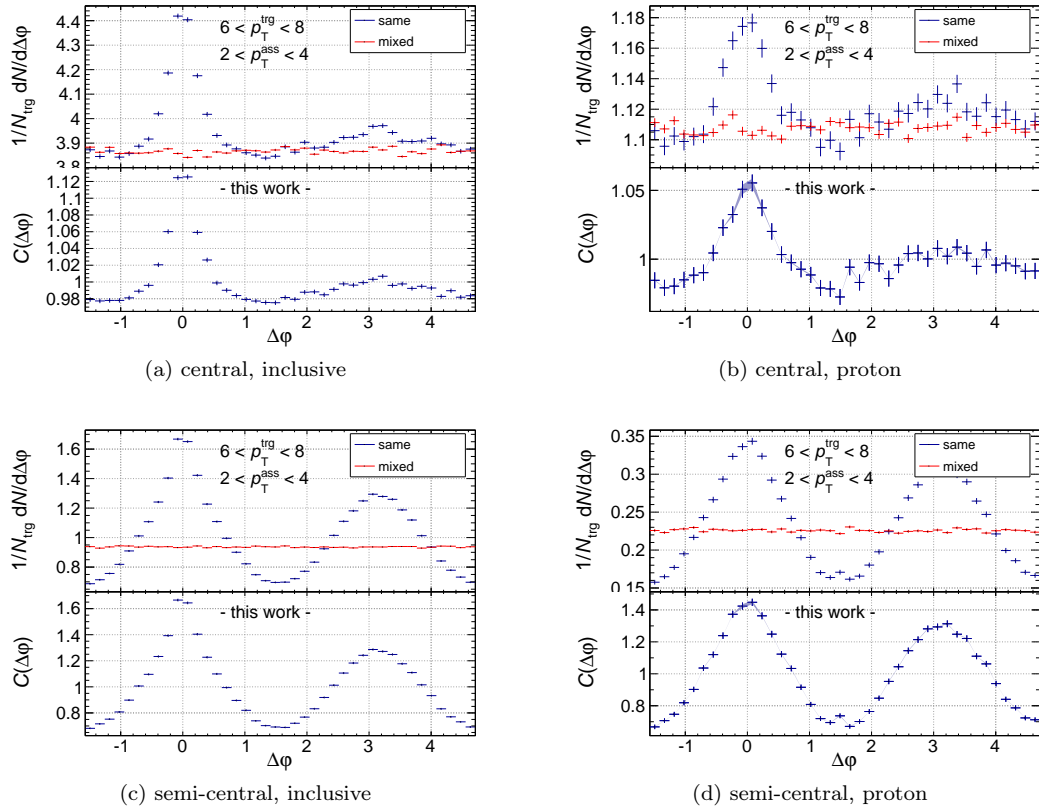


Figure 5.24: Azimuthal correlation functions for hadron triggers and inclusive or proton associates: The transverse momentum is required to be between $6 - 8 \text{ GeV}/c$ for the trigger and between $2 - 4 \text{ GeV}/c$ for the associate particles. For the associated protons, the blue band shows the change of the central values on varying the assumed PID efficiency, see Section 5.9.3.

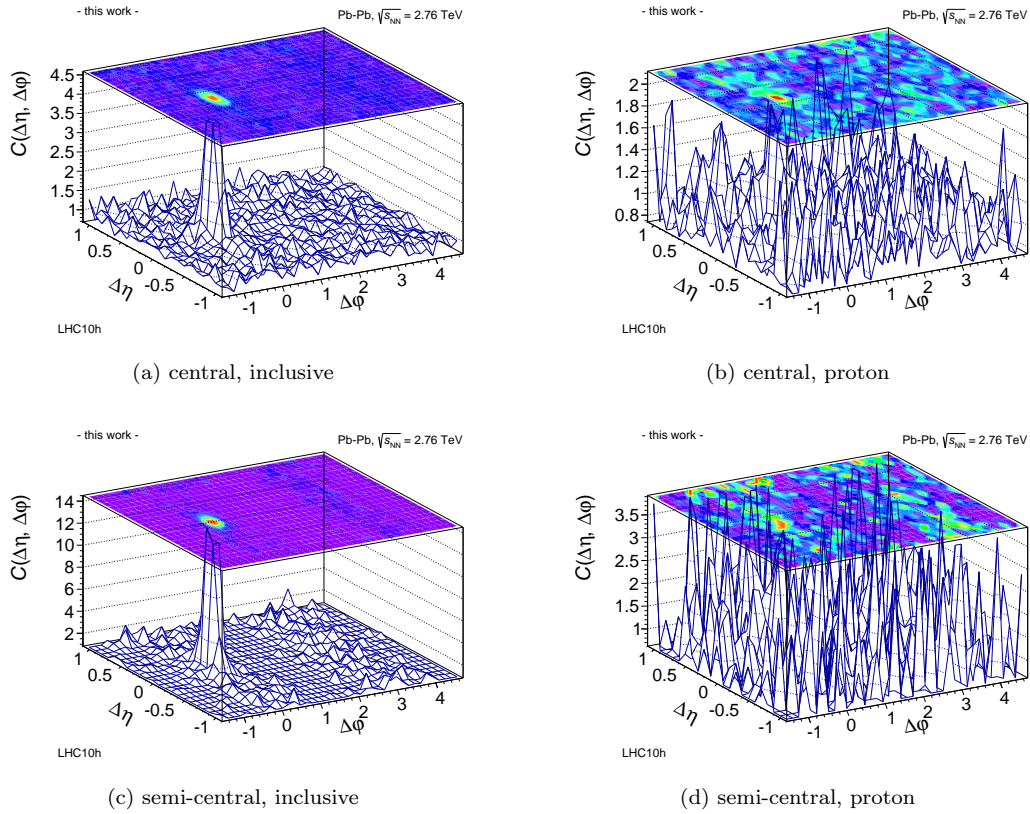


Figure 5.25: Correlation functions ($\Delta\eta, \Delta\phi$) for jet ($R = 0.2$) triggers and inclusive or proton associates: The transverse momentum is required to be between $30 - 80$ GeV/ c for the trigger and between $2 - 4$ GeV/ c for the associate particles.

Now, we use exactly the same procedure with jets as triggers. Without repeating the individual steps, Figure 5.25 shows the 2-dimensional correlation function. The smaller coverage in $\Delta\eta$ arises from the more restrictive η cut on the individual jets. We see similar features as for the hadron triggers, but with more limited statistics since the trigger requirement is stricter. Again, we also look at the azimuthal distribution in Figure 5.26. Compared with the hadron-triggered distributions, the jet-related near-side peak is now more pronounced. This is expected from the stronger requirement of a jet comprising multiple constituents. Also around $\Delta\phi = \pi$ an enhanced correlation is observed which can also be explained by the stronger bias from the trigger requirement. As before, the distributions for associated protons show a less prominent near-side peak. Otherwise, they are very similar.

Finally, we can compare the correlation functions for associated hadrons and protons, see Figure 5.27. We clearly see the reduced proton yield in the near-side peak around $\Delta\phi = 0$. Elsewhere, the ratio is flat for the hadron triggers. For the jets, the ratio shows some low points but no significant deviation from flatness can be claimed with the available statistics.

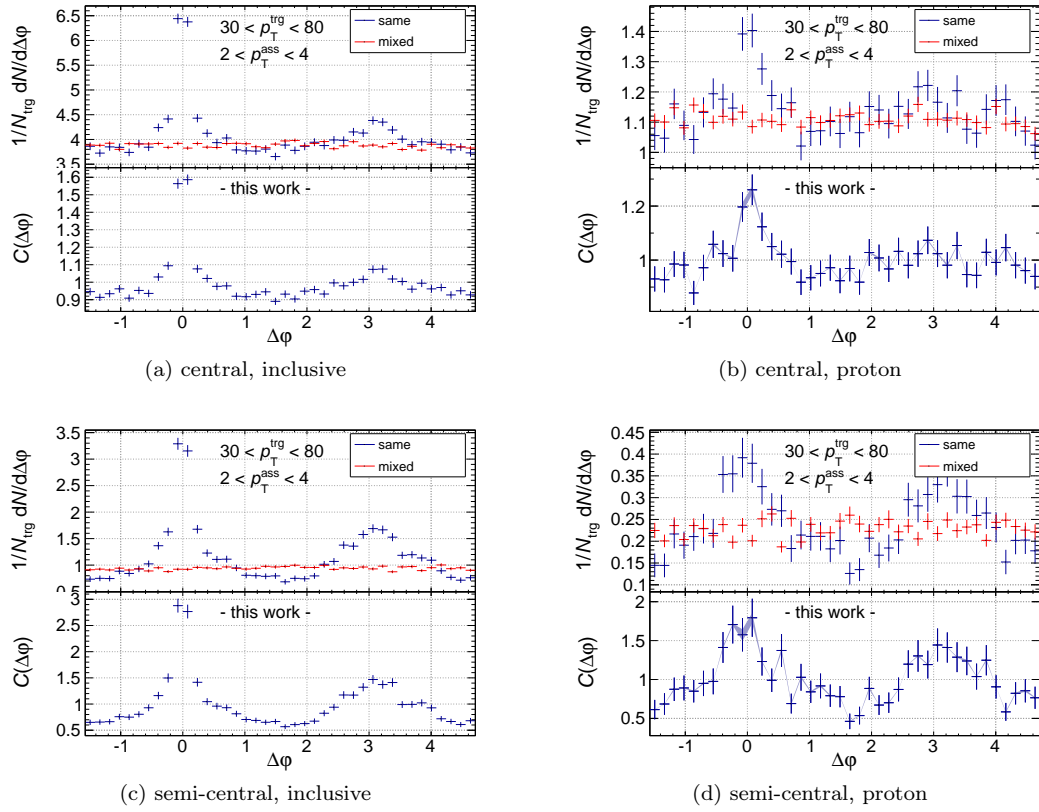


Figure 5.26: Azimuthal correlation functions for jet ($R = 0.2$) triggers and inclusive or proton associates: The transverse momentum is required to be between 30 – 80 GeV/ c for the trigger and between 2 – 4 GeV/ c for the associate particles. For the associated protons, the blue band shows the change of the central values on varying the PID efficiency, see Section 5.9.3.

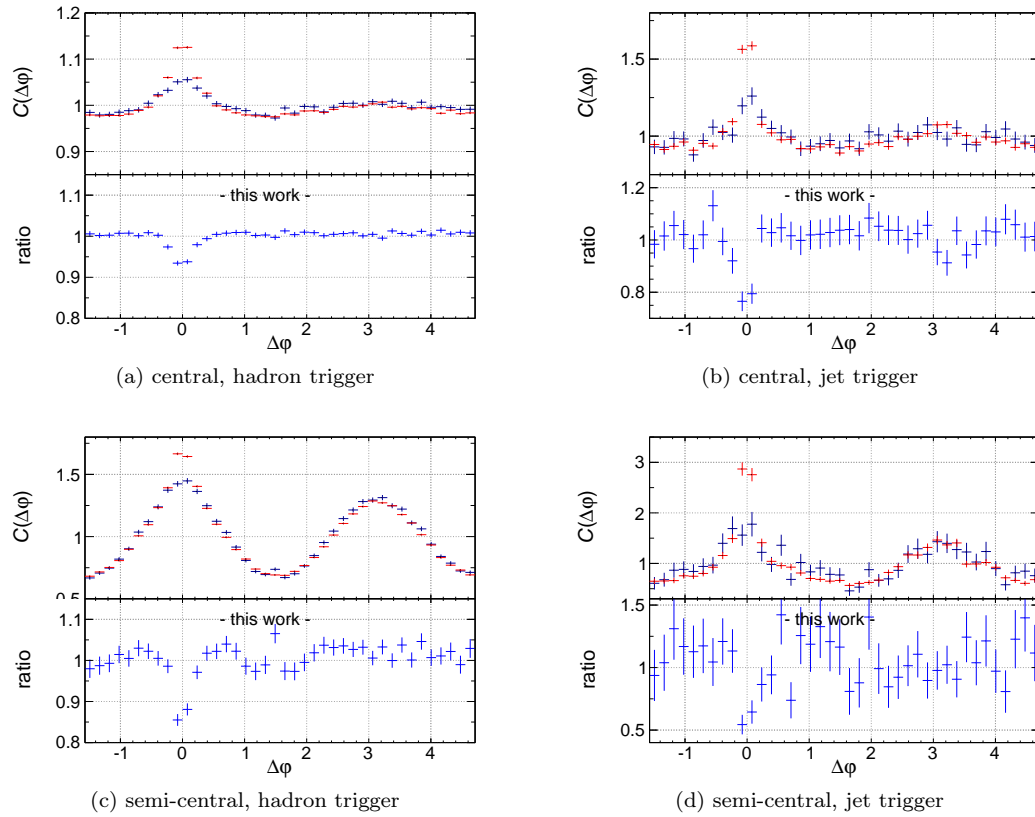


Figure 5.27: Comparison of correlation functions with associated hadrons (red) and protons (blue): Hadrons (left) and jets (right) triggers are used in central (top) and semi-central (bottom) events. Only the statistical uncertainties are shown, which are dominant on the away-side.

5.9 Systematic effects

In the discussion so far, we have shown statistical uncertainties only. Of course, there are also sources of systematic uncertainties, of which the most important ones will be discussed here.

5.9.1 Jet selection

Firstly, the selection of jets by the transverse momentum after background subtraction suffers from the large heavy-ion background. Jets can be found in purely combinatorial background, see Section 5.6. Even though the cuts were chosen to suppress these, a certain fraction passes them and enters the correlation function. The obvious solution of requiring higher p_{\perp} has to be paid by the resulting reduction of available statistics. Thus, a compromise has to be found here. Furthermore, a jet reconstructed with a certain p_{\perp} is more likely to arise from a lower true p_{\perp} with upwards fluctuations in the background than vice versa. These effects can be studied by embedding jets into background of a heavy-ion collision and comparing the results of the reconstruction procedure with the true input. This has not been done yet and limits the comparability of the results. In order to judge the importance of the effect, we compare the correlation functions extracted for different intervals of the jet p_{\perp} , see Figure 5.28. We distinguish jets of different radii. In all cases, we find the correlation functions in agreement with each other within the statistical uncertainties. Therefore, we conclude that the jet p_{\perp} interval used here indeed results in a meaningful selection of trigger jets.

5.9.2 Flow-induced effects

So far, we have not accounted for a part of the correlation function introduced by the correlation of the trigger particle with the event plane and flow of the associated particles. The impact is particularly important in the semi-central event class for which, in addition, we impose a selection criterion for the azimuthal trigger orientation. For the extraction of the purely jet-related correlation the flow-induced component must be subtracted.

We can emulate the effect by placing an artificial particle in the event, randomly sampling the azimuthal distribution with respect to the event plane. This requires the knowledge of the trigger correlation with the event plane v_2 . We use the following values for the considered trigger p_{\perp} range according to previous measurements [194, 212, 213]:

$$\text{central: } v_2^{\text{jet}} = 0.10 \qquad v_2^{\text{had}} = 0.04, \qquad (5.72)$$

$$\text{semi-central: } v_2^{\text{jet}} = 0.10 \qquad v_2^{\text{had}} = 0.10. \qquad (5.73)$$

We compensate the finite event plane resolution by increasing the modulation for the trigger placement by a factor $1/R$. The value for R is obtained from the spline interpolation for the centrality of a given event, see Section 5.4.3.

Having placed the artificial trigger particle in the event, we can correlate it with the associate candidates from the true event. It does not carry a jet-like correlation, but the flow component with the particle composition. Then, we can use the same procedure as before and extract a flow-only correlation function. For central events, we obtain a very small modulation in $C(\Delta\varphi)$. For semi-central events, the effect of flow is large. It should be remembered here that only jets oriented along the event plane are used as trigger, which enhances the impact of flow. We now compare the measurement to the flow-only expectation obtained by the procedure explained above. For this purpose we show the ratio in Figure 5.29. In case of hadrons as trigger, we find flow to account for most of the modulation, the only non-flow structure being the near-side jet peak. In case of jets, we also have a significant contribution of flow but still a small additional

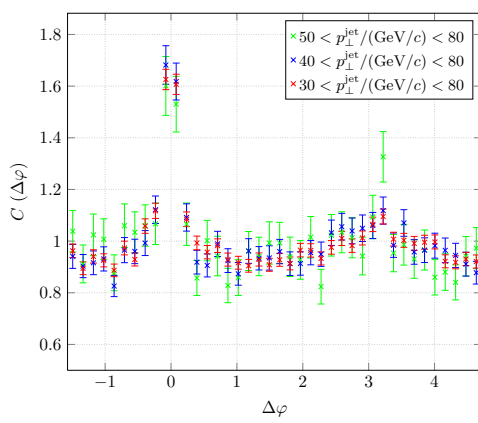
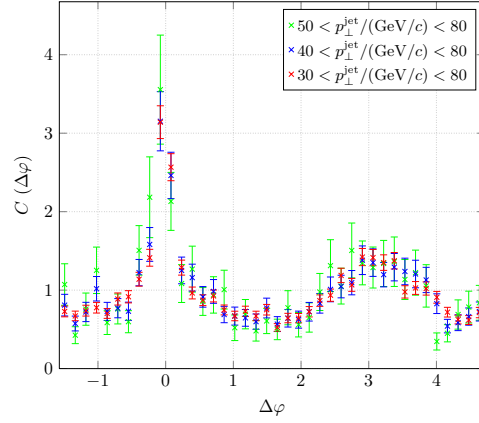
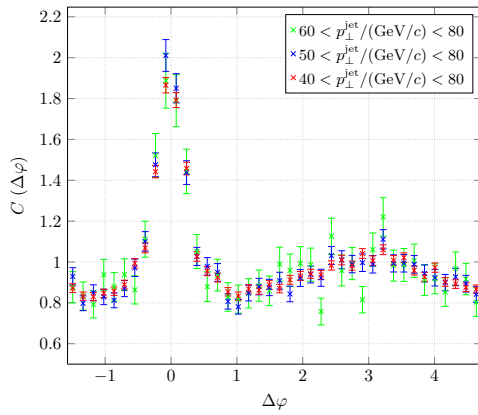
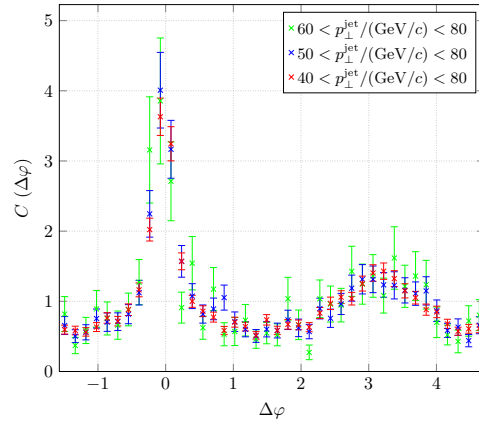
(a) central, $R = 0.2$ (b) semi-central, $R = 0.2$ (c) central, $R = 0.4$ (d) semi-central, $R = 0.4$

Figure 5.28: Jet-hadron correlation functions for different jet p_{\perp} intervals: The azimuthal correlation functions observed for different jet- p_{\perp} thresholds are compared for central (left) and semi-central (right) events, with $R = 0.2$ (top) and $R = 0.4$ (bottom).

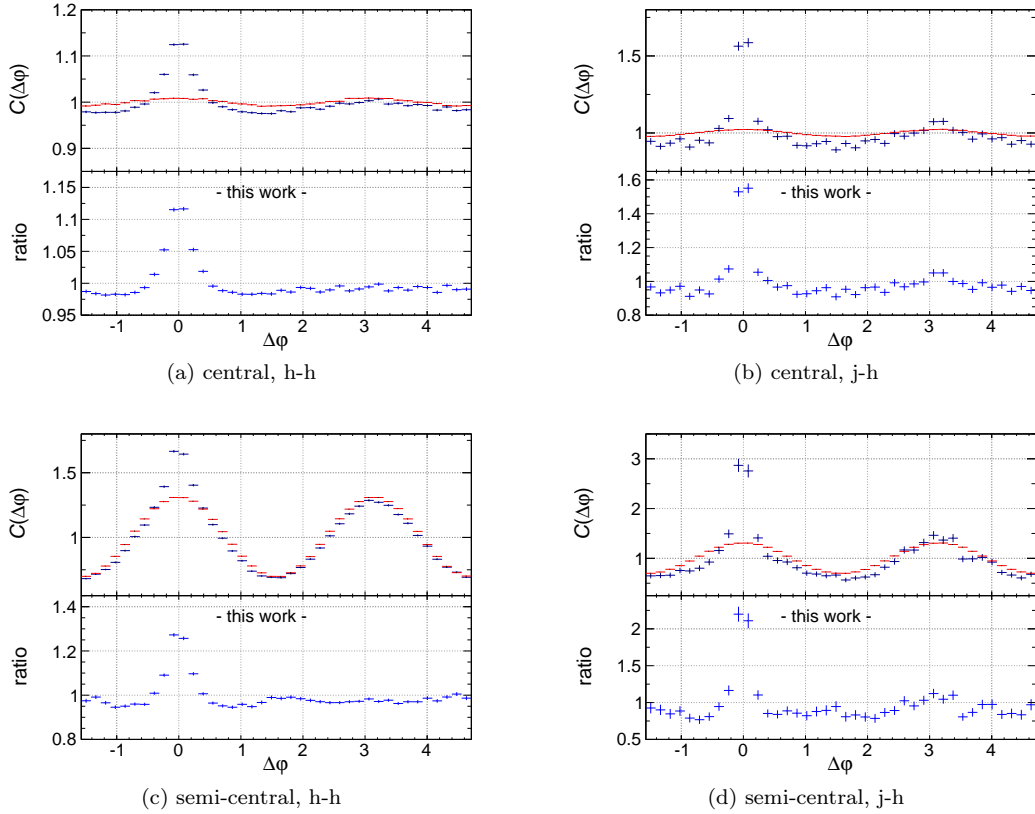


Figure 5.29: Comparison of the observed correlation (blue) with the expectation of flow only (red). The latter is symmetric and does not show jet peaks on the near- and away-side.

yield on the away-side. With the stronger bias of requiring a jet as trigger, this can be understood as the result of the back-to-back jet topology.

5.9.3 Proton identification

We judge the sensitivity of the extracted distributions for associated protons to the efficiencies by varying their values. The used range is motivated by the discussion in Section 5.7.3. We have for central and semi-central events the following efficiencies for protons (p) and non-protons (np) to pass the PID cuts:

$$\begin{array}{lll} \text{central:} & \varepsilon_p = (77 \pm 10) \% & \varepsilon_{np} = (1 \pm 1) \%, \\ \text{semi-central:} & \varepsilon_p = (81 \pm 10) \% & \varepsilon_{np} = (1 \pm 1) \%. \end{array}$$

The efficiencies shall be varied within the stated uncertainties for the evaluation of systematic effects. We use the p_\perp integrated efficiencies derived for all associate candidates and, hence, representing the correct p_\perp distribution. The effect is shown in the figures for identified protons as blue band. Being very similar to the inclusive case, the correlation functions for associated protons are hardly affected on the away-side.

5.9.4 Tracking efficiency

The lack of a single track efficiency correction can influence the measured correlation if both the efficiencies are not flat and the correlation changes with kinematic variables, e.g. with p_{\perp} . For the momentum ranges considered in this analysis the tracking efficiencies and also the matching efficiency to TOF are already saturated. Therefore, the correction was not implemented here. It shall be done in order to arrive at per-trigger yields which carry more information than the correlation functions.

5.10 Interpretation

In order to assess the impact of a possible Mach cone signal on the measured correlation function, we perform an analysis with a signal added from a toy Monte Carlo implementation. It is based on the simple idea that a fast parton traversing the medium should result in additional particle production inside a disc around the direction of flight [204, 205]. This can be realized by artificially placing excess particles in the event. We shall first discuss this simple modelling and then use it for comparison with data.

For the direction of the trigger particle or jet, we use the same random placement as for the previous study of the flow-induced correlation, i.e. with a v_2 -modulation relative to the event plane. In addition to correlating this trigger particle with the associates from the event, we now add particles as an artificial signal. Following the previously explained idea of a possible medium response, we first select the direction of the quenched jet. We assume it to be uncorrelated in pseudo-rapidity but enforce it to be within $|\eta| < 0.8$. In the azimuthal angle φ , we smear the back-to-back direction by a Gaussian of width $\sigma = 0.2$. Then, we place n particles homogeneously in a disc around this direction. n is sampled from a Poissonian distribution with mean \bar{N} . The fraction of particles embedded as protons is chosen according to the ratio observed for the respective event. In total, this results in the correlation from flow and the simulated medium response on the away-side of a trigger particle or jet. The latter remains invisible since we do not add particles around the trigger direction – our focus is on the medium response on the away-side. Also the jet-like fragmentation on the away-side is neglected here.

Technically, we use the excess particles to fill a separate pair histogram (same event) in $\Delta\eta$ and $\Delta\varphi$ as for the real measurement. Thus, we obtain the correlation from the modelled medium response alone. We can still scale the effect at this stage without re-running the full analysis. The histograms from the flow study are reused to account for the correlation with the remainder of the event, i.e. we add the two same-event pair distributions. The correction by mixed event division is done as before. Figure 5.30 shows the correlation in $\Delta\eta$ and $\Delta\varphi$ for flow and an added signal of $\bar{N} = 0.5$ in central and semi-central events. We see the azimuthal modulation from flow, which is much more pronounced for semi-central events. From the excess particles, we observe an additional band on top of the sinusoidal modulation around $\Delta\varphi = \pi$. Since we did not impose any correlation in η , it extends over all $\Delta\eta$.

For comparison with data, we look at the projections to $\Delta\varphi$, see Figure 5.31. First, we compare the measured correlation function with the expectation from the toy Monte Carlo. By construction, there is no near-side peak for the model and the away-side peak only accounts for possible excess particles. It is characterized by a sharper edge than the flow contribution. The average addition of $\bar{N} = 0.5$ detected particles between 2 and 4 GeV/c results in an away-side peak of about 10 % for central events. For a quantitative statement on the agreement, we calculate the χ^2 and the resulting p -value for the deviations between measurement and model (using the statistical uncertainties from the correlation functions). We limit ourselves to the away-side region $\frac{\pi}{2} \leq \Delta\varphi < \frac{3\pi}{2}$ and allow for a scaling of the modelled correlation function. The

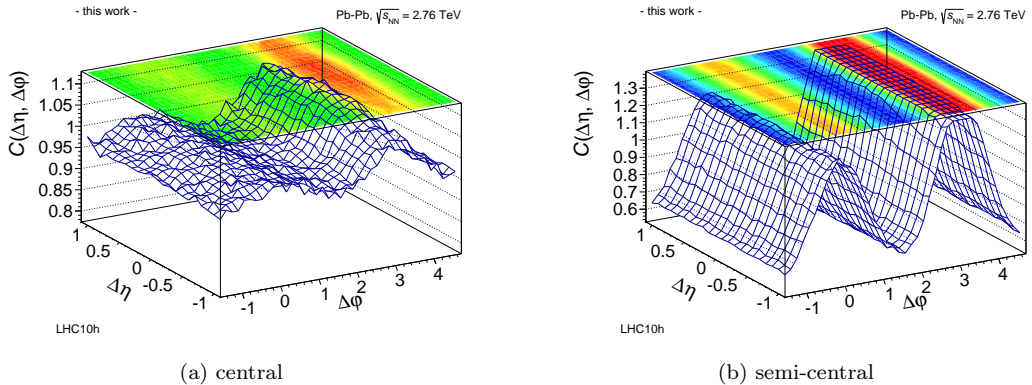


Figure 5.30: $\Delta\eta$ - $\Delta\phi$ correlations from toy Monte Carlo: The correlation functions show the contributions from flow and the excess particles. No jet-like component is added and, thus, no near-side peak is produced.

latter is required because the neglect of the near-side peak changes the normalization. For the jet-hadron correlations in central events, we find a small χ^2 and a resulting large p -value. For associated protons, the uncertainties are significantly larger and the calculated p -value is even higher.

For a clearer view on the suggested away-side excess, we scale the medium response (not the flow part) and calculate the p -values for different signal strengths, see Figure 5.32. In the presence of an away-side peak, we find $\bar{N} = 0$ to be disfavoured. For central events, the highest p -value is obtained for a slightly smaller excess than our choice $\bar{N} = 0.5$, with a quick drop off towards larger values. Thus, the correlations of jets and hadrons in central events favour an excess of about 0.4 particles. In semi-central events, we have a similar picture with lower overall values — there are some outliers in the measured correlation functions.

We have to conclude that the measured distribution is consistent with the model for $\bar{N} = 0.5$. Yet, we have to be careful on the interpretation and remember the neglect of jet fragmentation in the simplistic modelling. Thus, we cannot conclude on the presence of a Mach cone because we cannot uniquely attribute the away-side peak to the medium response. Rather do we have to consider its origin in the fragmentation of a recoil jet. For a medium response, the proton abundance should be the same as everywhere else in the bulk and the effect on the correlation should be the same as for hadrons. For a jet, we expect a significantly lower proton abundance and, thus, a reduced excess in the correlation function. Therefore, we again calculate the p -values for different scalings of the medium response into protons, see Figure 5.32. For central events, we find the favoured value to be lower but, with the analysed statistics, we cannot reject the hypothesis of the same response either — or any other in the considered range of scaling factors from 0 to 2.

In order to achieve the same significance of the model comparison for associated protons as we have now for the inclusive case, we need the same number of correlated pairs. Since about a quarter of the associated particles are protons, we would need about four times more events than analysed now. This is within reach using the data set from the 2011 Pb–Pb run, provided that the particle identification is under control and the events from the different run groups are merged. However, a clear separation of a medium response from jet fragmentation would require a significant result on the excess in the jet-proton correlation function.

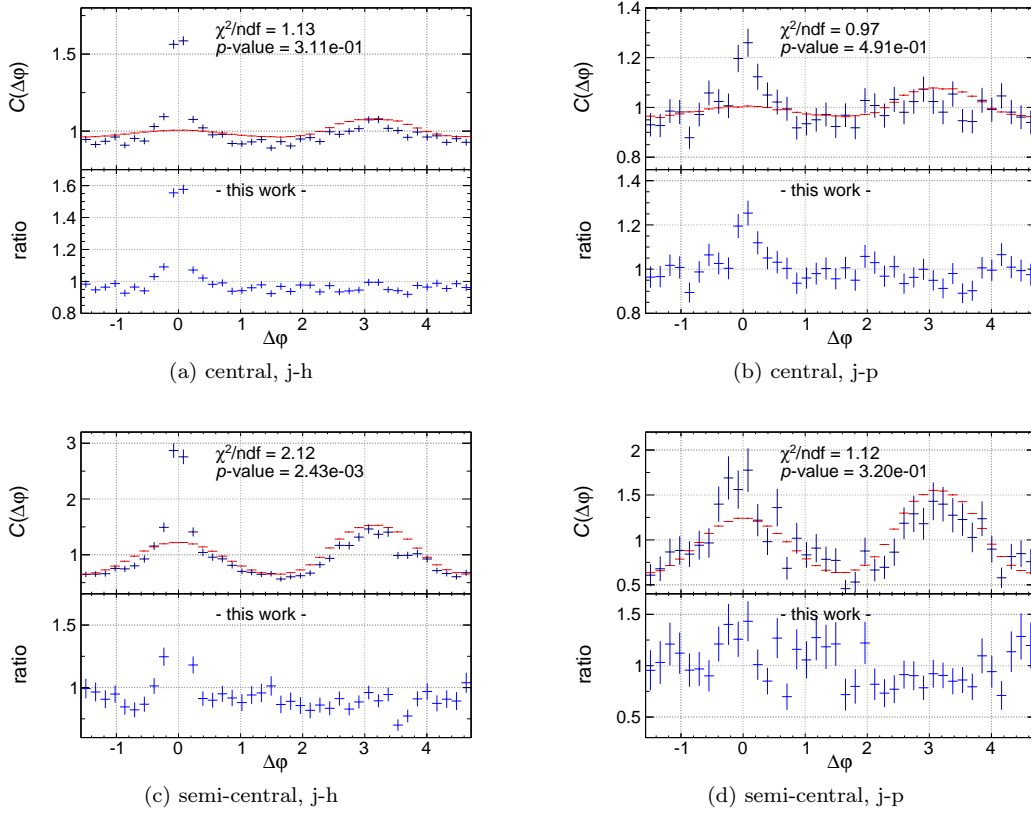


Figure 5.31: Comparison of measured correlation function (blue) with toy Monte Carlo model (red): Since no jet-like correlation was included in the model agreement cannot be expected on the near-side. On the away-side, the excess would have to be separated from the other components (flow and jet fragmentation).

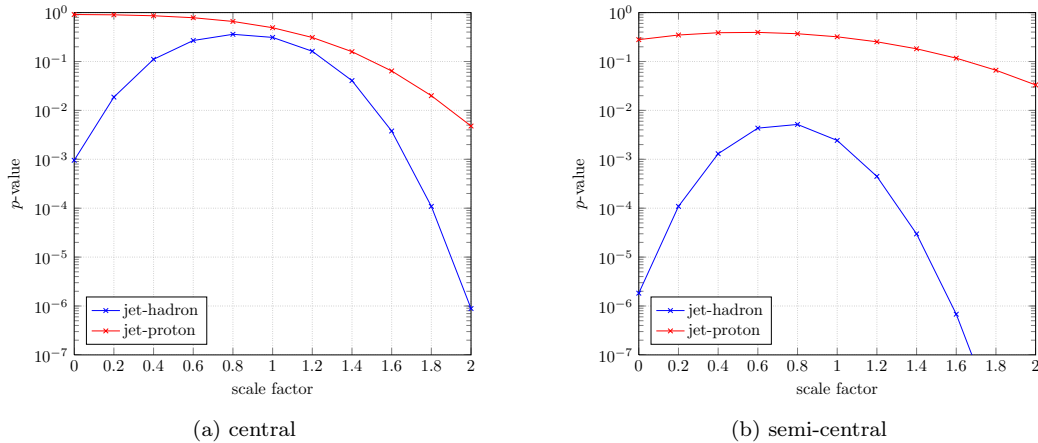


Figure 5.32: p -values for different strengths of the embedded signal. We scale the excess particles by the given factor and calculate the p -value to obtain the measured correlation function.

5.11 Conclusions

A highly energetic parton traversing the dense Quark-Gluon Plasma created in a heavy-ion collision is expected to induce a medium response, for which the emergence of a Mach cone was predicted. We have studied the correlations of high- p_{\perp} jets and associated hadrons to look for such an effect. In azimuth, the near-side peak is dominated by the jet. Our focus rests on the away-side, where the medium response is expected to contribute. The particle yield should consist of an admixture of the products from medium hadronization and the fragmentation of the recoil jet. The different proton abundance in jet and medium hadronization motivates the comparison of jet-hadron with jet-proton correlations.

We have designed an analysis which exploits the unique PID capabilities of ALICE to measure correlation functions of jets associated with hadrons and protons. It is targeted at the data from Pb-Pb collisions collected by ALICE. We have shown the results for the 2010 run only. First, we have discussed the steps for hadron-triggered (6 - 8 GeV/ c) correlations, for which more statistics is available. For associated hadrons (2 - 4 GeV/ c), we see a pronounced near-side peak. With the still soft p_{\perp} requirement on the trigger hadron, no clear away-side peak emerges beyond the flow-induced effect. We have further extracted the correlation function for associated protons, which are identified as such by cuts on the deviation of the TPC and TOF signals from the proton hypothesis ($N_{\sigma,p}$). A self-consistent method was established to check the efficiency and contamination of this selection procedure. The selection efficiencies depend crucially on a good parameterization of the detector response. For associated protons, we find a less pronounced near-side peak as was expected from the lower proton fraction in jets. On the away-side the correlation functions with associated hadrons and protons are found to be very similar. This limits the sensitivity of the away-side measurement to the PID efficiencies.

When using jets as trigger, the p_{\perp} threshold has to be chosen high enough to suppress jets dominated by combinatorial background. We use anti-kt jets above 30 GeV/ c with $R = 0.2$ as the small radius reduces the impact of the underlying event background. Still, statistics becomes a severe limitation. In the correlation functions, we now see an even more pronounced near-side peak, again lower for associated protons. We can also identify an away-side peak on top of the

flow-induced correlation. Here, the shape for hadrons and protons is again found to be very similar.

In order to judge the size of a possible effect, a simplistic toy Monte Carlo model was used to simulate an artificial signal on top of the flow-induced background. We find the observed correlation to be consistent with additional particle yield on the away-side, but it cannot be uniquely attributed to the response of the medium. A reduced proton content is favoured by the measured correlation functions, but we cannot discriminate between a medium-like or jet-like proton content with the available statistics. The additional statistics from the 2011 data should allow to achieve the same uncertainties for protons as we have seen now for hadrons, but still require control over the TPC PID and the changing running conditions. Discriminating between a medium-like and jet-like proton abundance might still be at the edge of the available statistics as the proton sample is not free of jet fragmentation, and the hadron sample not free of medium hadronization. An increase in statistics would further allow a stronger bias of the jet sample by raising the p_{\perp} threshold.

Based on the findings presented here, many improvements are possible and planned. With the measurement of correlation functions we are limited to comparisons in shape. An obvious improvement shall come from the transition to per-trigger yields, for which the tracking efficiencies have to be corrected. And while we have shown the influence of flow on the observed correlation, the contribution to the yield could be subtracted then. The knowledge of v_2 for the triggers is crucial, of course. For jets, this has been measured by ATLAS and ALICE [212, 213]. As the contribution from v_3 is similar in size, it should also be considered. However, it has not been measured yet for jets. Here, the composition of the jets considered as trigger is of crucial importance. By embedding jets into heavy-ion background we shall gain a complete understanding of the applied jet selection (with the ALICE background subtraction procedures). This is also important for a direct comparison with results from pp collisions.

Also other experiments have studied the production of identified hadrons in association with trigger jets or hadrons. Their focus was mostly on the production mechanisms and not so much on a possible medium response. For example, STAR has used identified protons as trigger for which a stronger dilution from medium hadronization is expected [214]. This results in reduced associated yields. Also the proton to pion ratio was measured in the near- and away-side region of a trigger hadron and compared with the inclusive measurements in central Au–Au collisions [215]. In both regions, the proton ratio is found to be reduced. Such a measurement has also been performed by ALICE [216].

Overall, the analysis developed within this thesis comprises many different ingredients, which makes it rather involved. The improvements discussed above and the higher statistics of the 2011 data and Run 2 shall provide a clearer picture on the medium response. But it should also be mentioned that for profound tests, better and more realistic models are needed, which provide final state particles that are comparable to experimental results.

Chapter 6

Summary

Three topics around jet physics were investigated within this thesis. Firstly, the modelling of jet quenching in JEWEL was studied for its sensitivity to details of the hydrodynamic evolution of the medium. Secondly, the TRD online tracking and trigger, with the focus on charged jets, were commissioned, brought to production, and studied in terms of their performance. Lastly, the azimuthal correlation between jets and associated hadrons in Pb–Pb collisions at $\sqrt{s_{NN}} = 2.76$ TeV was measured and compared with the correlation using identified protons.

In order to improve the understanding of the interplay of jet quenching with an evolving medium, the Monte Carlo event generator JEWEL has been extended by an interface to the output of numerical calculations of relativistic hydrodynamics. First, the medium-related part of the generator was split from the description of the parton shower evolution. Then, an additional interface for the common exchange format OSCAR2008H, which was introduced within the TECHQM collaboration, was realized. It allows for the flexible use of different data for the medium evolution and a systematic study of the influence on observables. A few scenarios of Au–Au collisions at the top RHIC energy $\sqrt{s_{NN}} = 200$ GeV were analysed here. For three different impact parameters (2.40, 3.16, 8.87 fm), we compare the suppression of high- p_{\perp} hadrons and jets for a medium evolution from numerical simulations of full relativistic hydrodynamics with a simpler Bjorken model. We further check the dependence of the nuclear modification factor on the azimuthal angle with respect to the event plane. In general, we find the modelling of these common jet quenching observables to be rather insensitive to the details of the medium evolution. The observed variations can be explained by the differences in the temporal evolution of temperature and density. They arise from other initial conditions, equation of state, and transverse expansion. For the scenarios discussed here, an evolution following the analytically accessible Bjorken expansion can be considered adequate. More data from hydrodynamic calculations exist and are under study for Pb–Pb collisions at the LHC energy $\sqrt{s_{NN}} = 2.76$ TeV. The higher p_{\perp} reach of hard probes allows new studies and it will be interesting to compare results obtained for different medium evolutions with higher precisions.

The Transition Radiation Detector in ALICE offers the possibility to contribute flexible track-based triggers at level-1. During the first years of LHC operation in Run 1, the operation of the online tracking required the implementation of the control and monitoring framework, as well as thorough testing for a stable and meaningful operation. A full simulation of all tracking stages was realized and has proved itself very useful for the detailed understanding of the algorithms. The implementation has been used in several other studies within the experiment. With the tracking operational, several level-1 triggers were realized. Within this thesis, a jet trigger based on the requirement of three geometrically close tracks above a p_{\perp} threshold was studied. It was

used during production data taking in pp and p-Pb collisions. In pp collisions at $\sqrt{s} = 8$ TeV, an integrated luminosity of about 200 nb^{-1} was sampled. The analysis of the triggered data confirmed the enhancement of high- p_{\perp} jets and the coverage of the anticipated target range from 100 to 200 GeV/ c . Furthermore, no bias on spectra and fragmentation functions is seen for jet p_{\perp} above 100 GeV/ c . The recorded data is now used for the measurement of fragmentation functions of high- p_{\perp} jets down to low track momenta, which can be further extended to identified fragmentation functions.

The third topic of this thesis was the measurement of jet-hadron correlations in Pb-Pb collisions at $\sqrt{s_{\text{NN}}} = 2.76$ TeV. Here, the main objective was to look for a possible response of the medium to a traversing hard parton or jet showing up as an away-side structure in the azimuthal correlation function. Furthermore, protons were considered as associates separately to distinguish components from jet- and medium-hadronization. A corresponding analysis was designed and run on the data from Pb-Pb collisions recorded with ALICE in 2010. Besides using jets as trigger, more abundant high- p_{\perp} hadrons are used as proxy, which also served as a cross check to previous analyses. A difference of proton and hadron associates can be seen on the near-side. This effect is expected from the smaller proton abundance in jet fragmentation as compared to medium hadronization (baryon enhancement). On the away-side no difference can be claimed with the statistics available from the 2010 data, although a reduced proton yield is favoured here as well. This would indicate a jet-like hadronization. However, a conclusive statement requires the analysis of further data. More statistics is available from the 2011 run and is being analysed, but the data sample requires additional work because of changes of detector conditions during the run period and for the dE/dx calibration of the TPC. Later, more data will become available in LHC Run 2. In addition, improvements to the analysis have been discussed which will help to gain sensitivity to the medium response.

In conclusion, there are many aspects of jet physics, which can be studied with ALICE in a unique way at LHC. Reconstructed jets at high- p_{\perp} allow us to study partonic energy loss in detail, both in terms of jet fragmentation and a possible medium response. A sufficiently large sample of jets can be accumulated using the established triggers. And with the particle identification in ALICE, we can go beyond the measurement of inclusive hadrons.

Acknowledgements

First and foremost, I want to thank Prof. Dr. Johanna Stachel for the opportunity to pursue my doctoral thesis in her group, for her continuous trust and support, and for a lot of freedom. It was a very active time, during which I could work on a broad range of topics, ranging from detector construction and commissioning to physics analysis and Monte Carlo phenomenology.

I am indebted to Dr. Korinna Zapp, who introduced me to the world of Monte Carlo event generators and jet quenching. I learned a lot from her when we shared the office. Further, I would like to thank her for the encouragement and support for my stay at the IPPP in Durham, UK.

I want to heartily thank Felix Rettig and Stefan Kirsch for the great collaboration, plenty of discussion, and the many (late) hours of commissioning and debugging. I am deeply grateful to Dr. Venelin Angelov, with whom I had many enlightening discussions and who was always available for help.

I have spent a lot of memorable days and nights with the people at point 2, including those of first collisions but many more which were not as prestigious. I want to thank everybody from the “P2 crew” for the splendid atmosphere and great collaboration, also during stressful times. My gratitude extends to all the people with whom I have spent so much time at CERN. In particular, I want to thank Stefan Kirsch, Dr. Yvonne Pachmayer, Dr. Ken Oyama, Dr. Bastian Bathen, Dr. Jörg Lehnert, Dr. Jochen Thaeder, Dr. Magnus Mager, and Torsten Alt.

For many discussions, I want to thank Dr. Tom Dietel, Dr. Oliver Busch, and Dr. Yvonne Pachmayer. To the latter I am also indebted for the help with and the reliable operation of the analysis trains at GSI. I further want to thank Benjamin Hess for his advice and help on the use of particle identification in ALICE.

For proof-reading of and discussions around my thesis, I would like to thank Dr. Yvonne Pachmayer, Dr. Oliver Busch, Dr. Korinna Zapp, Felix Rettig, Dr. Klaus Reygers, Michael Winn, Dr. Jorge Mercado, Dr. Kai Schweda, and Johannes Stiller.

It has been a pleasure and a privilege to work in the community of the ALICE collaboration. And there are many more people who deserve to be thanked. I sincerely apologize for the impossibility to list all of them here.

Appendix A

Medium implementation for JEWEL

A.1 Required interface

Different media can be linked against JEWEL. They must interoperate with the shower code through Fortran functions and subroutines. In the following, we document the required interface for any medium provided to JEWEL. They must also be supplied in the vacuum case for successful linking. All coordinates are to be understood in the lab frame.

The following functions and subroutines are required and the medium implementation should expect the specified calls:

MEDINIT A medium implementation is to expect

```
SUBROUTINE MEDINIT(FILE, ID, ETAM)
CHARACTER*80 FILE
INTEGER ID
DOUBLE PRECISION ETAM
```

to be called once before the first use of the medium. FILE is the filename of the configuration file containing the parameters, ID the file descriptor to be used for log messages, and ETAM the maximum space-time rapidity beyond which no medium needs to be simulated (reducing run-time). Any required one-time initialization should be done here.

MEDNEXTEVT A medium implementation is to expect

```
SUBROUTINE MEDNEXTEVT
```

to be called once before every event. This method can be used to initialize per-event settings, such as the impact parameter.

GETNEFF For a given space-time point (T, X, Y, Z)

```
DOUBLE PRECISION GETNEFF(X, Y, Z, T)
DOUBLE PRECISION X, Y, Z, T
```

should return the local effective density in GeV^3 .

GETTEMP For a given space-time point (T, X, Y, Z)

```
DOUBLE PRECISION GETTEMP(X, Y, Z, T)
DOUBLE PRECISION X, Y, Z, T
```

should return the local temperature in GeV.

GETMD For a given space-time point (T, X, Y, Z)

```
DOUBLE PRECISION GETMD(X,Y,Z,T)
DOUBLE PRECISION X,Y,Z,T
```

should return the local Debye mass in GeV.

GETMS For a given space-time point (T, X, Y, Z)

```
DOUBLE PRECISION GETMS(X,Y,Z,T)
DOUBLE PRECISION X,Y,Z,T
```

should return the local mass of a scattering centre in GeV.

GETSCATTERER For a given space-time point (T, X, Y, Z)

```
SUBROUTINE GETSCATTERER(X,Y,Z,T,TYP,PX,PY,PZ,E,MS)
```

must set the four-momentum (E, PX, PY, PZ) and the mass MS of the scattering centre. Because this method is only called with the space-time coordinates of a scattering, it can expect never to be called outside of the medium.

GETTEMPMAX A call to

```
DOUBLE PRECISION FUNCTION GETTEMPMAX()
```

should return the maximum possible temperature in GeV.

GETMDMAX A call to

```
DOUBLE PRECISION FUNCTION GETMDMAX()
```

should return the maximum possible Debye mass in GeV.

GETMSMAX A call to

```
DOUBLE PRECISION FUNCTION GETMSMAX()
```

should return the maximum possible screening mass in GeV.

GETLTIMEMAX A call to

```
DOUBLE PRECISION FUNCTION GETLTIMEMAX()
```

should return the maximum time at which a partonic medium could still exist, i.e. no medium has to be taken into account after this time.

GETNEFFMAX A call to

```
DOUBLE PRECISION FUNCTION GETNEFFMAX()
```

should return the maximum effective density occurring during the full evolution.

GETMDMIN A call to

```
DOUBLE PRECISION FUNCTION GETMDMIN()
```

should return the minimum Debye mass to be used.

GETNATMDMIN A call to

```
DOUBLE PRECISION FUNCTION GETNATMDMIN()
```

should return the effective density corresponding to the minimal Debye mass.

GETCENTRALITY A call to

```
DOUBLE PRECISION FUNCTION GETCENTRALITY()
```

should return the centrality of the current event.

AVSCATCEN For a space-time point (T, X, Y, Z)

```
SUBROUTINE AVSCATCEN(X, Y, Z, T, PX, PY, PZ, E, MS)
```

should set the average four-momentum of a scattering centre which includes flow.

MAXSCATCEN A call to

```
SUBROUTINE MAXSCATCEN(PX, PY, PZ, E, MS)
```

should set the four-momentum of a scattering centre corresponding to the maximum flow.

Of course, a medium implementation may contain further routines for internal use but one must be careful to avoid name clashes with routines in the main program (shower code).

A.2 Medium configuration

Often, a medium depends on parameters such as an initial temperature, centrality ranges etc. To override the default values parameters are read from a file configured by `MEDIUMPARAMS` in the main JEWEL configuration file. Values have to be specified in the form:

```
<PARAMETER> <VALUE>
```

The parameters for the Bjorken and OSCAR interface are listed in Tables A.1 and A.2. In case of the OSCAR interface, the nucleus-related parameters are used to determine the position of the hard interaction vertex. Only parameters deviating from the default values need to be specified. Unrecognized parameter names will be ignored after issuing a warning.

A.3 JEWEL parameters

The shower parameters used for the simulations of Au–Au collisions at RHIC energy $\sqrt{s} = 200$ GeV in Chapter 2 are listed in Table A.3. The major differences to the JEWEL default values are the centre-of-mass energy and the use of Au nuclei.

variable	meaning	default
TAUI	initial time at which the expansion starts	$0.6 \frac{\text{fm}}{c}$
TI	initial temperature of the medium	0.36 GeV
TC	critical temperature	0.17 GeV
WOODSSAXON	derive initial temperature from Woods-Saxon density	T(rue)
CENTRMIN	minimal centrality used to pick impact parameter	0 %
CENTRMAX	maximal centrality used to pick impact parameter	10 %
NF	number of active flavours	3
A	mass number	208
N0	nuclear density	0.17 fm^{-3}
D	thickness of nuclear edge	0.54 fm
SIGMANN	nucleon-nucleon cross section	6.2 fm^2
MDFACTOR	minimum Debye mass used for regularization	0.45 GeV
MDSCALEFACTOR	factor for Debye mass	0.9

Table A.1: Parameters for Bjorken medium. The default values, which are used if a parameter is not specified in the configuration file, are listed.

variable	meaning	default
OSCARFILE	name of the OSCAR data file	oscar.dat
WOODSSAXON	derive initial temperature from Woods-Saxon density	T(rue)
CENTRMIN	minimal centrality used to pick impact parameter	40 %
CENTRMAX	maximal centrality used to pick impact parameter	50 %
A	mass number	197
N0	nuclear density	0.17 fm^{-3}
D	thickness of nuclear edge	0.54 fm
SIGMANN	nucleon-nucleon cross section	4.2 fm^2
MDFACTOR	minimum Debye mass used for regularization	0.45 GeV
MDSCALEFACTOR	factor for Debye mass	0.9

Table A.2: Parameters for OSCAR medium. The default values, which are used if a parameter is not specified in the configuration file, are listed.

variable	meaning	value
NF	number of active flavours	3
LAMBDAQCD	Λ_{QCD}	0.40
Q0	cut-off scale for parton shower	1.5
PTMIN	minimal p_{\perp}	3.
PTMAX	maximal p_{\perp}	350.
ETAMAX	maximal space-time rapidity of medium	1.
PROCESS	hard process (PPJJ: $pp \rightarrow jj$, EEJJ: $e^+e^- \rightarrow jj$)	PPJJ
SQRTS	centre-of-mass energy	200.
PDFSET	LHAPDF id for proton PDF	10042
NSET	number of nuclear PDF set (1: central value)	1
MASS	atomic number of nucleus	197.
WEIGHTED	event weighting	T(rue)
WEXPO	exponent for event weighting	7.
ANGORD	angular ordering	T(rue)
KEEPRECOILS	keep recoils for hadronization	F(false)
HADRO	hadronize the partonic final state	T(rue)
HADROTYPE	colour arrangement in hadronization	0
SHORTHEPMC	HepMC output with stable particles only	T(rue)
COMPRESS	delete intermediate states in event record	T(rue)

Table A.3: Shower parameters used for the simulations in Chapter 2.

Appendix B

LHC operation

B.1 ALICE data taking periods

The LHC produced the first collisions with stable beam operation at the end of 2009. Since then the operation was structured in year-wise runs with longer breaks over Christmas. During the year technical stops (typically four days) were scheduled for maintenance of the machine and the experiments.

Within ALICE, the data taking was subdivided into data taking periods with constant beam parameters and detector configuration, e.g. magnetic field, composition of counting gases, etc. A list of the periods since the first physics data taking with stable beams is given in Table B.1.

period	start date	first run	comment
LHC09d	2009-11-24	101569	pp, 0.9 and 1.38 TeV
LHC10a	2010-01-07	105524	cosmics
LHC10b	2010-03-29	114650	pp, 7 TeV
LHC10c	2010-04-27	117631	pp, 7 TeV
LHC10d	2010-06-01	121527	pp, 7 TeV
LHC10e	2010-07-20	126461	pp, 7 TeV
LHC10f	2010-08-31	130931	pp, 7 TeV
LHC10f	2010-08-31	130962	pp, 7 TeV
LHC10g	2010-10-21	135394	pp, 7 TeV
LHC10h	2010-11-04	136782	Pb–Pb, 2.76 TeV
LHC11a	2011-01-10	139847	pp, 2.76 and 7 TeV
LHC11b	2011-03-29	146975	pp, 7 TeV
LHC11c	2011-05-05	150722	pp, 7 TeV
LHC11d	2011-07-07	155838	pp, 7 TeV
LHC11e	2011-08-24	159650	pp, 7 TeV
LHC11f	2011-10-05	162751	pp, 7 TeV
LHC11h	2011-10-31	165772	Pb–Pb, 2.76 TeV
LHC12a	2012-01-23	170719	pp, 8 TeV
LHC12b	2012-04-10	177312	pp, 8 TeV
LHC12c	2012-04-30	179357	pp, 8 TeV
LHC12d	2012-06-27	183174	pp, 8 TeV
LHC12e	2012-08-07	186346	pp, 8 TeV, rare
LHC12f	2012-08-14	186636	pp, 8 TeV, rare
LHC12g	2012-09-10	188167	pp, 8 TeV, rare; p–Pb pilot run
LHC12h	2012-09-20	188720	pp, 8 TeV, rare
LHC12i	2012-11-24	192739	pp, 8 TeV, rare
LHC12j	2012-12-17	193767	technical
LHC13a	2013-01-07	194480	cosmics
LHC13b	2013-01-16	195123	p–Pb, 5.02 TeV, –, first physics
LHC13c	2013-01-22	195517	p–Pb, 5.02 TeV, –, min. bias
LHC13d	2013-01-25	195679	p–Pb, 5.02 TeV, –, rare
LHC13e	2013-01-27	195875	p–Pb, 5.02 TeV, ++, rare
LHC13f	2013-02-01	196346	Pb–p, 5.02 TeV, ++, rare
LHC13g	2013-02-10	197412	pp, 2.76 TeV, –, rare

Table B.1: ALICE data taking periods since first physics data taking with stable beams in the LHC. The first run listed for a given period is not necessarily a physics run.

Appendix C

TRD operation and analysis

C.1 Overview

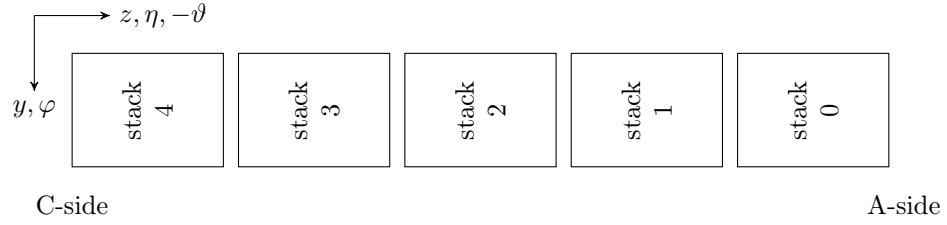
The details described in this appendix supplement the information given in the main text about the TRD installation. Figure C.1 sketches the installation of the TRD. In particular, the used geometrical variables are shown with their orientation in the ALICE coordinate system. Every layer (out of six) is composed of 5 Read-Out Chambers (ROC) corresponding to the 5 stacks. The ROCs in the central stack 2 are equipped with 6, the others with 8 Read-Out Boards (ROB). Every ROB hosts 17 or 18 MCMs which are connected through the Network Interface (NI) for read-out and through the Slow Control Serial Network (SCSN) for slow control. The numbering scheme used for the various entities can also be read from Figure C.1. Also, the pad tilting of $\alpha_{\text{tilt}} = \pm 2^\circ$ is shown.

Furthermore, the read-out scheme is shown as well as the TRAP configurations are listed in Section C.2. The data structures used for the off-line handling of the online tracklets and tracks are described in Section C.3. Lists of runs for trigger testing and the performance analysis are given in Section C.7.

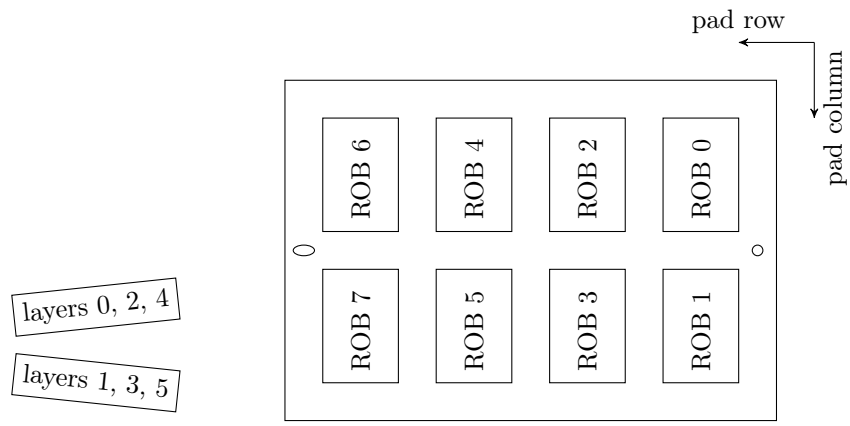
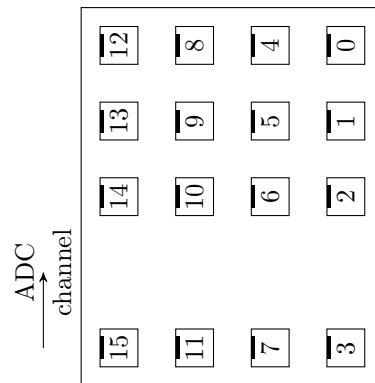
The online tracking requires the tracklet transmission to be ordered by increasing pad row ($-z$) and increasing pad column ($+y$). Both trigger and full raw data read-out are configured in this way by setting the registers NTRO and NRRO, correspondingly, on the half-chamber

143 ... 126	125 ... 108	107 ... 90	89 ... 72	71 ... 54	53 ... 36	35 ... 18	17 ... 0
17 ... 0	17 ... 0	17 ... 0	17 ... 0	17 ... 0	17 ... 0	17 ... 0	17 ... 0
2 ... 19	2 ... 19	2 ... 19	2 ... 19	2 ... 19	2 ... 19	2 ... 19	2 ... 19
165 ... 148	144 ... 127	123 ... 106	102 ... 85	81 ... 64	60 ... 43	39 ... 22	18 ... 1
1:3	1:2	1:1	1:0	0:3	0:2	0:1	0:0

Table C.1: Mapping of read-out pads and channels. The rows list the ranges covered by one MCM for: pad column, PASA channel, ADC channel, sequential channel number, ROB:MCM (top to bottom).



(a) ROCs in one layer

(b) ROBs on one ROC, $\alpha_{\text{tilt}} = \pm 2^\circ$ 

(c) MCMs on one ROB

Figure C.1: Top view of a TRD layer and its sub-components. The tilting direction of the pads is shown with an exaggerated angle. Further explanation is given in the text.

mergers (HCM), the board mergers (BM), and the column mergers (CM):

HCM $N[T,R]RO = 0xae1c = 0127034$ (for stack 2: $0xfe1c = 0177034$)

- port 4 - internal
- port 1 - ROB 0/1
- port 0 - ROB 2/3
- port 3 - ROB 4/5
- port 2 - ROB 6/7 (except for stack 2)

BM $N[T,R]RO = 0x3f0ca = 0770312$

- port 2 - MCM 02
- port 0 - MCM 06
- port 1 - MCM 10
- port 3 - MCM 14

CM $N[T,R]RO = 0x1fe21 = 0377041$

- port 1 - MCM $4 \cdot \text{row} + 0$
- port 0 - MCM $4 \cdot \text{row} + 1$
- port 4 - MCM $4 \cdot \text{row} + 2$ (internal)
- port 3 - MCM $4 \cdot \text{row} + 3$

C.2 TRAP configurations

All registers and memories of the TRAPs are set using a set of configurations. They are maintained in an svn repository at:

<https://alice.phys.uni-heidelberg.de/svn/trd/TRAPconfig>

Configurations are uniquely identified by name and version (svn revision). The name encodes the most relevant parameters. It consists of a fixed prefix “cf_” and groups of parameters which are separated by “_”. The order of the first groups is fixed while additional ones can be appended at the end. Within each group different parameters are separated by -. The general scheme is: `cf_<filter>_<zs>_<timebin>_<trkl>_<trgmode>`.

The different options are:

- <filter> p(edestal), g(ain), t(ail)
- <zs> (no)zs
- <timebin> tb<no. of timebins>
- <trkl> trkl... (includes PID table)
- <trgmode> ptrg/autotrg/...

Table C.2 lists the TRAP configurations used for physics data taking in the 2011 Pb–Pb, 2012 pp, and 2013 p–Pb runs. The configurations are also available from the OCDB in TRD/Calib/TrapConfig.

Table C.2: List of TRAP configurations used in runs since LHC11h which included the TRD in the read-out.

run	configuration	version
197692, 197691, 197669, 197643, 197619, 197618, 197615, 197613, 197612, 197611, 197610, 197609, 197608, 197606, 197584, 197583, 197582, 197580, 197555, 197553, 197531, 197530, 197529, 197527, 197501, 197500, 197499, 197498, 197497, 197496, 197471, 197470, 197469	cf_pg-fpnp32_zs-s16-deh_tb22_trkl-b5n-fs1e24-ht200-qs0e23s23e22-pidlhc11dv1-pt100_ptrg	r5037
197388, 197387, 197386, 197351, 197350, 197349, 197348, 197347, 197346, 197343, 197342, 197341, 197302, 197300, 197299, 197298, 197297, 197296, 197260, 197258, 197256, 197255, 197254, 197248, 197247, 197198, 197197, 197186, 197185, 197184, 197153, 197152, 197150, 197149, 197148, 197147, 197146, 197145, 197144, 197143, 197142, 197141, 197140, 197139, 197138, 197099, 197098, 197094, 197092, 197091, 197090, 197089, 197089, 197031, 197027, 197024, 197015, 197012, 197011, 197009, 197003, 197002, 196974, 196973, 196972, 196967, 196965, 196876, 196875, 196874, 196871, 196870, 196869, 196774, 196773, 196772, 196722, 196721, 196720, 196714, 196706, 196703, 196702, 196701, 196648, 196646	cf_pg-fpnp32_zs-s16-deh_tb22_trkl-b5p-fs1e24-ht200-qs0e23s23e22-pidlhc11dv1-pt100_ptrg	r5037
196645, 196644, 196642, 196641, 196640, 196638	cf_p_nozs_tb30_trk_ptrg	r4850
196608, 196605, 196601, 196568, 196567, 196566, 196564, 196563, 196535, 196534, 196533, 196528, 196477, 196475, 196474, 196433, 196432, 196311, 196310, 196309, 196308, 196215, 196214, 196208, 196203, 196202, 196201, 196200, 196199, 196197, 196194, 196190, 196187, 196185, 196184, 196107, 196105, 196099, 196098, 196096, 196091, 196090, 196089, 196086, 196085, 196083, 196006, 196005, 196004, 196000, 195999, 195994, 195993, 195991, 195990, 195989, 195988, 195958, 195957, 195956, 195955, 195954, 195953, 195952, 195951, 195950, 195949, 195935	cf_pg-fpnp32_zs-s16-deh_tb22_trkl-b5p-fs1e24-ht200-qs0e23s23e22-pidlhc11dv1-pt100_ptrg	r5037
195873, 195872, 195871, 195870, 195869, 195867, 195831, 195830, 195829	cf_pg-fpnp32_zs-s16-deh_tb22_trkl-b5n-fs1e24-ht200-qs0e23s23e22-pidlhc11dv1-pt100_ptrg	r5037
195827, 195826	mixed	r5037
195788, 195787, 195783, 195767, 195766, 195765, 195761, 195760, 195727, 195726, 195725, 195724, 195723, 195722, 195721, 195720, 195682, 195681, 195680, 195679, 195677, 195676, 195675, 195673, 195644, 195635, 195633, 195596, 195595, 195594, 195593, 195592, 195568, 195567, 195566, 195565, 195532, 195531, 195529, 195483, 195482, 195481, 195480, 195479, 195478, 195391, 195390, 195389, 195351, 195346, 195344, 193766, 193760, 193759, 193758, 193757, 193752, 193751, 193750, 193748, 193747, 193744, 193742, 193740, 193739, 193736, 193734, 193733, 193703, 193702, 193699, 193696, 193695, 193279, 193246, 193194, 193193, 193192, 193189, 193188, 193187, 193185, 193184, 193156, 193155, 193153, 193152, 193151, 193150, 193148, 193147, 193097, 193096, 193095, 193094, 193093, 193092, 193052, 193051, 193050, 193049, 193048, 193047, 193014, 193011, 193008, 193007, 193005, 193004, 192824, 192822, 192820, 192779, 192778, 192775, 192772, 192732	cf_pg-fpnp32_zs-s16-deh_tb22_trkl-b5n-fs1e24-ht200-qs0e23s23e22-pidlhc11dv1-pt100_ptrg	r5037
192731, 192730, 192729	cf_pg-fpnp32_zs-s16-deh_tb22_trkl-b5n-fs1e24-ht200-qs0e23s23e22-pidlhc11dv1h-pt100_ptrg	r5151
192712, 192709, 192708, 192707, 192688, 192551, 192548, 192542, 192537, 192535, 192534, 192511, 192510, 192505, 192504, 192499, 192497, 192492, 192471, 192468, 192461, 192453, 192451, 192417, 192416, 192415, 192414, 192349, 192348, 192347, 192346, 192345, 192344, 192342, 192246, 192205, 192202, 192201, 192200, 192199, 192197, 192196, 192194, 192193, 192177, 192176, 192174, 192173, 192172, 192141, 192140, 192136, 192133, 192132, 192130, 192128, 192125, 192121, 192095, 192079, 192078, 192077, 192075, 192074, 192073, 192072, 192004, 191587, 191548, 191547, 191451, 191450, 191449, 191248, 191247, 191245, 191244, 191242, 191241, 191240, 191239, 191234, 191232, 191231, 191230, 191229, 191227, 191226, 191225, 191129, 191128	cf_pg-fpnp32_zs-s16-deh_tb22_trkl-b5n-fs1e24-ht200-qs0e23s23e22-pidlhc11dv1-pt100_ptrg	r5037
191117, 191116, 191115, 190984, 190983, 190981, 190979, 190975, 190974, 190973, 190972, 190970, 190969, 190968, 190967, 190966, 190965, 190905, 190904, 190903, 190902, 190898, 190897, 190895, 190425, 190424, 190422, 190421, 190419, 190418, 190417, 190416, 190393, 190392, 190390, 190389, 190388, 190387, 190386, 190385, 190384, 190345, 190344, 190342, 190341, 190340, 190338, 190337, 190336, 190335, 190307, 190306, 190305, 190304, 190303, 190244, 190242, 190240, 190216, 190215, 190214, 190213, 190212, 190210, 190209, 190150, 189737, 189736, 189735, 189734, 189729, 189699, 189698, 189697, 189696, 189695, 189659, 189658, 189657, 189656, 189654, 189653, 189650, 189648, 189647, 189623, 189621, 189616, 189615, 189612, 189611, 189610, 189608, 189607, 189606, 189605, 189604, 189603, 189602, 189526, 189525, 189523, 189474, 189473, 189411, 189410, 189409, 189407, 189406, 189405, 189404, 189403, 189402, 189400, 189399, 189397, 189396, 189353, 189352, 189351, 189350, 189347, 189344, 189341, 189340, 189316, 189315, 189310, 189306, 189301, 189246, 189231, 189229, 189228, 189227, 189187	cf_pg-fpnp32_zs-s16-deh_tb24_trkl-b5n-fs1e24-ht200-qs0e23s23e22-pidlhc11dv1-pt100_ptrg	r4946
189183, 189182	cf_pg-fpnp32_zs-s16-deh_tb22_trkl-b5n-fs1e24-ht200-qs0e23s23e22-pidlhc11dv1-pt100_ptrg	r5037
189147, 189146, 189122, 188503, 188500, 188499, 188490, 188488, 188455, 188454, 188449, 188447, 188446, 188444, 188443, 188442, 188441, 188440, 188438, 188362, 188123, 188108, 188104, 188102, 188101, 188093, 188029, 188028, 188027, 188025, 188022, 188021, 187849, 187848, 187844, 187796, 187791, 187787, 187785, 187783, 187780, 187779, 187753, 187749, 187744, 187439, 187435, 187434, 187432, 187343, 187342, 187341, 187340, 187339, 187338, 187337, 187335, 187203, 187202, 187201, 187152, 187151, 187150, 187149, 187148, 187147, 187146, 187145, 187143, 187136, 187084	cf_pg-fpnp32_zs-s16-deh_tb24_trkl-b5n-fs1e24-ht200-qs0e23s23e22-pidlhc11dv1-pt100_ptrg	r4946
187047	cf_pg-fpnp32_zs-s16-deh_tb22_trkl-b5n-fs1e24-ht200-qs0e23s23e22-pidlhc11dv1-pt100_ptrg	r5037

run	configuration	version
186994, 186993, 186992, 186990, 186989, 186988, 186987, 186969, 186968, 186967, 186966, 186965, 186939, 186938, 186937, 186932, 186931, 186930, 186928, 186859, 186857, 186855, 186853, 186851, 186850, 186849, 186847, 186845, 186844, 186843, 186841, 186840, 186839, 186838, 186816, 186815, 186814, 186813, 186811, 186810, 186809, 186808, 186807, 186694, 186693, 186692, 186690, 186689, 186688, 186687, 186668	cf_pg-fpmp32_zs-s16-deh_tb24_trkl-b5n-fs1e24-ht200-qs0e23s23e22-pidlhc11dv1-pt100_ptrg	r4946
186602, 186601, 186600, 186598, 186514, 186511, 186510, 186509, 186508, 186507, 186460, 186459, 186457, 186456, 186453, 186432, 186429, 186428, 186389, 186388, 186387, 186386, 186365, 186320, 186319, 186208, 186205, 186167, 186165, 186164, 186163, 186084, 186083, 186082, 186079, 186078, 186073, 186011, 186009, 186007, 186006, 186003	cf_pg-fpmp32_zs-s16-deh_tb24_trkl-b5p-fs1e24-ht200-qs0e23s23e22-pidlhc11dv1-pt100_ptrg	r4946
185918, 185916	cf_pg-fpmp32_zs-s16-deh_tb24_trkl-b5p-fs1e24-ht200-qs0e23s23e22-pidlhc11dv1-pt2300_ptrg	r4946
185915	mixed	r4946
185784, 185778, 185776, 185775, 185768, 185765, 185764, 185738, 185701, 185700, 185699, 185698, 185697, 185692, 185690, 185689, 185688, 185687, 185682, 185659, 185658, 185589, 185588, 185585, 185583, 185582, 185581, 185580, 185578, 185575, 185574, 185569, 185567, 185475, 185474, 185472, 185467, 185465, 185461, 185460, 185459, 185378, 185375, 185371, 185368, 185363, 185362, 185361, 185360, 185359, 185356, 185351, 185350, 185349, 185348, 185303, 185302, 185301, 185300, 185299, 185296, 185293, 185292, 185291, 185290, 185289, 185288, 185284, 185282, 185281, 185227, 185221, 185217, 185214, 185213, 185210, 185208, 185206, 185204, 185203, 185198, 185196, 185193, 185192, 185191, 185190, 185189, 185164, 185163, 185160, 185159, 185134, 185133, 185132, 185131, 185129, 185128, 185127, 185126, 185125, 185116, 185115, 185114, 185031, 185029, 185027, 184990, 184988, 184987, 184968, 184967, 184964, 184938, 184933, 184932, 184930, 184928, 184846, 184845, 184786, 184784, 184719, 184716, 184687, 184682, 184678, 184673, 184389, 184383, 184374, 184371, 184216, 184215, 184214, 184210, 184209, 184208, 184207, 184206, 184205, 184190, 184188, 184183, 184147, 184146, 184145, 184144, 184140, 184139, 184138, 184137, 184135, 184134, 184133, 184132, 184131, 184127, 184126, 184125, 184000, 183946, 183942, 183938, 183937, 183936, 183935, 183934, 183933, 183932, 183916, 183915, 183913, 182744, 182741, 182740, 182730, 182729, 182728, 182727, 182726, 182725, 182724, 182692, 182691, 182687, 182686, 182685, 182684, 182639, 182638, 182635, 182513, 182509, 182508, 182325, 182323, 182302, 182300, 182299, 182298, 182296, 182294, 182293, 182292, 182291, 182290, 182111, 182110, 182109, 182108, 182107, 182023, 182022, 182021, 182020, 181705, 181704, 181703, 181702, 181701, 181698, 181697, 181696, 181694, 181663, 181652, 181620, 181619, 181618, 181617, 180720, 180717, 180716, 180715, 180201, 180200, 180199, 180195, 180133, 180132, 180131, 180130, 180129, 180127, 180121, 180120, 180046, 180044, 180042, 180000, 179920, 179919, 179918, 179917, 179916, 179859, 179858, 179840, 179839, 179837, 179807, 179806, 179805, 179803, 179802, 179801, 179799, 179796, 179794, 179679, 179678, 179639, 179638, 179621, 179618, 179617, 179604, 179603, 179595, 179593, 179591, 179590, 179585, 179584, 179571, 179569, 179568, 179564, 179444, 178167, 178166, 178165, 178163, 178053, 178052, 178031, 178030, 178029, 178028, 178026, 178025, 178024, 178023, 178021, 178018, 178017, 177990, 177982, 177981, 177980, 177942, 177938, 177869, 177868, 177866, 177864, 177861, 177860, 177858, 177857, 177854, 177810, 177805, 177804, 177802, 177799, 177798	cf_pg-fpmp32_zs-s16-deh_tb24_trkl-b5p-fs1e24-ht200-qs0e24s24e23-pidlhc11dv1-pt100_ptrg	r4866
177682, 177681, 177680, 177679, 177678, 177671, 177670, 177669, 177668, 177667, 177666, 177624, 177620, 177617, 177612, 177610, 177607, 177601, 177597, 177590	cf_p_zs-s16-deh_tb24_trkl-b0-fs1e24-ht200-qs0e24s24e23-pidlhc11dv1-pt100_ptrg	r4866
177501, 177497, 177496	cf_p_zs-s16-deh_tb24_trkl-b5p-fs1e24-ht200-qs0e24s24e23-pidlhc11dv1-pt100_ptrg	r4866
177182, 177181, 177180, 177179, 177177, 177176, 177175, 177174, 177173, 177172, 177171, 177169, 177167, 177165, 177164, 177163, 177160, 177159, 177157, 177155, 177153, 177150, 177149, 177148, 177124, 177120, 177074, 177073, 177072, 177049, 177048, 177047, 177045, 177042, 177041, 177040, 177039, 177011, 176929, 176927, 176926, 176924, 176923, 176859, 176857, 176854, 176852, 176849, 176842, 176840, 176838, 176753, 176752, 176749, 176730, 176729	cf_pg_zs-s16-deh_tb24_trkl-b5p-fs1e24-ht200-qs0e24s24e23-pidlhc11dv1-pt100_ptrg	r4874
176715, 176710, 176707, 176706, 176704, 176702, 176701, 176666, 176665, 176658	cf_p_zs-s16-deh_tb24_trkl-b5p-fs1e24-ht200-qs0e24s24e23-pidlhc11dv1-pt2300_ptrg	r4864
170593, 170572, 170556, 170552, 170546, 170390, 170389, 170388, 170387, 170315, 170313, 170312, 170311, 170309, 170308, 170306, 170270, 170269, 170268, 170267, 170264, 170230, 170228, 170226, 170208, 170207, 170206, 170205, 170204, 170203, 170195, 170193, 170163, 170162, 170161, 170159, 170155, 170152	cf_p_zs-s16-deh_tb24_trkl-b5p-fs1e24-ht200-qs0e24s24e23-pidlhc11dv1-pt2300_ptrg	r4862
170091, 170090, 170089, 170088, 170085, 170084, 170083, 170081, 170040, 170038, 170036, 170027	cf_p_zs-s16-deh_tb24_trkl-b5p-fs1e24-ht200-qs0e24s24e23-pidlhc11dv1-pt100_ptrg	r4862
169981, 169978, 169975, 169969, 169965, 169961, 169960, 169958, 169957, 169956, 169954, 169923, 169922, 169859, 169858, 169855, 169846, 169838, 169837, 169835	cf_p_zs-s16-deh_tb24_trkl-b5p-fs1e24-ht200-qs0e24s24e23-pidlhc11dv1-pt100_ptrg	r4850
169683, 169681	cf_p_zs-s16-deh_tb24_trkl-b5p-fs1e24-ht200-qs0e24s24e23-pidlhc11dv1-pt100_ptrg	r4850

run	configuration	version
169591, 169590, 169588, 169587, 169586, 169584, 169557, 169555, 169554, 169553, 169550, 169515, 169512, 169506, 169504, 169498, 169475, 169420, 169419, 169418, 169417, 169415, 169411, 169238, 169236, 169167, 169160, 169156, 169148, 169145, 169144, 169143, 169138, 169099, 169096, 169094, 169091, 169045, 169044, 169040, 169035, 168992, 168991, 168989, 168988, 168984, 168833, 168832, 168828, 168826, 168777, 168512, 168511, 168467, 168464, 168463, 168461, 168460, 168458, 168362, 168361, 168356, 168352, 168342, 168341, 168325, 168322, 168321, 168318, 168315, 168314, 168313, 168312, 168311, 168310, 168213, 168212, 168208, 168207, 168206, 168205, 168204, 168203, 168202, 168201, 168181, 168179, 168177, 168176, 168175, 168174, 168173, 168172, 168171, 168115, 168108, 168107, 168105, 168102, 168076, 168069, 168068, 168065, 168062, 168059, 168058, 168057, 167988, 167987, 167986, 167985, 167983, 167982, 167979, 167921, 167920, 167915, 167909, 167903, 167902, 167901, 167818, 167814, 167813, 167812, 167811, 167810, 167809, 167808, 167807, 167806, 167713, 167712, 167711, 167706, 167703, 167699, 167693	cf_p_zs-si6-deh_tb24_trkl-b5n-fs1e24-ht200-qs0e24s24e23-pidlinear-pt100_ptrg	r4850

information	ESD access	AOD access
number of half-chamber		<code>GetHCId()</code>
pad row in chamber		<code>GetBinZ()</code>
y -coordinate w.r.t. chamber centre (in 160 μm bins)		<code>GetBinY()</code>
y -coordinate w.r.t. chamber centre (in cm)		<code>GetLocalY()</code>
deflection d_y over 3 cm drift length (in 140 μm bins)		<code>GetBinDy()</code>
deflection d_y over 3 cm drift length (in cm)		<code>GetDyDx()</code>
PID value (look-up table dependent meaning)		<code>GetPID()</code>
label of Monte Carlo track		<code>GetLabel()</code>

Table C.3: Tracklet information available from `AliESDTrdTracklet` and `AliAODTrdTrack`.

C.3 Data structures for online information

For the use in analyses, the data from online tracking and triggering is made available in ROOT objects. For tracklets and tracks virtual base classes are used to provide a common interface for ESD and AOD analyses. The implemented methods and the data stored in the inherited classes for ESD and AOD events is shown in Tables C.3 and C.4. For ESDs, additional sector-wise trigger and timing information is stored as `AliESDTrdTrigger`, see Table C.5.

A certain convention for the Monte Carlo labels was introduced to encode their origin. In general, the global tracking simulation assigns the labels corresponding to tracklets contributing to a track or -1 if this fails. Monte Carlo tracklets get assigned the positive label of the originating track. If no such relation can be established the label -1 is assigned. Tracklets from real data get the fixed label -2 . Tracks from real data get the fixed label -3 . This allows for the distinction of tracks from raw data, re-simulation on raw tracklets, or re-simulation on re-simulated tracklets.

C.4 AliTRDTriggerAnalysis

Events from a specific TRD trigger can be selected in the ALICE analysis framework in a two stage approach. From the physics selection all events with any of the TRD triggers fired can be requested with the flag `AliVEvent::kTRD`. The class `AliTRDTriggerAnalysis` can then be used to further narrow down the selection. The class must be called to calculate the conditions for every event:

```
// once per task
AliTRDTriggerAnalysis trdSelection;

// once per event
trdSelection.CalcTriggers(vEvent);
```

Then, different methods can be used to check if a given trigger condition is fulfilled:

HasTriggeredConfirmed(trg) returns whether the event was read out for the given trigger and the corresponding condition is fulfilled. This should be used by default for an analysis on TRD triggered data.

information	AliESDTrdTrack	AliAODTrdTrack
TRD sector	<code>GetSector()</code>	
TRD stack	<code>GetStack()</code>	
transverse offset a from nominal vertex	<code>GetA()</code>	
slope b in transverse plane	<code>GetB()</code>	–
slope c in r - z plane	<code>GetC()</code>	–
approximate y position	<code>GetY()</code>	–
average tracklet PID	<code>GetPID()</code>	
mask of layers with contributing tracklet	<code>GetLayerMask()</code>	
index of tracklet in layer l	<code>GetTrackletIndex(Int_t l)</code>	–
tracking flags (high- p_{\perp} , electron, positron)	<code>GetFlags()</code>	–
timing flags	<code>GetFlagsTiming()</code>	
track in-time	<code>GetTrackInTime()</code>	
pointer to tracklet in layer l	<code>GetTracklet(Int_t l)</code>	
pointer to matched global track	<code>GetTrackMatch()</code>	
label of Monte Carlo track	<code>GetLabel()</code>	

Table C.4: Available information and access methods for ESD and AOD versions of AliVTrdTrack: Some information is only available from ESDs. Common getters available through the abstract base class are listed between the ESD and AOD columns.

information	ESD access	AOD access
trigger flags for sector s	<code>GetFlags(Int_t s)</code>	–

Table C.5: Available information and access methods for AliESDTrdTrigger: Currently, the information is only available from ESDs.

HasTriggered(trg) returns whether the event was read out for the given trigger.

HasFired(trg) returns whether the given trigger was fired. The event was not necessarily read out because of this trigger, i.e. the corresponding trigger class is not set.

CheckCondition(trg) returns whether the event fulfills the condition for the given trigger, i.e. whether the corresponding trigger should have fired.

A typical usage could look like

```
// for sections in which you want to look at one trigger only
if (trdSelection.HasTriggeredConfirmed(AliTRDTriggerAnalysis::kHJT)) {
    ...
}
```

where `kHJT` could be replaced by any of `kHCO`, `kHSE`, `kHQU`, or `kHEE`.

For more advanced studies, `AliTRDTriggerAnalysis` allows to adjust the track requirements considered for the evaluation of the trigger condition. By default, they are set to reproduce the results from the hardware trigger, but other conditions can be used for testing.

SetRequireMatch(Bool_t) consider only tracks which have been matched to a global ESD track (false by default). This suppresses tracks from photon conversions at large radii.

SetRequireMatchElectron(Bool_t) for the electron triggers, consider only tracks which have been matched to a global ESD track (false by default). This suppresses tracks from photon conversions at large radii.

SetRequireInTime(Bool_t) consider only tracks which have been found in time for the contribution to the CTP (true by default). Not requiring this allows to study triggers even though the track finding was not in time.

C.5 Test runs for TRD triggers

The TRD online tracking is in operation even if the trigger is not used. Thus, its performance can be studied from runs recorded without the TRD triggers. However, several runs with beam were taken to test the operation with high level-0 rates which are only possible with high rejections at level-1.

C.5.1 pp at $\sqrt{s} = 7$ TeV

Several test runs were recorded with pp collisions at $\sqrt{s} = 7$ TeV, see Table C.6. The threshold of 3 tracks above 3 GeV/c was lowered to 2 tracks in order to achieve enough triggered events for testing within the available time. They were reconstructed in the dedicated pass “TRD_trigger_1”. By now, the official standard reconstruction pass (currently pass1) should be used instead.

C.5.2 pp at $\sqrt{s} = 8$ TeV

During pp collisions at $\sqrt{s} = 8$ TeV, the TRD level-1 triggers were activated for testing in fill 2701 (LHC12c, e.g. run 182022). Further test runs with the HJT, HSE, HQU triggers were taken in the period LHC12d, namely 184682, 184673.

run	threshold	CINT7WU	CINT7WUHJT	CEMC7WU	triggers
159539	$3 \times 3 \text{ GeV}/c$	35 022	1	66 018	173
159575	$2 \times 3 \text{ GeV}/c$	9 999	19	15 627	547
159577	"	21 420	28	36 992	1 202
159580	"	44 377	61	78 976	2 602
159581	"	31 127	31	64 229	2 136
159582	"	141 656	175	271 703	8 851
159586	"	51 455	60	101 929	3 107
159593	"	9 628	9	19 994	645
159595	"	31 331	40	64 882	2 219
159599	"	7 225	6	15 141	532
159606	"	7 342	11	16 272	554
sum		390 582	441	751 763	22 568

Table C.6: Overview of test runs for the TRD jet trigger in pp collisions at $\sqrt{s} = 7 \text{ TeV}$ in 2011: The target threshold ($3 \times 3 \text{ GeV}/c$) was lowered to 2 tracks to record enough events for testing in the allocated time. We list the number of triggers in the relevant trigger classes.

C.6 Overview of TRD-triggered data

class name	periods	first run	last run
CINT7WUHJT-I-NOPF-ALL	LHC11d, LHC11e, LHC11f	159539	163911
CINT7WUHJT-B-NOPF-ALL	LHC11e, LHC13a, LHC13b, LHC13c, LHC13d, LHC13f, LHC13g	160676	197669
DEMC7WUHJT-B-NOPF-ALL	LHC11e	160683	161584
CEMC7WUHJT-B-NOPF-ALL	LHC11e	160722	162181
CEMC7WUHJT-B-NOPF-CENT	LHC11e, LHC11f	161722	165746
CINT7WUHJT-B-NOPF-CENT	LHC11e, LHC12i, LHC13a, LHC13d, LHC13e, LHC13f, LHC13g	162317	197531
CEMC7WUHJT-S-NOPF-CENT	LHC12c, LHC12d, LHC12e, LHC12f, LHC12g, LHC12h	182020	189699
CINT7WUHJT-S-NOPF-CENT	LHC12c, LHC12d, LHC12e, LHC12f, LHC12g, LHC12h, LHC12i, LHC13g	182020	197691
CEMC7WUHJT-ACE-NOPF-ALL	LHC12d	185459	185461
CEMC7WUHJT-S-NOPF-ALL	LHC12d	185459	185461
CINT7WUHJT-ACE-NOPF-ALL	LHC12d, LHC13a, LHC13b, LHC13c	185459	195568
CINT7WUHJT-S-NOPF-ALL	LHC12d	185459	185461
CEMC7WUHJT-ACE-NOPF-CENT	LHC12d, LHC12e, LHC12f, LHC12g	185465	188503
CINT7WUHJT-ACE-NOPF-CENT	LHC12d, LHC12e, LHC12f, LHC12g, LHC12h, LHC12i, LHC13a, LHC13d, LHC13e, LHC13f, LHC13g	185465	197691
CEMC8WUHJT-ACE-NOPF-ALL	LHC12f, LHC12g	186807	188490
CEMC8WUHJT-S-NOPF-ALL	LHC12f, LHC12g	186807	188490
CINT8WUHJT-ACE-NOPF-ALL	LHC12f, LHC12g	186807	188490
CINT8WUHJT-S-NOPF-ALL	LHC12f, LHC12g	186807	188490
CINT8WUHJT-ACE-NOPF-CENT	LHC12h	189340	189737
CINT8WUHJT-S-NOPF-CENT	LHC12h	189340	189737
CEMC8WUHJT-S-NOPF-CENT	LHC12h	189473	189737
CINT7WUHJT-ACE-NOPF-FAST	LHC13a, LHC13d	194792	195723
CINT7WUHJT-B-NOPF-FAST	LHC13a, LHC13d, LHC13e, LHC13f, LHC13g	194792	197531
CINT7WUHJT-I-NOPF-CENT	LHC13g	197553	197691
CINT7WUHJT-I-NOPF-FAST	LHC13g	197553	197584

Table C.7: Trigger classes with WU and HJT used in physics runs with at least TPC and TRD

class name	LHC12d	LHC12e	LHC12f	LHC12g	LHC12h	LHC12i
CEMC7WUHJT-S-NOPF-ALL	13	0	0	0	0	0
CEMC7WUHJT-S-NOPF-CENT	67094	18008	50407	21048	85243	0
CEMC7WUHQU-B-NOPF-CENT	0	0	0	0	0	6668
CEMC7WUHQU-S-NOPF-CENT	361	0	0	0	1401703	268892
CEMC7WUHSE-S-NOPF-CENT	488	0	0	0	0	0
CEMC8WUHJT-S-NOPF-ALL	0	0	14189	10386	0	0
CEMC8WUHJT-S-NOPF-CENT	0	0	0	0	10067	0
CINT7WUHJT-B-NOPF-CENT	0	0	0	0	0	20851
CINT7WUHJT-S-NOPF-ALL	8415	0	0	0	0	0
CINT7WUHJT-S-NOPF-CENT	139567	23625	67136	22717	1087118	222625
CINT7WUHQU-B-NOPF-CENT	0	0	0	0	0	168992
CINT7WUHQU-S-NOPF-CENT	984703	0	0	0	17656988	2485289
CINT7WUHSE-B-NOPF-CENT	0	0	0	0	0	221893
CINT7WUHSE-S-NOPF-CENT	1174755	0	0	0	20439022	3240736
CINT8WUHJT-S-NOPF-ALL	0	0	15670	11037	0	0
CINT8WUHJT-S-NOPF-CENT	0	0	0	0	23501	0
CINT8WUHQU-S-NOPF-CENT	0	0	0	0	613673	0
CINT8WUHSE-S-NOPF-CENT	0	0	0	0	790647	0

Table C.8: Statistics recorded in pp collisions at $\sqrt{s} = 8$ TeV

class name	LHC13b	LHC13c	LHC13d	LHC13e	LHC13f
CEMC7WUHEE-B-NOPF-CENT	0	0	0	0	599332
CEMC7WUHQU-B-NOPF-ALL	0	9596	0	0	0
CEMC7WUHSE-B-NOPF-ALL	0	10930	0	0	0
CINT7WUHJT-B-NOPF-ALL	14205	39690	0	0	0
CINT7WUHJT-B-NOPF-CENT	0	0	94806	277110	616654
CINT7WUHJT-B-NOPF-FAST	0	0	110099	327219	720200
CINT7WUHQU-B-NOPF-ALL	155266	478665	0	0	0
CINT7WUHQU-B-NOPF-CENT	0	0	887413	2348116	5119519
CINT7WUHQU-B-NOPF-FAST	0	0	1030034	2773006	5976227
CINT7WUHSE-B-NOPF-ALL	216859	527106	0	0	0
CINT7WUHSE-B-NOPF-CENT	0	0	1248785	3351732	7238154
CINT7WUHSE-B-NOPF-FAST	0	0	1449394	3958161	8449604

Table C.9: Statistics recorded in p–Pb collisions at $\sqrt{s_{NN}} = 5.02$ TeV

class name	LHC13g
CEMC7WUHEE-B-NOPF-ALL	323
CEMC7WUHEE-B-NOPF-CENT	2103
CEMC7WUHEE-I-NOPF-CENT	5392
CINT7WUHJT-B-NOPF-ALL	609
CINT7WUHJT-B-NOPF-CENT	7340
CINT7WUHJT-B-NOPF-FAST	9912
CINT7WUHJT-I-NOPF-CENT	26400
CINT7WUHJT-I-NOPF-FAST	19316
CINT7WUHJT-S-NOPF-CENT	427
CINT7WUHQU-B-NOPF-ALL	13704
CINT7WUHQU-B-NOPF-CENT	143694
CINT7WUHQU-B-NOPF-FAST	195546
CINT7WUHQU-I-NOPF-CENT	838290
CINT7WUHQU-I-NOPF-FAST	605706
CINT7WUHQU-S-NOPF-CENT	8868
CINT7WUHSE-B-NOPF-ALL	17922
CINT7WUHSE-B-NOPF-CENT	183587
CINT7WUHSE-B-NOPF-FAST	250236
CINT7WUHSE-I-NOPF-CENT	982331
CINT7WUHSE-I-NOPF-FAST	711843
CINT7WUHSE-S-NOPF-CENT	11582

Table C.10: Statistics recorded in pp collisions at $\sqrt{s} = 2.76$ TeV

C.7 Run lists for analysis of TRD-triggered data

The runs listed below can be used for analysis of TRD-triggered data. The selection follows the criteria given in the text. Also runs without active TRD triggers are listed since they can be used as untriggered reference.

C.7.1 pp at $\sqrt{s} = 8$ TeV

LHC12a 176701, 176707, 176710, 176715, 176730, 176749, 176753, 176849, 176854, 176859, 176924, 176926, 176927, 176929, 177011, 177049, 177072, 177120,

LHC12c 179444, 179569, 179571, 179584, 179585, 179591, 179595, 179603, 179604, 179618, 179621, 179638, 179639, 179678, 179796, 179803, 179837, 179858, 179916, 179917, 179918, 179919, 179920, 180000, 180042, 180044, 180127, 180129, 180130, 180131, 180132, 180195, 180199, 180200, 180201, 182509, 182513, 182684, 182691, 182692, 182725, 182730, 182740, 182741, 182744,

LHC12d 183916, 184127, 184131, 184132, 184134, 184135, 184137, 184138, 184140, 184144, 184145, 184147, 184183, 184188, 184208, 184209, 184210, 184215, 184371, 184374, 184383, 184389, 184673, 184678, 184682, 184687, 184716, 184719, 184784, 184786, 184845, 184846, 184928, 184930, 184933, 184938, 184964, 184967, 184968, 184987, 184988, 184990, 185029, 185031, 185116, 185126, 185127, 185132, 185133, 185134, 185160, 185164, 185189, 185196, 185198, 185203, 185206, 185208, 185213, 185217, 185221, 185282, 185284, 185288, 185289, 185291, 185292, 185293, 185296, 185299, 185300, 185302, 185303, 185348, 185349, 185350, 185351, 185356, 185359, 185360, 185361, 185362, 185363, 185368, 185371, 185375, 185459, 185460, 185461, 185465, 185467, 185472, 185475, 185569, 185574, 185575, 185578, 185580, 185581, 185582, 185583, 185588, 185589, 185659, 185687, 185692, 185697, 185698, 185699, 185700, 185701, 185738, 185764, 185765, 185768, 185775, 185776, 185778, 185784, 186003, 186006, 186007, 186009, 186011, 186073, 186078, 186079, 186082, 186163, 186164, 186165, 186167, 186205, 186208, 186319, 186320,

LHC12e 186386, 186387, 186388, 186389, 186429, 186432, 186453, 186460, 186507, 186508, 186509, 186510, 186511, 186514, 186598, 186601, 186602,

LHC12f 186843, 186844, 186845, 186851, 186853, 186857, 186859, 186938, 186965, 186987, 186989, 186990, 186992, 187136, 187143, 187145, 187146, 187149, 187150, 187151, 187152, 187201, 187202, 187203, 187335, 187337, 187339, 187340, 187341, 187343, 187744, 187749, 187753, 187783, 187785, 187787, 187791, 187849, 188021, 188025, 188027, 188028, 188029, 188093, 188101, 188108, 188123,

LHC12g 188362, 188438, 188440, 188442, 188443, 188444, 188446, 188447, 188449, 188454, 188455, 188488, 188490, 188499, 188500, 188503,

LHC12h 189122, 189146, 189228, 189229, 189231, 189246, 189301, 189306, 189310, 189315, 189316, 189340, 189341, 189344, 189347, 189350, 189351, 189352, 189353, 189397, 189400, 189402, 189406, 189407, 189409, 189410, 189411, 189473, 189523, 189526, 189603, 189605, 189610, 189611, 189612, 189616, 189621, 189623, 189647, 189648, 189650, 189654, 189656, 189658, 189659, 189696, 189697, 189698, 189699, 189736, 189737, 190209, 190210, 190212, 190214, 190215, 190216, 190240, 190303, 190337, 190338, 190340, 190341, 190342, 190386, 190388, 190389, 190390, 190392, 190393, 190416, 190417, 190418, 190419, 190421, 190422, 190424, 190425, 190895, 190898, 190903, 190904, 190968, 190970, 190974, 190979, 190981, 190983, 190984, 191129, 191227, 191229, 191230, 191231, 191232, 191234, 191241, 191242, 191244, 191245, 191247, 191248, 191450, 191451, 192004, 192072, 192073, 192075, 192095,

192125, 192128, 192136, 192140, 192141, 192172, 192174, 192177, 192194, 192197, 192199, 192200, 192201, 192202, 192205, 192246, 192344, 192347, 192348, 192349, 192415, 192417, 192453, 192461, 192468, 192471, 192492, 192497, 192499, 192505, 192510, 192511, 192688, 192707, 192708, 192709, 192729, 192731, 192732,

LHC12i 192772, 192775, 192778, 192779, 192820, 192822, 192824, 193004, 193005, 193007, 193008, 193011, 193014, 193047, 193049, 193051, 193092, 193093, 193148, 193150, 193151, 193152, 193153, 193184, 193750, 193752,

C.7.2 p–Pb at $\sqrt{s_{\text{NN}}} = 5.02$ TeV

LHC13b 195344, 195346, 195351, 195389, 195390, 195391, 195479, 195480, 195482, 195483,

LHC13c 195529, 195531, 195566, 195567, 195568, 195592, 195593, 195596, 195633, 195635, 195644, 195673, 195675, 195677,

LHC13d 195681, 195682, 195724, 195760, 195767, 195783, 195787, 195826, 195827, 195829, 195831, 195867, 195869, 195872,

LHC13e 195935, 195954, 195955, 195989, 195994, 196000, 196006, 196085, 196089, 196090, 196091, 196099, 196105, 196107, 196185, 196187, 196190, 196194, 196197, 196199, 196200, 196201, 196203, 196208, 196214,

LHC13f 196528, 196535, 196563, 196564, 196566, 196568, 196601, 196605, 196608, 196648, 196701, 196702, 196706, 196721, 196722, 196772, 196869, 196965, 196967, 196972, 196973, 196974, 197003, 197011, 197012, 197015, 197089, 197091, 197092, 197094, 197098, 197099, 197138, 197139, 197142, 197184, 197247, 197248, 197254, 197255, 197256, 197258, 197260, 197296, 197297, 197298, 197299, 197302, 197341, 197342, 197348, 197349, 197351, 197386, 197387, 197388,

C.7.3 pp at $\sqrt{s} = 2.76$ TeV

LHC13g 197470, 197471, 197496, 197497, 197499, 197500, 197501, 197529, 197531, 197583, 197584, 197606, 197608, 197611, 197613, 197643, 197669,

Appendix D

Jet-hadron correlation analysis

In this appendix, we first provide the list of runs used for the analysis, see Section D.1. In Section D.2, we list the used track cuts, the corresponding explanation can be found in the text. Section D.3 shows the $N_{\sigma,p}$ fits for all considered momentum slices. It further contains the extracted yields per particle species.

D.1 Run lists

LHC10h (ESD) 137161, 137162, 137231, 137232, 137235, 137236, 137243, 137366, 137431, 137432, 137434, 137439, 137440, 137441, 137443, 137530, 137531, 137539, 137541, 137544, 137546, 137549, 137595, 137608, 137638, 137639, 137685, 137686, 137691, 137692, 137693, 137704, 137718, 137722, 137724, 137751, 137752, 137844, 137848, 138190, 138192, 138197, 138201, 138225, 138275, 138364, 138396, 138438, 138439, 138442, 138469, 138534, 138578, 138579, 138582, 138583, 138621, 138624, 138638, 138652, 138653, 138662, 138666, 138730, 138732, 138837, 138870, 138871, 138872, 139028, 139029, 139036, 139037, 139038, 139105, 139107, 139173, 139309, 139310, 139314, 139328, 139329, 139360, 139437, 139438, 139465, 139503, 139505, 139507, 139510

LHC10h AOD086 139510, 139507, 139505, 139503, 139465, 139438, 139437, 139360, 139329, 139328, 139314, 139310, 139309, 139173, 139107, 139105, 139038, 139037, 139036, 139029, 139028, 138872, 138871, 138870, 138837, 138732, 138730, 138666, 138662, 138653, 138652, 138638, 138624, 138621, 138583, 138582, 138579, 138578, 138534, 138469, 138442, 138439, 138438, 138396, 138364, 138275, 138225, 138201, 138197, 138192, 138190, 137848, 137844, 137752, 137751, 137724, 137722, 137718, 137704, 137693, 137692, 137691, 137686, 137685, 137639, 137638, 137608, 137595, 137549, 137546, 137544, 137541, 137539, 137531, 137530, 137443, 137441, 137440, 137439, 137434, 137432, 137431, 137430, 137366, 137243, 137236, 137235, 137232, 137231, 137162, 137161

LHC11h AOD115 divided into sub-samples:

good: 167915, 167987, 167988, 168069, 168076, 168107, 168108, 168115, 168310, 168311, 168322, 168325, 168341, 168342, 168361, 168362, 168458, 168460, 168464, 168467, 168511, 168512, 168777, 168826, 168988, 168992, 169035, 169091, 169094, 169138, 169144, 169145, 169148, 169156, 169160, 169167, 169238, 169411, 169415, 169417, 169835, 169837, 169838, 169846, 169855, 169858, 169859, 169923, 170027, 170081

semi-good (I-C13): 170040, 170083, 170084, 170085, 170088, 170089, 170091, 170155,

170159, 170163, 170193, 170203, 170204, 170228, 170230, 170268, 170269, 170270, 170306, 170308, 170309

semi-good (O-C08): 169040, 169044, 169045, 169099, 169418, 169419, 169420, 169475, 169498, 169504, 169506, 169512, 169515, 169550, 169553, 169554, 169555, 169557, 169586, 169587, 169588, 169590, 169591

LHC11h AOD145 divided into sub-samples:

good: 167903, 167915, 167987, 167988, 168066, 168068, 168069, 168076, 168104, 168107, 168108, 168115, 168212, 168310, 168311, 168322, 168325, 168341, 168342, 168361, 168362, 168458, 168460, 168461, 168464, 168467, 168511, 168512, 168777, 168826, 168984, 168988, 168992, 169035, 169091, 169094, 169138, 169143, 169144, 169145, 169148, 169156, 169160, 169167, 169238, 169411, 169415, 169417, 169835, 169837, 169838, 169846, 169855, 169858, 169859, 169923, 169956, 170027, 170036, 170081

semi-good (I-C13): 169975, 169981, 170038, 170040, 170083, 170084, 170085, 170088, 170089, 170091, 170152, 170155, 170159, 170163, 170193, 170195, 170203, 170204, 170228, 170230, 170268, 170269, 170270, 170306, 170308, 170309

semi-good (OROC C08): 169040, 169044, 169045, 169099, 169418, 169420, 169475, 169498, 169504, 169506, 169512, 169515, 169550, 169553, 169554, 169555, 169557, 169584, 169586, 169587, 169588, 169590, 169591,

LHC11a10a (minimum bias Monte Carlo)

138653, 138662, 138666, 138730, 138732, 138837, 138870, 138871, 138872, 139028, 139029, 139036, 139037, 139038, 139105, 139107, 139173, 139309, 139310, 139314, 139328, 139329, 139360, 139437, 139438, 139465, 139503, 139505, 139507, 139510

LHC11a10a_bis (minimum bias Monte Carlo)

137161, 137162, 137231, 137232, 137235, 137236, 137243, 137366, 137431, 137432, 137434, 137439, 137440, 137441, 137443, 137530, 137531, 137539, 137541, 137544, 137546, 137549, 137595, 137608, 137638, 137639, 137685, 137686, 137691, 137692, 137693, 137704, 137718, 137722, 137724, 137751, 137752, 137844, 137848, 138190, 138192, 138197, 138201, 138225, 138275, 138364, 138396, 138438, 138439, 138442, 138469, 138534, 138578, 138579, 138582, 138583, 138621, 138624, 138638, 138652, 138653, 138662, 138666, 138730, 138732, 138837, 138870, 138871, 138872, 139028, 139029, 139036, 139037, 139038, 139105, 139107, 139173, 139309, 139310, 139314, 139328, 139329, 139360, 139437, 139438, 139465, 139503, 139505, 139507, 139510

D.2 Track cuts

The following track cuts were used for the associate candidates:

- at least 70 crossed TPC rows
- ratio of crossed rows and findable clusters in the TPC at least 0.8
- χ^2 per TPC cluster below 4
- reject kink daughters
- require TPC and ITS refit
- require hit in one SPD layer
- maximum longitudinal DCA to primary vertex 2 cm

- maximum transverse DCA to primary vertex $0.0105 \text{ cm} + \frac{0.0350 \text{ cm}}{(p_{\perp}/(\text{GeV}/c))^{1.1}}$
- TPC constrained global χ^2 below 36
- χ^2 per ITS cluster below 36

D.3 Proton identification

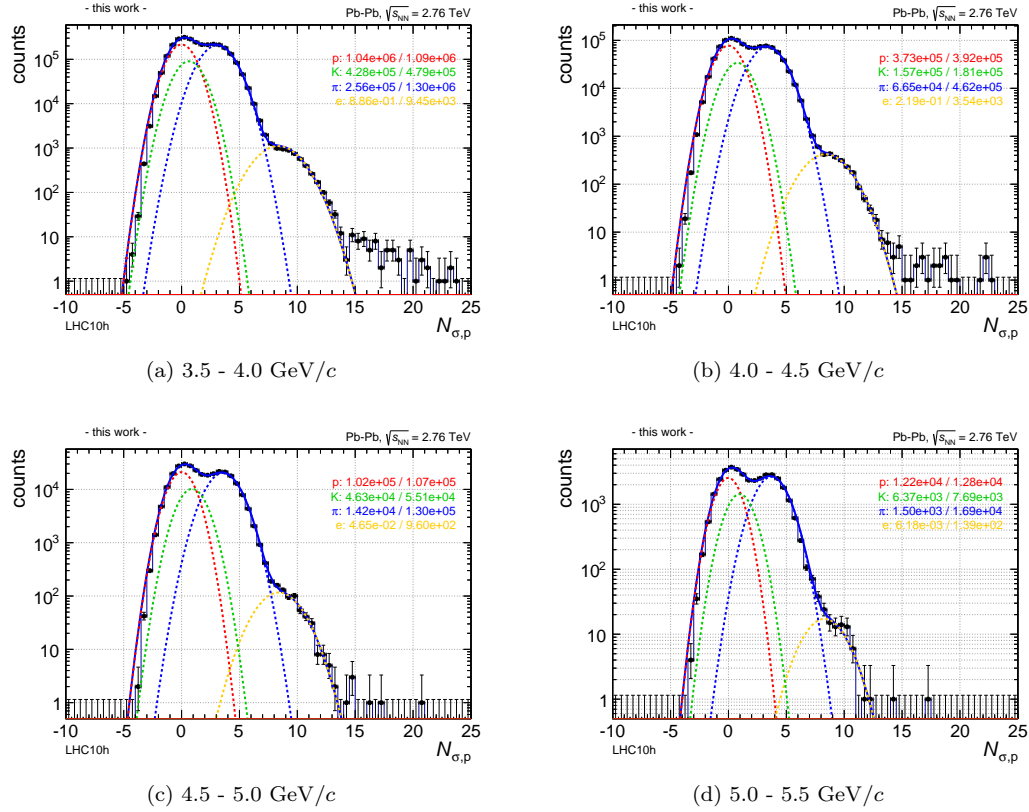


Figure D.1: TPC $N_{\sigma,p}$ fits (central): The measured distributions (associate candidates) are fitted with Gaussians for e, π , K, p. Only the yields are free parameters, while the mean and width are taken from the templates described in Section 5.7. The numbers give the particle yields in the range from -2 to $+2$ and the total integral of each Gaussian.

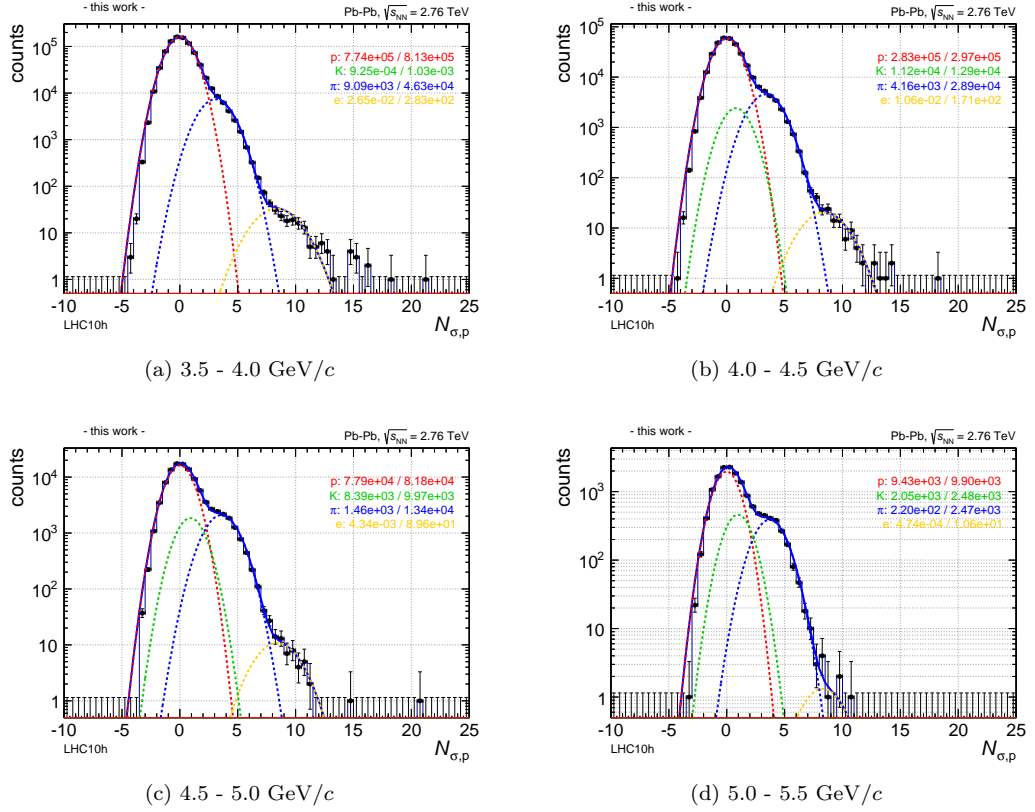


Figure D.2: TPC $N_{\sigma,p}$ fits after TOF cut (central): The measured distributions (associate candidates) after application of a 2σ cut on the TOF $N_{\sigma,p}$ are fitted with Gaussians for e, π , K, p. Only the yields are free parameters, while the mean and width are taken from the templates described in Section 5.7. The numbers give the particle yields in the range from -2 to $+2$ and the total integral of each Gaussian.

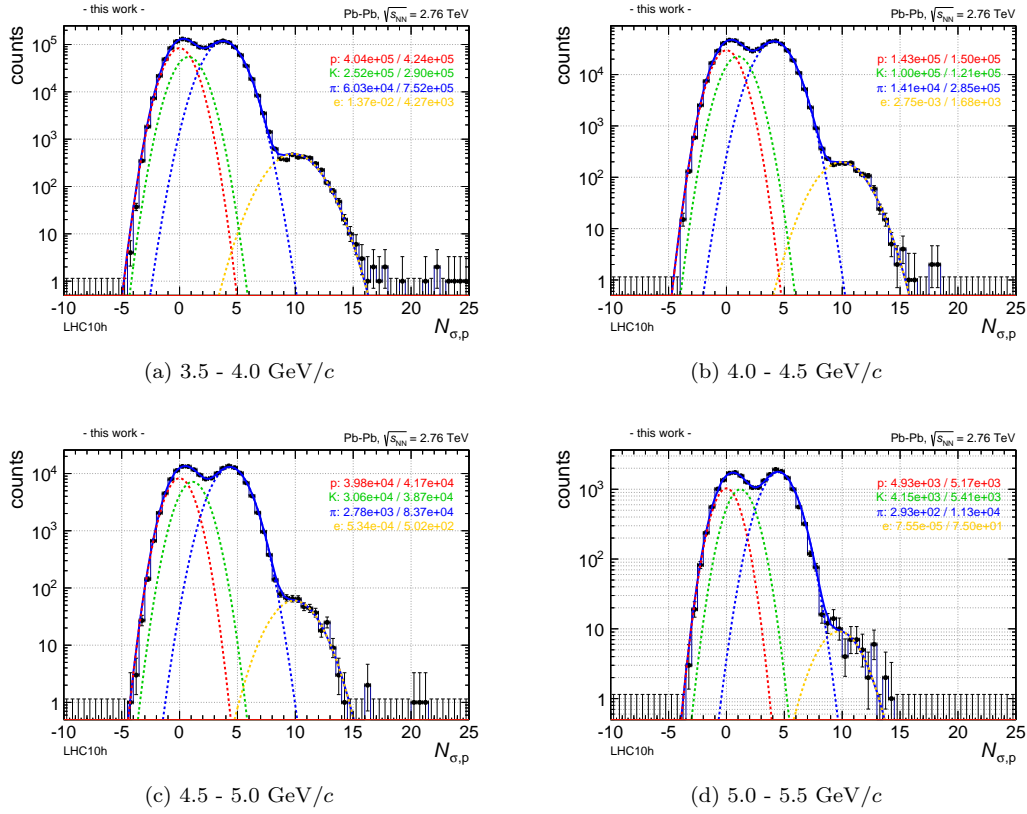


Figure D.3: TPC $N_{\sigma,p}$ fits (semi-central): The measured distributions (associate candidates) are fitted with Gaussians for e, π , K, p. Only the yields are free parameters, while the mean and width are taken from the templates described in Section 5.7. The numbers give the particle yields in the range from -2 to $+2$ and the total integral of each Gaussian.

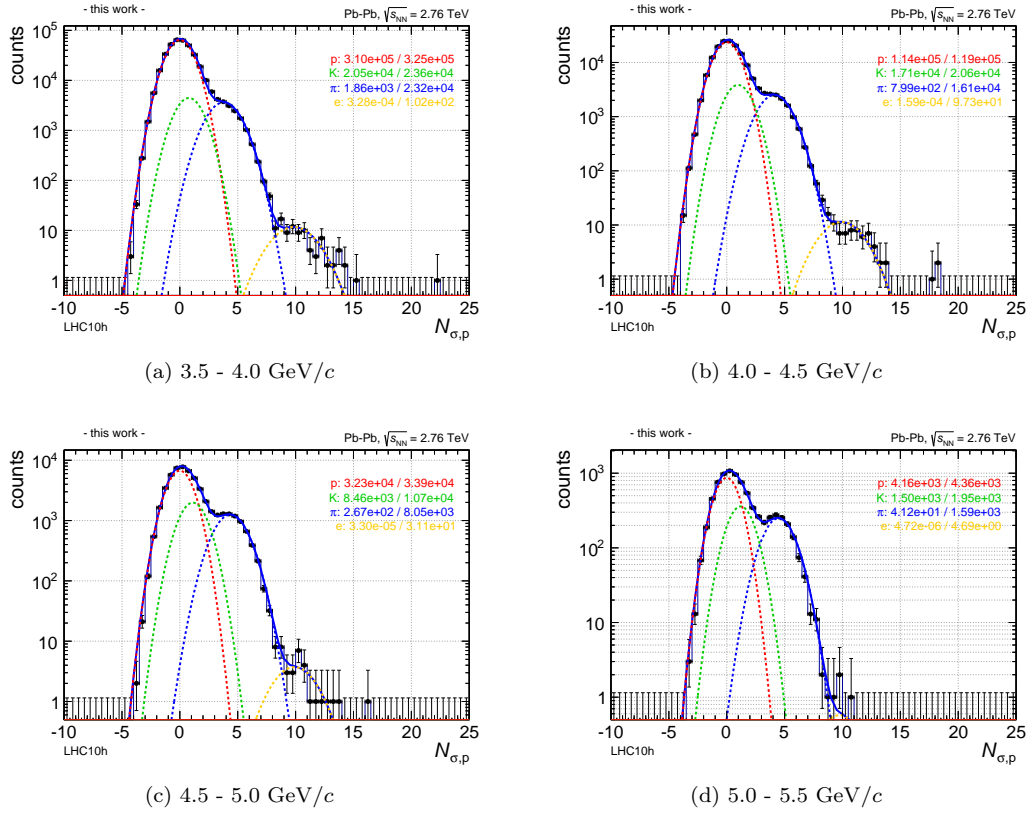


Figure D.4: TPC $N_{\sigma,p}$ fits after TOF cut (semi-central): The measured distributions (associate candidates) after application of a 2σ cut on the TOF $N_{\sigma,p}$ are fitted with Gaussians for e, π , K, p. Only the yields are free parameters, while the mean and width are taken from the templates described in Section 5.7. The numbers give the particle yields in the range from -2 to $+2$ and the total integral of each Gaussian.

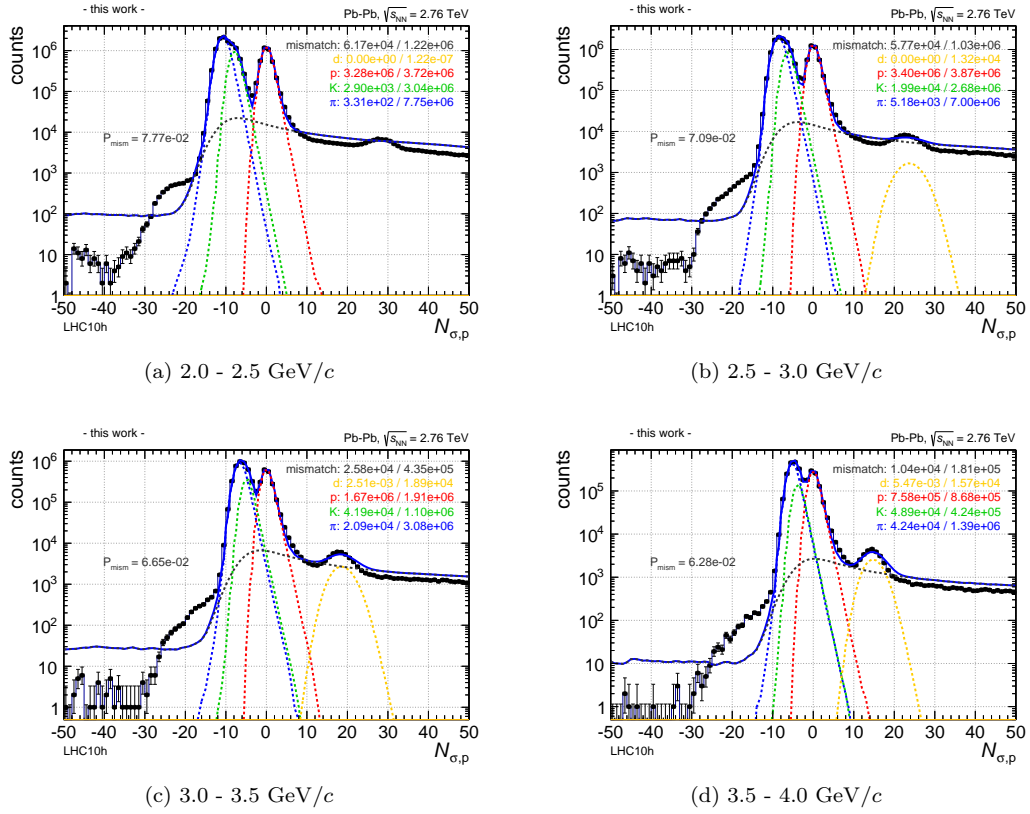


Figure D.5: TOF $N_{\sigma,p}$ fits (central): The measured distributions (associate candidates) are fitted with templates for π , K, p, d, and mismatches. Only the yields are free parameters, while the shapes are taken from the templates described in Section 5.7. The numbers give the particle yields in the range from -2 to $+2$ and the total integral of each template.

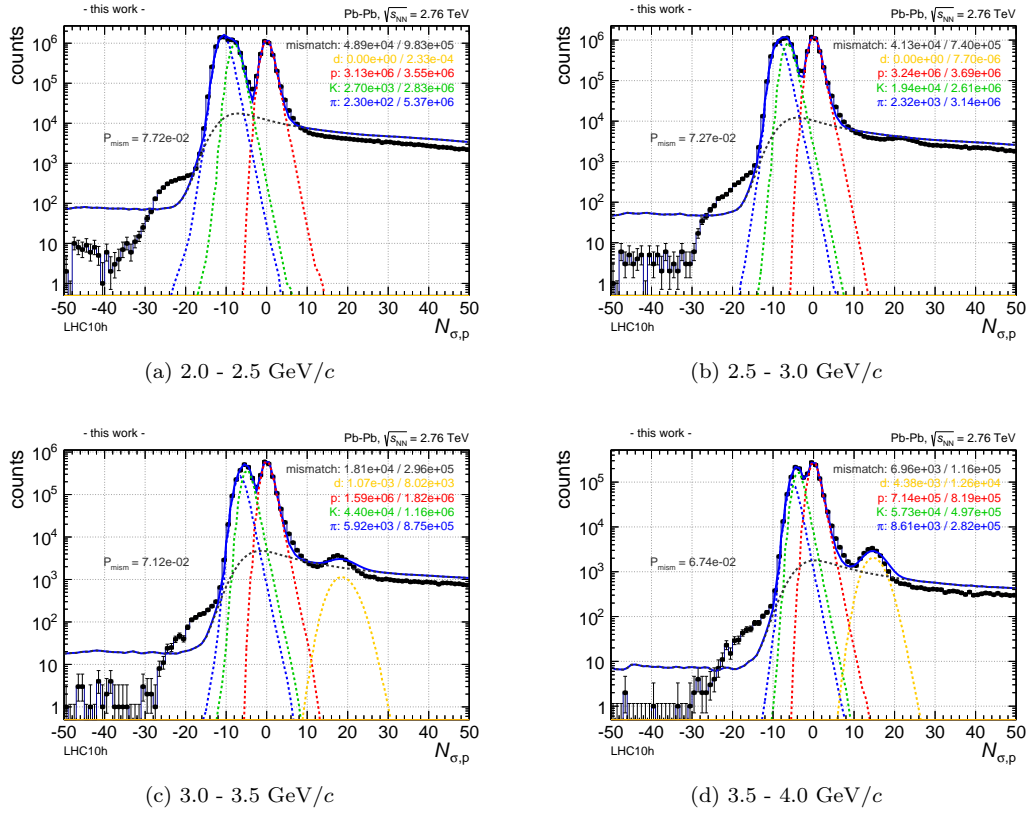


Figure D.6: TOF $N_{\sigma,p}$ fits after TPC cut (central): The measured distributions (associate candidates) after application of a 2σ cut on the TPC $N_{\sigma,p}$ are fitted with templates for π , K , p , d , and mismatches. Only the yields are free parameters, while the shapes are taken from the templates described in Section 5.7. The numbers give the particle yields in the range from -2 to $+2$ and the total integral of each template.

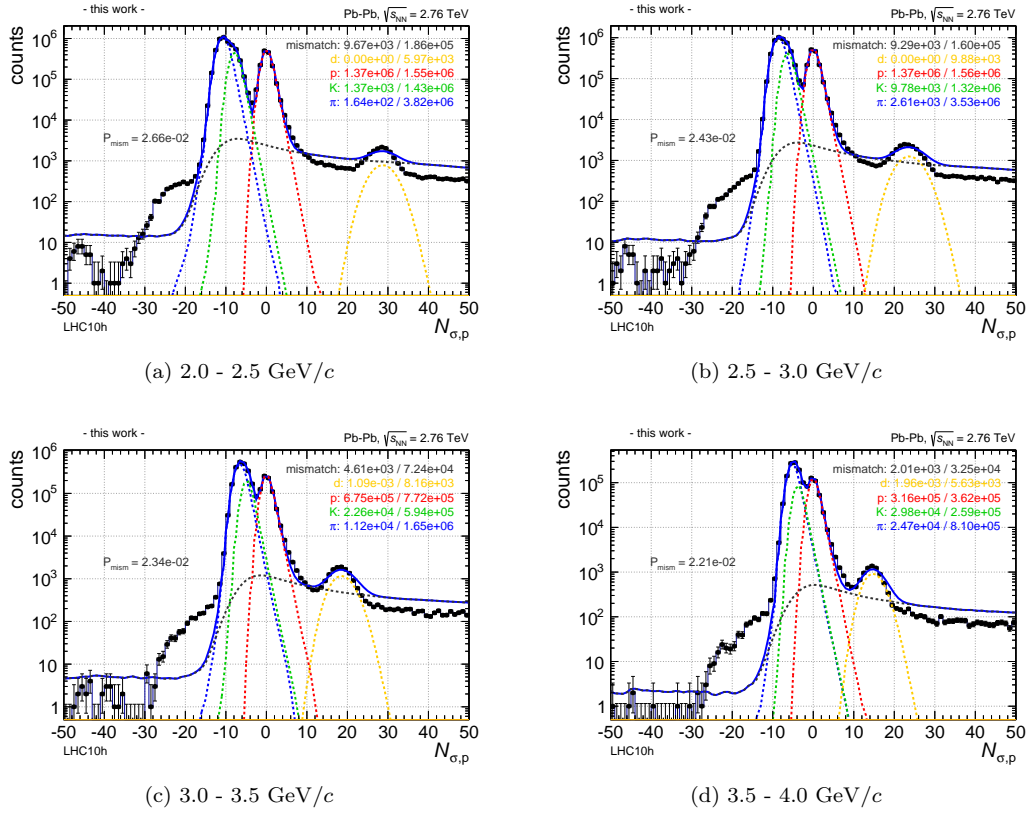


Figure D.7: TOF $N_{\sigma,p}$ fits (semi-central): The measured distributions (associate candidates) are fitted with templates for π , K, p, d, and mismatches. Only the yields are free parameters, while the shapes are taken from the templates described in Section 5.7. The numbers give the particle yields in the range from -2 to $+2$ and the total integral of each template.

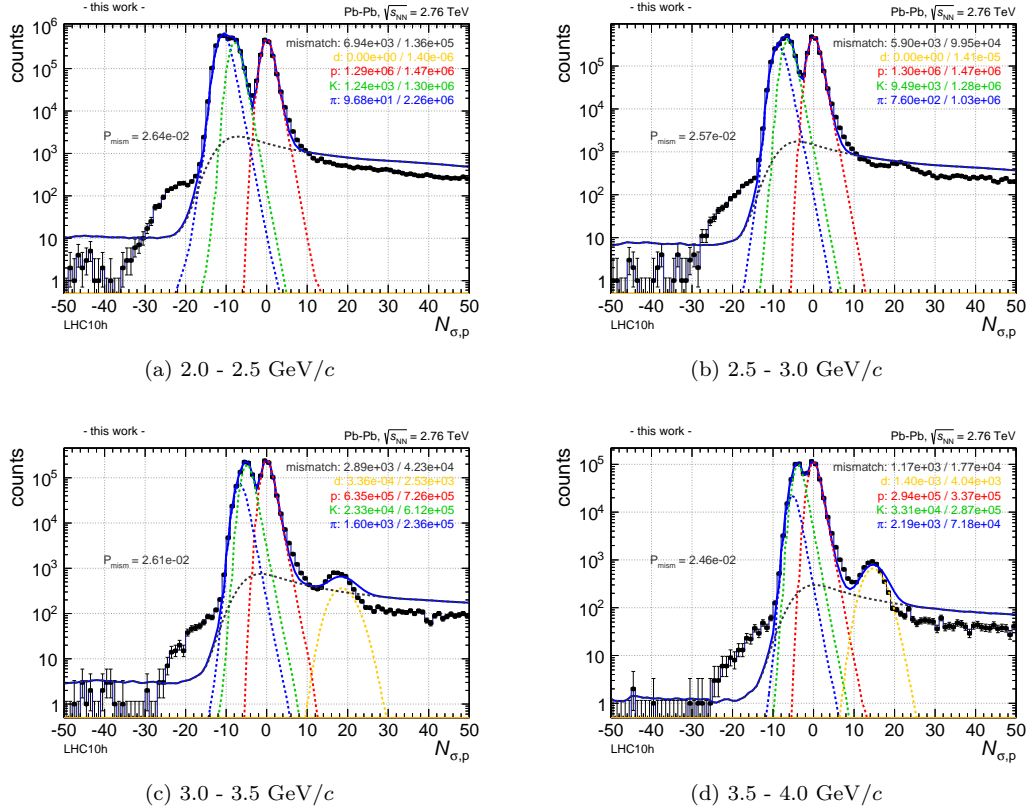


Figure D.8: TOF $N_{\sigma,p}$ fits after TPC cut (semi-central): The measured distributions (associate candidates) after application of a 2σ cut on the TPC $N_{\sigma,p}$ are fitted with templates for π , K, p, d, and mismatches. Only the yields are free parameters, while the shapes are taken from the templates described in Section 5.7. The numbers give the particle yields in the range from -2 to $+2$ and the total integral of each template.

p (GeV/ c)	Υ_p^{TPC}	Υ_p^{TOF}	$\hat{\Upsilon}_p^{\text{TPC}}$	Θ_p^{TOF}	$\hat{\Upsilon}_p^{\text{TOF}}$	Θ_p^{TPC}	$\hat{\Theta}_p^{\text{TPC}}$	$\hat{\Theta}_p^{\text{TOF}}$
2.0 - 2.5	4.99e+06	4.03e+06	4.75e+06	3.85e+06	3.30e+06	3.19e+06	3.03e+06	3.15e+06
2.5 - 3.0	7.42e+06	4.16e+06	7.07e+06	3.98e+06	3.41e+06	3.44e+06	3.27e+06	3.26e+06
3.0 - 3.5	2.58e+06	2.05e+06	2.46e+06	1.96e+06	1.68e+06	1.72e+06	1.64e+06	1.60e+06
3.5 - 4.0	1.09e+06	9.27e+05	1.04e+06	8.78e+05	7.61e+05	8.13e+05	7.74e+05	7.18e+05
4.0 - 4.5	3.92e+05	3.33e+05	3.73e+05	3.13e+05	2.74e+05	2.97e+05	2.83e+05	2.56e+05
4.5 - 5.0	1.07e+05	9.15e+04	1.02e+05	8.55e+04	7.53e+04	8.18e+04	7.79e+04	7.01e+04
5.0 - 5.5	1.28e+04	1.17e+04	1.22e+04	1.07e+04	9.60e+03	9.90e+03	9.43e+03	8.79e+03
total	1.66e+07	1.16e+07	1.58e+07	1.11e+07	9.51e+06	9.55e+06	9.09e+06	9.06e+06

p (GeV/ c)	$\Upsilon_{np}^{\text{TPC}}$	$\Upsilon_{np}^{\text{TOF}}$	$\hat{\Upsilon}_{np}^{\text{TPC}}$	Θ_{np}^{TOF}	$\hat{\Upsilon}_{np}^{\text{TOF}}$	Θ_{np}^{TPC}	$\hat{\Theta}_{np}^{\text{TPC}}$	$\hat{\Theta}_{np}^{\text{TOF}}$
2.0 - 2.5	1.07e+07	1.17e+07	7.95e+06	8.89e+06	4.91e+04	1.63e+05	1.25e+05	3.70e+04
2.5 - 3.0	7.17e+06	1.04e+07	3.08e+06	6.20e+06	6.63e+04	5.99e+04	2.55e+04	4.68e+04
3.0 - 3.5	3.97e+06	4.50e+06	1.68e+06	2.19e+06	8.05e+04	4.71e+04	1.30e+04	5.95e+04
3.5 - 4.0	1.79e+06	1.95e+06	6.84e+05	8.49e+05	9.83e+04	4.66e+04	9.09e+03	6.93e+04
4.0 - 4.5	6.47e+05	7.07e+05	2.23e+05	2.87e+05	6.76e+04	4.20e+04	1.54e+04	4.48e+04
4.5 - 5.0	1.86e+05	2.01e+05	6.05e+04	7.71e+04	3.10e+04	2.35e+04	9.85e+03	1.85e+04
5.0 - 5.5	2.47e+04	2.59e+04	7.88e+03	9.43e+03	5.36e+03	4.96e+03	2.27e+03	2.97e+03
total	2.45e+07	2.95e+07	1.37e+07	1.85e+07	3.98e+05	3.87e+05	2.00e+05	2.79e+05

Table D.1: Particle yields before and after TPC and TOF cuts in momentum bins for central events. The variables are explained in Section 5.7.3.

p (GeV/ c)	Υ_p^{TPC}	Υ_p^{TOF}	$\hat{\Upsilon}_p^{\text{TPC}}$	Θ_p^{TOF}	$\hat{\Upsilon}_p^{\text{TOF}}$	Θ_p^{TPC}	$\hat{\Theta}_p^{\text{TPC}}$	$\hat{\Theta}_p^{\text{TOF}}$
2.0 - 2.5	1.17e+06	1.59e+06	1.11e+06	1.51e+06	1.37e+06	1.13e+06	1.08e+06	1.30e+06
2.5 - 3.0	3.05e+06	1.60e+06	2.90e+06	1.51e+06	1.37e+06	1.39e+06	1.32e+06	1.30e+06
3.0 - 3.5	1.00e+06	7.90e+05	9.53e+05	7.45e+05	6.76e+05	7.00e+05	6.67e+05	6.36e+05
3.5 - 4.0	4.24e+05	3.70e+05	4.04e+05	3.46e+05	3.17e+05	3.25e+05	3.10e+05	2.95e+05
4.0 - 4.5	1.50e+05	1.36e+05	1.43e+05	1.26e+05	1.16e+05	1.19e+05	1.14e+05	1.08e+05
4.5 - 5.0	4.17e+04	3.90e+04	3.98e+04	3.60e+04	3.33e+04	3.39e+04	3.23e+04	3.07e+04
5.0 - 5.5	5.17e+03	5.25e+03	4.93e+03	4.72e+03	4.50e+03	4.36e+03	4.16e+03	4.04e+03
total	5.84e+06	4.53e+06	5.56e+06	4.28e+06	3.89e+06	3.71e+06	3.53e+06	3.67e+06

p (GeV/ c)	$\Upsilon_{np}^{\text{TPC}}$	$\Upsilon_{np}^{\text{TOF}}$	$\hat{\Upsilon}_{np}^{\text{TPC}}$	Θ_{np}^{TOF}	$\hat{\Upsilon}_{np}^{\text{TOF}}$	Θ_{np}^{TPC}	$\hat{\Theta}_{np}^{\text{TPC}}$	$\hat{\Theta}_{np}^{\text{TOF}}$
2.0 - 2.5	5.83e+06	5.41e+06	4.03e+06	3.65e+06	9.01e+03	2.55e+05	2.25e+05	6.25e+03
2.5 - 3.0	3.53e+06	4.98e+06	9.79e+05	2.36e+06	1.94e+04	1.93e+04	5.37e+03	1.38e+04
3.0 - 3.5	2.10e+06	2.31e+06	6.61e+05	8.73e+05	3.72e+04	1.91e+04	2.62e+03	2.64e+04
3.5 - 4.0	1.05e+06	1.10e+06	3.12e+05	3.72e+05	5.60e+04	4.69e+04	2.24e+04	3.59e+04
4.0 - 4.5	4.08e+05	4.22e+05	1.14e+05	1.32e+05	4.19e+04	3.68e+04	1.78e+04	2.44e+04
4.5 - 5.0	1.23e+05	1.26e+05	3.34e+04	3.75e+04	2.02e+04	1.88e+04	8.73e+03	1.04e+04
5.0 - 5.5	1.68e+04	1.67e+04	4.44e+03	4.70e+03	3.56e+03	3.55e+03	1.54e+03	1.70e+03
total	1.31e+07	1.44e+07	6.13e+06	7.44e+06	1.87e+05	4.00e+05	2.83e+05	1.19e+05

Table D.2: Particle yields before and after TPC and TOF cuts in momentum bins for semi-central events. The variables are explained in Section 5.7.3.

Appendix E

Acronyms

AOD	Analysis Object Data (event data)
BC	Bunch Counter
CTP	Central Trigger Processor
DAQ	Data AcQuisition
DCA	Distance of Closest Approach
DCS	Detector Control System
DDL	Detector Data Link
EMCAL	ElectroMagnetic CALorimeter
ESD	Event Summary Data (event data)
FEE	Front-End Electronics
FF	Fragmentation Function
FSM	Finite State Machine
GTU	Global Tracking Unit
HBT	Hanbury Brown-Twiss
HLT	High-Level Trigger
IP	Interaction Point
ITS	Inner Tracking System
JEWEL	Jet Evolution With Energy Loss (Monte Carlo event generator)
LHC	Large Hadron Collider
LPM	Landau-Pomerantschuk-Migdal
MCM	Multi-Chip Module

ME	Matrix Element
OCDB	Off-line Condition DataBase
ORI	Optical Read-out Interface
PASA	PreAmplifier and ShAper
PDF	Parton Density Function
PHOS	PHOton Spectrometer
PID	Particle IDentification
PT	PreTrigger
QGP	Quark-Gluon Plasma
RHIC	Relativistic Heavy-Ion Collider
ROB	Read-Out Board
SCSN	Slow Control Serial Network
SDD	Silicon Drift Detector
SMU	SuperModule Unit (GTU)
SPD	Silicon Pixel Detector
SSD	Silicon Strip Detector
TGU	TriGger Unit (GTU)
TMU	Track Matching Unit (GTU)
T0	forward quartz Cerenkov detectors
TOF	Time-Of-Flight detector
TPC	Time Projection Chamber
TRAP	TRAcklet Processor
TRD	Transition Radiation Detector
TTC	Timing and Trigger Control
V0	forward scintillator wheels
WU	Wake-Up
ZDC	Zero Degree Calorimeter

Bibliography

- [1] E. Rutherford. The scattering of α and β particles by matter and the structure of the atom. *Phil.Mag.*, 21(125):669–688, 1911. <http://dx.doi.org/10.1080/14786440508637080>.
- [2] J. J. Thomson. XL. Cathode rays. *Phil.Mag.*, 44(269):293–316, 1897. <http://dx.doi.org/10.1080/14786449708621070>.
- [3] J. C. Maxwell. A Dynamical Theory of the Electromagnetic Field. *Phil.Trans.Roy.Soc.Lond.*, 155:459–512, 1865. <http://dx.doi.org/10.1098/rstl.1865.0008>.
- [4] J. Chadwick. Possible Existence of a Neutron. *Nature*, 129:312, 1932. <http://dx.doi.org/10.1038/129312a0>.
- [5] C. D. Anderson. The Positive Electron. *Phys.Rev.*, 43:491–494, 1933. <http://dx.doi.org/10.1103/PhysRev.43.491>.
- [6] H. Yukawa. On the interaction of elementary particles. *Proc.Phys.Math.Soc.Jap.*, 17:48–57, 1935.
- [7] C. M. G. Lattes, G. P. S. Occhialini, and C. F. Powell. Observations on the Tracks of Slow Mesons in Photographic Emulsions. *Nature*, 160:453–456, 1947. <http://dx.doi.org/10.1038/160453a0>.
- [8] G. D. Rochester and C. C. Butler. Evidence for the Existence of New Unstable Elementary Particles. *Nature*, 160:855–857, 1947. <http://dx.doi.org/10.1038/160855a0>.
- [9] S. C. Frautschi. Statistical Bootstrap Model of Hadrons. *Phys.Rev.*, D3:2821–2834, 1971. <http://dx.doi.org/10.1103/PhysRevD.3.2821>.
- [10] J. Beringer et al. (Particle Data Group). Review of Particle Physics. *Phys.Rev.*, D86:010001, 2012. <http://dx.doi.org/10.1103/PhysRevD.86.010001>.
- [11] R. Hagedorn. Statistical thermodynamics of strong interactions at high-energies. *Nuovo Cim.Suppl.*, 3:147–186, 1965.
- [12] M. Gell-Mann. A Schematic Model of Baryons and Mesons. *Phys.Lett.*, 8(3):214–215, 1964. [http://dx.doi.org/10.1016/S0031-9163\(64\)92001-3](http://dx.doi.org/10.1016/S0031-9163(64)92001-3).
- [13] J. D. Bjorken. Asymptotic Sum Rules at Infinite Momentum. *Phys.Rev.*, 179(5):1547–1553, 1969. <http://dx.doi.org/10.1103/PhysRev.179.1547>.

- [14] E. D. Bloom, D. H. Coward, H. C. DeStaebler, et al. High-Energy Inelastic e-p Scattering at 6° and 10° . *Phys.Rev.Lett.*, 23:930–934, 1969. <http://dx.doi.org/10.1103/PhysRevLett.23.930>.
- [15] R. P. Feynman. The Behavior of Hadron Collisions at Extreme Energies. In M. Noz and Y. Kim, editors, *Special Relativity and Quantum Theory*, volume 33 of *Fundamental Theories of Physics*, pages 289–304. Springer Netherlands, 1988. http://dx.doi.org/10.1007/978-94-009-3051-3_25.
- [16] O. W. Greenberg. Spin and Unitary Spin Independence in a Paraquark Model of Baryons and Mesons. *Phys.Rev.Lett.*, 13:598–602, 1964. <http://dx.doi.org/10.1103/PhysRevLett.13.598>.
- [17] M. Y. Han and Y. Nambu. Three-Triplet Model with Double SU(3) Symmetry. *Phys.Rev.*, 139:B1006–B1010, 1965. <http://dx.doi.org/10.1103/PhysRev.139.B1006>.
- [18] M. L. Perl, E. R. Lee, and D. Loomba. Searches for Fractionally Charged Particles. *Ann.Rev.Nucl.Part.Sci.*, 59:47–65, 2009. <http://dx.doi.org/10.1146/annurev-nucl-121908-122035>.
- [19] D. J. Gross and F. Wilczek. Ultraviolet Behavior of Nonabelian Gauge Theories. *Phys.Rev.Lett.*, 30:1343–1346, 1973. <http://dx.doi.org/10.1103/PhysRevLett.30.1343>.
- [20] H. D. Politzer. Reliable Perturbative Results for Strong Interactions? *Phys.Rev.Lett.*, 30:1346–1349, 1973. <http://dx.doi.org/10.1103/PhysRevLett.30.1346>.
- [21] W. J. Marciano and H. Pagels. Quantum Chromodynamics. *Phys.Rep.*, 36C:137–276, 1978.
- [22] R. Brandelik et al. (TASSO Collaboration). Evidence for a spin-1 gluon in three-jet events. *Phys.Lett.*, B97:453, 1980. [http://dx.doi.org/10.1016/0370-2693\(80\)90639-5](http://dx.doi.org/10.1016/0370-2693(80)90639-5).
- [23] G. Aad et al. (ATLAS Collaboration). Observation of a new particle in the search for the Standard Model Higgs boson with the ATLAS detector at the LHC. *Phys.Lett.*, B716(1):1–29, 2012. arXiv:1207.7214, <http://dx.doi.org/10.1016/j.physletb.2012.08.020>.
- [24] S. Chatrchyan et al. (CMS Collaboration). Observation of a new boson at a mass of 125 GeV with the CMS experiment at the LHC. *Phys.Lett.*, B716(1):30–61, 2012. arXiv:1207.7235, <http://dx.doi.org/10.1016/j.physletb.2012.08.021>.
- [25] K. G. Wilson. Confinement of Quarks. *Phys.Rev.*, D10:2445–2459, 1974. <http://dx.doi.org/10.1103/PhysRevD.10.2445>.
- [26] N. Cabibbo and G. Parisi. Exponential Hadronic Spectrum and Quark Liberation. *Phys.Lett.*, B59:67–69, 1975. [http://dx.doi.org/10.1016/0370-2693\(75\)90158-6](http://dx.doi.org/10.1016/0370-2693(75)90158-6).
- [27] J. C. Collins and M. J. Perry. Superdense Matter: Neutrons Or Asymptotically Free Quarks? *Phys. Rev. Lett.*, 34:1353–1356, 1975. <http://dx.doi.org/10.1103/PhysRevLett.34.1353>.
- [28] L. D. McLerran and B. Svetitsky. A Monte Carlo Study of SU(2) Yang-Mills Theory at Finite Temperature. *Phys.Lett.*, B98:195–198, 1981. [http://dx.doi.org/10.1016/0370-2693\(81\)90986-2](http://dx.doi.org/10.1016/0370-2693(81)90986-2).

- [29] L. D. McLerran and B. Svetitsky. Quark Liberation at High Temperature: A Monte Carlo Study of SU(2) Gauge Theory. *Phys.Rev.*, D24:450, 1981. <http://dx.doi.org/10.1103/PhysRevD.24.450>.
- [30] J. Kuti, J. Polonyi, and K. Szlachanyi. Monte Carlo Study of SU(2) Gauge Theory at Finite Temperature. *Phys.Lett.*, B98:199–204, 1981. [http://dx.doi.org/10.1016/0370-2693\(81\)90987-4](http://dx.doi.org/10.1016/0370-2693(81)90987-4).
- [31] F. Karsch (RBC-Bielefeld and hotQCD). Equation of state and more from lattice regularized QCD. *J. Phys.*, G35(10):104096, 2008. arXiv:0804.4148, <http://dx.doi.org/10.1088/0954-3899/35/10/104096>.
- [32] S. Borsanyi et al. (Wuppertal-Budapest Collaboration). Is there still any T_c mystery in lattice QCD? Results with physical masses in the continuum limit III. *JHEP*, 1009:073, 2010. arXiv:1005.3508, [http://dx.doi.org/10.1007/JHEP09\(2010\)073](http://dx.doi.org/10.1007/JHEP09(2010)073).
- [33] N. Itoh. Hydrostatic Equilibrium of Hypothetical Quark Stars. *Prog.Theor.Phys.*, 44:291–292, 1970. <http://dx.doi.org/10.1143/PTP.44.291>.
- [34] A. Chodos, R. L. Jaffe, K. Johnson, et al. A New Extended Model of Hadrons. *Phys.Rev.*, D9:3471–3495, 1974. <http://dx.doi.org/10.1103/PhysRevD.9.3471>.
- [35] A. Chodos, R. L. Jaffe, K. Johnson, et al. Baryon Structure in the Bag Theory. *Phys.Rev.*, D10:2599, 1974. <http://dx.doi.org/10.1103/PhysRevD.10.2599>.
- [36] T. A. DeGrand, R. L. Jaffe, K. Johnson, et al. Masses and other parameters of the light hadrons. *Phys.Rev.*, D12:2060, 1975. <http://dx.doi.org/10.1103/PhysRevD.12.2060>.
- [37] P. Braun-Munzinger, J. Stachel, J. P. Wessels, et al. Thermal equilibration and expansion in nucleus-nucleus collisions at the AGS. *Phys.Lett.*, B344(1-4):43–48, 1995. arXiv:nucl-th/9410026, [http://dx.doi.org/10.1016/0370-2693\(94\)01534-J](http://dx.doi.org/10.1016/0370-2693(94)01534-J).
- [38] J. Cleymans, D. Elliott, A. Keränen, et al. Thermal model analysis of particle ratios in Ni+Ni experiments using exact strangeness conservation. *Phys.Rev.*, C57:3319–3323, 1998. arXiv:nucl-th/9711066, <http://dx.doi.org/10.1103/PhysRevC.57.3319>.
- [39] P. Braun-Munzinger, J. Stachel, J. Wessels, et al. Thermal and hadrochemical equilibration in nucleus-nucleus collisions at the SPS. *Phys.Lett.*, B365(1-4):1–6, 1996. arXiv:nucl-th/9508020, [http://dx.doi.org/10.1016/0370-2693\(95\)01258-3](http://dx.doi.org/10.1016/0370-2693(95)01258-3).
- [40] A. Andronic, P. Braun-Munzinger, and J. Stachel. Hadron production in central nucleus-nucleus collisions at chemical freeze-out. *Nucl.Phys.*, A772(1-4):167–199, 2006. arXiv:nucl-th/0511071, <http://dx.doi.org/10.1016/j.nuclphysa.2006.03.012>.
- [41] A. Andronic, P. Braun-Munzinger, K. Redlich, et al. The statistical model in Pb-Pb collisions at the LHC. *Nucl.Phys.A904-905*, 2013:535c–538c, 2013. arXiv:1210.7724, <http://dx.doi.org/10.1016/j.nuclphysa.2013.02.070>.
- [42] L. Lederman and J. Wesener, editors. *Report of the workshop on BeV/nucleon collisions of heavy ions: how and why, November 29–December 1, 1974, Bear Mountain, New York*. Brookhaven National Laboratory Associated Universities, Inc., 1974. <http://www.osti.gov/scitech/servlets/purl/4061527>.
- [43] H. Grunder, C. Leemann, and F. Selph. Relativistic Heavy Ion Accelerators. In *10th International Conference On High-Energy Accelerators (HEACC)*, pages 321–338. 1977.

- [44] GSI-Geschichte - Ein Forschungslabor für alle. http://www.gsi.de/start/ueber_uns/geschichte.htm.
- [45] The history of CERN. <http://timeline.web.cern.ch/timelines/The-history-of-CERN?page=1>.
- [46] M. Harrison, S. G. Peggs, and T. Roser. The RHIC accelerator. *Ann.Rev.Nucl.Part.Sci.*, 52:425–469, 2002. <http://dx.doi.org/10.1146/annurev.nucl.52.050102.090650>.
- [47] G. F. Sterman and S. Weinberg. Jets from Quantum Chromodynamics. *Phys.Rev.Lett.*, 39:1436, 1977. <http://dx.doi.org/10.1103/PhysRevLett.39.1436>.
- [48] S. Catani, Y. L. Dokshitzer, M. Olsson, et al. New clustering algorithm for multijet cross-sections in e^+e^- annihilation. *Phys.Lett.*, B269:432–438, 1991. [http://dx.doi.org/10.1016/0370-2693\(91\)90196-W](http://dx.doi.org/10.1016/0370-2693(91)90196-W).
- [49] S. D. Ellis and D. E. Soper. Successive combination jet algorithm for hadron collisions. *Phys.Rev.*, D48:3160–3166, 1993. arXiv:hep-ph/9305266, <http://dx.doi.org/10.1103/PhysRevD.48.3160>.
- [50] Y. L. Dokshitzer, G. Leder, S. Moretti, et al. Better jet clustering algorithms. *JHEP*, 9708:001, 1997. arXiv:hep-ph/9707323, <http://dx.doi.org/10.1088/1126-6708/1997/08/001>.
- [51] M. Cacciari, G. P. Salam, and G. Soyez. The anti- k_t jet clustering algorithm. *JHEP*, 0804:063, 2008. arXiv:0802.1189, <http://dx.doi.org/10.1088/1126-6708/2008/04/063>.
- [52] M. Cacciari, G. P. Salam, and G. Soyez. FastJet User Manual. *Eur.Phys.J.*, C72:1896, 2012. arXiv:1111.6097, <http://dx.doi.org/10.1140/epjc/s10052-012-1896-2>.
- [53] P. Braun-Munzinger, K. Redlich, and J. Stachel. *Particle production in Heavy Ion Collisions*, pages 491–599. World Scientific, 2003. arXiv:nucl-th/0304013.
- [54] R. J. Glauber and G. Matthiae. High-energy scattering of protons by nuclei. *Nucl.Phys.*, B21:135–157, 1970.
- [55] J. D. Bjorken. Highly relativistic nucleus-nucleus collisions: The central rapidity region. *Phys. Rev.*, D27:140–151, 1983. <http://dx.doi.org/10.1103/PhysRevD.27.140>.
- [56] E. Fermi. High Energy Nuclear Events. *Prog.Theor.Phys.*, 5(5):570–583, 1950. <http://dx.doi.org/10.1143/PTP.5.570>.
- [57] L. D. Landau. On the multiparticle production in high-energy collisions. *Izv.Akad.Nauk Ser.Fiz.*, 17:51–64, 1953.
- [58] J. D. Bjorken. Energy Loss of Energetic Partons in Quark - Gluon Plasma: Possible Extinction of High p_T Jets in Hadron - Hadron Collisions. *pre-print*, 1982. <http://lss.fnal.gov/archive/1982/pub/Pub-82-059-T.pdf>.
- [59] L. D. Landau and I. Pomeranchuk. Limits of applicability of the theory of bremsstrahlung electrons and pair production at high-energies. *Dokl.Akad.Nauk Ser.Fiz.*, 92:535–536, 1953.
- [60] L. D. Landau and I. Pomeranchuk. Electron cascade process at very high-energies. *Dokl.Akad.Nauk Ser.Fiz.*, 92:735–738, 1953.

- [61] A. B. Migdal. Bremsstrahlung and Pair Production in Condensed Media at High Energies. *Phys.Rev.*, 103:1811–1820, 1956. <http://dx.doi.org/10.1103/PhysRev.103.1811>.
- [62] U. A. Wiedemann. Jet Quenching in Heavy Ion Collisions. *pre-print*, pages 521–562, 2010. arXiv:0908.2306.
- [63] D. d’Enterria. Jet quenching. *pre-print*, 2009. arXiv:0902.2011.
- [64] R. Baier, Y. L. Dokshitzer, A. H. Mueller, et al. Radiative energy loss of high-energy quarks and gluons in a finite volume quark - gluon plasma. *Nucl.Phys.*, B483(1-2):291–320, 1997. arXiv:hep-ph/9607355, [http://dx.doi.org/10.1016/S0550-3213\(96\)00553-6](http://dx.doi.org/10.1016/S0550-3213(96)00553-6).
- [65] B. G. Zakharov. Fully quantum treatment of the Landau-Pomeranchuk-Migdal effect in QED and QCD. *JETP Lett.*, 63:952–957, 1996. arXiv:hep-ph/9607440, <http://dx.doi.org/10.1134/1.567126>.
- [66] R. Baier, Y. L. Dokshitzer, A. H. Mueller, et al. Radiative energy loss and p_{\perp} -broadening of high-energy partons in nuclei. *Nucl.Phys.*, B484(1-2):265–282, 1997. arXiv:hep-ph/9608322, [http://dx.doi.org/10.1016/S0550-3213\(96\)00581-0](http://dx.doi.org/10.1016/S0550-3213(96)00581-0).
- [67] R. Baier, Y. L. Dokshitzer, A. H. Mueller, et al. Medium induced radiative energy loss: Equivalence between the BDMPS and Zakharov formalisms. *Nucl.Phys.*, B531(1-3):403–425, 1998. arXiv:hep-ph/9804212, [http://dx.doi.org/10.1016/S0550-3213\(98\)00546-X](http://dx.doi.org/10.1016/S0550-3213(98)00546-X).
- [68] M. Gyulassy and X.-n. Wang. Multiple collisions and induced gluon Bremsstrahlung in QCD. *Nucl.Phys.*, B420:583–614, 1994. arXiv:nucl-th/9306003, [http://dx.doi.org/10.1016/0550-3213\(94\)90079-5](http://dx.doi.org/10.1016/0550-3213(94)90079-5).
- [69] C. A. Salgado and U. A. Wiedemann. Calculating quenching weights. *Phys.Rev.*, D68:014008, 2003. arXiv:hep-ph/0302184, <http://dx.doi.org/10.1103/PhysRevD.68.014008>.
- [70] M. Gyulassy, P. Levai, and I. Vitev. Jet quenching in thin quark–gluon plasmas I: formalism. *Nucl.Phys.*, B571(1-2):197–233, 2000. arXiv:hep-ph/9907461, [http://dx.doi.org/10.1016/S0550-3213\(99\)00713-0](http://dx.doi.org/10.1016/S0550-3213(99)00713-0).
- [71] M. Gyulassy, P. Levai, and I. Vitev. Reaction operator approach to non-abelian energy loss. *Nucl.Phys.*, B594(1-2):371–419, 2001. arXiv:nucl-th/0006010, [http://dx.doi.org/10.1016/S0550-3213\(00\)00652-0](http://dx.doi.org/10.1016/S0550-3213(00)00652-0).
- [72] P. B. Arnold, G. D. Moore, and L. G. Yaffe. Photon Emission from Ultrarelativistic Plasmas. *JHEP*, 2001(11):57, 2001. arXiv:hep-ph/0109064, <http://dx.doi.org/10.1088/1126-6708/2001/11/057>.
- [73] J. M. Maldacena. The Large- N Limit of Superconformal Field Theories and Supergravity. *Adv.Theor.Math.Phys.*, 2:231–252, 1998. arXiv:hep-th/9711200.
- [74] J. Casalderrey-Solana, H. Liu, D. Mateos, et al. Gauge/String Duality, Hot QCD and Heavy Ion Collisions. *pre-print*, 2011. arXiv:1101.0618.
- [75] M. Gyulassy and X.-N. Wang. HIJING 1.0: A Monte Carlo program for parton and particle production in high-energy hadronic and nuclear collisions. *Comput.Phys.Commun.*, 83:307–331, 1994. arXiv:nucl-th/9502021, [http://dx.doi.org/10.1016/0010-4655\(94\)90057-4](http://dx.doi.org/10.1016/0010-4655(94)90057-4).

- [76] I. P. Lokhtin and A. M. Snigirev. A Model of jet quenching in ultrarelativistic heavy ion collisions and high- p_T hadron spectra at RHIC. *Eur.Phys.J.*, C45(1):211–217, 2006. arXiv:hep-ph/0506189, <http://dx.doi.org/10.1140/epjc/s2005-02426-3>.
- [77] A. Dainese, C. Loizides, and G. Paic. Leading-particle suppression in high energy nucleus-nucleus collisions. *Eur.Phys.J.*, C38(4):461–474, 2005. arXiv:hep-ph/0406201, <http://dx.doi.org/10.1140/epjc/s2004-02077-x>.
- [78] T. Renk. YaJEM: a Monte Carlo code for in-medium shower evolution. *Int.J.Mod.Phys.*, E20:1594–1599, 2011. arXiv:1009.3740, <http://dx.doi.org/10.1142/S0218301311019933>.
- [79] N. Armesto, L. Cunqueiro, and C. A. Salgado. Q-PYTHIA: A medium-modified implementation of final state radiation. *Eur.Phys.J.*, C63:679–690, 2009. arXiv:0907.1014, <http://dx.doi.org/10.1140/epjc/s10052-009-1133-9>.
- [80] K. C. Zapp, F. Krauss, and U. A. Wiedemann. A perturbative framework for jet quenching. *JHEP*, 2013(3):080, 2013. arXiv:1212.1599, [http://dx.doi.org/10.1007/JHEP03\(2013\)080](http://dx.doi.org/10.1007/JHEP03(2013)080).
- [81] K. C. Zapp. JEWEL 2.0.0 - Directions for Use. *pre-print*, 2013. arXiv:1311.0048.
- [82] K. Zapp, J. Stachel, and U. A. Wiedemann. Local Monte Carlo Implementation of the Non-Abelian Landau-Pomeranchuk-Migdal Effect. *Phys.Rev.Lett.*, 103:152302, 2009. arXiv:0812.3888, <http://dx.doi.org/10.1103/PhysRevLett.103.152302>.
- [83] K. Zapp, G. Ingelman, J. Rathsman, et al. A Monte Carlo Model for 'jet quenching'. *Eur.Phys.J.*, C60:617–632, 2009. arXiv:0804.3568, <http://dx.doi.org/10.1140/epjc/s10052-009-0941-2>.
- [84] J. Casalderrey-Solana, E. V. Shuryak, and D. Teaney. Conical Flow induced by Quenched QCD Jets. *J.Phys.Conf.Ser.*, 27:22–31, 2005. arXiv:hep-ph/0411315, <http://dx.doi.org/10.1016/j.nuclphysa.2006.06.091>.
- [85] L. M. Satarov, H. Stoecker, and I. N. Mishustin. Mach shocks induced by partonic jets in expanding quark-gluon plasma. *Phys.Lett.*, B627(1-4):64–70, 2005. arXiv:hep-ph/0505245, <http://dx.doi.org/10.1016/j.physletb.2005.08.102>.
- [86] J. Casalderrey-Solana, E. V. Shuryak, and D. Teaney. Hydrodynamic Flow from Fast Particles. *pre-print*, 2006. arXiv:hep-ph/0602183.
- [87] K. Aamodt et al. (ALICE Collaboration). Charged-Particle Multiplicity Density at Midrapidity in Central Pb-Pb collisions at $\sqrt{s_{NN}} = 2.76$ TeV. *Phys.Rev.Lett.*, 105:252301, 2010. arXiv:1011.3916, <http://dx.doi.org/10.1103/PhysRevLett.105.252301>.
- [88] I. Arsene et al. (BRAHMS Collaboration). Quark gluon plasma and color glass condensate at RHIC? The Perspective from the BRAHMS experiment. *Nucl.Phys.*, A757:1–27, 2005. arXiv:nucl-ex/0410020, <http://dx.doi.org/10.1016/j.nuclphysa.2005.02.130>.
- [89] B. Back, M. Baker, M. Ballintijn, et al. (PHOBOS Collaboration). The PHOBOS perspective on discoveries at RHIC. *Nucl.Phys.*, A757:28–101, 2005. arXiv:nucl-ex/0410022, <http://dx.doi.org/10.1016/j.nuclphysa.2005.03.084>.

- [90] J. Adams et al. (STAR Collaboration). Experimental and theoretical challenges in the search for the quark gluon plasma: The STAR Collaboration's critical assessment of the evidence from RHIC collisions. *Nucl.Phys.*, A757:102–183, 2005. arXiv:nucl-ex/0501009, <http://dx.doi.org/10.1016/j.nuclphysa.2005.03.085>.
- [91] K. Adcox et al. (PHENIX Collaboration). Formation of dense partonic matter in relativistic nucleus-nucleus collisions at RHIC: Experimental evaluation by the PHENIX collaboration. *Nucl.Phys.*, A757:184–283, 2005. arXiv:nucl-ex/0410003, <http://dx.doi.org/10.1016/j.nuclphysa.2005.03.086>.
- [92] B. Muller, J. Schukraft, and B. Wyslouch. First Results from Pb+Pb collisions at the LHC. *Ann.Rev.Nucl.Part.Sci.*, 62:361–386, 2012. arXiv:1202.3233, <http://dx.doi.org/10.1146/annurev-nucl-102711-094910>.
- [93] R. Hanbury Brown and R. Q. Twiss. A New type of interferometer for use in radio astronomy. *Phil.Mag.*, 45(366):663–682, 1954.
- [94] R. Hanbury Brown and R. Q. Twiss. A Test of a New Type of Stellar Interferometer on Sirius. *Nature*, 178:1046–1048, 1956. <http://dx.doi.org/10.1038/1781046a0>.
- [95] K. Aamodt et al. (ALICE Collaboration). Two-pion Bose-Einstein correlations in central Pb-Pb collisions at $\sqrt{s_{NN}} = 2.76$ TeV. *Phys.Lett.*, B696:328–337, 2011. arXiv:1012.4035, <http://dx.doi.org/10.1016/j.physletb.2010.12.053>.
- [96] F. Noferini (ALICE Collaboration). Anisotropic flow of identified particles in Pb-Pb collisions at $\sqrt{s_{NN}} = 2.76$ TeV measured with ALICE at the LHC. *Nucl.Phys.*, A904-905:483c–486c, 2013. arXiv:1212.1292, <http://dx.doi.org/10.1016/j.nuclphysa.2013.02.058>.
- [97] K. Aamodt et al. (ALICE Collaboration). Suppression of Charged Particle Production at Large Transverse Momentum in Central Pb–Pb Collisions at $\sqrt{s_{NN}} = 2.76$ TeV. *Phys.Lett.*, B696:30–39, 2011. arXiv:1012.1004, <http://dx.doi.org/10.1016/j.physletb.2010.12.020>.
- [98] S. A. Voloshin, A. M. Poskanzer, and R. Snellings. Collective phenomena in non-central nuclear collisions, 2008. arXiv:0809.2949.
- [99] P. Kovtun, D. T. Son, and A. O. Starinets. Viscosity in Strongly Interacting Quantum Field Theories from Black Hole Physics. *Phys.Rev.Lett.*, 94:111601, 2005. arXiv:hep-th/0405231, <http://dx.doi.org/10.1103/PhysRevLett.94.111601>.
- [100] R. K. Ellis, W. J. Stirling, and B. R. Webber. *QCD and Collider Physics*. Cambridge University Press, 1996.
- [101] T. Sjöstrand, S. Mrenna, and P. Z. Skands. PYTHIA 6.4 physics and manual. *JHEP*, 2006(05):026, 2006. arXiv:hep-ph/0603175, <http://dx.doi.org/10.1088/1126-6708/2006/05/026>.
- [102] M. Bähr, S. Gieseke, M. Gigg, et al. Herwig++ physics and manual. *Eur.Phys.J.*, C58:639–707, 2008. arXiv:0803.0883, <http://dx.doi.org/10.1140/epjc/s10052-008-0798-9>.
- [103] T. Gleisberg, S. Höche, F. Krauss, et al. Event generation with SHERPA 1.1. *JHEP*, 2009(02):007, 2009. arXiv:0811.4622, <http://dx.doi.org/10.1088/1126-6708/2009/02/007>.

- [104] K. Zapp, J. Stachel, and U. A. Wiedemann. A Local Monte Carlo implementation of the non-abelian Landau-Pomerantschuk-Migdal effect. *Phys.Rev.Lett.*, 103:152302, 2009. arXiv:0812.3888, <http://dx.doi.org/10.1103/PhysRevLett.103.152302>.
- [105] K. J. Eskola, K. Kajantie, and J. Lindfors. Quark and gluon production in high energy nucleus-nucleus collisions. *Nucl.Phys.*, B323:37, 1989. [http://dx.doi.org/10.1016/0550-3213\(89\)90586-5](http://dx.doi.org/10.1016/0550-3213(89)90586-5).
- [106] C. Gale, S. Jeon, and B. Schenke. HYDRODYNAMIC MODELING OF HEAVY-ION COLLISIONS. *Int.J.Mod.Phys.*, A28:1340011, 2013. arXiv:1301.5893, <http://dx.doi.org/10.1142/S0217751X13400113>.
- [107] S. A. Bass. OSCAR format. https://wiki.bnl.gov/TECHQM/index.php/OSCAR_Standard_Output_Format_for_Hydro_Codes.
- [108] M. Dobbs and J. B. Hansen. The HepMC C++ Monte Carlo event record for High Energy Physics. *Comput.Phys.Commun.*, 134:41–46, 2001. [http://dx.doi.org/10.1016/S0010-4655\(00\)00189-2](http://dx.doi.org/10.1016/S0010-4655(00)00189-2).
- [109] A. Buckley, J. Butterworth, D. Grellscheid, et al. Rivet user manual. *Comput.Phys.Commun.*, 184(12):2803–2819, 2013. arXiv:1003.0694, <http://dx.doi.org/10.1016/j.cpc.2013.05.021>.
- [110] C. Nonaka and S. A. Bass. Space-time evolution of bulk QCD matter. *Phys. Rev.*, C75:014902, 2007. arXiv:nucl-th/0607018, <http://dx.doi.org/10.1103/PhysRevC.75.014902>.
- [111] S. A. Bass, C. Gale, A. Majumder, et al. Systematic comparison of jet energy-loss schemes in a realistic hydrodynamic medium. *Phys. Rev.*, C79:024901, 2009. arXiv:0808.0908, <http://dx.doi.org/10.1103/PhysRevC.79.024901>.
- [112] C. Shen, U. Heinz, P. Huovinen, et al. Systematic parameter study of hadron spectra and elliptic flow from viscous hydrodynamic simulations of Au+Au collisions at $\sqrt{s_{NN}} = 200$ GeV. *Phys.Rev.*, C82:054904, 2010. arXiv:1010.1856, <http://dx.doi.org/10.1103/PhysRevC.82.054904>.
- [113] T. Renk, H. Holopainen, U. Heinz, et al. Systematic comparison of jet quenching in different fluid-dynamical models. *Phys.Rev.*, C83:014910, 2011. arXiv:1010.1635, <http://dx.doi.org/10.1103/PhysRevC.83.014910>.
- [114] P. Huovinen and P. Petreczky. QCD Equation of State and Hadron Resonance Gas. *Nucl.Phys.*, A837:26–53, 2010. arXiv:0912.2541, <http://dx.doi.org/10.1016/j.nuclphysa.2010.02.015>.
- [115] F. Cooper and G. Frye. Single particle distribution in the hydrodynamic and statistical thermodynamic models of multiparticle Production. *Phys.Rev.*, D10:186, 1974. <http://dx.doi.org/10.1103/PhysRevD.10.186>.
- [116] A. Adare et al. (PHENIX Collaboration). Inclusive cross-section and double helicity asymmetry for π^0 production in p + p collisions at $\sqrt{s} = 200$ GeV: Implications for the polarized gluon distribution in the proton. *Phys.Rev.*, D76:051106, 2007. arXiv:0704.3599, <http://dx.doi.org/10.1103/PhysRevD.76.051106>.

- [117] S. S. Adler et al. (PHENIX Collaboration). Midrapidity Neutral Pion Production in Proton-Proton Collisions at $\sqrt{s} = 200$ GeV. *Phys.Rev.Lett.*, 91:241803, 2003. arXiv:hep-ex/0304038, <http://dx.doi.org/10.1103/PhysRevLett.91.241803>.
- [118] M. Ploskon (STAR Collaboration). Inclusive cross section and correlations of fully reconstructed jets in $\sqrt{s_{NN}} = 200$ GeV Au+Au and p+p collisions. *Nucl.Phys.*, A830:255C–258C, 2009. arXiv:0908.1799, <http://dx.doi.org/10.1016/j.nuclphysa.2009.10.095>.
- [119] S. Floerchinger and K. C. Zapp. Hydrodynamics and Jets in Dialogue, 2014. arXiv:1407.1782.
- [120] *ECFA-CERN Workshop on Large Hadron Collider in the LEP Tunnel, Lausanne and CERN, Geneva, Switzerland, 21-27 Mar 1984: Proceedings. 1.*, 1984.
- [121] *ECFA-CERN Workshop on Large Hadron Collider in the LEP Tunnel, Lausanne and CERN Geneva, Switzerland, 21-27 Mar 1984: Proceedings.2.*, 1984.
- [122] T. S. Pettersson and P. Lefèvre (LHC Study Group). The Large Hadron Collider: conceptual design. Technical Report CERN-AC-95-05 LHC, CERN, Geneva, 1995.
- [123] O. S. Brüning, P. Collier, P. Lebrun, et al. *LHC Design Report*, volume 1. CERN, Geneva, 2004.
- [124] O. S. Brüning, P. Collier, P. Lebrun, et al. *LHC Design Report*, volume 2. CERN, Geneva, 2004.
- [125] M. Benedikt, P. Collier, V. Mertens, et al. *LHC Design Report*, volume 3. CERN, Geneva, 2004.
- [126] L. Evans and P. Bryant. LHC Machine. *JINST*, 3:S08001, 2008. <http://dx.doi.org/10.1088/1748-0221/3/08/S08001>.
- [127] G. Aad et al. (ATLAS Collaboration). The ATLAS Experiment at the CERN Large Hadron Collider. *JINST*, 3:S08003, 2008. <http://dx.doi.org/10.1088/1748-0221/3/08/S08003>.
- [128] S. Chatrchyan et al. (CMS Collaboration). The CMS experiment at the CERN LHC. *JINST*, 3:S08004, 2008. <http://dx.doi.org/10.1088/1748-0221/3/08/S08004>.
- [129] A. Augusto Alves Jr et al. (LHCb Collaboration). The LHCb Detector at the LHC. *JINST*, 3:S08005, 2008. <http://dx.doi.org/10.1088/1748-0221/3/08/S08005>.
- [130] K. Aamodt et al. (ALICE Collaboration). The ALICE experiment at the CERN LHC. *JINST*, 3:S08002, 2008. <http://dx.doi.org/10.1088/1748-0221/3/08/S08002>.
- [131] O. Adriani et al. (LHCf Collaboration). The LHCf detector at the CERN Large Hadron Collider. *JINST*, 3:S08006, 2008. <http://dx.doi.org/10.1088/1748-0221/3/08/S08006>.
- [132] G. Anelli et al. (TOTEM Collaboration). The TOTEM experiment at the CERN Large Hadron Collider. *JINST*, 3:S08007, 2008. <http://dx.doi.org/10.1088/1748-0221/3/08/S08007>.
- [133] J. Pinfold, R. Soluk, Y. Yao, et al. (MoEDAL Collaboration). Technical Design Report of the MoEDAL Experiment. Technical Report CERN-LHCC-2009-006. MoEDAL-TDR-001, CERN, Geneva, 2009.

- [134] B. Abelev et al. (ALICE Collaboration). Measurement of inelastic, single- and double-diffraction cross sections in proton–proton collisions at the LHC with ALICE. *Eur.Phys.J.*, C73:2456, 2013. arXiv:1208.4968, <http://dx.doi.org/10.1140/epjc/s10052-013-2456-0>.
- [135] LHC statistics. <https://lhc-statistics.web.cern.ch/LHC-Statistics>.
- [136] ATLAS luminosity page. <https://twiki.cern.ch/twiki/bin/view/AtlasPublic/LuminosityPublicResults>.
- [137] CMS luminosity page. <https://twiki.cern.ch/twiki/bin/view/CMSPublic/LumiPublicResults>.
- [138] LHCb luminosity page. <http://lhcb-operationsplots.web.cern.ch/lhcb-operationsplots>.
- [139] B. B. Abelev et al. (ALICE Collaboration). Performance of the ALICE Experiment at the CERN LHC. *pre-print*, 2014. arXiv:1402.4476.
- [140] H. J. Specht. Experimental aspects of heavy ion physics at LHC energies. In G. Jarlskog, editor, *ECFA Large Hadron Collider Workshop, Aachen, Germany, 4-9 Oct 1990: Proceedings.2.* 1990.
- [141] J. Schukraft. A dedicated heavy ion experiment at the LHC: Expression of interest. In *General Meeting on LHC Physics and Detectors*, pages 479–510. CERN, Evian-les-Bains, France, 1992. <http://cds.cern.ch/record/236265>.
- [142] A. Collaboration (ALICE Collaboration). Letter of Intent for A Large Ion Collider Experiment [ALICE]. Technical Report CERN-LHCC-93-016. LHCC-I-4, CERN, Geneva, 1993.
- [143] *ALICE: Technical proposal for a Large Ion collider Experiment at the CERN LHC*. LHC Tech. Proposal. CERN, Geneva, 1995.
- [144] G. Dellacasa, L. Ramello, E. Scalas, et al. (ALICE Collaboration). *ALICE time projection chamber: Technical Design Report*. Technical Design Report ALICE. CERN, Geneva, 2000.
- [145] J. Alme, Y. Andres, H. Appelshäuser, et al. The ALICE TPC, a large 3-dimensional tracking device with fast readout for ultra-high multiplicity events. *Nucl.Instrum.Meth.*, A622:316–367, 2010. arXiv:1001.1950, <http://dx.doi.org/10.1016/j.nima.2010.04.042>.
- [146] G. Dellacasa et al. (ALICE Collaboration). *ALICE Time-Of-Flight system (TOF): Technical Design Report*. Technical Design Report ALICE. CERN, Geneva, 2000.
- [147] T. Cormier, C. W. Fabjan, L. Riccati, et al. The Electromagnetic Calorimeter Addendum to the Technical Proposal. Technical Report CERN-LHCC-2006-014. CERN-LHCC-96-32-Add-3, CERN, Geneva, 2006.
- [148] B. Taylor (RD12 Project Collaboration). TTC distribution for LHC detectors. *IEEE Trans.Nucl.Sci.*, 45:821–828, 1998. <http://dx.doi.org/10.1109/23.682644>.
- [149] V. Ginzburg and I. Frank. Radiation of a uniformly moving electron due to its transition from one medium into another. *J.Phys.(USSR)*, 9:353–362, 1945.

- [150] G. Dellacasa and P. Braun-Munzinger. ALICE: A Transition Radiation Detector for Electron Identification within the ALICE Central Detector - an addendum to the Technical Proposal. Technical Report CERN-LHCC-99-013. LHCC-P-3-Add-2, CERN, Geneva, 1999.
- [151] V. Angelov (ALICE TRD Collaboration). Design and Performance of the ALICE TRD front-end electronics. *Nucl.Instrum.Meth.*, A563(2):317–320, 2006. <http://dx.doi.org/10.1016/j.nima.2006.02.169>.
- [152] V. Angelov et al. *TRAP manual*. https://alice.physi.uni-heidelberg.de/svn/trd/TRAP_docu/trunk.
- [153] R. Gareus. *Slow Control Serial Network and its implementation for the Transition Radiation Detector*. Diploma thesis, University of Heidelberg, 2002.
- [154] K. Große. *GSI Scientific Report 2005 [GSI Report 2006-1]*, volume 2006-1 of *GSI Report*. GSI, Darmstadt, 2006. Wissenschaftlicher Ergebnisbericht der GSI, GSI Annual Report, <http://repository.gsi.de/record/53526>.
- [155] T. Krawutschke. *Reliability and Redundancy of an Embedded System used in the Detector Control System of the ALICE Experiment*. Doctoral thesis, University of Mannheim, 2009.
- [156] U. Westerhoff. *The FEE Server Control Engine of the ALICE-TRD*. Diploma thesis, University of Münster, 2009.
- [157] S. Kirsch, F. Rettig, D. Hutter, et al. An FPGA-based High-Speed, Low-Latency Processing System for High-Energy Physics. In *Field Programmable Logic and Applications*, pages 562 – 567. 2010. <http://dx.doi.org/10.1109/FPL.2010.110>.
- [158] I. Antcheva, M. Ballintijn, B. Bellenot, et al. ROOT: A C++ framework for petabyte data storage, statistical analysis and visualization. *Comput.Phys.Commun.*, 180:2499–2512, 2009. <http://dx.doi.org/10.1016/j.cpc.2009.08.005>.
- [159] R. Brun et al. ROOT. <http://root.cern.ch>.
- [160] AliRoot. <http://aliweb.cern.ch/Offline>.
- [161] B. Abelev et al. (ALICE Collaboration). Measurement of event background fluctuations for charged particle jet reconstruction in Pb-Pb collisions at $\sqrt{s_{NN}} = 2.76$ TeV. *Journal of High Energy Physics*, 2012(3):53, 2012. [http://dx.doi.org/10.1007/JHEP03\(2012\)053](http://dx.doi.org/10.1007/JHEP03(2012)053).
- [162] S. Kirsch. *High-Speed Event-Buffered Read-Out for the ALICE TRD*. Doctoral thesis, University of Frankfurt, 2014.
- [163] S. Zimmer. *Design, Implementation and Commissioning of the Pretrigger System for the Transition Radiation Detector at the ALICE experiment of CERN*. Diploma thesis, University of Heidelberg, 2008.
- [164] Xilinx DS099 Spartan-3 FPGA Family data sheet. http://www.xilinx.com/support/documentation/data_sheets/ds099.pdf.
- [165] Xilinx DS112 Virtex-4 Family Overview. http://www.xilinx.com/support/documentation/data_sheets/ds112.pdf.

- [166] S. Schmiederer. *Development and Implementation of the Control System for the Pre-Trigger System of the Transition Radiation Detector at ALICE*. Diploma thesis, University of Heidelberg, 2009.
- [167] *Trigger output logic – hardware guide for the front-end designers*.
- [168] M. Matsumoto and T. Nishimura. Mersenne twister: a 623-dimensionally equidistributed uniform pseudo-random number generator. *ACM Trans. Model. Comput. Simul.*, 8(1):3–30, 1998. <http://dx.doi.org/10.1145/272991.272995>.
- [169] CERN DIP. <http://j2eeps.cern.ch/wikis/display/EN/DIP+and+DIM>.
- [170] ProASIC3 Flash Family FPGAs Datasheet. http://www.microsemi.com/document-portal/doc_download/130704-proasic3-flash-family-fpgas-datasheet.
- [171] J. Klein. *Commissioning of and Preparations for Physics with the Transition Radiation Detector in A Large Ion Collider Experiment at CERN*. Diploma thesis, University of Heidelberg, 2008.
- [172] M. Gutfleisch. *Local Signal Processing of the ALICE Transition Radiation Detector at LHC (CERN)*. Doctoral thesis, University of Heidelberg, 2006.
- [173] M. Al Helwi. *Gain Calibration of the ALICE Transition Radiation Detector with Krypton-83*. Diploma thesis, University of Heidelberg, 2010.
- [174] J. Stiller. *Gain Calibration of the ALICE TRD using the Decay of $^{83\text{m}}\text{Kr}$ and Alignment of the ALICE TRD*. Diploma thesis, University of Heidelberg, 2011.
- [175] J. Klein (ALICE Collaboration). Triggering with the ALICE TRD. *Nucl.Instrum.Meth.*, A706:23–28, 2013. arXiv:1112.5110, <http://dx.doi.org/10.1016/j.nima.2012.05.011>.
- [176] M. Walter. *Performance of Online Tracklet Reconstruction with the ALICE TRD*. Diploma thesis, University of Münster, 2010.
- [177] U. Westerhoff. *No title*. Doctoral thesis, University of Münster, 2014.
- [178] C. Haltebourg. *Implementation of the ALICE TRD TRAP-chip into AliRoot*. Diploma thesis, University of Heidelberg, 2008.
- [179] J. de Cuveland. *Entwicklung der globalen Spurrekonstruktionseinheit für den ALICE-Übergangsstrahlungsdetektor am LHC (CERN)*. Diploma thesis, University of Heidelberg, 2003.
- [180] J. de Cuveland. *A Track Reconstructing Low-latency Trigger Processor for High-energy Physics*. Doctoral thesis, University of Heidelberg, 2009.
- [181] F. Rettig. *The Global Online Tracking and Trigger System for the ALICE Transition Radiation Detector at the Large Hadron Collider*. Doctoral thesis, University of Frankfurt, 2014.
- [182] B. von Haller et al. (ALICE Collaboration). The ALICE data quality monitoring system. *J.Phys.Conf.Ser.*, 331:022030, 2011. <http://dx.doi.org/10.1088/1742-6596/331/2/022030>.
- [183] B. Heß. *Online Electron Identification for Triggering with the ALICE Transition Radiation Detector*. Diploma thesis, University of Heidelberg, 2011.

- [184] N. Wahl. *Performance of the local on-line Tracking and of a track-based Jet Trigger Algorithm for the ALICE TRD on the Basis of Monte-Carlo Simulations*. Bachelor's thesis, University of Heidelberg, 2011.
- [185] F. Mücke. *Triggering on light nuclei with the ALICE Transition Radiation Detector*. Bachelor's thesis, University of Heidelberg, 2012.
- [186] B. Abelev et al. Charged jet production cross sections and properties in proton-proton collisions at $\sqrt{s} = 7$ TeV. *pre-print*, 2014.
- [187] P. Cortese et al. (ALICE Collaboration). *ALICE transition-radiation detector: Technical Design Report*. Technical Design Report ALICE. CERN, Geneva, 2001.
- [188] U. Grundinger. *GSI Scientific Report 2001 [GSI Report 2002-1]*, volume 2002-1 of *GSI Report*. GSI, Darmstadt, 2002. Wissenschaftlicher Ergebnisbericht der GSI, GSI Annual Report, <http://repository.gsi.de/record/53530>.
- [189] B. Bathen. *Jet Measurements and Reconstruction Biases in Proton-Proton and Pb-Pb Collisions with ALICE at the LHC*. Doctoral thesis, University of Münster, 2012.
- [190] J. Klein. ALICE TRD trigger. <https://twiki.cern.ch/twiki/bin/view/ALICE/TRDTriggers>.
- [191] K. Aamodt et al. (ALICE Collaboration). Higher Harmonic Anisotropic Flow Measurements of Charged Particles in Pb-Pb Collisions at $\sqrt{s_{NN}}=2.76$ TeV. *Phys.Rev.Lett.*, 107:032301, 2011. arXiv:1105.3865, <http://dx.doi.org/10.1103/PhysRevLett.107.032301>.
- [192] K. Aamodt et al. (ALICE Collaboration). Harmonic decomposition of two-particle angular correlations in Pb-Pb collisions at $\sqrt{s_{NN}} = 2.76$ TeV. *Phys.Lett.*, B708(3-5):249–264, 2012. arXiv:1109.2501, <http://dx.doi.org/10.1016/j.physletb.2012.01.060>.
- [193] S. Chatrchyan et al. (CMS Collaboration). Measurement of the elliptic anisotropy of charged particles produced in PbPb collisions at nucleon-nucleon center-of-mass energy = 2.76 TeV. *Phys.Rev.*, C87:014902, 2013. arXiv:1204.1409, <http://dx.doi.org/10.1103/PhysRevC.87.014902>.
- [194] B. Abelev et al. (ALICE Collaboration). Anisotropic flow of charged hadrons, pions and (anti-)protons measured at high transverse momentum in Pb-Pb collisions at $\sqrt{s_{NN}}=2.76$ TeV. *Phys.Lett.*, B719:18–28, 2013. arXiv:1205.5761, <http://dx.doi.org/10.1016/j.physletb.2012.12.066>.
- [195] K. Aamodt et al. (ALICE Collaboration). Elliptic flow of charged particles in Pb-Pb collisions at 2.76 TeV. *Phys.Rev.Lett.*, 105:252302, 2010. arXiv:1011.3914, <http://dx.doi.org/10.1103/PhysRevLett.105.252302>.
- [196] B. Abelev et al. (ALICE Collaboration). Measurement of charged jet suppression in Pb-Pb collisions at $\sqrt{s_{NN}} = 2.76$ TeV. *JHEP*, 1403:013, 2014. arXiv:1311.0633, [http://dx.doi.org/10.1007/JHEP03\(2014\)013](http://dx.doi.org/10.1007/JHEP03(2014)013).
- [197] G. Aad et al. (ATLAS Collaboration). Observation of a Centrality-Dependent Dijet Asymmetry in Lead-Lead Collisions at $\sqrt{s_{NN}} = 2.77$ TeV with the ATLAS Detector at the LHC. *Phys.Rev.Lett.*, 105:252303, 2010. arXiv:1011.6182, <http://dx.doi.org/10.1103/PhysRevLett.105.252303>.

- [198] H. Stöcker. Collective flow signals the quark gluon plasma. *Nucl.Phys.*, A750(1):121–147, 2005. arXiv:nucl-th/0406018, <http://dx.doi.org/10.1016/j.nuclphysa.2004.12.074>.
- [199] B. Abelev et al. (STAR Collaboration). Indications of Conical Emission of Charged Hadrons at RHIC. *Phys.Rev.Lett.*, 102:052302, 2009. arXiv:0805.0622, <http://dx.doi.org/10.1103/PhysRevLett.102.052302>.
- [200] P. M. Chesler and L. G. Yaffe. The Wake of a quark moving through a strongly-coupled plasma. *Phys.Rev.Lett.*, 99:152001, 2007. arXiv:0706.0368, <http://dx.doi.org/10.1103/PhysRevLett.99.152001>.
- [201] B. Betz, J. Noronha, G. Torrieri, et al. Conical Correlations, Bragg Peaks, and Transverse Flow Deflections in Jet Tomography. *Nucl.Phys.*, A830:777C–780C, 2009. arXiv:0907.2516, <http://dx.doi.org/10.1016/j.nuclphysa.2009.10.070>.
- [202] B. Betz, M. Gyulassy, D. H. Rischke, et al. Jet Propagation and Mach Cones in (3+1)d Ideal Hydrodynamics. *J.Phys.*, G35:104106, 2008. arXiv:0804.4408, <http://dx.doi.org/10.1088/0954-3899/35/10/104106>.
- [203] G. Torrieri, B. Betz, J. Noronha, et al. Mach cones in heavy ion collisions. *Acta Phys.Polon.*, B39:3281–3308, 2008. arXiv:0901.0230.
- [204] E. V. Shuryak. Jet/Fireball Edge should be observable! *pre-print*, 2011. arXiv:1101.4839.
- [205] V. Khachatryan and E. V. Shuryak. Sound Waves from Quenched Jets. *pre-print*, 2011. arXiv:1108.3098.
- [206] B. Abelev et al. (ALICE Collaboration). Centrality dependence of π , K, p production in Pb-Pb collisions at $\sqrt{s_{NN}} = 2.76$ TeV. *Phys.Rev.*, C88:044910, 2013. arXiv:1303.0737, <http://dx.doi.org/10.1103/PhysRevC.88.044910>.
- [207] S. Sapeta and U. A. Wiedemann. Jet hadrochemistry as a characteristics of jet quenching. *Eur.Phys.J.*, C55:293–302, 2008. arXiv:0707.3494, <http://dx.doi.org/10.1140/epjc/s10052-008-0592-8>.
- [208] B. Abelev et al. (ALICE Collaboration). Centrality determination of Pb-Pb collisions at $\sqrt{s_{NN}} = 2.76$ TeV with ALICE. *Phys.Rev.*, C88:044909, 2013. arXiv:1301.4361, <http://dx.doi.org/10.1103/PhysRevC.88.044909>.
- [209] A. M. Poskanzer and S. Voloshin. Methods for analyzing anisotropic flow in relativistic nuclear collisions. *Phys.Rev.*, C58:1671–1678, 1998. arXiv:nucl-ex/9805001, <http://dx.doi.org/10.1103/PhysRevC.58.1671>.
- [210] B. Heß. *No title*. Doctoral thesis, University of Tübingen, in preparation.
- [211] M. Völkl. *Study of the Transverse Momentum Spectra of Semielectronic Heavy Flavor Decays in pp Collisions at $\sqrt{s} = 7$ TeV and Pb-Pb Collisions at $\sqrt{s_{NN}} = 2.76$ TeV with ALICE*. Master’s thesis, University of Heidelberg, 2012.
- [212] G. Aad et al. (ATLAS Collaboration). Measurement of the Azimuthal Angle Dependence of Inclusive Jet Yields in Pb+Pb Collisions at $\sqrt{s_{NN}} = 2.76$ TeV with the ATLAS detector. *Phys.Rev.Lett.*, 111:152301, 2013. arXiv:1306.6469, <http://dx.doi.org/10.1103/PhysRevLett.111.152301>.

- [213] R. Bertens. Event plane dependence of charged jet yields in $\sqrt{s_{NN}} = 2.76$ TeV Pb–Pb collisions with ALICE, 2014.
- [214] A. Ohlson (STAR Collaboration). Jets and Jet-like correlations in STAR. *Nucl.Phys.*, A910-911:51–57, 2013. arXiv:1208.6362, <http://dx.doi.org/10.1016/j.nuclphysa.2012.12.071>.
- [215] A. Davila (STAR Collaboration). Proton/Pion Ratios in $\Delta\phi$ with Respect to a Jet in $\sqrt{s_{NN}} = 200$ GeV Au+Au Collisions at STAR. *Nucl.Phys.*, A910-911:310–313, 2013. arXiv:1207.7156, <http://dx.doi.org/10.1016/j.nuclphysa.2012.12.018>.
- [216] M. Veldhoen (ALICE Collaboration). p/π Ratio in Di-Hadron Correlations. *Nucl.Phys.*, A910-911:306–309, 2013. arXiv:1207.7195, <http://dx.doi.org/10.1016/j.nuclphysa.2012.12.103>.